Graphene Engineering:
An *ab initio* Study of the Thermodynamic Stability of Epitaxial Graphene and the Surface Reconstructions of Silicon Carbide

Dissertation

zur Erlangung des akademischen Grades

doctor rerum naturalium
(Dr. rer. nat.)

im Fach: Physik

Spezialisierung: Theoretische Physik

eingereicht an der Mathematisch-Naturwissenschaftlichen Fakultät

der Humboldt-Universität zu Berlin

von

Diplom Physikerin Lydia Nemec

Präsidentin/ Präsident der Humboldt-Universität zu Berlin
Prof. Dr. Jan-Hendrik Olbertz

Dekanin/ Dekan der Mathematisch-Naturwissenschaftlichen Fakultät
Prof. Dr. Elmar Kulke

Gutachter/innen:	1.	Prof. Dr. Claudia Draxl
	2.	Prof. Dr. Patrick Rinke
	3.	Prof. Dr. Ludger Wirtz
Tag der mündlichen Prüfung:		7. Juli 2015

Abstract

Graphene with its unique properties spurred the design of nanoscale electronic devices. Graphene films grown by Si sublimation on SiC surfaces are promising material combinations for future graphene applications based on existing semiconductor technologies. Obviously, the exact material properties of graphene depend on the its interaction with the substrate. Understanding the atomic and electronic structure of the SiC-graphene interface, is an important step to refine the growth quality. In this work, computational *ab initio* methods based on density-functional theory (DFT) are used to simulate the SiC-graphene interface on an atomistic level without empirical parameters. We apply state-of-the-art density-functional approximation (DFA), in particular the Heyd-Scuseria-Ernzerhof hybrid functional including van-der-Waals dispersion corrections to address the weak bonding between the substrate and graphene layers. DFA simulations allow to interpret and complement experimental results and are able to predict the behaviour of complex interface system.

Experimental work has shown that on the Si face of SiC, a partially covalently bonded carbon layer, the zero-layer graphene (ZLG), grows as $(6\sqrt{3} \times 6\sqrt{3})$-R30° commensurate periodic film. On top of the ZLG layer forms mono-layer graphene (MLG) as large ordered areas and then few-layer graphene. By constructing an *ab initio* surface phase diagram, we show that ZLG and MLG are at least near equilibrium phases. Our results imply the existence of temperature and pressure conditions for self-limiting growth of MLG key to the large-scale graphene production. At the interface to the substrate, the Si atoms can be passivated by H resulting in quasi-free-standing mono-layer graphene (QFMLG). We show that by H intercalation both the corrugation and doping are reduced significantly. Our calculations demonstrate that the electronic structure of graphene is influenced by unsaturated Si atoms in the ZLG and therefore confirm that H intercalation is a promising route towards the preparation of high-quality graphene films.

The situation on the C face of SiC is very different. In experiment, the growth of large areas of graphene with well defined layer thickness is difficult. At the onset of graphene formation a phase mixture of different surface phases is observed. We will address the stability of the surface phases that occur on the C side of SiC. However, the atomic structure of some of the competing surface phases, as well as of the SiC-graphene interface, is unknown. We present a new model for the (3×3) reconstruction – the *Si twist model*. The surface energies of this Si twist model, the known $(2\times2)_C$ adatom phase, and a graphene covered $(2\times2)_C$ phase cross at the chemical potential limit of graphite, which explains the observed phase mixture. We argue that on the C face the formation of a well-controlled interface structure like the ZLG layer is hindered by Si-rich surface reconstructions.

Zusammenfassung

Die außergewöhnlichen Eigenschaften einer einzelnen Graphenlage ermöglichen das Design von elektronischen Bauteilen im Nanometerbereich. Graphen kann auf der Oberfläche von Siliziumkarbonat (SiC) durch das Ausdampfen von Si epitaktisch gewachsen werden. Die Materialkombination SiC und Graphen ist daher hervorragend für die zukünftige Anwendung von Graphen basierten Technologien geeignet. Die genauen Eigenschaften von epitaktischem Graphen hängen von der Stärke und Art der Interaktion mit dem Substrat ab. Ein detailliertes Verständnis der atomaren und elektronischen Struktur der Grenzschicht zwischen Graphen und SiC ist ein wichtiger Schritt um die Wachstumsqualität von epitaktischem Graphen zu verbessern. Wir nutzen Dichtefunktionaltheorie (DFT) um das Hybridsystem Graphen-SiC auf atomarer Ebene ohne empirische Parameter zu simulieren. Die schwache Bindung zwischen dem Substrat und der Graphenlage beschreiben wir mit van-der-Waals korrigierten Austausch-Korrelations-Funktionalen, insbesonderen mit dem Hybrid Funktional von Heyd, Scuseria und Ernzerhof [138, 175]. Die Simulationen geben Aufschluß über das Verhalten und die Eigenschaften der komplexen Grenzschicht.

Experimentelle Arbeiten auf der Si-terminierten Oberfläche von SiC haben gezeigt, dass die Grenzschicht durch eine teilweise kovalent gebundene Kohlenstofflage als $(6\sqrt{3} \times 6\sqrt{3})$-R30° kommensurate periodische Struktur wächst. Die Grenzschicht zwischen SiC und Graphen wird häufig als ZLG bezeichnet. Über dem ZLG bildet sich die erste großflächig geordnete Graphenlage (MLG). Durch das Konstruieren eines *ab initio* Oberflächenphasendiagrams zeigen wir, dass sowohl ZLG als auch MLG Gleichgewichtsphasen sind. Unsere Ergebnisse implizieren, dass Temperatur- und Druckbedingungen für den selbstbegrenzenden Graphenwachstum existieren. Die Si Atome an der Grenzschicht können durch Wasserstoffatome abgesättigt werden und den ZLG zu quasi-freistehendem Graphen (QFMLG) umwandeln. Wir zeigen, dass durch die H-Interkalation das Doping und die Riffellung von epitaktischem Graphene reduziert werden. Aus unseren Rechnungen folgt, dass die ungesättigten Si Atome an der Grenzschicht die elektronischen Eigenschaften von Graphen beinflussen. Anhand unsere Ergebnisse zeigen wir, dass die H-Interkalation eine vielversprechende Methode ist um qualitativ hochwertiges Graphen zu wachsen.

Das Graphenwachstum auf der C-terminierten Oberfläche von SiC verhält sich im Experiment qualitativ anders als auf der Si Seite. Zu Beginn des Graphenwachstums wird eine Mischung verschiedener Oberflächenphasen beobachtet. Wir diskutieren die Stabilität dieser konkurierenden Phasen. Die atomaren Strukturen von einigen dieser Phasen, inklusive der Graphen-SiC Grenzschicht, sind nicht bekannt wodurch die theoretische Beschreibung erschwert wird. Wir präsentieren ein neues Model für die bisher unbekannte (3×3) Rekonstruktion – das *Si Twist*

Model. Die Oberflächenenergie vom Si Twist Model und von der bekannten $(2\times2)_C$ Oberflächenrekonstruktion schneiden sich direkt an der Grenze zur Graphitbildung. Dies erklärt die experimentell beobachtete Phasenkoexistenz zu Beginn des Graphenwachstums. Wir schlussfolgern, dass die Bildung von einer wohldefinierten Grenzschichtstruktur, wie der ZLG auf der Si Seite, auf der C Seite durch Si-reiche Oberflächenrekonstruktionen blockiert wird.

I do not try to dance better than anyone else,
I only try to dance better than myself.

Mikhail Baryshnikov

Contents

Introduction **1**

I Electronic Structure Theory **9**

1 The Many-Body Problem **11**
1.1 The Many-Body Schrödinger Equation 11
1.2 The Born-Oppenheimer Approximation 13

2 Basic Concepts of Density-Functional Theory **15**
2.1 The Hohenberg-Kohn Theorems 15
2.2 The Kohn-Sham Equations 17
2.3 Approximations for the Exchange-Correlation Functional 20
2.3.1 Local-Density Approximation (LDA) 20
2.3.2 Generalised Gradient Approximation (GGA) 21
2.3.3 Hybrid Functionals 22
2.4 Van-der-Waals Contribution in DFT 23
2.5 Computational Aspects of DFT: The FHI-aims Package 25

3 Swinging Atoms: The Harmonic Solid **29**

4 *Ab initio* Atomistic Thermodynamics **32**
4.1 The Gibbs Free Energy 32
4.2 The Surface Free Energy 34

5 The Kohn-Sham Band Structure **39**

II Bulk Systems **41**

6 Carbon-Based Structures **43**
6.1 The Ground State Properties of Diamond, Graphite and Graphene 45
6.2 The Challenge of Inter-planar Bonding in Graphite 50
6.3 The Electronic Structure of Graphene 58

7 Silicon Carbide: The Substrate **61**
7.1 Polymorphism in Silicon Carbide 62
7.2 The Electronic Structure of Silicon Carbide Polymorphs 66

III The Silicon Carbide Surfaces and Epitaxial Graphene **71**

8 The 3C-SiC(111) Surface phases **73**
8.1 The Silicon-Rich Reconstructions of the 3C-SiC(111) Surface 74

8.1.1 3C-SiC(111) ($\sqrt{3} \times \sqrt{3}$)-R30° Si Adatom Structure 74
8.1.2 The Silicon-Rich 3C-SiC(111) (3 × 3) Reconstruction 77
8.2 The Carbon-Rich Reconstructions of the 3C-SiC(111) Surface 79

9 Strain in Epitaxial Graphene 85
9.1 ZLG-Substrate Coupling and its Effect on the Lattice Parameter 85
9.2 Interface Models for Epitaxial Graphene 88
9.3 Defect Induced Strain in Graphene 95
9.4 Summary 100

10 Thermodynamic Equilibrium Conditions of Graphene Films on SiC 103

11 Band Structure Unfolding 107
11.1 The Brillouin Zone (BZ) 110
11.1.1 The Wave Function 112
11.2 The Unfolding Projector 113
11.3 The Hydrogen Chain: Practical Aspects of the Band Structure Unfolding 117

12 The Electronic Structure of Epitaxial Graphene on 3C-SiC(111) 122
12.1 The Electronic Structure of Epitaxial Graphene 123
12.2 The Influence of Doping and Corrugation on the Electronic Structure 127
12.3 The Silicon Dangling Bonds and their Effect on the Electronic Structure 133
12.4 Summary 135

13 The Decoupling of Epitaxial Graphene on SiC by Hydrogen Intercalation 137
13.1 The Vertical Graphene-Substrate Distance 138
13.2 The Electron Density Maps 140
13.3 Summary 142

14 Epitaxial Graphene on the C Face of SiC 143
14.1 The 3C-SiC ($\bar{1}\bar{1}\bar{1}$) Surface Reconstructions 143
14.1.1 The (2 x 2) Si Adatom Phase 143
14.1.2 The (3 x 3) Surface Reconstruction: An Open Puzzle 145
14.1.3 The Si Twist Model 150
14.2 Assessing the Graphene and SiC Interface 152
14.3 Summary 156

Conclusions 157

Appendices 161

A Thermal Expansion and Phase Coexistence I

B Numerical Convergence IX
B.1 The Basis Set IX
B.2 Slab Thickness XI
B.3 k-Space Integration Grids XII
B.4 The Heyd-Scuseria-Ernzerhof Hybrid Functional Family for 3C-SiC XIII

C Band Structure Plots of SiC XV
C.1 Cubic Silicon Carbide (3C-SiC) XV
C.2 Hexagonal Silicon Carbide 4H-SiC and 6H-SiC XVI
C.2.1 The HSE Band Structure of 4H-SiC XVI
C.2.2 The HSE Band Structure of 6H-SiC XVII

D Phonon Band Structure XVIII
D.1 The Phonon Band Structure of the Carbon Structures: Graphene, Graphite and Diamond XVIII
D.1.1 Graphene XVIII
D.1.2 Graphite XX
D.1.3 Diamond XXI
D.2 Phonon Band Structure of Silicon Carbide XXII

E Counting Dangling Bonds XXIII

F Comparing the PBE and HSE06 Density of States of the MLG Phase XXV
F.1 Influence of the DFT Functional XXV

G Bulk Stacking Order: The Si-terminated 6H-SiC(0001) Surface XXVIII

H Influence of the Polytype XXIX

I The 3C-SiC(111)-(3x3) Phase: Details on the Geometry XXX

J The History of Graphite Interlayer Binding Energy XXXII

Acronyms XXXV

List of Figures XLI

List of Tables LIII

Bibliography XCVII

Acknowledgements XCIX

Publication List CI

Selbständigkeitserklärung CIII

Introduction

The technological progress in the second half of the twentieth century was dominated by the development of microelectronics based on the semiconductor silicon. In the development and production of new electronic devices, silicon undeniably will continue to play a central role. Today, we aim to develop electronic devices at the nanoscale. To meet the challenges that come with advances in building components as small as a few nanometre, new materials are necessary. A promising material candidate to lead the field of device design is graphene. Graphene is a two-dimensional atom-thick layer of carbon atoms, ordered in a honeycomb structure. For many years graphene was considered a theoretician's toy model and was assumed not to exist in a free state [338]. Novoselov *et al.* [235] succeeded to isolate a single layer of graphene from a pencil stroke using Scotch tape. Ironically, their low-tech approach [235] paved the way to the production of nanoscale high-tech devices [102, 161, 344, 197, 122, 91, 287]. The discovery of graphene's outstanding electronic and structural properties was met with vast interest by the solid-state community [236, 351, 160, 50]. In 2010, Andre K. Geim and Konstantin S. Novoselov at the University of Manchester were awarded the Nobel Prize in Physics "for groundbreaking experiments regarding the two-dimensional material graphene".

The method of graphene exfoliation using Scotch tape is not practical for large-scale device production. For practical applications of graphene-based electronics, wafer-size high-quality graphene films are needed. The group of W. A. de Heer [18, 19] demonstrated that epitaxial graphene on *silicon carbide* (SiC) could be a successful alternative route towards wafer-size graphene growth. Instead of graphene exfoliation, they faciliate the surface graphitisation of high-temperature-treated SiC, e.g. Refs. [332, 95, 82, 263, 67, 302, 346]. In SiC, the vapor pressure of Si is higher than that of carbon. When heated, Si sublimates and leaves a graphene-covered surface behind [332, 95]. This makes graphene growth on SiC special in the sense that, instead of offering one or more of the components from the gas phase, graphene areas are formed by excess carbon at the surface [332, 95]. As of today, epitaxial growth of graphene on SiC by thermal decomposition is one of the most promising material combinations for future graphene applications based on established semiconductor technologies [18, 19, 82, 263, 197, 67, 137, 65, 302, 122, 346]. Indeed, graphene-based devices and even integrated circuits [161, 344, 287, 197, 137, 122, 91] were already created, employing epitaxial graphene grown on SiC substrate.

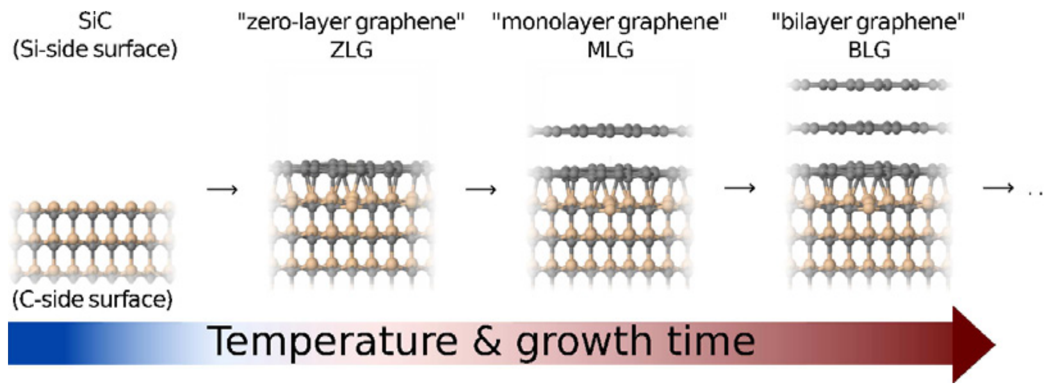

Figure 0.1.: Schematic illustration of the graphene growth on the Si-side of SiC. On the Si-side, epitaxial graphene growth starts with a clean Si-terminated surface. At temperatures above 1000 K first a carbon interface layer forms [263], the so-called zero-layer graphene (ZLG). Increased temperature and growth time lead to the formation of monolayer graphene (MLG) and bilayer graphene (BLG).

Graphene films grow on both polar surfaces of SiC, the C-terminated [18, 19, 334, 64, 302, 141, 83, 21, 337, 213] and the Si-terminated surface [332, 95, 264, 82, 263]. The growth mechanism and the resulting graphene film differ considerably between the two different SiC faces.

Figure 0.1 illustrates schematically the growth process of epitaxial graphene films on the Si side. In experiment the growth process starts from a clean Si-terminated SiC surface. With increased temperature the surface phases go from a Si-rich to a C-rich regime [332, 95, 263]. First, a (3×3) Si-rich reconstruction [310] can be prepared, then upon further annealing more Si sublimates and a simpler ($\sqrt{3} \times \sqrt{3}$)-R30° bulk-terminated Si rich surface forms [158, 308]. At temperatures above 1000 K a carbon interface layer forms [263] – the zero-layer graphene (ZLG) also called 'buffer-layer'. The ZLG is a carbon nanomesh with a honeycomb atomic structure similar to graphene, but it is bonded to the substrate by strong covalent bonds [109] as indicated in Fig. 0.1. With increased temperature and growth time underneath the already formed ZLG grows a new interface layer. The new interface layer lifts of the previous ZLG layer forming a mono-layer graphene (MLG). The system now consists of the ZLG layer covered by the MLG layer (see Fig. 0.1). Only the second carbon layer – the MLG – acts like a graphene layer displaying the linear π bands typical for the graphene band structure [35]. With increased layer thickness multi-layer graphene behaves more like graphite than graphene.

During annealing, the nucleation of excess carbon atoms starts at the step edge, allowing for a layer-by-layer growth process. On the Si side, the aim is to control the graphene layer thickness and reduce the coexistence of MLG

and bi-layer graphene (BLG) [18, 82, 92, 67]. Across MLG-BLG graphene junctions on the same Si-terminated surface a recent joint experimental-theoretical study finds particularly high local resistances [152]. This might be a possible contributing factor to low carrier mobilities in graphene on the Si face of SiC [82, 152]. Graphene films grown under ultrahigh vacuum (UHV) conditions are typically inhomogeneous [82, 67]. Improved MLG film homogeneity is achieved by increased growth temperature in an argon background buffer gas [82]. de Heer *et al.* [67] reported excellent wafer-size MLG films grown in a confined cavity that may retain a finite, well-defined Si background pressure as Si evaporates from the surface. Improving the quality of epitaxial graphene is a major and ongoing experimental goal [82, 67].

In the past, the appearance of different phases on the Si-terminated surface was often interpreted [83, 217, 67] as successive intermediates formed by an outgoing Si flux that ultimately leads to the growth of bulk-like graphite layers. Tromp and Hannon [329] demonstrated that the C-rich ZLG layer [332, 95, 264, 83] (not yet graphene) on the Si face is a reversible thermodynamic equilibrium phase at high T and a controlled disilane (Si_2H_6) background pressure. Reversibility is much harder to demonstrate once a complete graphene plane has formed [124]. What is still not clear, however, is whether MLG itself is an equilibrium phase under certain conditions.

Graphene growth on the C-terminated surface differs greatly resulting in multilayer graphene. During annealing a series of different surface structures were observed [332, 304, 145, 192, 24, 292, 208, 140, 307, 139]. In an Si-rich environment graphene growth starts with a Si-rich (2×2) phase [24, 192] or with an oxidic ($\sqrt{3} \times \sqrt{3}$) reconstruction [25, 192]. In the absence of a Si background gas like disilane (Si_2H_6) a disordered oxidic layer with a (1×1) periodicity of bulk SiC is observed [304]. Continued heating leads to a (3×3) phase.

Using low-energy electron diffraction (LEED), Bernhardt *et al.* [24] showed that the (3×3) reconstructions originating from different starting structures and environments are equivalent [24]. Further annealing leads to a (2×2) Si adatom phase, referred to as $(2\times2)_C$ (notation taken from Ref. [24]). Just before graphene forms on the surface, a coexistence of the two surface phases, the (3×3) and the $(2\times2)_C$, is observed [24, 337]. The atomic structure of the $(2\times2)_C$ was resolved by quantitative LEED [292], while the (3×3) reconstruction and the SiC-graphene interface remains a puzzle [192, 145, 139, 71].

Here, two very different scenarios have been invoked for the structural

properties of the SiC-graphene interface:

(a) The first carbon layer is strongly bound to the substrate [334, 213, 302]. Here, the Si sublimation rate during graphene growth is controlled by either using a confined geometry [129], by working in an inert gas atmosphere [82], or by providing an external Si gas phase [302, 94] for example disilane (Si_2H_6) background gas.

(b) For samples prepared under UHV conditions, the first carbon layer is weakly bound to the substrate and shows the characteristic behavior of the π-band at the K-point of the Brillouine zone. Here, an inhomogeneous interface is present since the (3×3) and the $(2\times2)_C$ reconstructions are observed underneath the graphene layers [141, 83, 307, 337].

For the weakly bound interface structure, a (2×2) and (3×3) LEED pattern was observed underneath the graphene layer [141, 83, 307]. An additional typical feature of this LEED pattern is a ring like structure originating from rotational disordered graphene films [130, 131, 141, 337, 141]. The rotational disorder originates from the growth process, where graphene layers nucleate on a terrace and grow in all directions on the surface [231]. Due to the rotational disorder the electronic structure of the single graphene sheet decouples from the underlying graphene layer and exhibits single-layer-like electronic properties, even for multilayer graphene films with very high electron mobilities [131, 301, 21].

A recent study on graphene grown by molecular beam epitaxy (MBE) on the C side exhibited the same structural characteristics as graphene grown by high-temperature annealing [218]. This is a strong indication that indeed the $(2\times2)_C$ as well as the (3×3) reconstruction prevails below the graphene films.

While some groups report the successful growth of large-scale MLG [146, 269], other reports suggest that the pure monolayer growth regime is difficult to achieve on the C side [213]. The exact material properties of graphene depend on the growth conditions and on the interaction between the graphene layer and the substrate.

The ultimate goal is to move the production of devices based on SiC-graphene hetero-structures from the laboratory to large scale production similar to today's semiconductor device fabrication. An important step to refine the growth process is to gain a deeper understanding of the atomic and electronic structure of the SiC-graphene interface. We will see below that there are at least narrow *thermodynamic* equilibrium conditions for ZLG,

MLG and even BLG grown on the Si-side of SiC. However, we found that a controlled graphene growth on the C-terminated surface is hindered by Si-rich surface reconstructions.

This thesis presents first principles studies of the SiC phases on the Si and C face, laying the groundwork for a detailed atomistic understanding of the phase equilibria and resulting electronic properties of the surfaces involved. In particular, we will perform a density-functional theory (DFT) study on the Si side and C side of the polar SiC surfaces, using the all-electron numeric atom-centered basis function code FHI-aims. Due to the lattice mismatch between the SiC and graphene large commensurate surface structures form consisting of up to $\sim$ 2800 atoms. DFT is challenging for these systems, because of the system sizes and van-der-Waals (vdW) interactions, not accounted for by most standard density functionals. We applied the *ab initio* atomistic thermodynamic formalism [340, 279, 280, 259, 260] to evaluate the interface structure of epitaxial graphene and its competing surface reconstructions. The formation energies of different reconstructions and widely-used model systems are presented as a function of the chemical potential of C.

We show below that graphene films on the Si face of SiC grow at least as near-equilibrium phases. Therefore, by tuning the chemical potential, which can be accomplished in experiment by varying the temperature and background pressure of C or Si, it should be possible to grow high-quality interfaces as well as graphene structures on the Si side. This makes the Si-terminated surface an ideal substrate for graphene growth. We found that the interface layer – ZLG interface structure – plays a central role for a layer-by-layer graphene growth. We demonstrate that the presence of the ZLG interface structure leads to a corrugated graphene film. Not all Si atoms at the SiC-graphene interface are saturated, some Si atoms remain unsaturated – the *Si dangling bonds*. We show that the ZLG, MLG and BLG are doped by the Si dangling bond states at the Fermi level. Using DFT Perdew-Burke-Ernzerhof generalised gradient approximation [246] (PBE) including van-der-Waals effects [326] (PBE+vdW) and Heyd-Scuseria-Ernzerhof hybrid functional [138, 175] (HSE06+vdW) calculations, we evaluate the influence of the Si dangling bonds on the electronic structure of the graphene films. A different route to improve the electronic properties of epitaxial graphene is to saturate the Si bonds at the SiC-graphene interface with hydrogen. Hydrogen intercalation decouples the ZLG layer from the substrate forming quasi-free-standing mono-layer graphene (QFMLG). The QFMLG is flat and almost undoped featuring a homogeneous charge density at the interface. The intercalation process improves the electronic properties of the graphene film [97, 315].

In experiment, the same mechanism which leads to graphene growth on the Si face fails, on the C face. Here, controlling the layer thickness of the graphene films remains a challenge [213]. Just at the onset of surface graphitisation, a phase mixture of different surface phases is observed. Studying the thermodynamic stability range of graphene films on the C side is difficult, since the atomic structure of some of the competing surface phases as well as of the SiC-graphene interface are unknown. We introduced a new model for the unknown 3×3-SiC($\bar{1}\bar{1}\bar{1}$) reconstruction – the Si-rich *Si twist model* inspired by the reconstruction known from the Si side [310, 276]. The Si twist model captures the experimentally observed characteristics. Comparing the formation energy of the Si twist model and different interface models indicates that the formation of a regulating interface structure like the ZLG layer is hindered by Si-rich surface reconstructions.

This thesis is structured in three parts:

The first part introduces the basic concepts of electronic structure calculations. Chapter 1 familiarises the reader with the *many-body problem* in the context of condensed matter physics. Throughout this work, results are obtained by solving the *many-body Schrödinger equation* (Eq. 1.1) using DFT for the electronic part. The fundamental concepts of DFT and the derivation of the *Kohn-Sham equations*, as well as the basic ideas behind the practical application of DFT are given in Chapter 2. The joint vibrational motion of nuclei in a lattice at a specific frequency are called *phonons*. Material properties, such as the heat capacity, thermal conduction or expansion, depend on phonons. In Chapter 3, the calculation of phonons in the DFT framework is explained. The central question throughout this work is whether *thermodynamic* equilibrium conditions like the temperature T and partial pressures p can be found to control the growth of certain structures. To tackle this question, we apply the *ab initio* atomistic thermodynamic formalism described in Chapter 4. In Chapter 5, we discuss the *Kohn-Sham band structure*, which can provide a first insight into the electronic structure of a surface, if interpreted with care.

In the second part the reference bulk systems, diamond, graphite, graphene and SiC are introduced. In Chapter 6, the structural and thermodynamic properties of diamond, graphite and graphene are characterised by *ab initio* electronic structure calculations. The three most relevant SiC polytypes, cubic silicon carbide (3C-SiC), and hexagonal 4H-SiC and 6H-SiC and their physical and electronic properties are discussed in Chapter 7.

The third part discusses epitaxial graphene growth on the polar surfaces of SiC. In Chapter8, we introduce the different Si- and C-rich surface phases

observed during graphene growth on the Si-terminated SiC surface. In epitaxial graphene there are two aspects to strain. Artificially induced strain by the choice of the coincidence lattice between the substrate and graphene and strain caused by the bonding between the ZLG and the substrate. Both aspects of strain are discussed in Chapter 9, published in Ref. [284]. In Chapter 10 we present our work on thermodynamic equilibrium conditions of graphene films on SiC, published in Ref. [227]. To evaluate the electronic structure of epitaxial graphene and the interface grown on the Si face of SiC, we developed a method for the band structure unfolding exploiting the Bloch-theorem in Chapter 12. In Chapter 13 we argue that the quality of epitaxial graphene can be improved by hydrogen intercalation, the experimetal and theoretical collaborative study was recently published in Ref. [294]. So far, the focus was on epitaxial graphene on the Si-terminated surface. In Chapter 14, we investigate the relative phase stability of the competing surface phases on the C-terminated surface in the thermodynamic range of graphitisation, accepted for publication at Phys. Rev. B: Rapid Comm. (Ref. [228]).

Part I

Electronic Structure Theory

This chapter introduces the theoretical toolbox applied in this thesis. We briefly retrace the underlying theory leading to the pragmatic aspects of density-functional theory (DFT). The starting point is the quantum mechanical many-body problem, Ch. 1, and the Born-Oppenheimer (BO) approximation, Sec. 1.2. The BO approximation formally separates the electronic coordinates from the nuclear ones. The electronic sub-problem is then solved for a fixed set of nuclear coordinates greatly simplifying the many-body problem. Then, the electronic Schrödinger equation is tackled in the DFT framework (Ch. 2). The foundation of DFT are the Hohenberg-Kohn theorems Sec. 2.1. Using the Hohenberg-Kohn theorems, the electronic many-body Hamiltonian is rewritten into a set of single particle Schrödinger equations, the Kohn-Sham equations. To finally turn DFT into practice for system sizes up to several thousand atoms, approximations for the unknown terms in the Kohn-Sham equations have to be introduced. For a reliable description of solids, surfaces or weakly bonded layered materials, such as graphite, it is essential to include van-der-Waals (vdW) contributions (Sec. 2.4). Once the Kohn-Sham equations are solved, in this work using the FHI-aims package (Ch. 2.5), the resulting total energy can be used to determine the stability of structures and surface reconstructions (Ch. 4). So-called phonons (Ch. 3), the movement of the nuclei in a solid within the harmonic limit, can also be included. The Kohn-Sham eigenvalues can be used to obtain a first impression of the electronic structure of the system. The discussion in this chapter follows the books by Kohanoff [170], Martin [211], Capelle [46] and the lecture given by Patrick Rinke in 2013[1].

[1] Electronic Structure Theory - Technical University of Berlin, Winter Term 2013
`http://www.fhi-berlin.mpg.de/~rinke/`

A piece of matter is a collection of interacting atoms. The atoms can be arranged periodically into a bulk solid, surface or wire. They can also form molecules and clusters or a mixture like a molecule absorbed on a surface. However, the description of materials on a quantum mechanical level is challenging - known as the many-body problem. For example, a 1 cm^3 large cube of 3C-SiC contains $N_e \simeq 10^{25}$ electrons and $N_n \simeq 10^{24}$ nuclei. Here, the N_e electrons interact with each other and with N_n nuclei. In the following, we discuss the approach used throughout this work to gain insight into material properties by finding approximations to the many-body problem.

1.1. The Many-Body Schrödinger Equation

The non-relativistic quantum-mechanical description of an N-particle system, such as bulk 3C-SiC, is governed by the many-body Schrödinger equation. In this work we focus on the time-independent Schrödinger equation

$$\hat{\mathcal{H}}\Psi = E\Psi \tag{1.1}$$

where $\hat{\mathcal{H}}$ is the many-body Hamiltonian of the system, E the energy and Ψ the many-particle wave function. Although the mathematical form of the Schrödinger equation (Eq. 1.1) is known, an analytic solution is only possible in certain special cases, e.g. the hydrogen atom [e.g. see 285, Ch. 6.3].

The many-body Hamiltonian ($\hat{\mathcal{H}}$) is a coupled electronic and nuclear problem. Throughout this thesis we will use atomic units, this means

$$m_e = e = \hbar = \frac{1}{4\pi\varepsilon_0} = 1.$$

Then, the general $\hat{\mathcal{H}}$ in our system is given by Eq. 1.2.

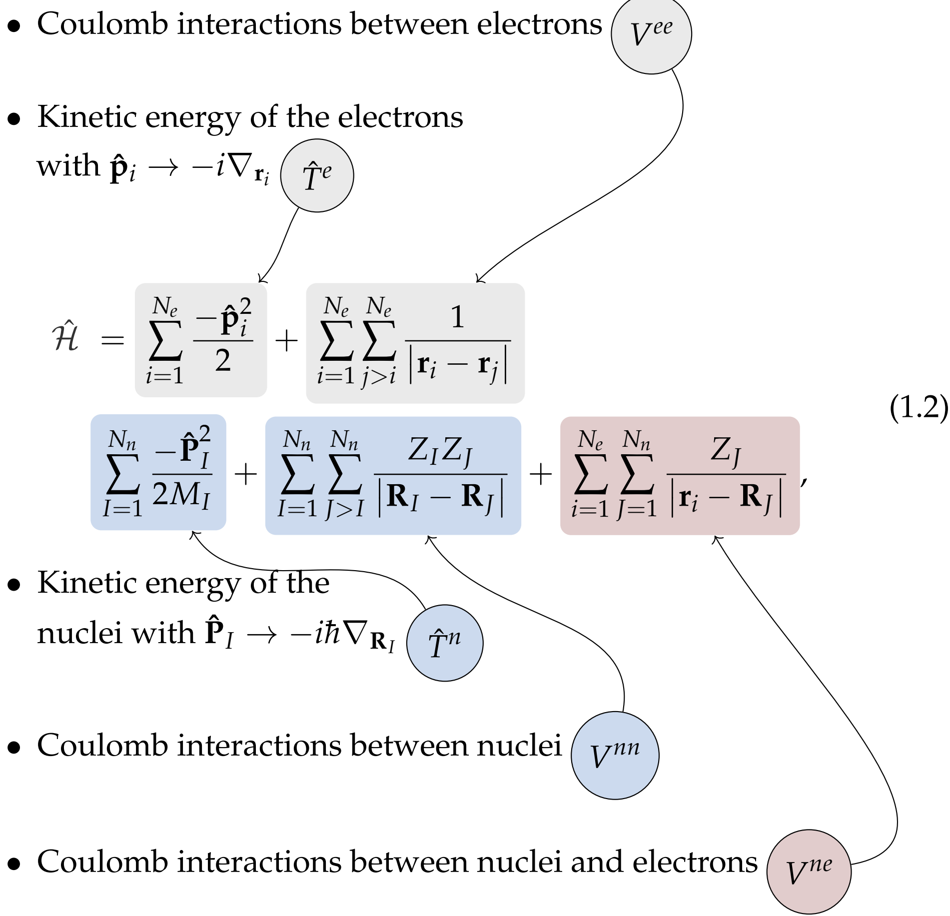

$$
\begin{aligned}
\hat{\mathcal{H}} &= \sum_{i=1}^{N_e} \frac{-\hat{\mathbf{p}}_i^2}{2} + \sum_{i=1}^{N_e}\sum_{j>i}^{N_e} \frac{1}{|\mathbf{r}_i - \mathbf{r}_j|} \\
&\quad \sum_{I=1}^{N_n} \frac{-\hat{\mathbf{P}}_I^2}{2M_I} + \sum_{I=1}^{N_n}\sum_{J>I}^{N_n} \frac{Z_I Z_J}{|\mathbf{R}_I - \mathbf{R}_J|} + \sum_{i=1}^{N_e}\sum_{J=1}^{N_n} \frac{Z_J}{|\mathbf{r}_i - \mathbf{R}_J|},
\end{aligned}
\tag{1.2}
$$

N_e :	number of electrons	N_n :	number of nuclei
m_e :	electron mass	M_n :	nuclear mass
e :	electronic charge	Z :	nuclear charge
$\mathbf{r}$:	electronic coordinate	$\mathbf{R}$:	nuclear coordinate
$\hat{\mathbf{p}}$:	electronic momentum	$\hat{\mathbf{P}}$:	nuclear momentum

The electronic contributions in Eq. 1.2, $\hat{T}^e$ and V^{ee}, and the nuclear contributions, $\hat{T}^n$ and V^{nn}, are coupled through the Coulomb interaction between nuclei and electrons V^{ne}. The Schrödinger equation (Eq. 1.1) thus takes the form

$$\left(\hat{T}^e + V^{ee}\right) + V^{ne} + \left(\hat{T}^n + V^{nn}\right)\Psi_\eta = \mathcal{E}_\eta \Psi_\eta, \tag{1.3}$$

where $\Psi_\eta \equiv \Psi_\eta(\{\mathbf{R}_I, \mathbf{r}_i\})$ is the many-body wave function that depends on the coordinates of all electons $\mathbf{r}_i$ and nuclei $\mathbf{R}_I$. The ground state wave func-

tion (Ψ_0) is a $(N_e + N_n) \cdot 3$ dimensional object and $\mathcal{E}_0$ is the corresponding ground state energy. All higher ($n>0$) states correspond to (neutral) excited states.
Previously, we estimated the total number of particles in a 3C-SiC cube to be $\sim 10^{25}$. Therefore the input to the ground state wave function is a $\sim 10^{25}$ dimensional object. The wave function Ψ_0 has to be stored for many combinations of coordinate values. Usually, Ψ_0 is represented on a grid. To store Ψ_0 of this cube in a single grid point we would need a $\sim 10^{13}$ Terabyte disc [1]. Evidently, we have to find approximations to solve the many-body Schrödinger equation.

1.2. The Born-Oppenheimer Approximation

The first approximation we apply is the Born-Oppenheimer (BO) approximation [see 285, Ch. 15.2]. The underlying idea is to reduce the complexity of the many-body problem by separating the electronic problem from the nuclear one. In the Born-Oppenheimer (BO) approximation the electrons are calculated in an external potential (V^{ext}) generated by a fixed nuclear configuration. The electronic Hamiltonian ($\hat{\mathcal{H}}^e$) within the BO approximation has the form

$$\mathcal{H}^e = T^e + V^{ee} + V^{\text{ext}}. \tag{1.4}$$

The external potential (V^{ext}) is generated by the Coulomb attraction between electrons and nuclei given by (V^{ne}) in Eq. 1.2 with the ion positions $\mathbf{R} = \mathbf{R}_J$ kept fixed. The electronic Schrödinger equation then reads

$$\mathcal{H}^e(\{\mathbf{r}_i, \mathbf{R}\})\phi_\nu(\{\mathbf{r}_i, \mathbf{R}\}) = \mathcal{E}^e_\nu \phi_\nu(\{\mathbf{r}_i, \mathbf{R}\}), \tag{1.5}$$

where ϕ_ν are the eigenfunctions of the electronic Hamiltonian and $\mathcal{E}^e_\nu$ its eigenvalues. The electronic spectrum parametrically depends on $\mathbf{R}$. For any fixed nuclear configuration ($\mathbf{R}$), the eigenfunctions $\phi_\nu(\{\mathbf{r}_i, \mathbf{R}\})$ of $\mathcal{H}^e$ form a complete basis set. In the BO approximation the wave function Ψ_η of the many-body Schrödinger equation (Eq. 1.3) can be approximated by an expansion in terms of the electronic eigenfunctions

$$\Psi_\eta(\mathbf{R}, \mathbf{r}_i) = \sum_\nu c_{\nu_\eta}(\mathbf{R})\phi_\nu(\{\mathbf{r}_i, \mathbf{R}\}), \tag{1.6}$$

[1] In the case of a 1 cm^3 SiC cube Ψ_0 is a $(N_e + N_n) \cdot 3 \sim 3.3 \cdot 10^{25}$ dimensional object. If we store every entry of Ψ_0 for a single grid point as a floating point number with single precision (4 byte per entry), $\sim 13.2 \cdot 10^{25}$ byte $\sim 10^{13}$ Terabyte are needed.

where the expansion coefficients $c_{\nu_\eta}(\mathbf{R})$ depend on the ionic configuration. The BO approximation holds, when we can assume that the electrons adjust to the nuclear positions almost instantaneously. This is a valid assumption for systems with well-separated adiabatic electronic states, in which the movement of the nuclei (e.g. because of phonons or vibrations) does not lead to electronic transition. All results shown in this work use the BO approximation.

In solid state physics, material science or quantum chemistry electronic structure theory is applied to gain information about material properties. One of the most successful and popular quantum mechanical approaches is density-functional theory (DFT). It is routinely applied for calculating ground-state properties, such as cohesive energies, phase stabilities or the electronic structure of solids and surfaces.

2.1. The Hohenberg-Kohn Theorems

The Hohenberg-Kohn theorems [144] are the foundation of density-functional theory (DFT), which formally introduces the electron density as basic variable. In essence, the electronic many-body problem (Eq. 1.5) is reformulated in terms of the ground state density $n_0(\mathbf{r})$ instead of the ground state wave function $\Psi_0(\{\mathbf{r}_i\})$. The advantage is that $n_0(\mathbf{r})$ depends on only 3 and not $3N_e$ spatial coordinates, but still contains all the informations needed to determine the ground state. The ground state density is defined as

Definition 2.1.1. *Ground State Density*

$$n_0(\mathbf{r}) \equiv N_e \int d^3r_2 \ldots \int d^3r_{N_e} \left|\Psi_0(\mathbf{r}, \mathbf{r_2}, \ldots, \mathbf{r_{N_e}})\right|^2 .$$

N_e is the number of electrons and Ψ_0 is the normalised ground state wave function.

For simplicity it is assumed, that the ground state is non-degenerate. The first Hohenberg-Kohn theorem states that there is a one to one mapping between $n_0(\mathbf{r})$, $\Psi_0(\{\mathbf{r}_i\})$ and the external potential (V^{ext}) [see Eq. 1.5]. In other words, the V^{ext} uniquely defines the density.

The second Hohenberg-Kohn theorem [144, Part I.2] introduces the variational principle. The electron energy $\mathcal{E}$ of a system can be formulated as a functional of the electron density $n(\mathbf{r})$

$$\mathcal{E}[n(\mathbf{r})] = \underbrace{\int d^3r\, n(\mathbf{r}) v^{\text{ext}}}_{\text{specific}} + \underbrace{\mathcal{F}[n(\mathbf{r})]}_{\text{universal}} . \tag{2.1}$$

$\mathcal{F}[n(\mathbf{r})]$ is called the Hohenberg-Kohn functional. It contains the electron kinetic energy and the electron-electron interaction as functionals of $n(\mathbf{r})$, but it is independent of the external potential (V^{ext}).

Definition 2.1.2. *Hohenberg-Kohn functional*

$$\mathcal{F}[n(\mathbf{r})] \equiv T^{e}[n(\mathbf{r})] + E^{ee}[n(\mathbf{r})].$$

The second Hohenberg-Kohn theorem states that for any V^{ext} the ground state density ($n_0(\mathbf{r})$) minimises the energy functional $\mathcal{E}[n(\mathbf{r})]$. The minimising density of Eq. 2.1 is $n_0(\mathbf{r})$

$$\mathcal{E}_0 = \mathcal{E}[n_0(\mathbf{r})] \leq \mathcal{E}[n(\mathbf{r})]. \tag{2.2}$$

The Hohenberg Kohn theorems allow for an iteratively improvement of an initially chosen trial density by minimising $\mathcal{E}[n(\mathbf{r})]$. However, the major challenge is that $\mathcal{F}[n]$ is unknown. In the original work by Hohenberg *et al.* the density variation was limited to a non-degenerate ground states and *v-representable* densities. These are densities that can be generated by a unique external potential. The minimisation can be generalised by Levy's constrained search approach [191].

2.2. The Kohn-Sham Equations

The Hohenberg-Kohn theorems in Sec. 2.1 provide the mathematical basis of density-functional theory (DFT). However, guidance is not provided on how to built the Hohenberg-Kohn functional ($\mathcal{F}[n]$) (Def. 2.1.2) whose minimisation gives the ground state energy and density. One challenge is the kinetic energy $T^e[n(\mathbf{r})]$ of the electrons, because an explicit expression in terms of the electron density is not known. Kohn and Sham cast the calculation of the ground state energy into a set of single particle Schrödinger equations. Their approach is based on a non-interacting system of electrons, which can be described by a Slater determinant of one-particle orbitals, also-called Kohn-Sham orbitals ($\varphi_i(\mathbf{r})$s).

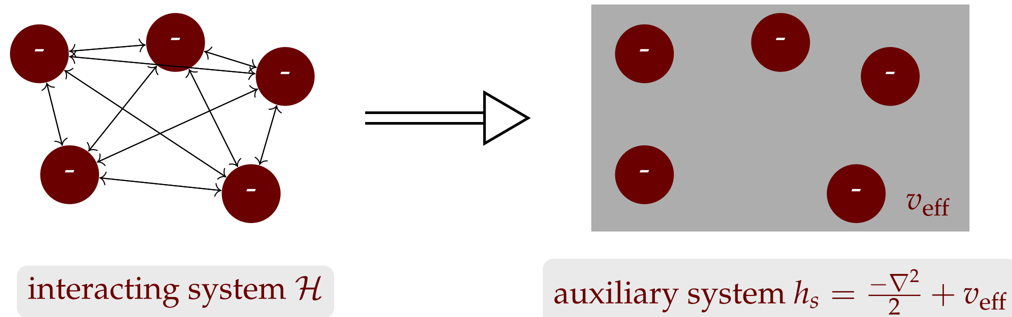

Figure 2.1.: The interacting system is mapped to a non-interacting auxiliary system.

The central idea of the Kohn-Sham approach is to map the real physical system onto a *non-interacting reference system*, as sketched in Fig. 2.1. The interaction of the electrons is described by the many-body Hamiltonian in Eq. 1.5. Here, all electrons interact with each other (indicated by arrows in Fig. 2.1). The system can be converted into a system of non-interacting electrons governed by an effective potential v_{eff}. v_{eff} is an effective interaction that guarantees that the orbitals corresponding to the non-interacting electrons give the same density as the density of the interacting system. Since the density is uniquely determined by the external potential (see Sec. 2.1) the density of the Kohn-Sham system has to equal that of the fully interacting system. However, the wave function of the fully interacting and the non-interacting system are different. In Sec. 2.1, the Hohenberg-Kohn functional (Def. 2.1.2) was introduced. It contains the electron-electron interaction $E^{ee}[n(\mathbf{r})]$ and the kinetic energy $T^e[n(\mathbf{r})]$ of the electrons. Unfortunately, the functional form of this two terms is unknown. The electron-electron interaction term can be separated into the classical Coulomb repulsion E^H

and a non-classical part $E^{ncl}[n(\mathbf{r})]$ containing all other contributions

$$E^{ee}[n(\mathbf{r})] = \underbrace{\frac{e^2}{2}\iint d^3r\, d^3r' \frac{n(\mathbf{r})n(\mathbf{r}')}{|\mathbf{r}-\mathbf{r}'|}}_{E^H[n(\mathbf{r})]} + E^{ncl}[n(\mathbf{r})]. \tag{2.3}$$

The kinetic energy term can be separated in a known part, the kinetic energy of the non-interacting reference system and in an unknown part

$$T^e[n(\mathbf{r})] = \underbrace{-\frac{\hbar}{2m}\sum_{i=1}^{N}\int d^3r\, \varphi^*(\mathbf{r}_i)\nabla^2\varphi(\mathbf{r}_i)}_{T^s[n(\mathbf{r})]} + T^c[n(\mathbf{r})]. \tag{2.4}$$

The Hohenberg-Kohn functional can then be rewritten as

$$\mathcal{F}[n(\mathbf{r})] = T^s[n(\mathbf{r})] + E^H[n(\mathbf{r})] + \underbrace{E^{ncl}[n(\mathbf{r})] + T^c[n(\mathbf{r})]}_{E_{XC}[n(\mathbf{r})]}. \tag{2.5}$$

The exchange-correlation functional (E_{XC}) contains the difference between the real, interacting system and the non-interacting, single particle system.

Definition 2.2.1. *Exchange-correlation energy*

$$E_{XC}[n(\mathbf{r})] \equiv T^e[n(\mathbf{r})] - T^s[n(\mathbf{r})] + E^{ee}[n(\mathbf{r})] - E^H[n(\mathbf{r})]$$

The two dominant terms $T^s[n(\mathbf{r})]$ and $E^H[n(\mathbf{r})]$ can be calculated and are often much higher in energy than E_{XC}. Although E_{XC} is not easier to approximate than $\mathcal{F}[n(\mathbf{r})]$, the error relative to the total energy made by approximations is smaller. The energy functional $\mathcal{E}[n(\mathbf{r})]$ (Eq. 2.1) can now be rewritten containing all known terms and the unknown exchange-correlation energy as

unknown

$$\mathcal{E}[n(\mathbf{r})] = T^s[n(\mathbf{r})] + E^H[n(\mathbf{r})] + \int d^3r\, n(\mathbf{r})\, v_{\mathrm{ext}}(\mathbf{r}) + E_{XC}[n(\mathbf{r})]. \tag{2.6}$$

known

All terms in Eq. 2.6 are functionals of the density except for T^s which is

explicitly expressed as a functional of the non-interacting wave function and is unknown as an explicitfunction of $n(\mathbf{r})$. The Hamiltonian $\mathcal{H}_s$ can be written as a sum of effective one particle Hamiltonians $h_s(\mathbf{r}_i)$

$$\mathcal{H}_s(\mathbf{r}) = \sum_{i=1}^{N_e} h_s(\mathbf{r}_i) = -\frac{1}{2}\sum_{i=1}^{N_e} \nabla^2 + \sum_{i=1}^{N_e} v_{\text{eff}}(\mathbf{r}_i). \tag{2.7}$$

$\varphi_i(\mathbf{r})$ are the eigenfunctions of the one-electron Hamiltonian $h_s(\mathbf{r})$. They are obtained by solving the one-electron Schrödinger equation

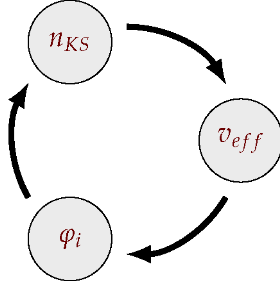

Figure 2.2.: The effective potential v_{eff} of the many-body system depends on Kohn-Sham density ($n_{KS}(\mathbf{r})$), which we are searching, which depends on the Kohn-Sham orbital ($\varphi_i(\mathbf{r})$), which in turn depends on v_{eff}

$$\begin{aligned} h_s(\mathbf{r}_i)\varphi_i &= \varepsilon_i\varphi_i \\ \left(-\frac{1}{2}\nabla^2 + v_{\text{eff}}(\mathbf{r}_i)\right)\varphi_i &= \varepsilon_i\varphi_i. \end{aligned} \tag{2.8}$$

Equation 2.8 defines the Kohn-Sham equations. The Kohn-Sham density $n_{KS}(\mathbf{r})$ is given by the occupied $\varphi_i(\mathbf{r})$

$$n_{KS}(\mathbf{r}) = \sum_{i=1}^{N_{\text{occ}}} |\varphi_i(\mathbf{r})|^2. \tag{2.9}$$

The minimisation problem of the interacting many-body system is replaced by the Kohn-Sham equations (2.8). Using the Rayleigh-Ritz principle and varying the wave function under an additional orthonormalisation constraint one finds the effective potential as

$$v_{\text{eff}} = \frac{\delta E_{\text{XC}}[n(\mathbf{r})]}{\delta n(\mathbf{r})} + V^H + V^{\text{ext}}. \tag{2.10}$$

The effective potential $v_{\text{eff}}[n(\mathbf{r})]$ depends on the density, therefore the Kohn-Sham equations have to be solved self-consistently. As illustrated in Fig. 2.2, the *self-consistency cycle* starts with an initial guess for $n_{KS}(\mathbf{r})$; next the corresponding effective potential v_{eff} can be obtained. Then Eq. 2.8 is solved for $\varphi_i(\mathbf{r})$. From these orbitals a new density is calculated and used as a trial density to calculate the new v_{eff} and start again. The process is repeated until the trial density and v_{eff} equal the new density and the newly obtained v_{eff}. However, the exact forms of E_{XC} is unknown. The DFT total energy E_{tot} is typically calculated using the sum over the Kohn-Sham eigenvalues

ε_i

$$E_{\text{tot}}[n(\mathbf{r})] = \sum_{i=1}^{N_{el}} \varepsilon_i - E^H[n(\mathbf{r})] + E_{\text{XC}}[n(\mathbf{r})] - \int d^3r \frac{\delta E_{\text{XC}}[n(\mathbf{r})]}{\delta n(\mathbf{r})} n(\mathbf{r}). \quad (2.11)$$

The Kohn-Sham orbitals are introduced to simplify the problem, but their meaning is purely mathematical. Neither the orbitals nor their corresponding eigenvalues ε_i have a strict physical meaning, except for the eigenvalue of the highest occupied orbital ε_{VBM} [150]. The energy level ε_{VBM} equals the ionisation energy of the system. This is the minimum amount of energy required to remove an electron of an atom, molecule or solid to infinity.

2.3. Approximations for the Exchange-Correlation Functional

In the following sections, we will discuss approximations for the exchange-correlation functional (E_{XC}) Def. 2.2.1 necessary in any real application since the true functional is not available. The Kohn-Sham approach maps the many-body problem exactly onto a one-electron problem. It is possible to solve the problem if approximations for E_{XC} can be found. Exact solutions are available for very few systems, but good approximations can be applied to a large class of problems. The search for better functionals is an active field of research.

2.3.1. Local-Density Approximation (LDA)

In the pioneering paper by Kohn and Sham in 1965 an approximation for the exchange-correlation functional (E_{XC}) was proposed - the local-density approximation (LDA). Kohn and Sham's idea was to approximate the exchange-correlation functional (E_{XC}) of an heterogenous electronic system as *locally homogenous* and use E_{XC} corresponding to the homogenous electron gas at point $\mathbf{r}$ in space. Assuming a slowly varying electron density ($n(\mathbf{r})$), they expressed

$$E_{\text{XC}}[n(\mathbf{r})] = \int d^3r \; n(\mathbf{r}) \epsilon^{\text{xc-LDA}}[n(\mathbf{r})], \quad (2.12)$$

where $\epsilon^{\text{xc-LDA}}[n(\mathbf{r})]$ denotes the exchange-correlation energy per electron of the homogenous electron gas. $\epsilon^{\text{xc-LDA}}[n(\mathbf{r})]$ can be rewritten as a sum of the exchange and correlation contributions

$$\epsilon^{\text{xc-LDA}}[n(\mathbf{r}))] = \epsilon^{\text{x-LDA}}[n(\mathbf{r})] + \epsilon^{\text{c-LDA}}[n(\mathbf{r})] \tag{2.13}$$

The exchange part $\epsilon^{\text{x-LDA}}[n(\mathbf{r})]$ of the homogeneous electron gas was evaluated analytically by Dirac [73].

$$\varepsilon^{\text{x-LDA}}[n(\mathbf{r})] = \frac{3}{4}\sqrt[3]{\frac{3n(\mathbf{r})}{\pi}} \approx \frac{0.458}{r_s} \tag{2.14}$$

where r_s is the mean inter-electronic distance expressed in atomic units [73]. For the correlation part the low- and high-density limits are known, but an analytic expression for the range between the limits is not known. However, for the homogeneous electron gas, excellent parametrisations of accurate quantum Monte Carlo (QMC) calculations exist [52]. The LDA appears to be oversimplified, in particular for strongly varying densities, as one might expect in real materials. Nonetheless, LDA forms the basis for most of the widely used approximations to E_{XC}.

2.3.2. Generalised Gradient Approximation (GGA)

The LDA only takes the density at a given point $\mathbf{r}$ into account. One of the first extension to the LDA was the generalised gradient approximation (GGA). In the GGA, the treatment of inhomogeneities in the electron density is refined by a first order Taylor series with respect to density gradients

$$\begin{aligned} E_{\text{XC}} \approx E^{\text{XC-GGA}}[n(\mathbf{r})] &= \int d^3r\, n(\mathbf{r})\varepsilon^{\text{xc-GGA}}[n(\mathbf{r}), |\nabla n(\mathbf{r})|] \\ &\equiv \int d^3r\, n(\mathbf{r})\varepsilon^{\text{x-hom}}\, F^{\text{XC}}(n(\mathbf{r}), |\nabla n(\mathbf{r})|) \end{aligned} \tag{2.15}$$

where F^{XC} is a dimensionless enhancement factor. As before, the exchange-correlation energy per electron $\varepsilon^{\text{xc-GGA}}$ is split into an exchange and correlation contribution. The exchange contribution is the same as in the LDA (Eq. 2.14). Unlike the LDA, the functional form of GGAs and thus F^{XC} is not unique. As a result, a large number of GGAs have been proposed. A comprehensive comparison of different GGAs have been given for example by Filippi *et al.* [90, chap 8] or Korth and Grimme [172].

The GGA suggested by Perdew *et al.* is used throughout this work. The aim of the Perdew-Burke-Ernzerhof generalised gradient approximation

[246] (PBE) is to satisfies as many formal constraints and known limits as possible, sacrificing only those being energetically less important [246]. PBE improves the description of bulk properties like cohesive energies and lattice constants, as compared to LDA [311, 312, 328].

2.3.3. Hybrid Functionals

In the approximations for the exchange-correlation functional (E_{XC}) discussed so far, a spurious self-interaction error remains. The self-interaction error, as the name suggests, is the spurious interaction of the electron density with itself. For example, the Hamiltonian of an one-electron system depends only on the kinetic energy and the potential due to the nuclei. In the Kohn-Sham framework the energy of such a system is given by Eq. 2.6 and contains two additional terms, the Hartree term (Eq. 2.3) and the exchange-correlation functional (E_{XC}) (Def. 2.2.1). The exact exchange-correlation functional (E_{XC}) would cancel the self-interaction introduced by the Hartree term. However, in DFT most approximations to the exchange-correlation functional (E_{XC}) leave a spurious self-interaction error. This is different to the Hartree-Fock approximation, where the self-interaction error is cancelled by the exchange term

$$E_x^{\mathrm{HF}} = -\frac{1}{2}\sum_{i,j}\iint d^3r\, d^3r' \frac{e^2}{|\mathbf{r}-\mathbf{r}'|}\varphi_i^*(\mathbf{r})\varphi_i(\mathbf{r}')\varphi_j^*(\mathbf{r}')\varphi_j(\mathbf{r}). \tag{2.16}$$

However, Hartree-Fock theory neglects all correlation except those required by the Pauli exclusion principle. This leads to sizeable errors in the description of chemical bonding. Combining DFT with Hartree-Fock exact-exchange is a pragmatic approach to deal with the problem. These so-called hybrid functionals were first introduced by Becke[16]. His main idea was to replace a fraction of the DFT exchange E_X^{DFT} energy by the exact exchange E_X^{HF} energy. In this work, we use the Heyd-Scuseria-Ernzerhof hybrid functional [138, 175] (HSE), therefore the discussion focuses on HSE. For hybrid functionals, E_{XC} is reformulated as

$$E_{\mathrm{XC}}^{\mathrm{hyb}} = \alpha E_X^{\mathrm{HF}} + (1-\alpha)\, E_X^{\mathrm{DFT}} + E_C^{\mathrm{DFT}} \tag{2.17}$$

where α specifies the fraction of exact exchange E_X^{HF}. This approach works well for a varity of systems reaching from semiconductors to molecules and mitigates the effects of the self-interaction error reasonably well. Heyd *et al.* introduced a screening parameter ω to separate the Coulomb operator

$\frac{1}{|\mathbf{r}-\mathbf{r}'|} = \frac{1}{\boldsymbol{r}}$ into a short- and long-range part using the error function

$$\frac{1}{\boldsymbol{r}} = \underbrace{\frac{1-\mathrm{erf}(\omega \boldsymbol{r})}{\boldsymbol{r}}}_{SR} + \underbrace{\frac{\mathrm{erf}(\omega \boldsymbol{r})}{\boldsymbol{r}}}_{LR} . \tag{2.18}$$

That way only the short-range part of the Hartree-Fock exchange is included [138, 175]. Combining Eq. 2.17 and Eq. 2.18

$$E_{\mathrm{XC}}^{\mathrm{HSE}}(\alpha,\omega) = \alpha E_X^{HF,SR}(\omega) + (1-\alpha)\, E_X^{\mathrm{PBE},SR}(\omega) + E_X^{\mathrm{PBE},LR}(\omega) + E_C^{\mathrm{PBE}} \tag{2.19}$$

gives the so-called HSE functional. Equation 2.19 contains two parameters α and ω; one controls the amount of exact-exchange α and the second separates the short- and long-range regime ω. In the case of $\alpha = 0$ and $\omega = 0$ we fully recover PBE, $\alpha = 0.25$ and $\omega = 0$ gives the PBE0 exchange-correlation functional [248]. In the 2006 version of HSE α is set to 0.25 and the range-separation parameter ω to 0.11 bohr^{-1} [175], so-called HSE06. The authors chose the value of ω by testing the performance of the functional for different test sets of atoms, molecules and solids covering insulators, semiconductors and metals. For bulk systems, they showed that band gaps are very sensitive to variations of the screening parameter ω, while bulk properties like the bulk modulus or lattice parameters are less affected. In addition to an improved description of the underlying physics, the range-separation reduces the computational effort if compared to hybrid functionals without range-separation, mainly because the Hartree-Fock exchange decays slowly with distance ($1/\boldsymbol{r}$-decay).

2.4. Van-der-Waals Contribution in DFT

Materials as well as molecules are stabilised by primary interatomic bonds, such as covalent, ionic or metallic bonds. In this section, we discuss the secondary bonding by van-der-Waals (vdW) interactions. Van-der-Waals forces are usually weaker than for example covalent interatomic forces. Of particular importance for this work is their role for the interlayer binding of graphite and few-layer graphene. However, all the exchange-correlation functionals introduced in Sec. 2.3 do not include the long range vdW tail. Different scientific communities define vdW forces differently; throughout this work the term *vdW energy* or *dispersion energy* will be used to describe the energy contributions originating from induced dipole - induced dipole interactions. The dispersion correction that we use in this thesis is based on a non-empirical method that includs a sum over pairwise C_6/R_{AB}^6

interactions between atoms A and B [343, 116, 117, 326]. It reads,

$$E_{\text{vdW}} = -\frac{1}{2}\sum_{A,B} f_{\text{damp}}(R_A, R_B)\frac{C_{6,AB}}{|R_A - R_B|^6} \tag{2.20}$$

where $|R_A - R_B| = R_{AB}$ is the distance between atom A and B and $C_{6,AB}$ is the corresponding C_6 coefficient. The last term, f_{damp} is the damping function. In practice, the functional form of f_{damp} is chosen in such a way that it eliminates the $\frac{1}{R_{AB}^6}$ singularity. The challenge is to find a good estimate for the $C_{6,AB}$ coefficient in Eq. 2.20. Using the so-called Casimir-Polder integral, the $C_{6,AB}$ coefficients are heteromolecular and can be written as

$$C_{6,AB} = \frac{3}{\pi}\int_0^\infty d\omega\ \alpha_A(i\omega)\alpha_B(i\omega) \tag{2.21}$$

where $\alpha_{A;B}(i\omega)$ is the frequency-dependent polarisability of atom A and B. This expression can be approximated by homonuclear parameters ($C_{6,AA}$, $C_{6,BB}$) and their static polarisabilities (α_A^0 and α_B^0) only:

$$C_{6,AB} = \frac{2C_{6,AA}C_{6,BB}}{\left(\frac{\alpha_B^0}{\alpha_A^0}C_{6,AA} + \frac{\alpha_A^0}{\alpha_B^0}C_{6,BB}.\right)} \tag{2.22}$$

In this work, we use the scheme proposed by Tkatchenko and Scheffler (TS-vdW). In this approach, the homonuclear C_6 coefficients become density-dependent. To this end an effective volume for an atom in a crystal or molecule, is defined by

$$V_A = \int d^3r\ w_A(\mathbf{r})n(\mathbf{r}), \tag{2.23}$$

where $n(\mathbf{r})$ is the total electron density and $w_A(\mathbf{r})$ is the Hirshfeld atomic partitioning weight [142]. It is defined as

$$w_A(\mathbf{r}) = \frac{n_A^{\text{free}}(\mathbf{r})}{\sum_B n_B^{\text{free}}(\mathbf{r})}. \tag{2.24}$$

$n_A^{\text{free}}(\mathbf{r})$ is the electron density of the free atom A and the sum goes over all atoms in the system. The electron densities for the free atom as well as for the full system are calculated within DFT. Finally, the effective C_6 coefficients ($C_{6,AA}^{\text{eff}}$) can be expressed in terms of the $C_{6,AA}^{\text{free}}$ coefficient of the

free atom (obtained from a database) and the Hirshfeld volume:

$$C_{6,AA}^{\mathrm{eff}} = \left(\frac{V_A}{V_A^{\mathrm{free}}} \right)^2 C_{6,AA}^{\mathrm{free}} \tag{2.25}$$

The C_6/R_{AB}^6 terms of the TS-vdW scheme are derived from the self consistent electronic density, and thus adapt to their environment.

As a final remark, the nature of long-range dispersion is inherently a many-body effect. The induced dipole moment of an atom in a solid (or molecule) depends on the induced dipole moments of all surrounding atoms. These additional screening contributions, due to many-body effects cannot be accounted for in a pairwise summation of vdW corrections. Tkatchenko *et al.* proposed a refinement to the above scheme, that corrects for the missing screening effects by modeling the dispersion interactions as coupled quantum harmonic oscillators located at individual atomic sites. That way it additionally captures nonadditive contributions originating from simultaneous dipole fluctuations at different atomic sites, leading to an overall improved screening and accounts for long-range anisotropic effects. This approach includes long-range many-body dispersion (MBD) effects employing a range-separated (rs) self-consistent screening (SCS) of polarisabilities [324, 5] and is therfore called MBD@rsSCS [325, 324, 5] [1].

2.5. Computational Aspects of DFT: The FHI-aims Package

The Kohn-Sham equations 2.8 are solved self-consistently as described in Sec. 2.2. Usually the first step is to expand the Kohn-Sham orbitals $\{\varphi_i(\mathbf{r})\}$ into a set of basis functions $\{\phi_j(\mathbf{r})\}$,

$$\varphi_i(\mathbf{r}) = \sum_j c_{ij}\phi_j(\mathbf{r}). \tag{2.26}$$

Many basis function choices have been explored, to list a few commonly used basis functions and a selection of electronic structure codes using them[2]:

[1] We use the MBD@rsSCS formalism as implemented in the FHI-aims code since 06-2014.

[2] An extensive list of quantum chemistry and solid-state physics software including information about the basis set used can be found at WIKIPEDIA.

Planewaves:

abinit [110]
CASTEP [58]
VASP [173]
Quantum Espresso [104]

Gaussians:

Gaussian [98]
Crystal [78]

Full-potential (linearised) augmented planewaves (fp-LAPW):

Wien2k [30, 286]
Exciting [121]

numeric atom-centered orbitals (NAOs):

SIESTA [155]
Dmol^3 [69, 70]
FHI-aims [32].

In this work, we use the FHI-aims package [32, 133]. FHI-aims is an all-electron/full-potential code that is computationally efficient without compromising accuracy. In order to achieve this for bulk solids, surfaces or other low-dimensional systems and molecules, the choice of basis functions is crucial. FHI-aims is based on numerically tabulated atom-centered orbitals (NAOs) of the following form

$$\phi_j(\mathbf{r}) = \frac{u_j(r)}{r} Y_{lm}(\Theta, \Phi), \tag{2.27}$$

where $Y_{lm}(\Theta, \Phi)$ are spherical harmonics and $u_j(r)$ is a radial part function. The choice of $u_j(r)$ is flexible and is obtained by solving a radial Schrödinger-like equation

$$\left[-\frac{1}{2} \frac{d^2}{dr^2} + \frac{l(l+1)}{r^2} + v_j(r) + v_{\text{cut}}(r) \right] u_j(r) = \varepsilon_j u_j(r). \tag{2.28}$$

The potential $v_j(r)$ defines the main behaviour of $u_j(r)$. Different potentials can be chosen. However, the most common choices in FHI-aims are a self-consistent free-atom (or ion) radial potential or a hydrogen-like potential. The second potential in Eq. 2.28 is a confining potential $v_{\text{cut}}(r)$. It ensures that the radial function is strictly zero beyond the confining radius r_{cut} and decays smoothly. In Fig. 2.3 the silicon 3s basis function is shown with the two potentials $v_j(r)$ and $v_{\text{cut}}(r)$. The basis functions are obtained by solving Eq. 2.28 on a logarithmic grid. An advantage of NAO is that they

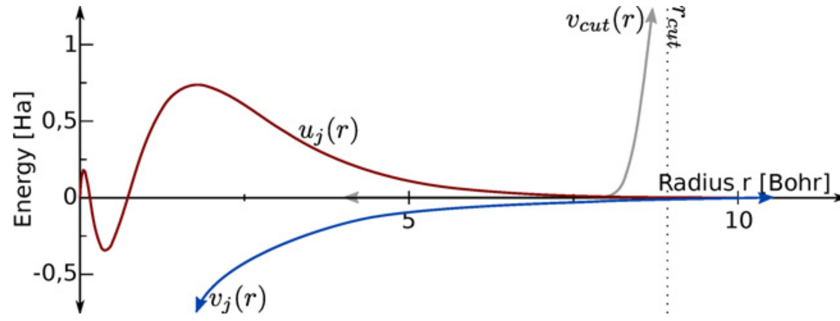

Figure 2.3.: The radial function $u_j(r)$ of the 3s orbital for a free silicon atom is plotted along radius r. Also shown are the free-atom like potential $v_j(r)$ and the steeply increasing confining potential $v_{\text{cut}}(r)$. The dotted line indicates the confining radius r_{cut}.

are localised around the nucleus, which is essential to achieve linear scaling and calculating systems with 1000s of atoms. The oscillatory behaviour of the electronic wave function close to the nucleus can be captured with just a few basis function, as the oscillations are included by construction. NAOs are non-orthogonal, therefore the overlap s_{ij} of two basis functions localised at two different atoms i and j

$$\int d^3r \, \phi_j^*(\mathbf{r})\phi_j(\mathbf{r}) = s_{ij} \tag{2.29}$$

is taken into account. An analytic treatment of the NAOs is not possible, instead FHI-aims uses accurate and efficient numeric tools. The main draw back is that the implementation of such algorithms is often more difficult. However, a major advantage of NAOs is that there are only basis functions in regions with atoms, e.g. the vacuum in a slab calculation contains no basis functions.

While plane waves allow a systematic improvement of the basis set by increasing the number of plane waves, NAOs cannot systematically be improved by a single parameter. To allow a systematic convergence of the calculation with respect of the basis size, FHI-aims provides a library of pre-defined settings for all species which govern the key parameters regarding the numerical accuracy. The library contains three different levels of accuracy, *light*, *tight* and *really tight* (see Appendix B.1). These three levels specify the accuracy of the real space grids, Hartree potential and the basis set size. The basis sets are organised in *Tier*s, ordered by increasing accuracy. Each *Tier* contains several basis functions of different angular momenta. The basis functions are determined by selecting them based on test sets of non-selfconsistent symmetric dimers in LDA. That way the accuracy and performance of calculations can be improved systematically by enabling

additional tiers one after another. Further details on the construction of the FHI-aims basis set and the species default library can be found in Blum *et al.* [32].

We use *light* settings to gain a first insight into a system's properties or for structural to find a good first guess of the equilibrium atomic positions. The next level, the *tight* species defaults are rather safe for a variety of systems. The *really tight* settings are over-converged for most purposes. The convergence with respect to numerical and basis settings used for a specific property or system was ensured (see Appendix B.

For structural relaxations and phonons, total energy gradients with respect to nuclear positions are calculated. In Section 2.2 the total energy of a system is obtained by solving the Kohn-Sham equations self-consistently. Forces are then given by the first derivative of the total energy E_{tot} (Eq. 2.11) with respect to the nuclear coordinate $\mathbf{R}_I$

$$\begin{aligned} \mathbf{F}_I &= -\frac{dE_{\text{tot}}}{d\mathbf{R}_I} \\ &= -\frac{\partial E_{\text{tot}}}{\partial \mathbf{R}_I} - \sum_{ij} \underbrace{\frac{\partial E_{\text{tot}}}{\partial c_{ij}}}_{=0} \frac{\partial c_{ij}}{\partial \mathbf{R}_I}. \end{aligned} \tag{2.30}$$

The derivative $\frac{\partial E_{\text{tot}}}{\partial c_{ij}} = 0$, because the self-constant energy E_{tot} is variational with respect to the molecular orbital coefficients c_{ij} [101]. The forces Eq. 2.30 are derived by calculating the derivative of the total energy Eq. 2.11 term by term, resulting in additional correcting terms (a full derivation and discussion is given in Gehrke [101]):

- The *Pulay forces* [255] originating from the dependency of the basis functions on the nuclear coordinates.

- The *Hellman-Feynman forces* [89, 136] correspond to the classical forces arising from the embedding of each nucleus in a field generated by the electronic charge density of all other nuclei.

- The *multipole-correction term* originates from the derivative of the Hartree energy Eq. 2.3, because in FHI-aims the Hartree potential is based upon a multipole expansion of the density instead of the electron density [32].

In this chapter, we discuss the collective vibrational motion of nuclei in a lattice at a specific frequency, so-called phonons (a detailed discussion can be found e.g. in the book by Dove Ref. [77]). Many physical properties of materials, such as the heat capacity, conduction or thermal expansion, depend on phonons.

So far the nuclei were fixed at their nuclear positions $\mathbf{R}_I$ and decoupled from the motion of the electrons by the Born-Oppenheimer (BO) approximation, Sec. 1.2. The many-body Hamiltonian (Eq. 1.2) separates into an electronic and a nuclear part. In this sections, we are dealing with the Hamiltonian of the nuclear system

$$\mathcal{H} = \mathcal{H}^{nuc} + \mathcal{E}^e = \hat{T}^n + \mathcal{E}^e + \frac{1}{2}\sum_{I,J;I\neq J} V(\mathbf{R}_I - \mathbf{R}_J) = \hat{T}^n + \mathcal{U}(\mathbf{R}) \tag{3.1}$$

where $\mathcal{E}^e_n$ are the eigenvalues of the electronic Schrödinger Eq. 1.5, $\frac{1}{2}\sum_{I,J;I\neq J} V(\mathbf{R}_I - \mathbf{R}_J)$ is the interatomic potential V^{nn} and $\hat{T}^n$ is the kinetic energy of the nuclei given in Eq. 1.2. In a crystalline solid the instantaneous atomic positions $\mathbf{R}_I = \mathbf{R}^0_I + \mathbf{u}_I(t)$ is given by the atomic equilibrium positions $\mathbf{R}^0_I$ and a time-dependent displacement $\mathbf{u}_I(t)$. For small displacements from the atomic equilibrium positions, we can expand $\mathcal{U}(\mathbf{R})$ from Eq. 3.1 in a Taylor series

$$\begin{aligned}\mathcal{U}(\mathbf{R}_I) = \mathcal{U}(\mathbf{R}^0_I) + \underbrace{\sum_I \left.\frac{\partial\mathcal{U}(\mathbf{R}_I)}{\partial\mathbf{R}_I}\right|_{\mathbf{R}^0_I}\left(\mathbf{R}_I - \mathbf{R}^0_I\right)}_{=0} \\ + \frac{1}{2}\sum_{IJ}\left(\mathbf{R}_I - \mathbf{R}^0_I\right)\underbrace{\left.\frac{\partial^2\mathcal{U}(\mathbf{R}_I)}{\partial\mathbf{R}_I\partial\mathbf{R}_\mathbf{J}}\right|_{\mathbf{R}^0_I}}_{C_{IJ}}\left(\mathbf{R}_\mathbf{J} - \mathbf{R}^\mathbf{0}_\mathbf{J}\right) + \mathcal{O}^3 = V^{harm}(\mathbf{R}_I).\end{aligned} \tag{3.2}$$

up to the second order, this is known as the *harmonic approximation*. The first derivative is zero, because all atoms are in their equilibrium position. The second derivative with respect to the displacement $\mathbf{u}_I(t)$ defines the interatomic force constant matrix $\bar{\mathrm{C}}$ in real space. The Fourier transformed interatomic force constant matrix $\tilde{C}_{IJ}(\mathbf{q})$ is used to built the dynamical matrix $\tilde{D}_{IJ}(\mathbf{q})$

$$\tilde{D}_{IJ}(\mathbf{q}) = \frac{\tilde{C}_{IJ}(\mathbf{q})}{\sqrt{M_I M_J}}. \tag{3.3}$$

The full solution for all vibrational states is given by the $3N_{\text{at}} \times 3N_{\text{at}}$ determinant equation to be solved for any wave vector $\mathbf{q}$ within the first Brillouin zone (BZ) with vibrational frequencies $\omega_{\eta,\mathbf{q}}$

$$\det\left|\bar{\bar{D}}(\mathbf{q}) - \omega^2\mathbb{1}\right| = 0, \tag{3.4}$$

with the identity matrix $\mathbb{1}$. The dependency of the vibrational frequencies $\omega_\eta(\mathbf{q})$ on the wave vector $\mathbf{q}$ is known as the phonon dispersion and η is the band index. If there are N_{at} atoms per unit cell, Eq. 3.4 gives $3N_{\text{at}}$ eigenvalues – vibrational frequencies – per reciprocal lattice vector $\mathbf{q}$. These correspond to the $3N_{\text{at}}$ branches of the dispersion relation. In a one-atomic unit cell, there are only three phonon bands for which $\omega_\eta(\mathbf{q} = 0) = 0$, they are called the acoustic modes. They split in one longitudinal and two transverse acoustic modes. In crystals with more than one atom per unit cell ($N^{at} > 1$), in addition to the three acoustic modes are higher branches, so-called optical modes. For a crystal with more than one atom in the primitive cell, there are $3N^{at} - 3$ optical modes.

The harmonic oscillator energy levels or eigenvalues for the mode $\omega_{\mathbf{q}}$ are given by

$$E_n(\omega_{\mathbf{q}}) = \hbar\omega_{\mathbf{q}}\left(n + \frac{1}{2}\right), \text{ with } n = 1, 2, 3, \cdots. \tag{3.5}$$

The full knowledge of the detailed dispersion relation $\omega_\eta(\mathbf{q})$ is not always necessary. For expectation values of thermodynamic potentials or their derivatives, the information about the number of phonon modes per volume at a certain frequency or frequency range is sufficient, the so-called phonon density of states (phonon-DOS). The phonon-DOS, $g_{\text{phon}}(\omega, \eta)$, of each branch η and the total phonon-DOS, $g_{\text{phon}}(\omega)$ are given by counting the respective number of phonons with a particular frequency $\omega_\eta(\mathbf{q})$ within the BZ:

$$g_{\text{phon}}(\omega) = \sum_\eta \frac{1}{(2\pi)^3} \int_{BZ} d^3q \, \delta(\omega - \omega_\eta(\mathbf{q})) \tag{3.6}$$

Phonons from first-principles: The finite difference method

The interatomic force constant matrix $\bar{C}$ can be computed using *ab initio* quantum-mechanical techniques such as density-functional theory (DFT). Two different methods are commonly used to compute phonons:

1. The *finite difference method*: This scheme is based on numerical differentiation of forces acting on the nuclei when atoms are displaced by a small amount from their equilibrium positions. In this work, we

use the phonopy software package to calculate phonons applying the finite difference method [327].

2. The *linear response function* or *Green's function method*: Derivatives of the energy are calculated perturbatively up to third order. A detailed discussion is given for example in [8, 111].

In the following, we focus on the discussion of the *finite difference method*, as this is the methodology used in this work. In practice, a single atom in a supercell (SC) is displaced by $\mathbf{u}_{I,n}$ and the induced forces on the displaced atom I and all other atoms in the SC are calculated. The forces are

$$\mathbf{F}(n,I) = -\sum_{n'} \bar{C}_{n,I;n',J} \cdot \mathbf{u}_{J,n=0} \tag{3.7}$$

where $\bar{C}_{n,I;n',J}$ is the interatomic force constant matrix relating atoms I in the unit cell n and J in unit cell n' (Eq. 3.2). Then, the dynamical matrix in reciprocal space $\tilde{\bar{D}}(\mathbf{q})$ (Eq. 3.4) becomes

$$\tilde{\bar{D}}(\mathbf{q}) = \sum_{n',J} \frac{\bar{C}_{0,I;n',J}}{\sqrt{M_I M_J}} \times \exp\left(-2\pi i\, \mathbf{q} \cdot (\mathbf{R}_{I,0} - \mathbf{R}_{J,n'})\right) \tag{3.8}$$

M_I, M_J and $\mathbf{R}_{I,0}$, $\mathbf{R}_{J,n'}$ are masses and positions of each atom plus an additional phase factor, because the atom I is located in the primitive unit cell and J in the n' unit cell of the supercell. Effects due to periodic boundary conditions are included by displacing only atoms in the central unit cell ($n = 0$) and calculating the effect of the displacement on all the atoms in the SC. At discrete wave vectors $\mathbf{q}$ the finite difference method is exact, if the condition

$$\exp\left(2\pi i\, \mathbf{q} \cdot \mathbf{L}\right) = 1 \tag{3.9}$$

is fulfilled ($\mathbf{L}$ is the lattice vector of the SC). Better accuracy of the phonon dispersion is achieved by choosing a larger SC.

The great advantage is that the calculation uses the same computational setup as other electronic structure calculations. To describe the phonon modes at a reciprocal-lattice vector $\mathbf{q}$, the linear dimension of the SC is of the order of $\frac{2\pi}{\|\mathbf{q}\|}$. Calculating a detailed phonon dispersion is demanding, because the cost of an interatomic-force constant calculation will scale as $3N_{\mathrm{at}} \times N_{\mathrm{UC}}$ where N_{UC} is the number of unit cells in the SC and the factor 3 accounts for the three generally independent phonon polarisations. Fortunately, making use of symmetry relations in the crystal can reduce the computational effort and phonons are often well behaved in regular solids and can be interpolated reducing the SC size needed [245].

So far, density-functional theory (DFT) was used to gain insight into material properties. To include the effects of temperature and pressure on the macroscopic system, *ab initio* atomistic thermodynamics is applied. It combines the results from DFT with concepts from thermodynamics and statistical mechanics [340, 279, 280, 259, 260]. Of particular interest in this work are phase diagrams to show conditions at which thermodynamically distinct phases can occur at equilibrium.

In this chapter the *ab initio* atomistic thermodynamic formalism are described and its connection to DFT calculations. In particular, two question are relevant for this work:

1. How to determine the coexistence of materials in different phases?

2. How can the energetics of different surface phases be compared?

4.1. The Gibbs Free Energy

The coexistence of different phases as well as the stability of different single-component surface phases are best represented in a p-T-diagram. Such a diagram is described by an isothermal-isobaric ensemble. In this ensemble, the number of particles N, the pressure p, and the temperature T are independent variables. The corresponding characteristic state function is the Gibbs free energy

$$G(T, p) = U - T \cdot S^{conf} + p \cdot V, \tag{4.1}$$

where U is the internal energy, S^{conf} is the configurational entropy and V is the volume. In the harmonic approximation, we can rewrite U as a sum of the Born-Oppenheimer (BO) energy E^{BO} (obtained from electronic structure calculations) and the vibrational free energy F^{vib}.

$$U = E^{BO} + F^{vib} \tag{4.2}$$

The vibrational free energy F^{vib} then can be written as

$$F^{vib} = E^{vib} - TS^{vib} \tag{4.3}$$

where E^{vib} is the vibrational energy and S^{vib} the vibrational entropy.

The vibrational free energies: In the previous chapter, the phonon dispersion in the harmonic approximation $\omega_\eta(\mathbf{q})$ and the phonon density of states (phonon-DOS) were calculated using the *finite difference method*. The microscopic partition function $Z(T, \omega)$ can be calculated from the phonon-DOS and then be used to determine the thermodynamic state functions E^{vib} and S^{vib} of a solid

$$\begin{aligned} E^{vib} &= -\frac{\partial}{\partial \beta} \ln\left(Z(T,\omega)\right) \\ S^{vib} &= k_B \left(\ln\left(Z(T,\omega)\right) + \beta E^{vib}\right). \end{aligned} \tag{4.4}$$

Inserting Eq. 4.4 into Eq. 4.3 leads to

$$\begin{aligned} F^{vib} &= -\frac{1}{\beta} \ln\left(Z(T,\omega)\right) \\ &= \int d\omega\; g_{\text{phon}}(\omega) \left[\frac{\hbar\omega}{2} + \frac{1}{\beta} \ln\left(1 - e^{-\beta\hbar\omega}\right)\right] \end{aligned} \tag{4.5}$$

In some cases, it is sufficient to include only the vibrational free energy contribution that originates from zero point vibrations. In this case the temperature goes to zero $T \to 0$ and Eq. 4.5 becomes

$$F^{ZPE} = \int d\omega\; g_{\text{phon}}(\omega) \frac{\hbar\omega}{2}. \tag{4.6}$$

Phase stabilities and the quasiharmonic approximation

Materials of the same chemical composition can occur in different phases, such as graphite and diamond or the different polytypes observed for silicon carbide. The most stable phase for a given temperature and pressure is the one with the lowest Gibbs free energy (Eq. 4.1).

The volume of a material changes with the temperature at constant pressure. This phenomenon is referred to as *thermal expansion*. The basic physical idea is that as the temperature rises the amplitude of the lattice vibrations increases, so that due to anharmonicities, the average value of the nuclear

displacement changes. The nuclei, then, spend more time at distances greater or smaller than the original interatomic spacing and on average the atomic bond length changes. The whole crystal changes, so that the volume dependent free energy is minimised.

In this work, we only consider free energy contributions from phonons, as they dominate the thermal properties in the systems of interest. The equilibrium structure at any temperature is always that with the lowest free energy

$$F(T, V) = E(V) + F^{vib}(T, V) \tag{4.7}$$

where $E(V)$ is the volume dependent total energy, F^{vib} is the vibrational free energy (Eq. 4.5). We use a phonon-based model, the so-called quasiharmonic approximation (QHA), to describe volume-dependency of the vibrational free energy (Eq. 4.5) thermal effects. In the QHA the unit cell volume is an adjustable parameter. The basic assumption is that the harmonic approximation holds separately for a range of different volumes, so that the temperature dependence of the phonon frequencies arises only from the dependence on the crystal volume. Since by expanding the volume the local minimum of the BO surface changes, so does the phonon dispersion leading to a change in the phonon-DOS and therefore in the vibrational free energy.

4.2. The Surface Free Energy

In this section, we focus on different surface phases. We are interested in the surface phase in equilibrium with its environment (e.g., background gas or the silicon carbide (SiC) bulk). This means that the environment acts as a reservoir, because it can give or take any amount of atoms to or from the sample without changing the temperature or pressure. The Gibbs free energy (Sec. 4.1) is the appropriate thermodynamic potential to describe such a system. The Gibbs free energy $G(T, p, N_i)$ depends on the temperature and pressure, and on the number of atoms N_i per species i in the sample. The most stable surface phase and geometry is then the one that minimises the surface free energy. For a surface system that is modeled by a slab with two equivalent surfaces the surface free energy is defined as:

Definition 4.2.1. *The surface free energy (γ)*

$$\begin{aligned}\gamma &= \frac{1}{2A}\left[G^{slab}(T,p,N_i) - \sum_i^{N_c} N_i\mu_i\right] \\ &= \frac{1}{2A}\left[E^{BO} + F^{vib} - T\cdot S^{conf} + p\cdot V - \sum_i^{N_c} N_i\mu_i\right],\end{aligned} \tag{4.8}$$

where A is the area of the surface unit cell, $G(T,p,N_i)$ is the Gibbs free energy of the surface under consideration, N_i is the number of atoms of element i and μ_i the element's chemical potential and N_c the total number os different chemical species. The Gibbs free energy is given by Eq. 4.1 with Eq. 4.2 as an approximation to the internal energy U.

In this work, we are interested in surface phases in equilibrium with the bulk phase. In a solid like SiC the compressibility is extremely low [1]. Therefore, the contribution of the $p \cdot V$ term in Def. 4.2.1 to the surface free energy will be neglected. In general, vibrational energy contributions can be included and may lead to small shifts. However, the necessary phonon calculations of a large surfaces including more than 1000 atoms are computationally demanding and not always feasible. We neglect vibrational free energy F^{vib} and configurational entropy contribution $T \cdot S^{conf}$ to the surface free energy. Only the total energy term E^{BO} is left as the predominant term. This allows us to rewrite Def. 4.2.1 to

$$\gamma = \frac{1}{2A}\left[E^{BO} - \sum_i^{N_c} N_i\mu_i\right]. \tag{4.9}$$

For the input energies E^{BO} we use total energies obtained from DFT calculations. DFT total energies are related to a thermodynamical quantity only in a restricted way. They correspond to the internal energy U Eq. 4.2 at zero temperature and neglecting zero-point vibrations.

Range of the chemical potential

The limits of the chemical potentials are given by the formation enthalpy of

[1] The volume of cubic silicon carbide (3C-SiC) changes by a factor of $V/V_0 = 0.927$ at a pressure of 21.6 GPa and temperature of $T = 298$ K [300, 313]. In this work we are interested in a low-pressure regime (< 1MPa). In this pressure regime the change of the 3C-SiC bulk volume is negligible.

SiC. The enthalpy of a system is

$$H(T,p) = G(T,p) + T \cdot S^{conf} = U + p \cdot V, \tag{4.10}$$

The enthalpy of formation ΔH_f is the energy released or needed to form a substance from its elemental constituents in their most stable phases.

Definition 4.2.2. *The enthalpy of formation ΔH_f*

The enthalpy of formation ΔH_f is the difference between the standard enthalpies of formation of the reactants and of the products.

$$\Delta H_f(T,p) = \sum_i^{N_p} N_i H_i - \sum_j^{N_r} N_j H_j, \tag{4.11}$$

where N_p is the total number of products involved in the process, H_i is the enthalpy of the product i and its respective stoichiometric coefficient, N_i, and N_r is the total number of reactants, H_j is the enthalpy of the reactant j and N_j its stoichiometric coefficient.

$$\Delta H_f(SiC)(T,p) \begin{cases} < 0 \ldots \textit{products form} \\ = 0 \ldots \textit{reactants and products are in equilibrium} \\ > 0 \ldots \textit{products precipitate into its reactants} \end{cases}$$

As before for the surface free energy (Def. 4.2.1), we will neglect the $p \cdot V$ and temperature and vibrational contributions to the internal energy U in Eq. 4.10. Then, we can express the enthalpy of formation ΔH_f in terms of total energies obtained from DFT calculations.

Throughout this work, we address SiC surfaces grown by high temperature silicon (Si) sublimation. Here, the SiC bulk is in equilibrium with the surrounding gas phase. The gas phase is atomic carbon (C) and Si reservoirs, which supplies or takes away atoms from the surface. The stability of the SiC bulk dictates $\mu_{Si} + \mu_C = E^{bulk}_{SiC}$ where E^{bulk}_{SiC} is the total energy of a SiC bulk 2-atom unit cell.

As a next step the limits of the chemical potential have to be defined. The allowable range of the chemical potentials μ_{Si} and μ_{C} under equilibrium conditions are fixed by the elemental crystal phases of Si and C. The diamond structure for Si is the appropriate bulk phase, but for C, there is a close

competition between diamond and graphite [23, 347, 348]. Both reference systems will be included in our analysis. In Ch. 6 and Appendix A a detailed discussion on the competition between the two C phases is presented.

Finding the maximum of the chemical potentials:

The bulk phases define the upper chemical potential limits. Above these limits the SiC crystal decomposes into Si or C

$$\begin{aligned}\max(\mu_{\mathrm{Si}}) &= \frac{1}{2}H_{\mathrm{Si}}^{\mathrm{bulk}}(T,p)\\ \max(\mu_{\mathrm{C}}) &= \frac{1}{2}H_{\mathrm{C}}^{\mathrm{bulk}}(T,p).\end{aligned} \tag{4.12}$$

Applying the approximations to the enthalpy of the products and reactants in Def. 4.2.2 discussed above, we will use total energies E obtained from DFT calculations in the following derivation of the limits of the chemical potentials, leading to

$$\max(\mu_{\mathrm{Si}}) = \frac{1}{2}E_{\mathrm{Si}}^{\mathrm{bulk}}, \quad \max(\mu_{\mathrm{C}}) = \frac{1}{2}E_{\mathrm{C}}^{\mathrm{bulk}} \tag{4.13}$$

for the maximum chemical potential of Si and C.

Finding the minimum of the chemical potentials:

Using the equilibrium condition of Def. 4.2.2 $\mu_{\mathrm{C}} + \mu_{\mathrm{Si}} = E_{\mathrm{SiC}}^{\mathrm{bulk}}$, we find for the minimum chemical potential for C

$$\min(\mu_{\mathrm{C}}) = E_{\mathrm{SiC}}^{\mathrm{bulk}} - \frac{1}{2}E_{\mathrm{Si}}. \tag{4.14}$$

At the end we find for the limits of the chemical potential μ_{C}:

$$E_{\mathrm{SiC}}^{\mathrm{bulk}} - \frac{1}{2}E_{\mathrm{Si}} \leq \mu_{\mathrm{C}} \leq \frac{1}{2}E_{\mathrm{C}}^{\mathrm{bulk}}. \tag{4.15}$$

Within the approximations to the enthalpy Eq. 4.10, the limits can be rewritten as

$$\frac{1}{2}E_{\mathrm{C}}^{\mathrm{bulk}} + \Delta H_f(\mathrm{SiC}) \leq \mu_{\mathrm{C}} \leq \frac{1}{2}E_{\mathrm{C}}^{\mathrm{bulk}} \tag{4.16}$$

with $\Delta H_f(\mathrm{SiC}) = E_{\mathrm{SiC}}^{\mathrm{bulk}} - \frac{1}{2}E_{\mathrm{C}}^{\mathrm{bulk}} - \frac{1}{2}E_{\mathrm{Si}}^{\mathrm{bulk}}$.

The chemical potentials, μ_{C} and μ_{Si}, can be experimentally manipulated for

example through the substrate temperature and background pressure of gases that supply Si or C [259, 329, 67, 302]. A precise control of the reservoirs provided by the background gases (for instance, disilane (Si_2H_8) [329]) is desirable, but calibration variations [202] may require exact (T, p) ranges to be adjusted separately for a given growth chamber.

It is important to note, that small changes in the chemical potentials do not necessarily correspond to small changes in the experimental conditions (temperature and pressure). For example, a drastic change in the number of Si (N_{Si}) and C (N_C) atoms can correspond to a small change of the corresponding μ. To cross beyond the carbon rich limit of graphite (or diamond) *in equilibrium* all Si has to be removed from the SiC crystal.

In this chapter, a bridge between DFT calculations and macroscopic phase stability was built. The *ab initio* atomistic thermodynamics approach is a tool to compare different systems, bulk or surfaces, that are in thermodynamic equilibrium. However, it cannot give any information about the process of the phase formation or kinetic effects during the growth process. Nonetheless, a first very important step when dealing with systems in different phases, is to identify the thermodynamic equilibrium state.

Chapter 2 introduced the basic concepts of density-functional theory (DFT). Kohn and Sham turned the Hohenberg-Kohn theorems (Sec. 2.1) into a computationally feasible scheme (Sec. 2.2) by mapping the system of interacting particles onto a fictitious system of non-interacting particles, that reproduces the same electron density as the many-body problem of interest. The central quantities obtained in DFT are the total energy and the electron density.

In this section and throughout this work, we will look at the Kohn-Sham band structure by plotting the Kohn-Sham eigenvalues $\varepsilon_i(\mathbf{k})$ along high-symmetry lines in the Brillouin zone (BZ). Also DFT is a ground-state theory, the Kohn-Sham band structure can provide a first insight into the electronic structure of a surface or crystal, if interpreted with care.

The Bulk Projected Band Structure In an electronic structure calculation, the transition from a three dimensional crystal with periodic boundary conditions in all three directions to a two dimensional surface breaks the symmetry of the direction perpendicular to the surface. For a surface, the periodicity in the x-y-plane is conserved, but broken along the z-direction. Figure 5.1 illustrates, how the periodicity of a periodic solid is broken along the z-axis. In practice, the surface is calculated within periodic boundary conditions. Surface calculations are realised by inserting a vacuum region between the surface slabs as illustrated in Fig. 5.1b. The slab, then is re-

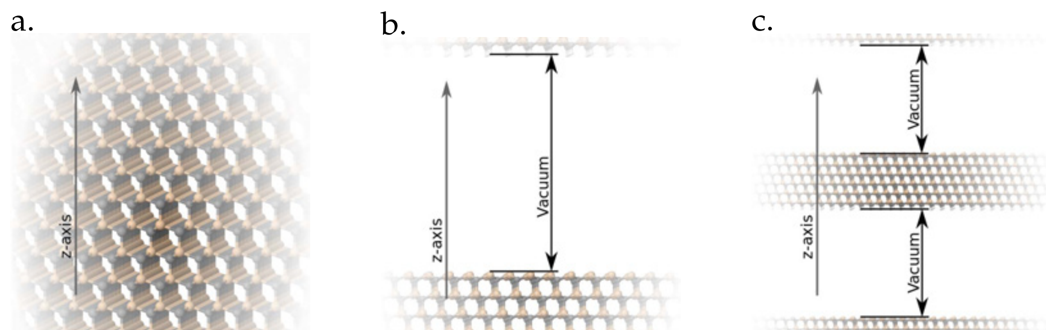

Figure 5.1.: (a) shows a periodic cubic silicon carbide (3C-SiC) crystal. In (b) the periodicity is broken by inserting a vacuum region along the z-axis. The bottom C atoms of the slab are terminated by H atoms. In all surface calculations periodic boundary conditions are applied. Hence the surface slab is periodically repeated along the z-direction as shown in (c).

peated periodically along the z-direction (Fig. 5.1c). Hydrogen (H) saturates the dangling bonds of the bottom carbon (C) atoms in order to avoid spurious interactions or electron transfer. As a consequence of the symmetry breaking, the wave number $\mathbf{k}_z$ of the Bloch waves is no longer a good quantum number. In the lateral directions the crystal surface is still periodic. Therefore the wave vector $\mathbf{k}_{\|}$ are still good quantum numbers.

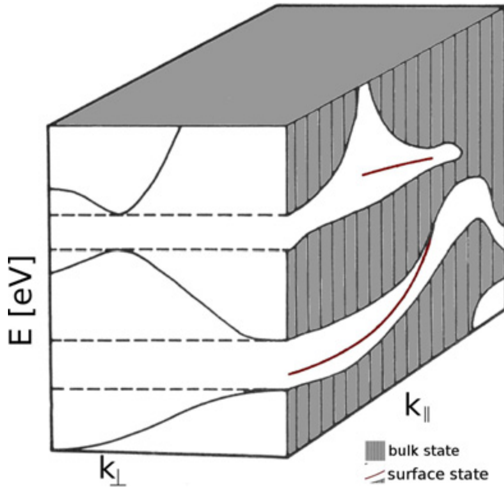

Figure 5.2.: A projected bulk band structure is illustrated schematically. For wave vectors $\mathbf{k}_{\perp}$ perpendicular to the surface bulk states appear. For different $\mathbf{k}_{\perp}$ the band energies between the lowest and highest values correspond to regions of bulk states. These bulk states are shaded in grey in the band structure along wave vectors parallel to the surface $\mathbf{k}_{\|}$. Outside the shaded bulk regions surface states can occur. (Figure courtesy of Johan M. Carlsson International Max-Planck Research School *"Theoretical Methods for Surface Science Part I"* (Presentation))

The surface band structure can be characterised by a two dimensional surface BZ[1]. A projected band structure, as shown in Fig. 5.2, is a very helpful tool to identify and analyse electronic surface states. Any wave vector $\mathbf{k}$ in the BZ splits into a component perpendicular to the surface $\mathbf{k}_{\perp}$ and one parallel $\mathbf{k}_{\|}$

$$\mathbf{k} = \mathbf{k}_{\|} + \mathbf{k}_{\perp}. \tag{5.1}$$

For each k-point in the surface plane there is a range of k-vectors with a perpendicular component. To identify the bulk states in the 2-dimensional surface BZ the bands are calculated along a path in the surface BZ for different $\mathbf{k}_{\perp}$. Due to the broken symmetry, the band energies for different $\mathbf{k}_{\perp}$ change. The region between the minimum and maximum band energy is shaded, like illustrated in Fig. 5.2. The shaded regions correspond to bulk states. Outside the bulk regions surface bands can appear. They correspond to states localised at the surface for example due to unsaturated bonds at the surface.

[1] A detailed discussion of the projection of 3 dimensional onto 2 dimensional Brillouin Zone can be found in Bechstedt [13]

Part II

Bulk Systems

Before investigating the hybrid SiC-graphene structures, we will focus on the pure bulk structures of crystalline carbon (C) and the substrate SiC. Both, the substrate SiC and crystalline carbon phases exhibit a close competition of different polymorphs.

We introduced the *ab initio* atomistic thermodynamics formalism in Ch. 4. This formalism allows us to compare the stability of different phases in a chemical potentials range. The reference bulk phases SiC and crystalline C and Si determine the limits of the chemical potential (Sec. 4.2). In this part we will discuss bulk SiC, crystalline C in detail.

SiC is observed in more than 250 different crystalline forms [57]. The basic building block of any SiC polymorph is a Si-C-bilayer ordered in a hexagonal lattice. The different polytypes of SiC differ in the stacking order of these Si-C-bilayers. Only the technologically most relevant polytypes are introduced in this chapter: 3C-SiC, and the hexagonal structures 4H-SiC and 6H-SiC.

The situation of the carbon polymorphs is very different, in the sense that the bonding characteristics change from a strong covalent tetrahedral - sp^3 hybridisation in the case of C-diamond to planes of carbon atoms covalently bonded by planar sp^2 hybrid orbitals. A single plane is called graphene, graphene layers stacked on top of each other and bonded by van-der-Waals (vdW) forces form graphite. It is a challenge for electronic structure theory to correctly describe the interlayer bonding in graphite. In the following, we discuss the accuracy we can achieve with the methodology used in this work. The energetic competition between graphite and diamond at room temperature is very close. In Appendix A, we discuss the phase coexistence of graphite and diamond.

6 Carbon-Based Structures

Carbon is arguably the most versatile element in the periodic table of chemical elements, due to its ability to form up to four covalent bonds by s-p orbital hybridisation in various ways: tetrahedral - sp^3, planar - sp^2 or linear - sp bonds. If we take oxygen and hydrogen also into consideration, carbon builds the structural backbone of an enormous variety of organic molecules providing the basic building blocks of life itself. Even if we only consider materials solely built from carbon atoms the structural diversity is large. The two most commonly known carbon allotropes are the three dimensional crystalline structures: diamond and graphite.

In diamond, carbon atoms arrange in a face-centered cubic lattice with two atoms in the unit cell, called diamond structure (see Fig. 6.1 a). The bond network is build from four identical sp^3-tetrahedral hybrid orbitals. The strong covalent C-C-bonds make diamond an extremely strong and rigid material with an exceptionally high atom-number density. Diamond is an insulator with an optical band gap corresponding to ultraviolet wavelength resulting in its clear and colourless appearance.

Graphite on the other hand is a semimetal with good in-plane conductance giving it its opaque grey-black appearance with a slight metallic shimmer. Its structure differs from the diamond structure as it is a layered material (see Fig. 6.1 b). Each layer is formed by carbon atoms arranged in a honeycomb lattice. The s, p_x and p_y orbitals hybridise to form planar sp^2 bonds. The non-hybridised p_z orbitals are oriented perpendicular to the plane and form weak π bonds with each of its neighbours [250]. The carbon planes are stacked on top of each other and bonded by weak vdW forces. This weak inter-plane bonding makes graphite soft enough to draw a line on a paper. The very different nature of the in-plane and out-of-plane bonding leads to highly anisotropic electronic, mechanical, thermal and acoustic properties, because electrons as well as phonons propagate quickly parallel to the graphite planes, but they travel much slower from one plane to the other.

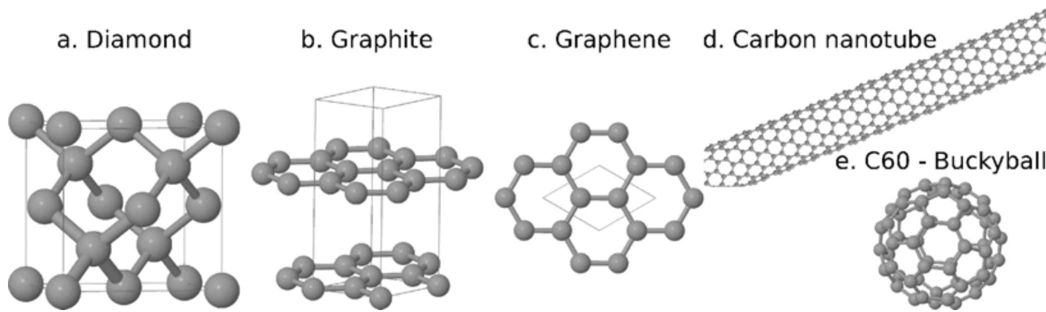

Figure 6.1.: Shows five different carbon structures. The two commonly known three dimensional carbon crystals: a. diamond and b. graphite. A single layer of graphite forms graphene a sp^2 bonded two-dimensional structure, labeled c. d. shows an example of a carbon nanotube and e. the Buckminster-Fullerene - C60, also-called Buckyball.

A single graphite sheet is called graphene (see Fig. 6.1 c). In one of the earliest graphene related studies, graphene was used as a theoretical model to gain a deeper understanding of the graphite band structure [338]. Wallace [338] first showed the unusual band structure with linear dispersing electronic excitations characterising graphene as a semimetal. At that time, two-dimensional crystals such as graphene were expected to be thermodynamically unstable and therefore served as theoretical model systems only [50]. 57 years after Wallace's publication [338], the modern era of the graphene *"gold-rush"* started when Novoselov, Geim *et al.* succeeded in isolating a single layer of graphene from a pencil stroke using Scotch tape [235]. Since 2004 the interest in graphene has boomed and the publication trends in this area have been nearly exponential. The extent of the *"graphene hype"* is visualised in Fig. 6.2. For comparison the number of publications per year for SiC and for the hybrid SiC-graphene system are included as well. Figure 6.2 clearly demonstrates the rapid growth of interest in this extraordinary two-dimensional material, while the number of publications for SiC has been almost constant for the last 20 years. In 2010, Andre K. Geim and Konstantin S. Novoselov at the University of Manchester were arwarded the Nobel Prize in Physics "for groundbreaking experiments regarding the two-dimensional material graphene". This atomically thin and highly robust carbon layer is a promising material for future nano-electronic components [333, 102, 287, 233, 234].

A single sheet of graphene rolled along a given direction and reconnected the C-C bonds at the end, gives carbon nanotubes shown in Fig. 6.1 d [149]. For many physical aspects they show the behaviour of a one-dimensional object.

Introducing pentagons in a single sheet of graphene creates a positive curvature. In this way, the carbon atoms can be arranged spherically form-

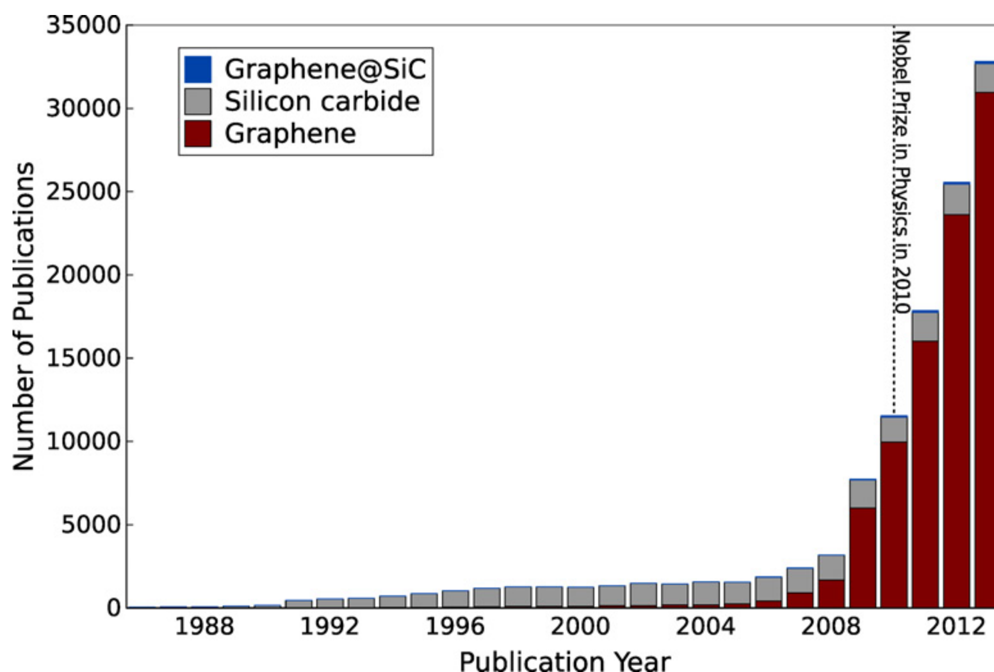

Figure 6.2.: Number of publications per year as given in a Web-of-Science search for the keywords 'graphene', 'silicon carbide' and both keywords together [321].

ing so-called fullerenes molecules [174] (see Fig. 6.1 e). They have discrete energy states and can be thought of as zero-dimensional objects.

In summary, we introduced zero-, one-, two-, and three-dimensional carbon structures. In this work, we are mainly interested in the three- and two-dimensional carbon allotropes, graphene, graphite and diamond.

6.1. The Ground State Properties of Diamond, Graphite and Graphene

The aim of this Section is to characterise the structural properties and the thermodynamic stability of diamond, graphite and graphene from *ab initio* electronic structure calculations (Part I). In the description of thermodynamic properties, such as the thermal expansion of the bulk phases, vibrational properties play a crucial role. The crystalline carbon structures have been subject to extensive theoretical and experimental studies (e.g. [349, 164, 103, 221, 250] and references therein).

We employ density-functional theory (DFT) using the FHI-aims all-electron

code [32, 133] with '*tight*' numerical settings (Appendix B). We compare results obtained from different approximation to the exchange-correlation functional using the Perdew-Burke-Ernzerhof generalised gradient approximation [246] (PBE), the local-density approximation (LDA) [249] and the HSE hybrid functional with α=0.25 and ω=0.11 bohr^{-1} [175] (HSE06). For an accurate description of the different crystalline phases, in particular the interlayer bonding in graphite, we include the effect of long-range electron correlations in an effective way using a vdW correction (Ch. 2.4) forPBE and Heyd-Scuseria-Ernzerhof hybrid functional [138, 175] (HSE).

To calculate equilibrium lattice parameters two different methods are used in this work. The first method minimises the energy with the help of analytic forces and stress tensor as implemented in the FHI-aims-code [169]. For finding a minimum of the DFT based potential energy surface (PES) corresponding to the equilibrium lattice parameters, a minimisation based on analytic forces and stress tensor gives the most accurate results. The second method is based on numerically fitting computated energies for different volumes to the Birch-Murnaghan (B.-M.) equation of states Def. 6.1.1, which is used to account for temperature effects.

Table 6.1 lists the structural parameter and the cohesive energy for diamond, graphite and graphene for different exchange-correlation functionals (LDA, PBE, HSE06 and vdW corrected PBE+vdW and HSE06+vdW) based on minimising the Born-Oppenheimer potential energy surface with the help of analytic forces and stress tensor.

The experimentally reported energy difference between diamond and graphite at T=0 K is 25 meV/atom [23] and 150 meV/atom [40]. Based on the potential energy minima (no zero-point vibrational correction (ZPC)) Tab. 6.1 graphite is found to be more stable than diamond in PBE+vdW by 60 meV/atom. This is qualitatively consistent with the extrapolated experimental phase hierarchy. In plain PBE graphite is overstabilised by 130 meV/atom. In LDA, both phases are similarly stable: Considering only the potential energy surface, diamond is slightly more stable (by 12 meV), but already the inclusion of ZPC[347] neutralises this balance (graphite more stable by 3 meV/atom).

As a next step, we include temperature effects by accounting for zero-point vibrational effects. At constant pressure, the equilibrium volume of a material changes with temperature. In Sec. 4.1, we saw that the thermal expansion can be understood in terms of lattice vibrations. We introduced the quasiharmonic approximation (QHA) to calculate the volume dependent potential energy surface. The basic assumption of the QHA is that the anharmonicity

Diamond					
Functional		a_0 [Å]		V/atom [Å^3]	E_{coh} [eV/atom]
LDA	PES	3.533		5.51	-8.95
PBE	PES	3.572		5.70	-7.74
PBE+vdW	PES	3.551		5.60	-7.94
HSE06	PES	3.548		5.58	-7.56
HSE06+vdW	PES	3.531		5.51	-7.76
Exp.		3.567 [330]		5.67 [330]	$-7.356^{+0.007}_{-0.039}$ [40]

Graphite					
Functional		a_0 [Å]	c_0 [Å]	V/atom [Å^3]	E_{coh} [eV/atom]
LDA	PES	2.445	6.643	8.598	-8.94
PBE	PES	2.467	8.811	11.606	-7.87
PBE+vdW	PES	2.459	6.669	8.762	-8.00
HSE06	PES	2.450	8.357	9.017	-7.65
HSE06+vdW	PES	2.444	6.641	8.591	-7.78
Exp.	288.15K [226]	$2.456 \pm 1e^{-4}$ [226]	$6.694 \pm 7e^{-4}$ [226]	8.744	$-7.371^{+0.007}_{-0.039}$ [40]

Graphene					
Functional		a_0 [Å]		A/atom [Å^2]	E_{coh} [eV/atom]
LDA	PES	2.445		2.589	-8.92
PBE	PES	2.467		2.634	-7.87
PBE+vdW	PES	2.463		2.627	-7.91
HSE06	PES	2.450		2.599	-7.65
HSE06+vdW	PES	2.447		2.596	-7.69

Table 6.1.: The structural and cohesive properties of diamond, graphite and graphene are listed for different exchange-correlation functionals (LDA, PBE, HSE06 and vdW corrected PBE+vdW and HSE06+vdW): The lattice parameters a_0 [Å] and for graphite c_0 [Å] calculated by minimising the energy with the help of analytic forces and stress tensor as implemented in the FHI-aims-code [169]. The cohesive energy E_{coh} [eV] as obtained in this work. Reference data from experiment is included. "PES" refers to results computed based on the Born-Oppenheimer potential energy surface without any corrections.

is restricted to the change of the volume without any further anharmonicities, so that the lattice dynamics can still be treated within the harmonic approximation (Ch. 3). The equilibrium volume for every temperature is given by minimising $F(T,V) = E(V) + F^{vib}(T,V)$ (Eq. 4.7) with respect to the volume at a fixed T. For $F(T,V)$ analytical gradients are not available. In this case, the free energy potential surface is sampled by calculating the Helmholtz free energy (Eq. 4.7) for different volumes. Then, the equilibrium volume is calculated by fitting the $F(T,V)$ pairs to the B.-M. equation of states Def. 6.1.1 for every temperature T [223, 27].

The B.-M. equation of state describes the change of energy with the volume at constant temperature.

Definition 6.1.1. *Birch-Murnaghan equation of state*

$$E(V) = E_0 + \frac{B_0 V}{B_0'}\left[\frac{(V_0/V)^{B_0'}}{B_0'-1} + 1\right] - \frac{B_0 V_0}{B_0'-1}$$

with

E_0	...	*equilibrium energy*	$B_0 = -V\left(\frac{\partial P}{\partial V}\right)_T$	...	*Bulk modulus*
V_0	...	*equilibrium volume*	B_0'	...	*Bulk modulus derivative with respect to pressure at* $p = 0$

Table 6.2 gives the ground state lattice parameter for graphite and diamond calculated without any temperature effects by fitting to Def. 6.1.1. We also include the ZPC lattice parameter calculated with PBE+vdW. The ZPC lattice parameter were calculated by Florian Lazarevic and were presented as part of his Master thesis [184]. Exemplary phonon band structures and the details of the underlying phonon calculations are given in Appendix D.1. Temperature effects beyond the ZPC and the diamond graphite phase coexistence line are presented in the Master thesis by Florian Lazarevic [184] or in Appendix A.

For diamond, only one lattice parameter has to be determined, so the fitting routine is straightforward to apply. In graphite, two parameters have to be obtained: the in-plane lattice parameter a and the out-of-plane lattice parameter c. In this case, first the ratio $\frac{a}{c}$ that minimises the energy for a fixed volume is determined by a polynomial fit. Then the minimum energy obtained from the polynomial fit enters the B.-M.-fit.

Functional		Diamond			Graphite			
		a_0 [Å]	$V/atom$ [Å^3]	E_{coh} [eV]	a_0 [Å]	c_0 [Å]	$V/atom$ [Å^3]	E_{coh} [eV]
LDA	PES	3.533	5.512	-8.95	2.445	6.647	8.603	-8.94
	ZPC	3.547	5.58					
PBE	PES	3.573	5.702	-7.86	2.446	8.653	11.39	-8.00
PBE+vdW	PES	3.554	5.611	-8.06	2.464	6.677	8.777	-8.13
	ZPC	3.581	5.74		2.465	6.674	8.780	

Table 6.2.: Calculated ground state lattice parameter a_0 and c_0, unit cell volume per atom and cohesive energies for diamond and graphite using Def. 6.1.1. "PES" refers to results computed based on the Born-Oppenheimer potential energy surface without any corrections. We also include ZPC lattice parameters. (Data taken from Master thesis by Florian Lazarevic [184])

The lattice parameters obtained by fitting show good agreement with the lattice parameter obtained by lattice relaxation Tab. 6.1. The only exception is the out-of-plane lattice parameter c_0 of graphite calculated using the PBE exchange-correlation functional. We present a detailed discussion of the interlayer bonding of graphite for different exchange-correlation functional in Sec. 6.2. It shows, that using PBE gives a very weak interlayer bonding resulting in large interlayer spacing. This means, that small changes in the energy can correspond to large changes in the lattice parameter c_0, making an accurate polynomial fit as well as a stress minimisation difficult. Apart from this special complication, the minimisation procedure is able to give reliable and accurate equilibrium volumes.

We also calculated the lattice paramter including ZPC for graphene using PBE+vdW. The phonon band structure of graphene and the details of the underlying phonon calculation used, are given in Appendix D.1. For the zero-point corrected lattice parameter in graphene, we found 2.471Å.

The difference between the cohesive energies obtained for the stress tensor based lattice relaxation (Tab. 6.1) and the B.-M.-fit (Tab. 6.2) are more pronounced. The largest cohesive energy difference was found for graphite. For the PBE and PBE+vdW exchange-correlation functionals the difference is 0.13 eV. The cohesive energies in Tab. 6.1 are obtained from self-consistent DFT total energies, while the energies in Tab. 6.2 were obtained by a fitting procedure. For graphite two different energy fits are included in the cohesive energy, first a polynomial fit to obtain the ratio between the minimum energy with respect to the ration between the lattice parameter a and c. This energy then enters the B.-M.-fit.

6.2. The Challenge of Inter-planar Bonding in Graphite

In Section 6.1 and Appendix A, we are confronted with the challenge of determining the equilibrium crystal structure of graphite. The difficulty originates from the strongly anisotropic bonding in graphite. While the bond length of the strong covalent in-plane bonds are well described for a variaty of exchange-correlation functionals (see Tab. 6.1 and 6.2), the interaction between the layers is very weak and is generally attributed to vdW forces. Closely related to the question of the interlayer bond distance is the interlayer energy. Unfortunately, a computational investigation within DFT of the interlayer bonding in graphite is a challenge. The problem arises from the local and semi-local approximation to the exchange-correlation functional commonly used in DFT and the intrinsically long-range nature of vdW-bonding. For an accurate description of the interlayer bonding in graphite long range electron correlation effects have to be included in DFT calculations (Ch. 2.4). The inclusion of vdW effects is a very active scientific area of its own (e.g. see [271, 116, 182, 117, 188, 326, 325, 324, 5] and references therein). Björkman *et al.* [28] and Graziano *et al.* [115] gave a detailed discussion of incorporating vdW-effects in the theoretical description of layered materials.

In this section, we focus on the comparison of two different vdW correction schemes: the well established Tkatchenko-Scheffler (TS) scheme [326] and the latest progress incorporating many-body effects [325, 324, 5]. Both vdW schemes depend on the electronic density. Recapping briefly the summary of the vdW section (Sec. 2.4), the TS approach is based on a non-empirical method that includs a sum over pairwise interactions. The many body approach includes long-range many-body dispersion (MBD) effects employing a range-separated (rs) self-consistent screening (SCS) of polarisabilities [324, 5] (MBD@rsSCS). It captures non-additive contributions originating from simultaneous dipole fluctuations at different atomic sites, leading to an improved overall screening and accounts for long-range anisotropic effects.

However, the determination of the graphite interlayer binding energy is not just a challenge for theory. To our knowledge, four different experiements have been published reporting binding energies in the order of 30-55 meV/atom [106, 17, 350, 201]. In the literature, three different energies are used to describe the interlayer binding energy: *exfoliation energy*, *binding energy* and *cleavage energy*. The differences between these three terms are subtle. Björkman *et al.* [29] gave an illustative description of this three

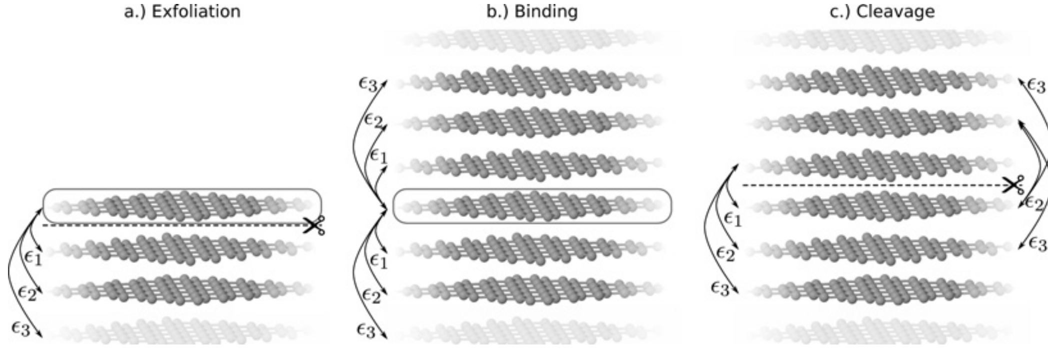

Figure 6.3.: The interlayer binding energy sketch for three different types of binding: *a.) exfoliation energy, b.) binding energy, c.) cleavage energy*. In (a) and (b), the layer of interest is marked by a box. The scissor and dashed line for the exfoliation (a) and cleavage (c) cases illustrates how the crystal is cut.

energies in the supplemental material of Ref. [29]. We here will follow their line of argumentation. For completeness we will briefly derive the three energies.

Figure 6.3 shows a sketch of the different terms for the binding energy. The interaction energies between two layers are labelled as ϵ_1 for nearest neighbours, ϵ_2 for second nearest neighbours *etc*. The exfoliation energy (E_{XF}) is the energy to remove a single carbon layer (marked by a box in Fig. 6.3 (a)) from the graphite bulk structure. We assume that energy contributions originating from in-plane relaxation are neglectible, which is a good assumption for AB stacked graphite [1]. From Fig. 6.3 (a) we see, that E_{XF} is a sum of the interaction energies

$$E_{XF} = \epsilon_1 + \epsilon_2 + \ldots = \sum_{n=1}^{\infty} \epsilon_n. \tag{6.1}$$

We determine E_{XF} by calculating the total energy of a graphite slab with n layers (E_n), of a graphite slab with $n-1$ layers (E_{n-1}) and an isolated graphene layer E_1. E_{XF} then is given as

$$E_{XF}(n) = \frac{1}{N_{\text{atom}}} \left(E_n - (E_{n-1} + E_1) \right) \tag{6.2}$$

where E stands for calculated DFT total energies and N_{atom} is the number of atoms in the graphite slab.

[1] The assumption does not necessarily hold for graphite layers rotated by an arbitray angle, because due to the rotation there might be regions close to AA and other close to AB stacking. AA and AB stacked graphite have different interlayer distances [220]. This difference results in a layer corrugation and consequently in in-plane relaxation, which leads to sizeable energy contributions.

Another relevant energy is the energy needed to separate all layers from each other by increasing the interlayer distance – the binding energy (E_B) (Fig. 6.3 (b)). When we stretch the crystal to separate the individual layers from each other we break two bonds, but since the bonds are shared the sum of interaction energies (ϵ_n) is halved

$$E_B = \frac{1}{2} \sum_{n=1}^{\infty} 2 \cdot \epsilon_n. \tag{6.3}$$

A comparison of Eq. 6.1 and Eq. 6.3 shows that the exfoliation energy is equal to the binding energy per layer. We calculate the binding energy of an infinite graphite crystal separated into isolated graphene layers

$$E_B = \frac{1}{N_{\text{atom}}} \left(E_{\text{graphite}} - N_{\text{layer}} E_{\text{graphene}} \right) \tag{6.4}$$

where E_{graphite} (E_{graphene}) is the total energy of graphite (graphene) and N_{layer} is the number of layers. In the case of an infinite large slab, Eq. 6.2 gives the same energy as Eq. 6.4. In practice, Eq. 6.4 is used to calculate interlayer binding energies.

The cleavage energy is the energy required to split a graphite crystal in two halves (see Fig. 6.3 (c)) or, in other terms, it is the energy to create two units of surface. The cleavage energy expressed in terms of ϵ_n is

$$E_{cleav} = \epsilon_1 + 2 \cdot \epsilon_2 + \cdots + n \cdot \epsilon_n = \sum_{n=1}^{\infty} n \cdot \epsilon_n = 2 \cdot E_{surf} \tag{6.5}$$

Comparing Eq. 6.3 and Eq. 6.5 shows, that Eq. 6.5 is greater than the binding energy and can only serve as an upper bound of the binding energy. The definitions of the exfoliation energy, binding energy and cleavage energy will be helpful when interpreting experimentally obtained graphene interplanar binding energies.

Figure 6.4.: History of the graphite interlayer binding energy (meV/atom) since the first experiment in 1954 [106]. The experimental values [106, 17, 350, 201, 113] are given as crosses and the theoretical values as filled circles. The colour of each circle depends on the experimental work cited in the publication. Girifalco and Lad [106] gave the binding energy in units of ergs/cm^2, their value of 260 ergs/cm^2 was erroneously converted to 23 meV/atom (shown in light green) instead of the correct 42 meV/atom (dark green). A full list of references and binding energies is given in Appendix J

Finding an accurate description of the graphite interlayer binding energy is an ongoing quest in experiment and theory alike. We first summarise the history of the search for the graphite interlayer binding energy (Fig. 6.4). The four experiments [106, 17, 350, 201] and the improved interpretation of the 2012 experiment [113] are shown as crosses. Girifalco and Lad [106] gave their measured binding energy in units of ergs/cm^2, the value of 260 ergs/cm^2 was erroneously converted to 23 meV/atom (included in Fig. 6.4 as a dashed line) instead of the correct 42 meV/atom. In the literature both values were used reference. The different theoretical values are shown as filled circles. The colour of each circle depends on the experimental work cited. A full list of theoretical and experimental values of the graphite binding energy is given in Appendix J.

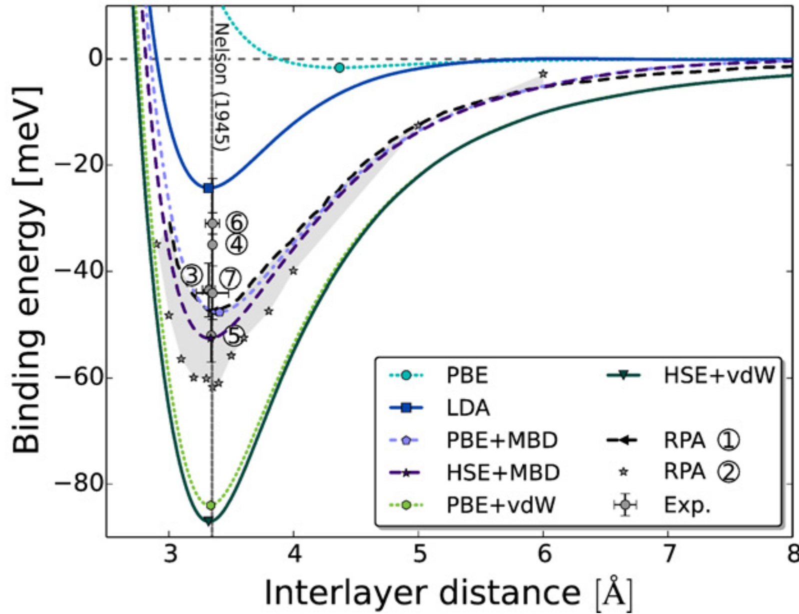

Figure 6.5.: Binding energy E_B of graphite as a function of the interplanar distance d using LDA, PBE, HSE06 and two different vdW correction schemes (TS [326] and MBD [325, 324, 5]). The symbols mark E_B at the equilibrium interlayer distance. The vertical line marks the experimental lattice spacing of $c_0 = 6.694$Å [226]. For comparison E_B values from RPA@PBE calculations ((1) Lebègue *et al.* [185], (2) Olsen *et al.* [239]) and from experiment ((3) Girifalco *et al.* [106], (4) Benedict *et al.* [17], (5) Zacharia *et al.* [350], (6) and (7) Liu *et al.* [201, 113]) are included.

We first discuss the experimental data included in Fig. 6.4. In 1954, Girifalco and Lad provided the first experimental value $E_{XF} = (42.5 \pm 5)$ meV/atom for the graphite exfoliation energy obtained indirectly from *heat of wetting* measurements [106]. In a unique experiment Benedict *et al.* determined the binding energy of twisted graphite based on transmission electron microscopy (TEM) measurements of the radial deformation of collapsed multiwall

carbon nanotubes. Carbon nanotubes with large radii collapse and lose their circular cross-section, because of an interplay between the intersheet attraction and the resistance to elastical deformation of the curvature of the carbon nanotube (*mean curvature modulus*). The TEM data was evaluated by continuum elasticity theory and a Lennard-Jones (LJ) potential for the description of the graphite sheet attraction. They found a binding energy of $E_B = (35^{+15}_{-10})$ meV/atom [17]. Zacharia *et al.* investigated the graphite interlayer bonding by thermal desorption of polyaromatic hydrocarbons, including benzene, naphthalene, coronene, and ovalene, from a basal plane of graphite. To determine the interlayer binding energy of graphite Zacharia *et al.* used the thermal desorption data. They assumed the interaction of carbon and hydrogen atoms to be pairwise additive to the total binding energy of the molecules. For the graphite cleavage energy they found $E_{cleav} = (61.65 \pm 5)$ meV/atom and $E_B = (52.65 \pm 5)$ meV/atom for the binding energy [350]. Liu *et al.* performed the first direct measurement of the graphite cleavage energy based on displacement measurements facilitating mechanical properties of graphite [353]. In the experiment a small graphite flake (a few micrometer) was sheared from a graphite island. The profile of the cantilever graphite flake was measured using atomic force microscopy (AFM). They derived a relationship between the cleaving force and the displacement from a parameterised LJ potential. They estimated the binding energy to be 85% of the cleavage energy and obtained a value of $E_B = (31 \pm 2)$ meV/atom. In a recent work Gould *et al.* suggested that the binding energy in the latter experiment might be substantially underestimated, because the experimental data were analysed using a LJ potential. At large separation the LJ potential gives qualitatively incorrect interlayer binding energies [75]. The other experimental results in the literature might also be affected by the same difficulty!

From a theoretical point of view the description of the interlayer binding energy is equally challenging. Various methods were employed, ranging from semi-empirical approaches to advanced first-principles calculations. The obtained values for the graphite interlayer binding energy scatter widely (see Fig. 6.4). In Sec. 2.4, we already pointed out that standard local and semi-local approximations such as the LDA and the PBE approximation to the exchange-correlation functional cannot capture the inherently long range nature of vdW interactions. A common technique to include the long-range tail of dispersion interactions is to add energies obtained using pairwise interatomic potential to DFT total energies [116, 117, 128, 326, 118]. This approach led to binding energies between 43-82 meV/atom [119, 128, 7, 114, 200, 38, 42, 45]. Another approach is the seamless inclusion of vdW interaction in the exchange-correlation functional [271, 72, 182, 53, 322, 207, 272] resulting in binding energies between

24-66 meV/atom [271, 167, 59, 207, 115, 272, 323, 22]. Spanu *et al.* [299] applied a quantum Monte Carlo (QMC) method (variational Monte Carlo and lattice regularized diffusion Monte Carlo [51]) to determine the layer energetics ($E_B = (56 \pm 5)$ meV/atom) and equilibrium lattice parameter ($d = 3.426$ Å) of graphite. The calculations were performed in very small simulation supercells ($2 \times 2 \times 2$) and finite-size effects may limit the accuracy of their results. Two groups applied DFT (PBE) based random phase approximation (RPA) calculations of the correlation. RPA@PBE calculations provide a more sophisticated method for treating vdW interactions. Both groups found an equilibrium interplanar distance $d = 3.34$ Å. However their binding energies differ by 14 meV/atom ($E_B = 48$ meV/atom [185] and $E_B = 62$ meV/atom [239]). Lebègue *et al.* confirmed the E_B(d)$\sim c_3/d^3$ behavior of the correlation energy at large distances as predicted by analytic theory for the attraction between planar π-conjugated systems [75]. Olsen and Thygesen [239] also calculated the binding energy with the same k-point sampling as Lebègue *et al.* [185] and found a binding energy of 47 meV/atom. The remaining difference might originate from a different setup of the projector augmented wave method. Using a very dense k-point sampling of ($26 \times 26 \times 8$) to obtain the Hartree-Fock wave function they found 62 meV/atom for the binding energy.

We calculated the graphite interlayer binding energy as a function of the interplanar distance $d = c_0/2$ for different exchange-correlation functionals (LDA, PBE, HSE06) and vdW correction schemes (TS [326] and MBD [325, 324, 5]) shown in Fig. 6.5. LDA is a purely local approximation to the exchange-correlation functional. Therefore it is not capable of capturing the long-range dispersion interactions. However, it gives a surprisingly good equilibrium lattice parameter of 6.643 Å (Tab. 6.1), but it clearly underestimates the binding energy in comparison to available experimental and RPA@PBE values [275, 54, 318, 127, 185, 239]. The PBE curve shows a very weak bonding ($c_0 = 8.811$ Å). More interesting is the performance of the vdW corrected exchange-correlation functionals. We first compare the two different vdW correction schemes. For the pairwise TS scheme we find an equilibrium lattice parameter of $c_0 = 6.669$ Å for PBE+vdW and $c_0 = 6.641$ Å for HSE06+vdW in very good agreement with the experimental value of 6.694 Å [226]. The binding energies are overestimated with 84.0 meV/atom (87.1 meV/atom) for PBE+vdW (HSE06+vdW), respectively. Combining the MBD@rsSCS scheme with exchange-correlation functionals (PBE and HSE06) should improve the overall description of the graphite inter-planar bonding, because it additionally captures non-additive contributions and accounts for long-range anisotropic effects. Indeed, for the binding energy we find 47.6 meV/atom and 52.5 meV/atom for PBE including van-der-Waals effects with full many-body treatment (MBD@rsSCS)

[325, 324, 5] (PBE+MBD) and HSE06+MBD, respectively. In Fig. 6.5 in particular the PBE+MBD but also the HSE06+MBD curve show a good agreement with the RPA data of Lebègue *et al.* [185] close to the minimum.

As discussed above, the interpretation of the experimental data is usually based on the LJ potential, which might lead to an underestimation of the binding energy in graphite [113]. Here, high quality theoretical values of the graphite binding energy are a challenge because electronic structure calculations are difficult to converge [239]. In the case of graphite interlayer binding energies reliable benchmark data is still missing. However, a recent high quality QMC study provides a benchmark value for bilayer graphene [220]. In the work of Mostaani *et al.* [220], finite size effects were controlled by using large supercells (6×6). They obtained a binding energy for AB stacked bilayer graphene of E_B= 17.7 meV/atom and an inter-planar lattice constant of 3.384 Å [220]. In comparison, we find binding energies of bilayer graphene of E_B= 22.0 meV/atom using PBE+MBD and of E_B= 36.5 using PBE+vdW. For bilayer graphene, we find good agreement for the binding energy between PBE+MBD and high level benchmark data (QMC) and an overestimation for PBE+vdW.

The MBD@rsSCS method is a very recent development. At the current state of the implementation it is not yet optimised well enough to treat large systems containg 1000s of atoms. Therefore, we will use the TS scheme for most of the results presented in this work. The TS scheme is an accurate non-empirical method to obtain the C_6 coefficients from ground-state electron density and reference values for the free atoms allowing for an equally accurate treating of atoms in different chemical environments. On the other hand, most methods based on the pairwise summation of C_6/R^6 coefficients rely on empirical or at least semiempirical determination of the C_6 coefficients [343, 116, 117]. In these methods the accuracy depends on the detailed determination of the C_6 coefficients. However, all methods based on the pairwise summation of C_6/R^6 coefficients cannot capture the non-additive contributions originating from simultaneous dipole fluctuations at different atomic sites.

In summary, a reliable benchmark value for the graphite interlayer binding energy is still missing both experimentally and theoretically. The main obstacle is the correct description of the binding energy at large separations. In computational studies, a sum over pairwise C_6/R^6 interactions is often used, leading to a $E_B(d) \sim c_5/d^5$ behaviour, which is incorrect for graphite [75]. The same problem arises when interpreting experimental data [113]. The best result currently available is given by RPA calculations, because RPA does not rely on assumptions of locality, additivity, nor C_6/R^6

contributions [185, 239]. However, a very dense sampling of the Brillouin zone (BZ) is needed for converged RPA calculations on graphite due to its semimetallic behavior at the Fermi level, which is computationally challenging. In this section we demonstrated clearly the importance but at the same time problematic description of the anisotropic long-range dispersion effects in graphite. The best method currently available with FHI-aims is the MBD@rsSCS correction scheme which accounts for non-additive contributions. However, as this is very recent development most of the results presented in this work were calculated using the pairwise TS correction scheme.

6.3. The Electronic Structure of Graphene

The electronic properties of graphene originate from its very special crystal structure. The graphene honeycomb lattice can be seen as two triangular sublattices lattice A and lattice B with one C atom in each. The two sublattices are bonded by sp^2 hybridisation of the $2s$, the $2p_x$ and $2p_y$ C orbitals forming strong in-plane σ bonds. The remaining $2p_z$ orbital is oriented perpedicular to the graphene x-y-plane. The neighbouring $2p_z$ orbital form delocalised states across the graphene plane, so-called π-bonds. Electrons move easily in these π states resulting in the exceptionally electrical conductivity of graphene.

Figure 6.6 a shows the hexagonal graphene Brillouin zone (shaded in grey). The graphene reciprocal lattice vectors $\mathbf{b}_1$, $\mathbf{b}_2$ connect the Γ-point of the first Brillouin zone to the neighbouring Γ-points (indicated as blue arrows). The graphene Brillouin zone contains three high symmetry points:

Γ-point in the zone center,

***M*-point** at the mid point of the Brillouin zone edge,

***K*-point** at the corners of the Brillouin zone.

The graphene band structure of pritstine graphene on the level of PBE is shown in Fig. 6.6 b. We used the PBE+vdW lattice parameter given in Tab. 6.1. The graphene unit cell contains two π orbitals forming two bands. These bands are referred to as π band, the bonding lower energy valence band (indicated by an arrow in Fig. 6.6 b), and π^* band, the anti-bonding higher energy conduction band. The π bands touch at the K-point and close the band gap which is why graphene is often referred to as a zero-gap

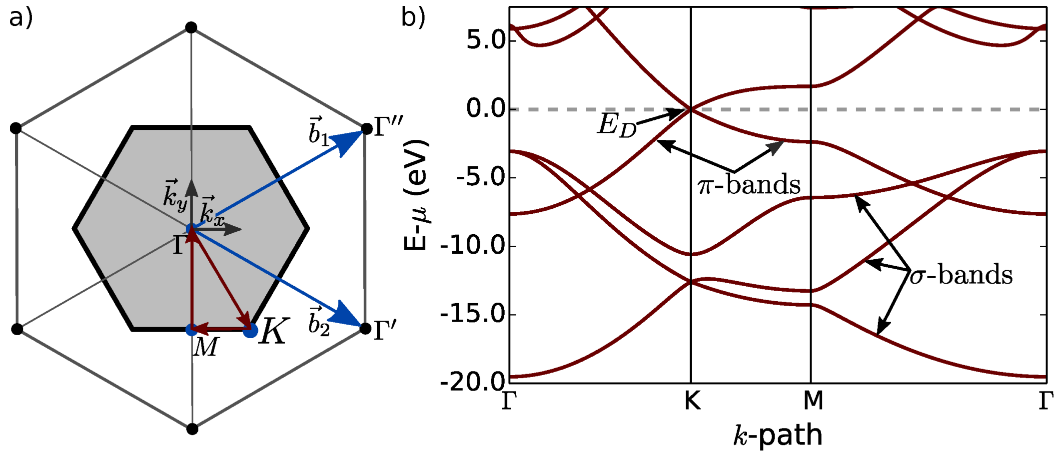

Figure 6.6.: Subfigure (a) shows the graphene Brillouin zone (shaded in grey) and the high symmetry points Γ, M and K (marked by blue points). (b) The band dispersion of graphene on the level of PBE. The k-path is chosen along the high symmetry lines of the graphene Brillouin zone as indicated by arrows in Subfigure (a).

semiconductor. The energy-momentum dispersion of the π and π^* bands around the K-point is approximately linear. The energy where the two π bands touch is called the Dirac point (E_D) (see Fig 6.6 b). The π bands of an undoped graphene sheet are half-filled, E_D equals the Fermi energy.

The doping of the graphene layer shifts the Dirac point with respect to the Fermi level. In a neutral graphene layer E_D equals the Fermi energy. The position of the Dirac point is very sensitive to small doping concentrations. This is a direct consequence of the linear dispersion of the bands in the close vicinity of the K-point in the graphene BZ. In reciprocal space the electronic structure of graphene in the vicinity of the Dirac point is formed like a cone. The amount of dopants is proportional to the area enclosed by the Fermi surface which can be approximated by a circle with the area ${k_\mathrm{F}}^2\pi$. In this simple model we find that the position of the Dirac point (E_D) is proportional to the amount of dopants (δq) in the graphene layer as $E_D \propto \sqrt{|\delta q|}$.

However, as can be seen in Fig 6.6 b the π bands are not fully symmetric in the vicinity of the k-point [35, 50, 79]. In the following, we examine the shift of the Dirac point with respect to the Fermi level for different doping concentrations. The position of the Dirac point with respect to the Fermi level is influenced by hole and electron doping of the graphene layer. We simulate the doping of the graphene layer using the virtual-crystal approximation (VCA) [336, 278, 261]. The VCA ensures that the simulation cell remains neutral and therefore allows to calculate a doped crystal using periodic boundary conditions. This is achieved by removing a fraction of

the positive nuclear charge δq of all carbon atoms and adding the same amount of negative charge to the conduction electrons. This means that a fractional electron of the charge $-\delta q$ is transferred to the conduction band, which gives the Fermi level in the VCA.

We used the two atomic graphene cell introduced in Sec. 6.1 with the lattice parameter optimised on the level of PBE+vdW as given in Tab. 6.1. The Fermi surface for different doping changes only in a small region around the K-point in the graphene Brillouin zone. In order to accurately account for these small changes, we chose a very dense off-Γ k-grid with 48 points in the in-plane x and y direction. A full band structure similar to Fig 6.6 b was calculated for 28 different doping concentrations using PBE. We chose a doping range of ± 0.005 e^-/atom, which corresponds to a doping concentrations of 0.08%. Within the VCA higher doping concentrations could be included. However, for doping concentrations much higher than the ones considered here at the order of a few tenth of the atomic charge local effects in the electronic structure may not be captured by the VCA [261].

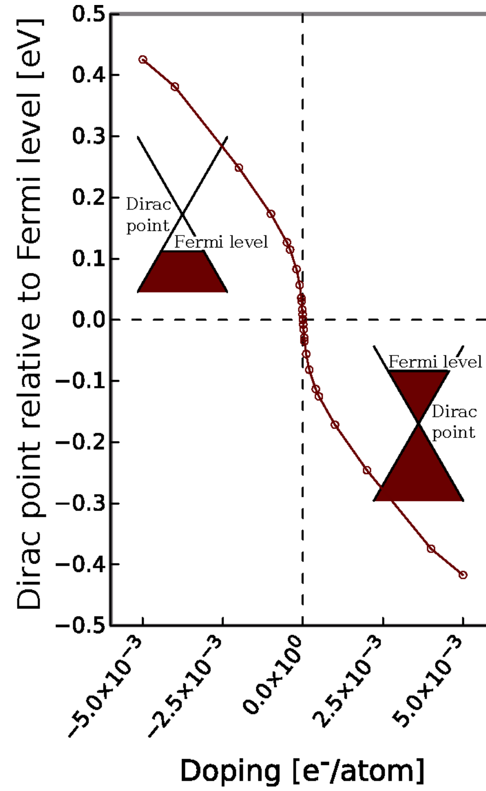

Figure 6.7.: The position of the graphene Dirac point with respect to the Fermi level for doping in the range of $\pm$ 0.005 e^-/atom on the level of PBE. PBE+vdW lattice parameter were used (Tab. 6.1).

Figure 6.7 shows the Dirac energy (E_D) with respect to the Fermi level. In the range between -0.005 e^-/atom and zero the graphene layer is hole doped, so that the Dirac point lies above the Fermi level. In this case the Dirac cone is not fully occupied resulting in a p-type doped graphene layer (see diagram in Fig. 6.7). In the range between zero and 0.005 e^-/atom the graphene layer is n-type doped and the Dirac point is shifted below the Fermi level. In Chapter 12, we will use the here presented analysis of doping in pristine graphene to aid a better understanding of the doping of epitaxially grown graphene.

7 Silicon Carbide: The Substrate

The wide band gap semiconductor SiC is extremly rare in nature. Edward G. Acheson found a wide-scale production method to synthesise SiC in the early 1890's [2]. The new material quickly found industrial application as an abrasive because of its hardness[1]. Since then the interest in SiC has continued. In the last 15 years, there has been a continuous interest in SiC with an average number of publications of 1450 ± 350 per year (see Fig. 6.2).

SiC has been applied in various fields, in particular for electronic devices such as Schottky diodes and metal-oxide-semiconductor field-effect transistors for temperatures up to 973 K [26, 49]. The first prototype of a light emitting diode (LED) was built using SiC in 1907 [282]. Later, SiC was commercially used for blue LEDs [216] until the much more efficient gallium nitride LEDs replaced it. SiC is also a promising material for nanoelectromechanical systems such as ultrafast, high-resolution sensors, and high frequency signal processing components [345]. For high-temperature applications such as temperature sensors or turbine engine combustion monitoring, SiC is commonly used [49], due to its comparablely high thermal conductivity of $490\,\frac{\mathrm{W}}{\mathrm{m\,K}}$ for 6H-SiC compared to $149\,\frac{\mathrm{W}}{\mathrm{m\,K}}$ for Si [295, 26] and its low thermal expansion coefficient [195, 194, 159]. However, the industrial application of SiC is limited, as the quality of the substrate material is still below that of Si wafers although advances and improvements in the growth process have been made [224]. Recently, SiC has received much attention, because of its use as a substrate for epitaxial graphene growth by high-temperature Si sublimation [18, 238, 20, 64, 82, 263]. It is regarded as the most promising route to large scale growth of high quality graphene for practical applications.

One of the most intriguing properties of SiC is the structural diversity with more than 250 different crystalline forms [57]. In this chapter, we introduce the three SiC polytypes, 3C-SiC, and hexagonal 4H-SiC and 6H-SiC most relevant for this work, and their physical and electronic properties.

[1]On Mohs scale of mineral hardness SiC scales between 9-9.5; for comparison diamond scales as 10 and talc as 1

7.1. Polymorphism in Silicon Carbide

The silicon carbide (SiC) crystal is composed of an equal number of silicon (Si) and carbon (C) atoms forming strong covalent tetrahedral bonds by sp^3 hybridisation. Four C atoms surround a Si atom and vice versa. Figure 7.1 shows a SiC-bilayer. The central Si atom (marked A) forms three in-plane bonds with neighbouring C atoms (marked B). A single SiC-bilayer can be pictured as a sheet of Si-C pairs arranged in a hexagonal point lattice with an Si-C pair at each point. The out-of-plane bonds connect the SiC-bilayers with each other. In a closed hexagonal structure there are three possible stacking positions labeled A, B, and C in Fig. 7.1. The SiC-bilayers can be stacked on top of each other by shifting the central Si atom. In Fig. 7.1 the central Si atom is labeled A. The position of the central Si atom of the next SiC-bilayer is shifted either to position B or C.

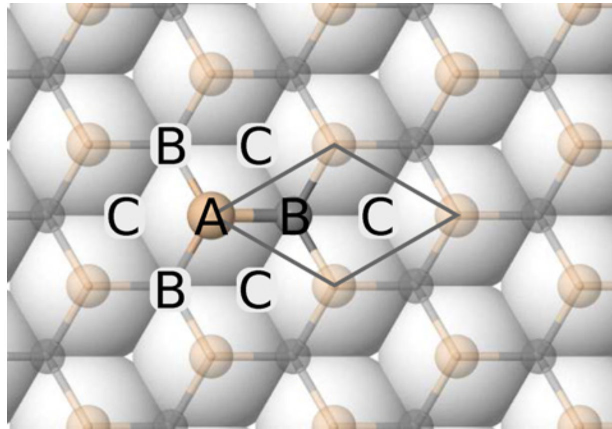

Figure 7.1.: The white spheres represent a hexagonal structure. The possible stacking positions of a closed hexagonal structure are marked as A, B, and C. A SiC-bilayer overlayers the hexagonal structure. The primitive unit cell of the SiC-bilayer is shown.

We use the notation proposed by Ramsdell [258] to identify different SiC polytypes. The notation consists of a letter and a number. The number gives the number of SiC-bilayers stacked along the z-axis to complete the unit cell. The letter C, H or R describes the Bravais lattice type: cubic C, hexagonal H or rhombohedral R. Every SiC polytype can be constructed by five basic polytypes with small stacking periods: 2H, 3C, 4H, 6H and 15R [180]. The 2H-SiC has a wurtzite structure. It consists of two SiC bilayers in AB stacking. 3C-SiC, also known as β-SiC, has a cubic Bravais lattice with two atoms in the unit cell (zinc blende structure). This structure can also be understood as three SiC-bilayers stacked along the (111)-axis with ABC stacking. Figure 7.2 shows the atomic structure of the three different polytypes 3C-SiC, 4H-SiC, and 6H-SiC.

We list the structural and cohesive properties of 3C-SiC, 4H-SiC and 6H-SiC

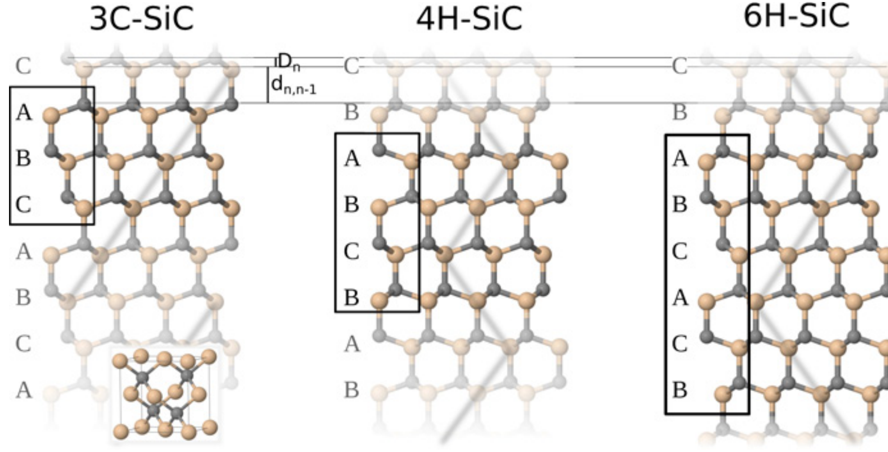

Figure 7.2.: The atomic structure of three different SiC polytypes are shown, cubic silicon carbide (3C-SiC) (left), and two hexagonal structures 4H-SiC (middle) and 6H-SiC (right). The atoms in the black box mark the unit cell. The stacking sequence of the SiC-bilayers is shown for every polytype and indicated by a grey line in the structure. 3C-SiC is also shown in its zinc blende structure (bottom, left). The distance $d_{n,n-1}$ between two bilayers and the distance D_n between a Si and C atoms within a SiC bilayer are shown.

for different exchange-correlation functionals (LDA, PBE, HSE06 and vdW corrected PBE+vdW and HSE06+vdW) in Tab. 7.1 and Tab. 7.2. We used the stress tensor based lattice relaxation to optimise the crystal structure. The choice of approximation to the exchange-correlation functional changes the lattice parameter by less than 0.05 Å for all three polytypes.

	PBE		PBE+vdW		LDA		HSE06		HSE06+vdW	
	$d_{n,n-1}$[Å]	D_n[Å]	$d_{n,n-1}$[Å]	D_n[Å]	$d_{n,n-1}$[Å]	D_n[Å]	$d_{n,n-1}$[Å]	D_n[Å]	$d_{n,n-1}$[Å]	D_n[Å]
3C-SiC	1.904	0.635	1.890	0.630	1.876	0.625	1.886	0.629	1.878	0.626
4H-SiC	1.901	0.625	1.891	0.618	1.878	0.617				
6H-SiC	1.901	0.631	1.892	0.626	1.879	0.623			1.880	0.622

Table 7.1.: The distance $d_{n,n-1}$ between two SiC-bilayer and the distance D_n between the Si and C sublayer with in SiC-bilayer are listed for 3C-SiC, 4H-SiC and 6H-SiC calculated for different exchange-correlation functionals (LDA, PBE, HSE and vdW corrected PBE+vdW and HSE06+vdW).

In Table 7.2, we also include the lattice parameters and bulk moduli including zero-point vibrational correction (ZPC). To calculate the ZPC lattice parameters, we applied the QHA (see Sec. 4.1). We calculated the Helmholtz free energy (Eq. 4.7) for different volumes by full phonon calculations in a finite-difference approach (details about the underlying phonon calculations are given in Appendix D.2). For 3C-SiC, we used a $5 \times 5 \times 5$ supercell for 5 volumes. We optimised the hexagonal structure in the same way as for graphite (Sec. A). Here, we performed phonon calculations in a $3 \times 3 \times 2$ su-

percell for 7 volumes and for every volume we use 9 different ratios between the lattice parameters a and c. The minimum-energy lattice parameter for T=0 K was obtained by fitting to the Birch-Murnaghan equation of state (Def. 6.1.1). The inclusion of ZPCs changes the bullk cohesive properties only slightly.

The numerical convergence with respect to the integration grid in reciprocal and real space, as well as with the number of basis functions included in the calculation, is discussed in Appendix B. Differences in the lattice parameters obtained by B.-M.-fitting and the stress tensor based lattice relaxation were smaller than 10^{-3} Å.

For 3C-SiC, we also tested density functionals that account for long-range dispersion. In Table 7.2, we include the TS scheme [326] (PBE+vdW and HSE06+vdW) and the recently developed many body vdW treatment [325, 324, 5] (PBE+MBD). The effect of the many body vdW treatment on the lattice parameter, cohesive energy and enthalpy of formation ΔH_f is small. However, using the PBE+MBD instead of the PBE+vdW method improves the bulk modulus by 0.1 Mbar for the groundstate calculation and by 0.07 Mbar for the bulk modulus including ZPC. The experimental value is 2.48 Mbar [313].

Table 7.1 lists the distance $d_{n,n-1}$ between two SiC-bilayers and the distance D_n between the Si and C sublayer where n denotes the number of the SiC-bilayer. D_n and $d_{n,n-1}$ are illustrated in Fig. 7.2. In SiC the intralayer distance is given by the Si-C bond length and the tetrahedral angle. In a perfectly symmetric tetrahedron, the central angle between any two vertices is the arccos $(-1/3)$ (70.52°). However, in the hexagonal structures the bond tetrahedrons deviate from the symmetric tetrahedral angle by 0.36% for 4H-SiC and 0.14% for 6H-SiC in PBE+vdW.

The enthalpy of formation ΔH_f of SiC is calculated using the reference phases, bulk silicon and carbon in the diamond structure. ΔH_f is between -0.53 eV and -0.59 eV, depending on the density-functional and polytype used, and shows good agreement with a calculated literature value of -0.58 eV using the pseudopotential plane wave (PSP-PW) method and LDA [355, 126]. The calculated enthalpy of formation is notably smaller (less energy gain) than the experimental room temperature value obtained by an electromotive force (emf) measurement by Kleykamp [168], but in fair agreement with the value tabulated in the *Handbook of Chemistry & Physics* Haynes [134].

The enthalpies of formation ΔH_f of the three SiC polytypes are very similar.

3C-SiC						
		a_0 [Å]		B_0 [Mbar]	E_{coh} [eV]	ΔH_f [eV]
PBE+vdW	PES	4.36		2.10	-6.76	-0.56
	ZPC	4.38		2.09	-6.65	-0.58
PBE	PES	4.38		2.10	-6.52	-0.53
	ZPC	4.40		2.06	-6.41	
LDA	PES	4.33		2.30	-7.41	-0.56
	ZPC	4.34		2.23	-7.30	
PBE+MBD[5]	PES	4.36		2.20	-6.78	-0.58
	ZPC	4.38		2.16	-6.67	
HSE06	PES	4.36		2.31	-6.35	-0.58
HSE06+vdW	PES	4.34		2.31	-6.59	-0.59
Experiment	T=300K	4.358 [195]		2.48 [313]	-6.34 [225]	-0.77 [168]
	T=0K	4.357 [317]				-0.65 [134]
Theory (LDA)	PES	4.29 [157]		2.22 [157]	-8.46 [157]	-0.56 [126]
PSP-PW (LDA)	PES	4.33 [355]		2.32 [12]		-0.58 [355]

4H-SiC						
		a_0 [Å]	c_0/n [Å]	B_0 [Mbar]	E_{coh} [eV]	ΔH_f [eV]
PBE+vdW	PES	3.08	2.51	2.15	-6.69	-0.57
	ZPC	3.09	2.53	2.12	-6.78	-0.59
PBE	PES	3.10	2.53		-6.43	-0.54
LDA	PES	3.07	2.49		-7.42	-0.57
Experiment	T=0K	3.07 [108]	2.51 [108]			-0.62 [134]
PSP-G (LDA)	PES	3.04 [12]	2.49 [12]			

6H-SiC						
		a_0 [Å]	c_0/n [Å]	B_0 [Mbar]	E_{coh} [eV]	ΔH_f [eV]
PBE+vdW	PES	3.08	2.52	2.15	-6.69	-0.57
	ZPC	3.09	2.53	2.10	-6.58	-0.59
PBE	PES	3.10	2.53		-6.43	-0.54
LDA	PES	3.06	2.50		-7.42	-0.57
HSE06+vdW	PES	3.06	2.50		-6.59	-0.61
Experiment		3.08 [1]	2.52[1]	2.30 [10]		-0.77[168]
Theory (LDA)	PES	3.08 [15]	2.52[15]			
	PES	3.07 [244]	2.52[244]	2.04 [244]		

Table 7.2.: The structural and cohesive properties of 3C-SiC, 4H-SiC and 6H-SiC are listed for different exchange-correlation functionals (LDA, PBE, HSE06 and vdW corrected PBE+vdW and HSE06+vdW): The lattice parameters a_0 [Å], and for the two hexagonal polytypes c_0 [Å$/n$] where n is the number of SiC bilayers, the bulk modulus B_0 [Mbar], cohesive energy E_{coh} [eV], and enthalpy of formation ΔH_f [eV] as obtained in this work. Reference data from experiment and theory is included. The theoretical reference data was calulated using DFT codes based on pseudopotentials with a plane-wave basis (PSP-PW) [15, 244, 157, 355, 126] or Gaussian basis (PSP-G) [12] in the LDA. "PES" refers to results computed based on the Born-Oppenheimer potential energy surface without any corrections. We also include zero-point vibrational correction (ZPC) lattice parameters and bulk moduli.

Davis *et al.* [63] measured ΔH_f for 3C-SiC ($\Delta H_f = -0.65$ eV) and hexagonal SiC ($\Delta H_f = -0.65$ eV) under normal conditions and found the same value for both polytypes. The energetic close competion between the different polymorphs is the main reason why it is difficult to grow high-quality SiC of a specific polytype [224]. In a recent experiment Haynes [134] found a energy difference of 0.03 eV between 3C-SiC and 4H-SiC.

However, once a specific polytype is grown the transformation from one to the other occurs at temperatures as high as 2400 K by a reconstructive transformation proceeding through a vapour transport mechanism involving gaseous silicon [342].

7.2. The Electronic Structure of Silicon Carbide Polymorphs

In Section 7.1, we introduced the atomic structure of SiC polytypes. The nearest neighbour configuration is the same for all polytypes, because of the tetrahedral sp^3 hybridisation, but the polytypes differ in their long range order. These changes have a profound influence on the electronic structure. For example, the band gap depends on the polytype with the smallest gap in 3C-SiC (2.2 eV) and the largest band gap in 2H-SiC (3.5 eV) [204]. If one could control the stacking order during the SiC growth process, the band gap could be tuned in this range. In this section we investigate the electronic structure of 3C-SiC, 4H-SiC and 6H-SiC.

Figure 7.3 and Figure 7.5 show the calculated density of states (DOS) of 3C-SiC using the HSE06 and PBE exchange-correlation functional in comparison with experimental soft x-ray spectroscopy data. In HSE06 the amount of exact exchange is set to α=0.25 and the range-separation parameter ω=0.2 Å^{-1} (for details about HSE see Sec. 2.3.3 or [175]). Ramprasad *et al.* [257] proposed to judge the quality of the exchange-correlation functionals with respect to the valence band width instead the Kohn-Sham (KS) band gap. They observed a linear relationship between the valence band width and formation energies for point defects over the (ω; α) parameter space of the HSE family. We tested the influence of α on the band gap and valence band width Appendix B.4.

Lüning *et al.* [204] performed synchrotron radiation excited soft x-ray emission (SXE) and absorption (SXA) spectroscopy to measure the band gap of bulk SiC. The measured transition probability is to a good approximation

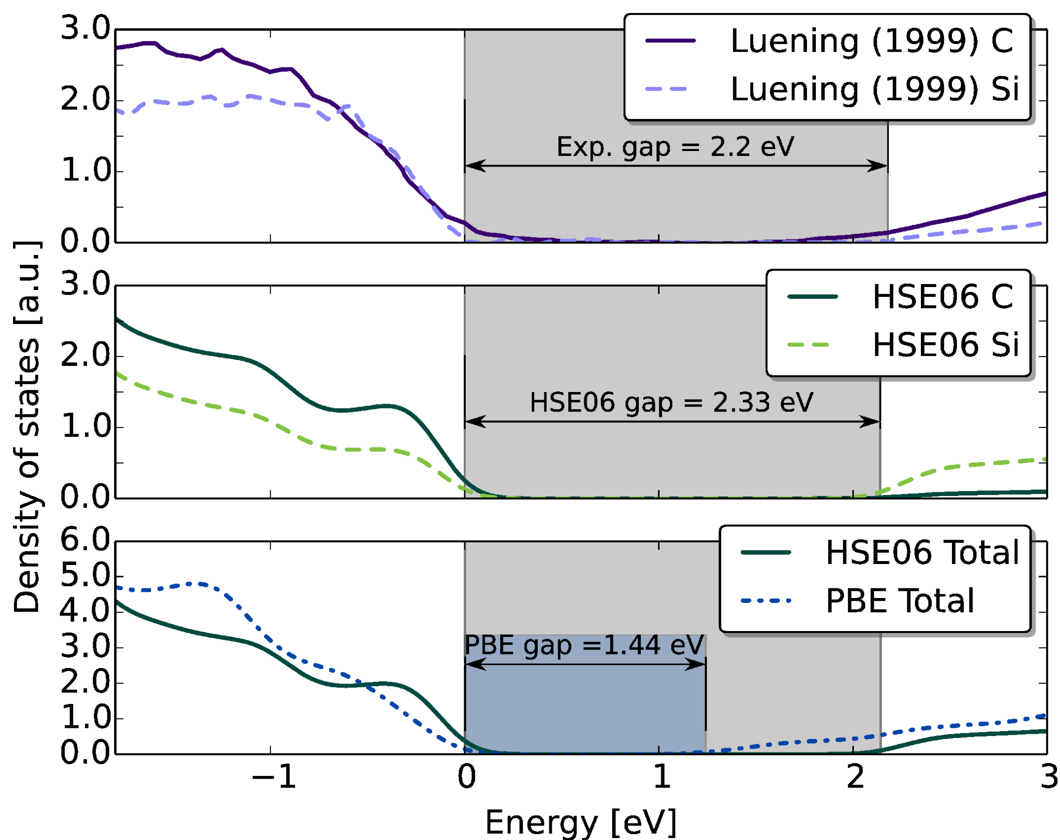

Figure 7.3.: Density of states (DOS) around the band gap for 3C-SiC: The top panel shows the experimental species projected DOS (C solid line and Si dashed line) measured by soft x-ray spectroscopy with a band gap of 2.2 eV [204]. The middle panel shows the calculated species projected DOS using the HSE06 exchange-correlation functional with a band gap of 2.33 eV. In the bottom panel the calculated total Kohn-Sham DOS using the HSE06 exchange-correlation functional is compared to the total DOS calculated with PBE. The theoretical magnitude of the peaks in the spectra depends on the number of basis functions included in the calculation.

proportional to the local partial DOS. The method is orbital and symmetry selective due to the selection rules, and because of the core excitations it allows for element and site selectivity. We included their spectra for 3C-SiC in the top panel of Fig. 7.3.

We calculated a species projected density of states (with a Gaussian broadening of 0.1 eV) using the HSE06 exchange-correlation functional and the vdW corrected lattice parameter from Tab. 7.2. The species projected DOS around the band gap is plotted in Fig. 7.3. For HSE06 we find a band gap of 2.33 eV in good agreement with experiment. For comparison, we include the total DOS for HSE06 and PBE (bottom panel Fig. 7.3).

In Figure 7.4 the calculated HSE06 band structure of 3C-SiC is compared to

experimental photoemission data [143]. The calculated bands agree well in shape with the experimental band dispersion in Ref. [143]. The X_{5v} energy level in our calculation is at -3.51 eV compared to -2.68 eV in Ref. [143]. By optical reflectivity measurements Lambrecht *et al.* [181] found for the X_{5v} energy level -3.6 eV, which is in good agreement with our results and previous theoretical studies X_{5v}=-3.47 eV (HSE06) [237], X_{5v}=-3.49 eV (G_oW_o@LDA) [341]. Appendix C shows the full band structure calculated with HSE06 for 3C-SiC, 4H-SiC, and 6H-SiC.

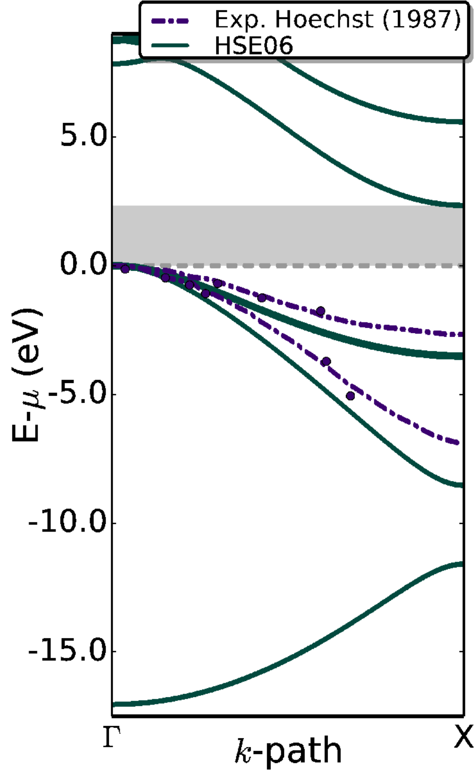

Figure 7.4.: Plot of the band structure of 3C-SiC from Γ to X. The band structure (solid line) is calculated using HSE06 exchange-correlation functional and the vdW corrected lattice parameter (HSE06+vdW from Tab. 7.2). The shaded area (in grey) marks the band gap of 2.33 eV. In addition, experimental photoemission data is included (filled cicle) and parameterised bands (dashed line) taken from Ref. [143].

Figure 7.5 shows the density of states (DOS) of the valence band for 3C-SiC. For comparison, we include the photoemission data taken from Ref. [296]. The photoemission data gives a valence band width of 11.3 eV. The calculated DOS (with a Gaussian broadening of 0.1 eV) using HSE06 gives a band width of 9.3 eV and PBE 8.42 eV. HSE06 underestimates the band width by ∼18%. However, in the experimental spectra it is not clear what the best starting and end point would be to determine the band width. We chose two characteristic peaks in the experimental and HSE06 spectra (dashed line in Fig. 7.5): the first one at -2.5 eV (HSE06 -2.4 eV) and a second one at -9.5 eV (HSE06 -8.5 eV). If the peak-to-peak distance is used as an reference HSE06 underestimates it by 1.1 eV. The species projected DOS (mid panel Fig. 7.3) identifies the first peak at -2.5 eV to be dominated by C states and the second peak at -9.5 eV is dominated by Si states in agreement with experiment Lüning *et al.* [204].

In Table 7.3 we listed the direct and indirect band gap and the band width for different exchange-correlation functionals (PBE, LDA, HSE06). PBE and LDA underestimate the band gap by ∼30% for 4H-SiC and 6H-SiC. The band gap of 3C-SiC is underestimated by ∼35% in PBE and ∼40% in LDA. Including a fraction of exact-exchange in

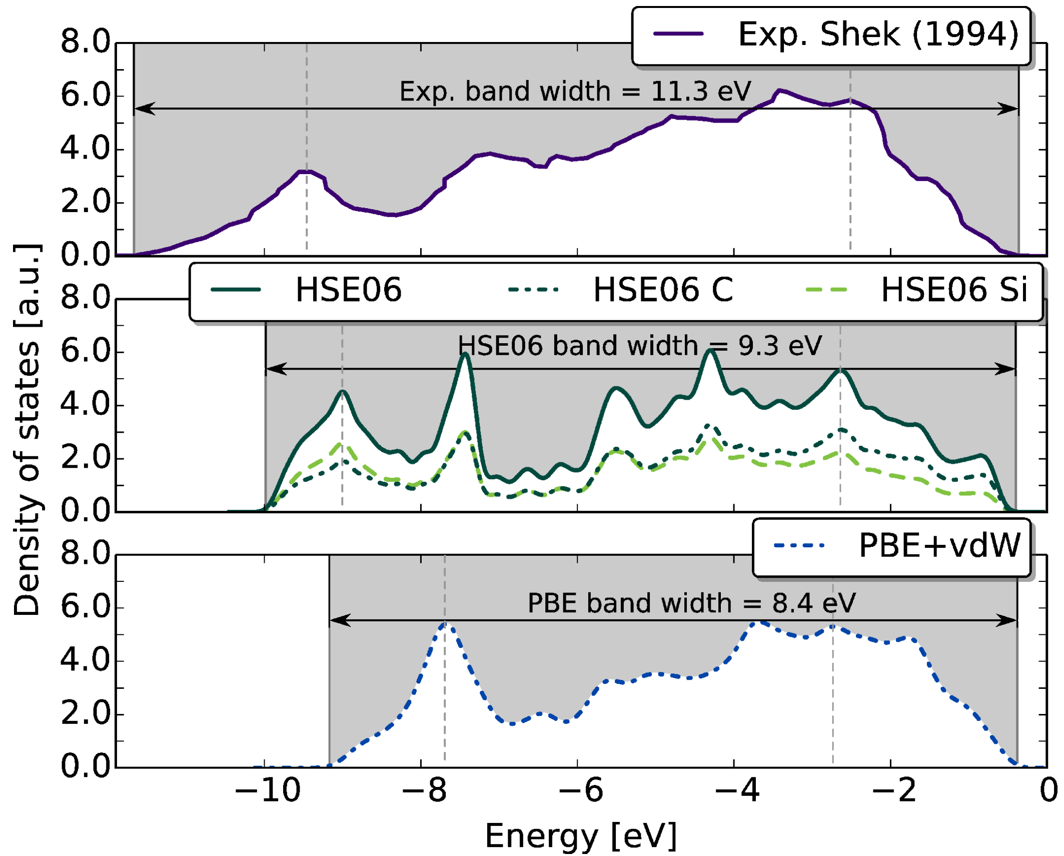

Figure 7.5.: Shows the Density of states (DOS) of the valence band for 3C-SiC. The top panel shows the experimental DOS measured by photoemission spectroscopy with a band width of 11.3 eV [296]. The calculated DOS using the HSE06 exchange-correlation functional with a band width of 9.3 eV is shown in the middle panel and using PBE with a band width of 8.4 eV in the bottom panel.

HSE06 improves the description of the band gap and the band width over PBE, but it still underestimates the band width if compared to the experimental spectra. The agreement between the experimental band gaps and the HSE06 calculated one is good for the polytypes 3C-, 4H- and 6H-SiC.

We demonstrated that the polymorphs of SiC relevant for this work are well described by the level of theory applied. In particular, we achieved a very good agreement for the structural properties Sec. 7.1 independent of the approximation to the exchange-correlation functional. The band gap Tab. 7.3 is underestimated by PBE, LDA. However, a good agreement with high-level theoretical calculations (G_0W_0@LDA) and experiment can be achieved, when a fraction of exact-exchange α=0.25 is included in the calculation by using HSE06 with a range-separation parameter set to ω=0.2 Å^{-1}. We found that the default HSE06 value of α=0.25 captures both the band gap and the band width well and we therefore adopt it for our calculations.

	PBE			LDA			HSE06			Ref. (theory)	Exp.	
	g_X [eV]	$g_{\Gamma-X}$ [eV]	$w_{L-\Gamma}$ [eV]	g_X [eV]	$g_{\Gamma-X}$ [eV]	$w_{L-\Gamma}$ [eV]	g_X [eV]	$g_{\Gamma-X}$ [eV]	$w_{L-\Gamma}$ [eV]	$g_{\Gamma-X}$ [eV]	$g_{\Gamma-X}$ [eV]	w [eV]
3C-SiC	4.57	1.44	8.42	4.55	1.32	8.64	5.85	2.33	9.3	1.37 (PBE) 2.35 (HSE06) [199]	2.2 [204]	11.3[296]
										2.69 (G_oW_o@LDA) [341]	2.42 [148]	
	g_M [eV]	$g_{\Gamma-M}$ [eV]	w_Γ [eV]	g_M [eV]	$g_{\Gamma-M}$ [eV]	w_Γ [eV]	g_M [eV]	$g_{\Gamma-M}$ [eV]	w_Γ [eV]	$g_{\Gamma-M}$ [eV]	$g_{\Gamma-M}$ [eV]	w [eV]
4H-SiC	3.40	2.26	8.55	3.35	2.22	8.67	4.52	3.26	9.33	2.23 (PBE) 3.28 (HSE) [237]	3.2 [204]	11.2 [204]
										3.56 (G_oW_o@LDA) [341]	3.285 [212]	
6H-SiC	3.15	2.05	8.56	3.10	1.99	8.69		2.92	9.40	2.02 (PBE) 3.02 (HSE) [237]	2.9 [204]	11.9 [154]
										3.25 (G_oW_o@LDA) [341]	3.101 [212]	

Table 7.3.: The direct and indirect band gap and the valence band width are listed for 3C-SiC, 4H-SiC and 6H-SiC calculated for different exchange-correlation functionals (PBE, LDA, HSE06). We used the geometries given in Tab. 7.2 for PBE, HSE06 the vdW corrected values were chosen.

Part III

The Silicon Carbide Surfaces and Epitaxial Graphene

In Chapter 7, we introduced the wide-band-gap semiconductor SiC which crystallises in various polytypes. The technologically most relevant polytypes are the zinc-blende polytype 3C and the hexagonal polytypes 4H and 6H shown in Fig. 7.2.

The natural growth direction of SiC is along the stacking axis of the SiC-bilayers that is, the [111] direction for 3C-SiC and [0001] for the hexagonal polytypes. SiC is a polar material, the two opposite faces, the 3C-SiC-{111} and the 6H-SiC-{0001}, differ by their surface termination. The 3C-SiC-(111) (6H-SiC-(0001)) face consists of Si atoms and the opposite face, the 3C-SiC-($\bar{1}\bar{1}\bar{1}$) (6H-SiC-(000$\bar{1}$)), of C-atoms. Throughout this work, we focus on the surface perpendicular to the natural growth direction.

Epitaxial graphene can be grown by high temperature Si sublimation on the Si-terminated [332, 95, 264, 82, 263] and on the C-terminated surface [18, 19, 334, 64, 302, 141, 83, 21, 337, 213] of SiC.

In this part we investigate the surface reconstructions observed during SiC annealing and the hybrid SiC-graphene structures for the two polar SiC surfaces.

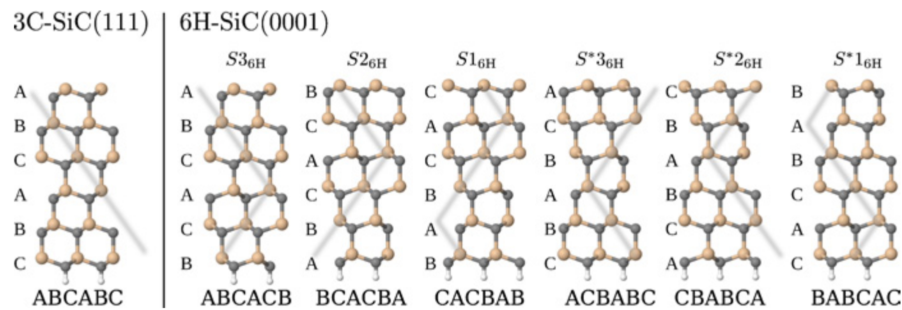

Figure 8.1.: The surface termination of 3C-SiC and 6H-SiC is shown for a clean surface. In 6H-SiC every third Si-C bilayer is rotated by 30° indicated by a kink in the grey line. This rotation in the stacking order leads to different surface terminations $\mathrm{S}n_{6\mathrm{H}}$ and $\mathrm{S}^{*}n_{6\mathrm{H}}$ where n runs from one to three.

For the 3C-SiC(111) surface, the bulk like stacking order close to the surface is independent of where the surface is cut, but for specific surface reconstruction the stacking can change at the surface. However, for 6H-SiC(0001) this is different as here the SiC bilayers are rotated by 30° every third layer. The position of the rotation is indicated in Fig. 8.1 by a kink in the grey line. Due to these rotations the 6H-SiC offers more-or-less favourable step terminations, introducing an additional degree of freedom – the choice of the surface termination. The six different surface terminations are often labeled with $\mathrm{S}n_{6\mathrm{H}}$ where n runs from one to three. The symmetry equivalent surfaces are marked by an additional asterix $\mathrm{S}^{*}n_{6\mathrm{H}}$ (see Appendix G).

Independent of the polytype, during graphene growth a series of surface reconstructions is observed starting with a Si-rich (3×3) reconstruction [310]. With increased temperature, more Si sublimates and a simpler $(\sqrt{3} \times \sqrt{3})$-R30° bulk-terminated Si rich surface forms [158, 308] followed by the C-rich surface reconstruction, the so-called zero-layer graphene (ZLG) or "buffer layer", followed by mono-layer graphene (MLG), bi-layer graphene (BLG) and few-layer graphene [332, 95, 264, 83].

We performed DFT calculations for the Si-rich $(\sqrt{3} \times \sqrt{3})$-R30° and (3×3) reconstruction (Sec. 8.1) and the C-rich phases ZLG, MLG and BLG (Sec. 8.2). The calculations were carried out using the all-electron, localised basis set code FHI-aims Sec. 2.5 ('*tight*' settings see Appendix B). For the approximation to the exchange-correlation functional we use LDA, PBE. We include long-range dispersion effects by using the TS scheme [326] (PBE+vdW). The bulk lattice parameters of SiC are listed in Tab. 7.2, the impact of different standard functionals is well understood and systematic

(see Ch.7). Predicted lattice parameters for diamond C and graphite are listed in Tab. 6.1. For the interplanar lattice parameter c of graphite, vdW effects must be included into the PBE functional (see discussion in Sec. 6.2). To simulate the substrate in the surface calculations, we use six SiC-bilayers stacked along the z-axis (see Fig. 8.1 and Appendix B.2) and a sufficiently thick vacuum region. We fully relaxed the top three SiC-bilayers and all atoms above (residual energy gradients: $8{\cdot}10^{-3}$ eV/Å or below).

8.1. The Silicon-Rich Reconstructions of the 3C-SiC(111) Surface

8.1.1. 3C-SiC(111) ($\sqrt{3} \times \sqrt{3}$)-R30° Si Adatom Structure

A Si-rich reconstruction with $\sqrt{3} \times \sqrt{3}$ translational symmetry was first reported by Van Bommel *et al.* [332]. The structure was determined by DFT calculations [232, 273, 156] and scanning tunnelling microscopy (STM) [241] and later confirmed by quantitative low-energy electron diffraction (LEED) measurements [305]. The structure consists of a Si adatom on top of a bulk-like Si layer (shown in Fig. 8.2). The adatom is at position B in Fig. 7.1, also known as T_4-site. At this position the adatom forms bonds with the three Si atoms of the top SiC-bilayer, reducing the number of dangling bond orbitals at the surface from 3 to 1. The new p_z-like dangling bond orbital contains one unpaired electron per unit cell. The Si adatom pushes the C atom underneath into the substrate leading to a corrugation δ_{1_C} in the top C-layer, indicated by an arrow in Fig. 8.2 [232, 273, 305, 276].

The electronic structure of the 6H-SiC(0001)-($\sqrt{3} \times \sqrt{3}$) surface was studied by angle-resolved photoemission spectroscopy (ARPES) and **k**-vector-resolved inverse photoemission spectroscopy [154, 319]. The one-electron band corresponding to a localised state at the Si-adatom splits into two bands, resulting in a semiconducting surface with a bandgap of 2.0 eV [319]. The band splitting was discussed in the context of G_oW_o@LDA calculations [99, 267]. Their calculations showed that the band splitting is driven by electron correlation effects of the top Si dangling bond. In conventional DFT, the spin-unpolarised surface is by necessity metallic with a half-filled band at the Fermi level. Introducing spin-polarisation opens a gap at the surface.

Alternativly, the strong correlation between the Si adatoms was addressed within the LDA+U framework by Furthmüller *et al.* [99].

We use the $\sqrt{3} \times \sqrt{3}$ reconstruction to evaluate the influence of the exchange-correlation functional and the polytype by comparing results for the 3C-SiC and 6H-SiC. We took the SiC bulk lattice parameter from Tab. 7.2. We also have to take into account the stacking order for hexagonal SiC (see Fig. 8.1). We tested the influence of the stacking order on the $(\sqrt{3} \times \sqrt{3})$-R30° Si adatom structure. We found the lowest surface energy (Eq. 4.9) for ABCACB and the symmetry equivalent ACBABC stacking order, the so-called $S3_{6H}$ and $S3^{*}_{6H}$ terminations (see Appendix G). LEED data also indicates a $S3_{6H}$ surface termination [291].

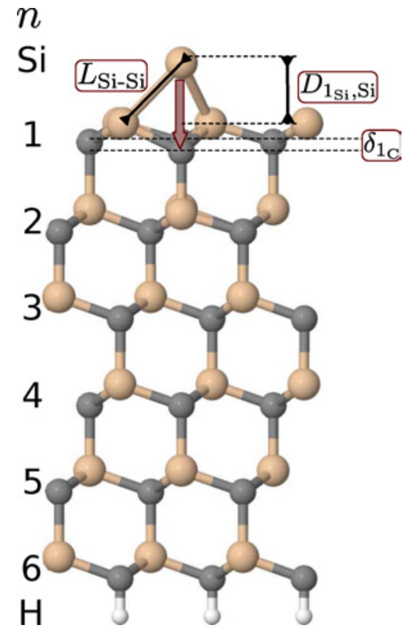

Figure 8.2.: Geometry of the 3C-SiC(111) $(\sqrt{3} \times \sqrt{3})$-R30° Si adatom structure. The bond length of the adatom with the top Si atom ($L_{\text{Si-Si}}$), the distance from the surface ($D_{1_{\text{Si}},\text{Si}}$) and the corrugation of the top C layer ($\delta_{1_{\text{C}}}$) are shown.

In Tab. 8.1 we list the three characteristic parameters of the Si adatom structure: the bond length between the adatom and the top layer Si atoms $L_{\text{Si-Si}}$, the distance between the adatom and top layer Si atoms along the z-axis $D_{1_{\text{Si}},\text{Si}}$, and the corrugation of the top C-layer $\delta_{1_{\text{C}}}$ (see Fig. 8.2). We include results from spin-polarised and unpolarised calculations for the 3C-SiC(111) and 6H-SiC(0001) surface. The surface energetics will be discussed in Ch. 10.

Interestingly, the first Si-layer shows no corrugation with $\delta_{1_{\text{Si}}} < 1 \cdot 10^{-4}$ Å for all exchange-correlation functionals used. The Si-Si bond length is slightly larger than in bulk Si (PBE+vdW: 2.36 Å). Although changing from a spin-unpolarised calculation to a spin-polarised one has a profound effect on the electronic structure by opening a band gap, the atomic structure is hardly affected.

3C-SiC(111)		$L_{\text{Si-Si}}$	$D_{1_{\text{Si}},\text{Si}}$	δ_{1_C}
spin-unpolarised	LDA	2.43	1.75	0.26
	PBE	2.46	1.76	0.27
	PBE+vdW	2.45	1.77	0.28
spin-polarised	LDA	2.44	1.75	0.26
	PBE	2.46	1.76	0.27
	PBE+vdW	2.45	1.77	0.28
	HSE06+vdW	2.44	1.75	0.27

6H-SiC(0001)		$L_{\text{Si-Si}}$	$D_{1_{\text{Si}},\text{Si}}$	δ_{1_C}
spin-polarised	PBE+vdW	2.45	1.77	0.27

References:		$L_{\text{Si-Si}}$	$D_{1_{\text{Si}},\text{Si}}$	δ_{1_C}
6H-SiC(0001) [305]	exp. LEED	2.44	1.75	0.33
4H-SiC(0001) [276]	exp. LEED	2.47	1.77	0.34
3C-SiC(111) [232]	LDA	2.42	1.75	0.22
6H-SiC(0001) [273]	LDA	2.41	1.71	0.25

Table 8.1.: Atomic position of the Si adatom relative to the surface for different exchange-correlation functionals. The bulk lattice parameter were taken from Tab. 7.2. For 6H-SiC we chose a ABCACB stacking order (see Appendix G). $L_{\text{Si-Si}}$ is the bond length between the adatom and the top layer Si atoms, $D_{1_{\text{Si}},\text{Si}}$ is the distance between the adatom and top layer Si atoms along the z-axis, and δ_{1_C} is the corrugation of the top C-layer (see Fig. 8.2). (All values in Å)

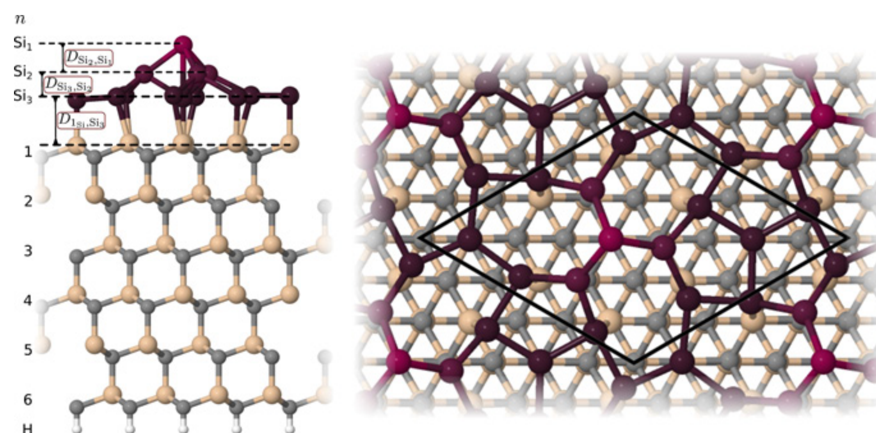

Figure 8.3.: The twist model of the 3C-SiC(111)-(3 × 3) reconstruction. On the left: The twist model from a side view. The layer distance between the substrate and the Si-ad-layer D_{1_{Si},Si_3}, as well as the distance between the ad-layer and the Si-trimer D_{Si_3,Si_2} and trimer-Si-adatom D_{Si_2,Si_1} are indicated by arrows. On the right: The twist model from a top view. The unit cell is shown in black.

Comparing the structural data in Tab. 8.1, we find that the change in the adatom geometry between the 3C-SiC(111) and 6H-SiC(0001) surface is negligible for PBE+vdW. In good agreement with a LEED analysis of the 3C-SiC(111) and hexagonal (0001) surfaces [305]. It seems that the surface Si adatom reconstruction on Si-terminated SiC surface is not affected by the polytype [156, 100, 277, 243].

In contrast to 6H-SiC only one type of stacking order is present at the surface of 3C-SiC [304]. In fact, the stacking sequence for the 6H-SiC and 3C-SiC are the same down to at least four SiC-bilayers below the surface (see Fig. 8.1). However, the growth process [179] and the electronic structure [243] differ among these two polytypes (see Sec. 7.2).

8.1.2. The Silicon-Rich 3C-SiC(111) (3×3) Reconstruction

On the Si-terminated surface, a (3 × 3) structure forms during annealing under simultaneous exposure to Si [158]. The reconstruction was identified as a Si-rich structure by Auger electron spectroscopy (AES) and electron-energy loss spectroscopy (ELS) [158]. The (3 × 3) reconstruction attracted great attention after its stabilising role during SiC thin film growth by molecular beam epitaxy (MBE) [316, 93] was identified. However, the detailed atomic structure of the (3 × 3) reconstruction remained a mystery for many years.

We briefly review the unsuccessful models of the 3C-SiC(111)-(3×3) reconstruction on the Si terminated SiC surface. Later, we will use these models as structure models for the unknown (3×3) reconstruction on the C terminated SiC surface (Ch. 14). The first structure was suggested by Kaplan [158]. Based on AES and ELS measurements they rationalise that the structure contains a Si ad-layer. They suggested an adaption of the dimer ad-atom stacking fault (DAS) model in analogy to the (7×7) reconstruction of the Si(111) surface. In this model the substrate is covered by a layer of eight Si atoms. On top of the ad-layer is a second layer consisting of six Si atoms, occuping three-fold surface sites. Finally, a Si dimer saturates the dangling bonds of the underlying Si atoms. However, STM images did not support the DAS model, because they showed only one protrusion per unit cell [178, 192, 309]. Kulakov *et al.* [178] suggested a model consisting of a Si ad-layer and a single ad-cluster. Li and Tsong [192] proposed a tetrahedral ad-cluster structure without a Si ad-layer.

	$D_{\mathrm{Si}_2,\mathrm{Si}_1}$	$D_{\mathrm{Si}_3,\mathrm{Si}_2}$	$D_{1_{\mathrm{Si}},\mathrm{Si}_3}$
LDA	1.43	1.12	2.33
PBE+vdW	1.44	1.14	2.36
PhD J.Schardt [276]	1.45	0.97	2.37

Table 8.2: Layer distances of the Si adatom structure relative to the surface for different exchange-correlation functionals (LDA and PBE+vdW) of the 3C-SiC(111)-(3×3) reconstruction. For comparison, the layer distances obtained from quantitative LEED measurements are included [276]. (All values in Å)

In 1998, Starke *et al.* proposed the now widely accepted structure of the 3C-SiC(111)-(3×3) reconstruction in a combined STM, LEED and DFT study [310]. The *twist model*, shown in Fig. 8.3, consists of three layers. First a Si-ad-layer, then a ad-layer formed by a tetrahedral Si-ad-cluster. The Si-ad-cluster is built from a Si-trimer and a single adatom on top. The trimer is twisted with respect to the bulk position by a twist angle of 9° [306] and 9.3° (PBE+vdW) in this work. The six atoms in the Si-ad-layer connected to the trimer perform a rotation and expansion movement leading to the formation of five- and seven-membered rings arranged in a cloverleaf pattern (top view in Fig. 8.3). In Appendix I, we list the structural details calculated using PBE+vdW and compare it with quantitative LEED data from Schardt [276] finding an overall good agreement.

8.2. The Carbon-Rich Reconstructions of the 3C-SiC(111) Surface

In experiment, the first stage of graphitisation is the carbon rich surface structure, the so-called zero-layer graphene (ZLG) or 'buffer-layer'. The detailed atomic structure was debated for many years as there is conflicting experimental evidence in the literature. In STM a (6×6) pattern is imaged [192, 210, 55, 307]. On the other hand, LEED measurements indicate a $(6\sqrt{3}\times6\sqrt{3})$-R30° periodicity [332, 264]. Also, the detailed atomic structure of the carbon nano-mesh has been under debate until recently. Chen *et al.* [55] suggested a nano-mesh structure with isolated carbon islands and Qi *et al.* [256] suggested an arrangement of C-rich hexagon-pentagon-heptagon (H5,6,7) defects in the ZLG (the defects are discussed in more detail in Sec. 9.2). In 2009, Riedl *et al.* [262] demonstrated that the ZLG can be converted into sp^2 bonded graphene layer, the so-called quasi-free-standing mono-layer graphene (QFMLG) (see Ch. 13), by intercalation of hydrogen at the SiC-graphene interface. This was interpreted as a strong argument in favour of the hexagonal atomic arrangement in the ZLG [109]. Goler *et al.* [109] clarified the atomic structure of the ZLG by atomically-resolved STM imaging. They demonstrated that the ZLG is indeed topologically identical to a graphene monolayer and thus represents a true periodic carbon honeycomb structure. They could not observe any obvious atomic defects in the QFMLG and concluded that also the defect concentration in the ZLG is most likely very low. Today, the general consensus is that the C atoms arrange in a hexagonal atomic lattice such as in free-standing graphene [264, 83, 335, 166, 183, 263, 109].

The $(6\sqrt{3}\times6\sqrt{3})$-R30° periodicity originates from the lattice mismatch between the SiC and the graphene lattice parameter. The large, commensurate ZLG unit cell consists of a $(6\sqrt{3}\times6\sqrt{3})$ SiC supercell (108 Si and 108 C atoms per bilayer) covered by a (13×13) honeycomb graphene-like supercell (338 C atoms) [264, 83, 335, 166, 263, 109, 227]. The lattice match is almost strain-free compared to a graphene plane in graphite (experiment: 0.2 % at T=0 K [195, 9], PBE+vdW: 0.1 % Tab. 7.2, see Ch. 9). The C atoms in the ZLG-layer are partially covalently bonded to the top Si atoms of the substrate.

Continued heating and extended growth times detaches the C-plane of the ZLG from the substrate to form MLG and a new ZLG-layer underneath [293, 125]. The MLG-layer is a sp^2 bonded graphene layer. Further heating leads to a successive formation of BLG [238] and few-layer graphene films. In

the following, we address the C-rich surface phases in their experimentally observed, large commensurate $(6\sqrt{3} \times 6\sqrt{3})$-R30° supercells, using slabs containing six SiC-bilayers under each reconstructed phase (1742 up to 2756 atoms for ZLG up to three-layer graphene (3LG), respectively).

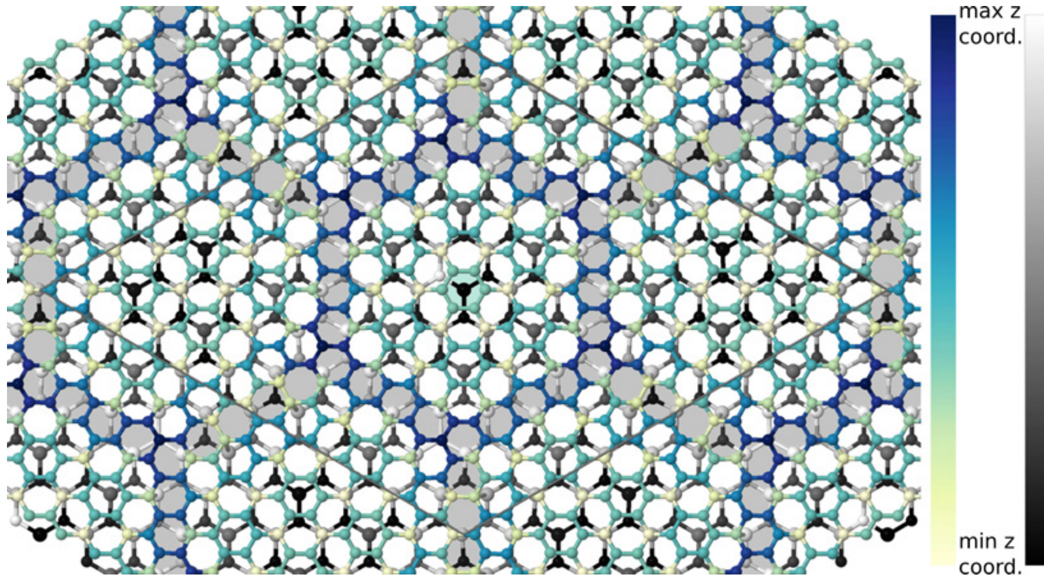

Figure 8.4.: Top view of the relaxed ZLG structure using PBE+vdW. The unit cell in the x-y-plane is indicate by a grey rhombus. The C atoms in the ZLG layer are coloured according to their z-coordinate (the colour scale reaches from yellow for atoms close to the substrate to blue for atoms away from it). The top Si-C bilayer is shown as well, here the z-coordinate scales from black to white, where black indicates that the atom is pushed towards bulk SiC. The ZLG hexagons furthest away from the substrate form a hexagonal pattern (marked in grey). The Si atom of the top Si-C bilayer in the middle of a ZLG carbon ring has the minimum z-coordinate (in the middle of the unit cell marked in light green).

Figure 8.4 shows the geometric structure of the ZLG-layer and the top Si-C bilayer from a top view. The unit cell in the x-y-plane is indicate by a grey rhombus. The atoms in the structure are coloured depending on their position along the z-axis. The atoms of the top Si-C bilayer are coloured from black to white, where black indicates an atom position close to the substrate and white close to the ZLG-layer. The colour scale for the atoms in the ZLG-layer ranges from yellow for atom positions close to the substrate to blue for atoms away from it. In the ZLG-layer, the atoms furthest away from the substrate (shown in blue) form a hexagonal pattern (marked in grey). The corrugation of the ZLG-layer is also observed in STM experiments [166, 335, 263, 68, 80]. Riedl *et al.* [263] used atomically resolved STM images to construct a model of the $(6\sqrt{3} \times 6\sqrt{3})$-R30° interface structure they found a quasi (6×6) periodicity in good agreement with the pattern in Fig. 8.4 (see Ref. [263] Figure 3.d). The Si atom of the top Si-C bilayer with the minimum z-coordinate is located in the middle of a ZLG carbon ring (in the center of the unit cell shown in Fig. 8.4). The corrugation originates from an interplay

between C atoms covalently bonded to the substrate and sp^2 hybridised ones.

The next C-rich phase consists of the ZLG phase covered by a purely sp^2 bonded graphene layer, the MLG. The MLG layer is a (13×13) graphene cell stacked on top of the ZLG-layer in graphite-like AB stacking. The BLG phase consists of the ZLG structure covered by two graphene layer in graphite-like ABA stacking.

Figures 8.5a-c show the ZLG, MLG and BLG phases together with key geometry parameters predicted at the level of PBE+vdW. To capture the extend of the corrugation shown in Fig. 8.4 and analyse its effect on the substrate and the adsorbed graphene layer, we plotted histograms for the atomic z-coordinates. For illustration purposes, we broadened the histogram lines using a Gaussian with a width of 0.05 Å.

The corrugation from the highest C atom to the lowest C atom in the ZLG-layer is 0.83 Å. Emery *et al.* [80] found a corrugation of 0.9 Å by x-ray standing-wave-enhanced x-ray photoemission spectroscopy (XSW-XPS) and x-ray reflectivity (XRR) measurements [80]. Few of the Si atoms of the top Si-C bilayer are pushed into the carbon layer of the top Si-C bilayer. We highlighted the lowest Si atom in Fig. 8.4, as pointed out above the Si atom is underneath the midpoint of a carbon hexagon in the ZLG-layer. The dangling bond of this Si atom pushes against the π-bonded parts of the C interface plane [334].

The addition of more graphene planes hardly affects the interface geometry. The corrugation of the ZLG-layer transfers to the MLG phase, leading to a significant buckling of the topmost graphene layer (0.41 Å between top and bottom of the plane). This strong corrugation is qualitatively consistent with x-ray characterisation techniques (XSW-XPS, XRR) [80] and STM images [55, 65, 21]. The corrugation is reduced in the BLG phase to 0.32 Å in the first graphene layer and 0.24 Å in the second one. This buckling reflects some coupling to the covalently bonded interface C-rich plane, which is much more corrugated (0.8 Å in our work, similar to experimental estimates [109, 68]). The observed graphene interplanar distances near the interface are slightly expanded compared to experimental bulk graphite (3.34 Å [9]) and in good qualitative agreement with estimates from STM [21] and TEM [230].

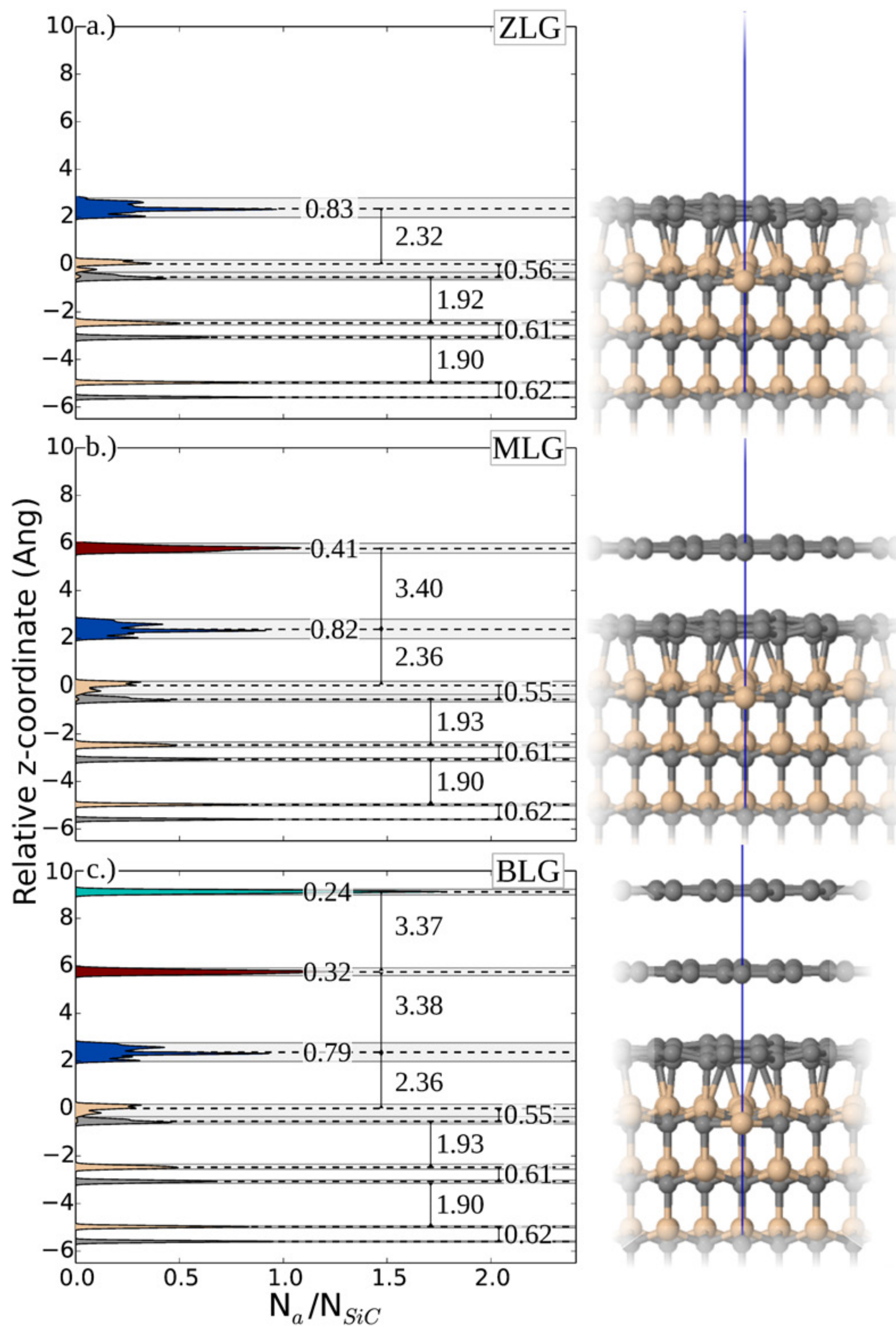

Figure 8.5.: Geometry and key geometric parameters determined by DFT-PBE+vdW for the three phases (a) ZLG, (b) MLG and (c) BLG on the Si face of 3C-SiC(111) and histograms of the number of atoms (N_a) versus the atomic coordinates (z) relative to the topmost Si layer (Gaussian broadening: 0.05 Å). N_a is normalised by N_{SiC}, the number of SiC unit cells. All values are given in Å. (Data published in Nemec *et al.* [227])

We compared our findings to geometries for the PBE functional without vdW correction, and for LDA (Fig. 8.6). The LDA and PBE functional show a similar trend for the interplanar bonding of the MLG-layer as for graphite (see Ch. 6.2). In PBE, the interplanar distance between the ZLG and MLG-layer is unphysically expanded to 4.42 Å. In contrast, the LDA geometry of the carbon planes agrees qualitatively with PBE+vdW, although LDA incorporates no long-range vdW interactions. The first qualitative geometry difference between the PBE+vdW and LDA treatments appears in the corrugation of the Si atoms in the top Si-C bilayer. In PBE+vdW the distance between top an bottom Si atom is 0.76 Å, but in LDA it is reduced to 0.53 Å (PBE: 0.08 Å). The difference mainly originates from the central Si atom (shown in Fig. 8.4), where the Si dangling bond pushes against the π-bonded parts of the C interface plane.

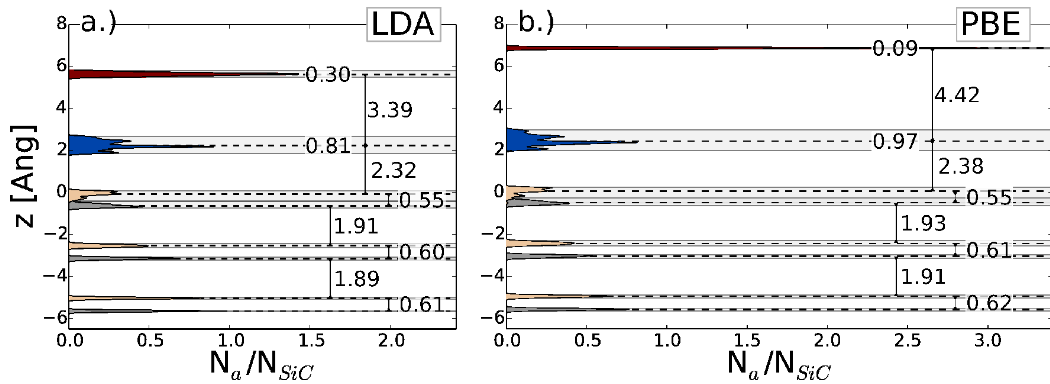

Figure 8.6.: Histogramm of the number of atoms N_a versus the atomic coordinates (z) relative to the topmost Si layer (Gaussian broadening: 0.05 Å). The key geometric parameter of the MLG on the Si face of 3C-SiC(111) at the level of a) LDA and b) PBE. All values are given in Å.

The atomic density map derived from combined XSW-XPS and XRR analysis [80], also shows a significant broadening for the Si atoms in the top Si-C bilayer. However, the corrugation in the top Si-C bilayer was not the focus of the experimental work [80] and therefore cannot clarify the observed difference in the geometry obtained by using the LDA and PBE+vdW functional. We will keep these subtle differences in mind, when discussing our results.

The Si-terminated surface of 6H-SiC is widely used to achieve a controlled formation of high quality epitaxial graphene monolayers [95, 82, 307, 263]. In the following, we discuss the structural difference between 3C-SiC- and 6H-SiC-MLG. For the 6H-SiC-MLG, we use the $S3_{6H}$ terminated surface (see Fig. 8.1) and the lattice parameter listed in Tab. 7.2. For the structure optimisation, we used the PBE+vdW exchange-correlation functional.

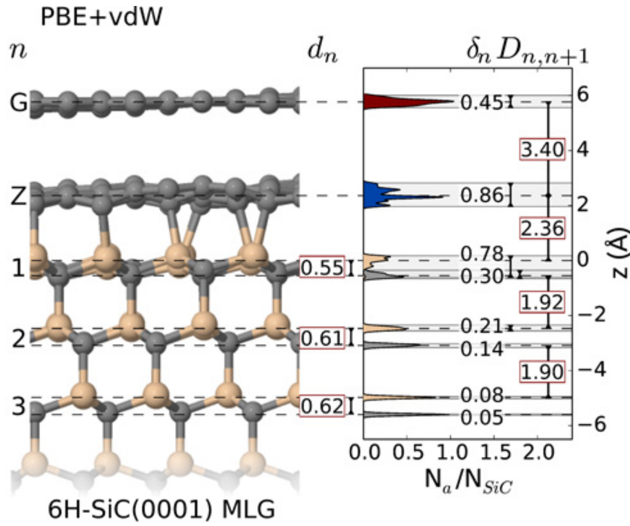

Figure 8.7: MLG on 6H-SiC(0001) and histogram of the number of atoms N_a versus the atomic coordinates (z) relative to the topmost Si layer (Gaussian broadening: 0.05 Å). N_a is normalised by N_{SiC}, the number of SiC unit cells. $D_{n,n+1}$ is the distance between the layer n and $n+1$, d_n gives the Si-C distance within the SiC bilayer n, and δ_n the corrugation of the layer n. All values are given in Å. (Figure published in Ref. [294])

Overall, the atomic structure of 3C-SiC-MLG (Fig. 8.5 b) and 6H-SiC-MLG (Fig. 8.7 are very similar. For 6H-SiC-MLG, the corrugation of the MLG-layer and of the ZLG-layer is slightly increased to 0.45 Å and 0.86 Å, respectively. However, the layer distances $D_{n,n+1}$ are the same for 6H-SiC-MLG and 3C-SiC-MLG. Overall, the changes with the polytype are minor, which is not surprising as the Si-C bilayer stacking order is identical for 3C-SiC and $S3_{6H}$ terminated 6H-SiC.

There are two aspects to strain in epitaxial graphene. The first one is specific to epitaxial graphene on the Si face of SiC, caused by the coupling between the ZLG and the epitaxial graphene layer (MLG) [229, 87]. In the following we discuss both aspects of strain in epitaxial graphene. The second one is caused by the choice of the coincidence lattice between the substrate and graphene: Depending on the interface structure used in the calculations artificially induced residual strain may effect the energetics and the detailed bonding at the interface [290].

9.1. ZLG-Substrate Coupling and its Effect on the Lattice Parameter

By means of Raman spectroscopy, signatures of compressive strain were observed in epitaxial graphene on the Si face of SiC [229, 87, 266, 281]. The strain in the MLG is caused by the coupling between the ZLG and the MLG layer [88, 109]. Conversely, in grazing-incidence x-ray diffraction (GID) an increase of the in-plane lattice parameter was measured for the ZLG layer (2.467 Å) [283] if compared to lattice parameter of the MLG-layer (2.456 Å [283]) or the in-plane lattice parameter of graphite (2.456 Å [226]).

In Section 8.2, we introduced the ZLG interface structure. In Figure 9.1 (a) the ZLG layer and the top SiC bilayer is shown from atop. The C atoms in the ZLG are coloured depending on their vertical distance from the average height of the top Si layer from black to white. The in-plane bonds between the C atoms in the ZLG layer are coloured from blue to red depending on their bond length. In regions close to C atoms covalently bonded to the substrate the C-C bond length is streched compared to free-standing graphene. For example, the previously discussed Si atom in the middle of a carbon hexagon (marked in Fig. 8.4 or at the center of Fig. 9.1 (a)) is surrounded by 6 Si atoms covalently bonded to C atoms in the ZLG-layer. The Si-C bond length is 1.995 Å, for comparison the Si-C bond length in 3C-SiC is 1.896 Å. The mixture of sp^2 and sp^3 hybridised carbon at the substrate/ZLG interface results in a corrugation of 0.83Å (see Fig. 8.5).

As alluded to above, Schumann *et al.* showed by GID that the lattice parameter of the ZLG layer is larger than the in-plane lattice parameter of

graphite. Figure 9.1 (b) shows the bond length distribution in the ZLG layer. We applied a Gaussian broadening of 0.002 Å for visualisation purposes only. The area under the curve is shaded with the same colour gradient used in Fig. 9.1 a). The bond length of free-standing graphene in the optimised structure on a PBE+vdW level and the average bond length in the ZLG layer are indicated by two vertical lines.

The bond length distribution curve shows two maximum a sharp one at a bond length of 1.406 Å and a second between 1.468 Å and 1.504 Å. The first maximum corresponds to a compression of the C-C bond length of 1.1% compared to free-standing graphene. On average, the bond length in the ZLG layer is 1.6% larger (1.445 Å). The double peak in the bond length distribution can be understood when examining Fig. 9.1 a). In regions where a C atom of the ZLG layer is covalently bonded to a Si atom in the substrate, the three in-plane C-C bonds are extended, while in regions with a sp^2-like hybridisation in the ZLG layer the bond length is closer to free-standing graphene with a slight compression. This result is not surprising, because an increase of the C-C bonds length has been observed when moving from sp to sp^2 to sp^3 hybridised C-C bonds [41]. The presence of inhomogeneous compressive strain was also suggested on the basis of Raman spectroscopy by Roehrl *et al.* [266] and Schmidt *et al.* [281]. The corrugation of the interface layer is reduced by an additional MLG layer on top of the ZLG (see Fig. 8.5 b) resulting in a slightly smaller average C-C bond length.

In GID measurements, the lattice parameter is measured as a projection onto the x-y-plane. The changes in the bond length due to corrugation is not captured by the experiment [283]. This makes a direct comparison with our calculations difficult, because the average C-C bond length projected on the x-y-plane is fixed by the choice of lattice vectors used in the calculation. However, the general trend is well captured in our calculations. The increased lattice parameter can be explained by the mixture of the sp^3 and sp^2-like hybridisation of the C atoms in the ZLG layer.

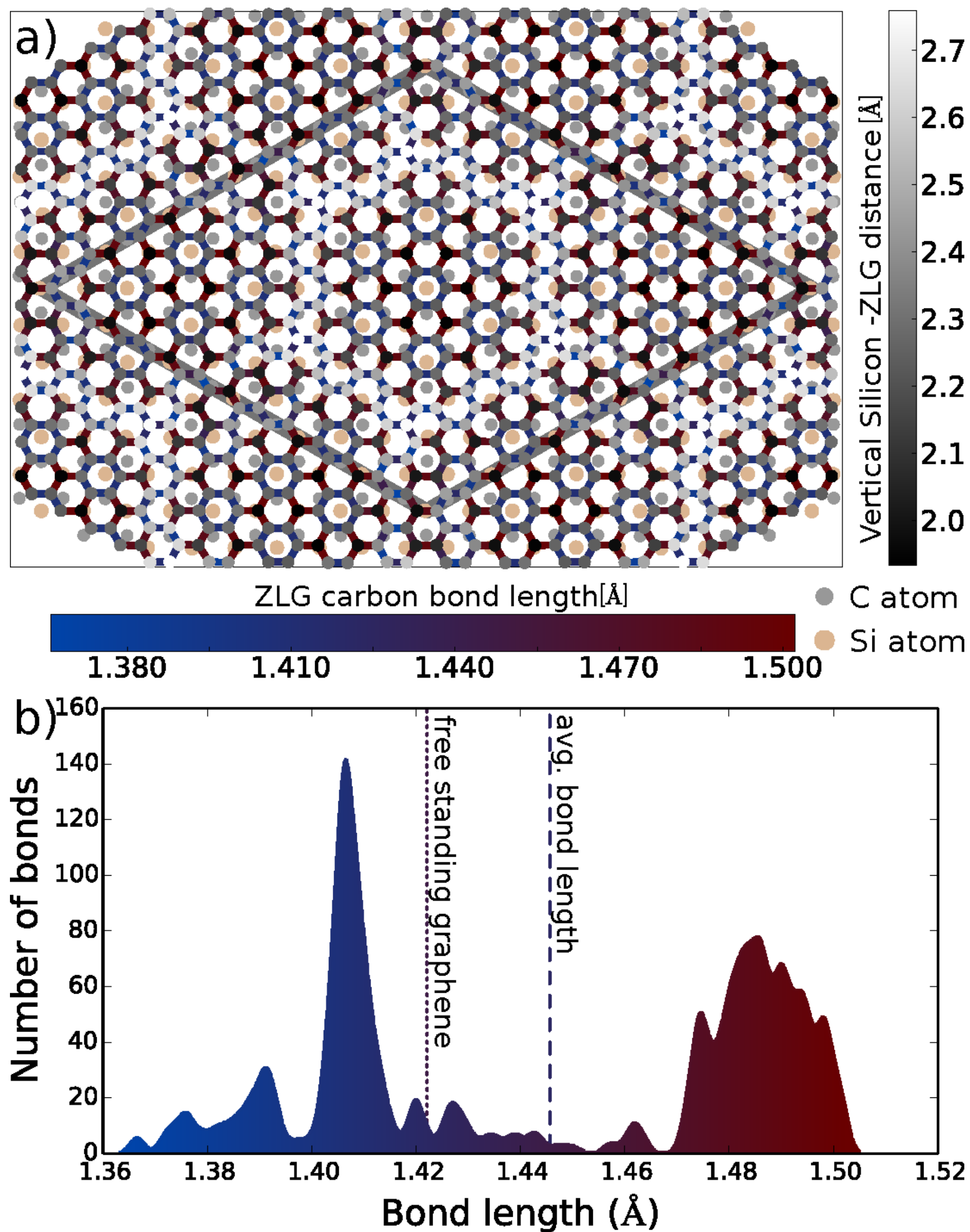

Figure 9.1.: a) Top view of the ZLG layer and the top SiC bilayer fully relaxed using PBE+vdW. The carbon atoms of the ZLG layer are coloured according to their vertical distance from the average height of the Si-layer ranging from black being close to the Si layer to white for C atoms away from the Si-layer. The bonds between the ZLG C atoms are coloured from blue to red for increasing bond length. b) Bond length distribution in the ZLG layer. A Gaussian broadening of 0.002 Å was applied for visualisation purposes only. The two vertical lines indicate the bond length of free-standing graphene in the optimised structure on a PBE+vdW level and the average bond length in the ZLG layer.

9.2. Interface Models for Epitaxial Graphene

It would be computationally more efficient to use smaller-cell approximant phases to the true $(6\sqrt{3}\times6\sqrt{3})$-R30° supercell. Indeed, different smaller-cell approximant phases have been used in literature [214, 215, 334, 335, 289, 243]. However, the residual artificial strain and incorrect bonding in those phases hinder a meaningful surface energies comparison. Sclauzero and Pasquarello [288] compared three different structural models to the ZLG phase, a SiC-$(\sqrt{3}\times\sqrt{3})$-R30° supercell covered by an (2×2) graphene cell, an unrotated (4×4) SiC cell covered by a (5×5) graphene cell and the experimentally observed SiC-$6\sqrt{3}\times6\sqrt{3}$-R30° ZLG structure. They compared the energy of the three SiC-graphene interface models and identified the SiC-$6\sqrt{3}\times6\sqrt{3}$-R30° ZLG structure to be the most stable one.

We constructed commensurate graphene-3C-SiC(111) interface structures from rotated hexagonal supercells of 3C-SiC(111) and graphene. We address artificially induced strain, dangling bond saturation, corrugation in the carbon nanomesh and the surface energy for different coincidence structures.

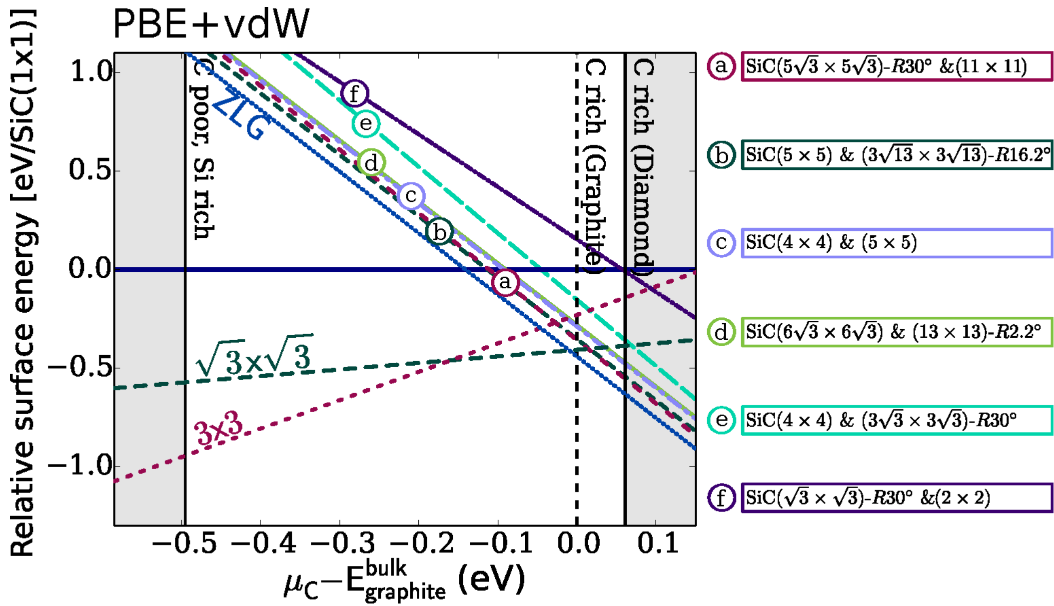

Figure 9.2.: Comparison of the surface energies for six different smaller-cell approximant models of the 3C-SiC(111) ZLG phase, relative to the bulk-terminated (1×1) phase, as a function of the C chemical potential within the allowed ranges using PBE+vdW. The Si rich (3×3) and $(\sqrt{3}\times\sqrt{3})$ reconstructions as well as the $(6\sqrt{3}\times6\sqrt{3})$-R30° ZLG phase from Fig. 10.1 are included for comparison. The shaded areas indicate chemical potential values outside the strict thermodynamic stability limits of Eq. 4.15.

By rotating a graphene layer on a SiC substrate Sclauzero and Pasquarello [290] found several model interfaces which give almost perfect commensurability between the graphene and SiC supercells. For a selection of such interface models, they calculated the change in energy of a plane free-standing graphene layer due to the strain necessary to built a commensurate SiC-graphene interface model [290]. They found a change in energy to be smaller than 40 meV for all structures except the $(\sqrt{3} \times \sqrt{3})$-R30° model. We include six different smaller-cell approximant models of the 3C-SiC(111) ZLG phase in our analysis:

(ZLG) SiC-$(6\sqrt{3} \times 6\sqrt{3})$-R30° & (13×13) [19, 95, 83, 55]

(a) SiC-$(5\sqrt{3} \times 5\sqrt{3})$-R30° & (11×11)

(b) SiC-(5×5) & $(3\sqrt{13} \times 3\sqrt{13})$-R16.2° [242]

(c) SiC-(4×4) & (5×5) [290]

(d) SiC-$(6\sqrt{3} \times 6\sqrt{3})$ & (13×13)-R2.2° [131]

(e) SiC-(4×4) & $(3\sqrt{3} \times 3\sqrt{3})$-R30°

(f) SiC-$(\sqrt{3} \times \sqrt{3})$-R30° & (2×2) [334, 214]

To our knowledge, structure (a) and (e) have not yet been discussed in literature. We calculated a slightly rotated (5×5) approximant to the ZLG phase [242] (structure (b)), a periodicity sometimes seen in experiment [210, 264, 307]. Structure (b) has also been discussed in Ref. [290] and Ref. [289]. Structure (c) was first introduced by Sclauzero and Pasquarello [290]. Hass *et al.* [131] used basic trigonomy to show that for the $(6\sqrt{3} \times 6\sqrt{3})$ SiC supercell, three rotational angle relative to SiC substrate can be found the experimentally observed 30° (ZLG) and two additional rotational angle ±2.204°. The graphene layer rotated by 2.204° can be constructed with the supercell matrix ($\mathcal{N}$), introduced in Sec. 11

$$\mathcal{N} = \begin{bmatrix} 8 & 7 & 0 \\ -7 & 15 & 0 \\ 0 & 0 & 1 \end{bmatrix}. \tag{9.1}$$

In addition to the ZLG structure, we include the SiC-$(6\sqrt{3} \times 6\sqrt{3})$ supercell with a graphene layer rotated by 2.204° (structure (d)). In Figure 9.2, we compare the surface energies of the six different smaller-cell approximant models listed above. We also included the Si rich (3×3) and $(\sqrt{3} \times \sqrt{3})$

	SiC cell	ZLG cell	Angle α	N_{SiC}^{surf}	N_{ZLG}	N_{Si}^{DB}	δ_C[Å]	Strain [%]	γ [eV/SiC(1x1)]
ZLG	$6\sqrt{3}\times6\sqrt{3}$	13×13	30°	108	338	19	0.83	0.14	−0.44
(a)	$5\sqrt{3}\times5\sqrt{3}$	11×11	30°	75	220	19	0.95	−0.65	−0.36
(b)	5×5	$3\sqrt{13}\times3\sqrt{13}$	16.2°	25	78	3	0.83	0.27	−0.35
(c)	4×4	5×5	0°	16	50	3	0.65	0.19	−0.29
(d)	$6\sqrt{3}\times6\sqrt{3}$	13×13	2.2°	108	338	19	0.74	0.14	−0.29
(e)	4×4	$3\sqrt{3}\times3\sqrt{3}$	30°	16	54	10	1.45	3.6	−0.15
(f)	$\sqrt{3}\times\sqrt{3}$	2×2	30°	3	8	1	0.30	9.3	0.15
	3×3	$2\sqrt{3}\times2\sqrt{3}$	30°	9	24	3	0.30	9.3	0.15

Table 9.1.: Parameters of the simulated ZLG-3C-SiC(111) interface structures in different commensurate supercells: the 3C-SiC and ZLG periodicity, the rotation angle (α), the number of surface Si atoms (N_{SiC}^{surf}) and C atoms in the ZLG (N_{ZLG}), the number of unsaturated Si bonds (N_{Si}^{DB}) (see Appendix E), the corrugation of the ZLG layer (δ_C), the strain in the carbon layer, and the relative surface energy at the carbon rich graphite-limit ($\gamma|_{\mu_C=E_{graphite}^{bulk}}$).

reconstructions as well as the $(6\sqrt{3}\times6\sqrt{3})$-R30° ZLG phase from Ch. 8. All structural models consist of six 3C-SiC bilayer covered by a graphene lattice, the bottom C atoms of the SiC substrate have been saturated by hydrogen. The top three SiC-bilayers and the carbon layer above are fully relaxed using PBE+vdW (residual energy gradients: $8{\cdot}10^{-3}$ eV/Å or below). The surface energies (γ) were calculated using Eq. 4.9. All surface energies are given relative to the bulk-terminated (1×1) surface. The range of the Si and C chemical potential are given in Sec. 4.2. For instance, the popular $(\sqrt{3}\times\sqrt{3})$-R30° [334, 214] approximant intersects the graphite stability line at a relative surface energy in the carbon rich limit (ref. Graphite) of 0.15 eV, far above the actually stable phases.

In Table 9.1 we listed the parameters of the simulated ZLG-3C-SiC(111) interface structures for the different smaller-cell approximant models shown in Fig. 9.2: the 3C-SiC and ZLG periodicity, the rotation angle (α), the number of surface Si atoms (N_{SiC}^{surf}) and C atoms in the ZLG (N_{ZLG}). We also list the number of unsaturated Si bonds (N_{Si}^{DB}). The Si dangling bonds were identified on the basis of geometric position and bond length differences (for a detailed discussion see Appendix E). Table 9.1 further includes the corrugation of the ZLG layer (δ_C), the strain in the carbon layer, and the relative surface energy at the carbon rich graphite-limit ($\gamma|_{\mu_C=E_{graphite}^{bulk}}$).

In structure (b) the strain in the carbon ad-layer is small with 0.27% and the Si dangling bond saturation is improved if compared to the experimentally observed $6\sqrt{3}\times6\sqrt{3}$-R30°. However, the relative surface energy intersects

with the chemical potential limit for graphite at −0.35 eV, still higher by 0.06 eV than even the closest competing Si-rich phase, the ($\sqrt{3} \times \sqrt{3}$)-R30° Si adatom phase. The (5×5) phase is either a nonequilibrium phase, or its structure is not the same as that assumed in Ref. [242].

So far different mechanisms were assumed to stabilise the SiC-($6\sqrt{3} \times 6\sqrt{3}$)-R30° & (13 × 13)-ZLG structure. First, the surface energy is reduced by minimising the strain between the SiC substrate and the ZLG layer [290]. Sclauzero and Pasquarello [288] pointed out a correlation between the binding energy and the corrugation of the ZLG-layer. In their study, the binding energy was reduced with a reduction of the corrugation. It also has been discussed that the structural properties are driven by saturation of dangling Si bonds of the top SiC-bilayer through bond formation with the ZLG C atoms [83, 290]. Structure (d) and the ZLG experience the same lattice mismatch. Both phases saturate 89 Si atoms at the SiC-ZLG interface, leaving 19 Si dangling bonds (Tab 9.1). The corrugation of the ZLG-phase is higher by 0.09 Å. If we follow the line of argument and compare the two structure models, the ZLG and structure (d), we would assume that the binding energy of strucutre (d) should be lower, because the lattice mismatch and the Si dangling bond saturation is the same, but the corrugation of structure (d) is lower. However, this is not observed. The ZLG phase is 0.15 eV lower in surface energy Tab 9.1 and in LEED measurement show a 30° rotation between the substrate and the ZLG-layer, e.g. in Ref. [263].

Certainly, the lattice mismatch, the corrugation and the dangling bond saturation play a crucial role in the stabilisation of the ZLG phase, but these three factors cannot explain why the 30° rotation is preferred energetically over the 2.2° (Tab. 9.1, and Fig. 9.2). To shed some light on the origin of the difference in surface energy between the two different rotation angles, we compare the bond length distribution of these two phases.

Figure 9.3 shows the bond length distribution in the ($6\sqrt{3} \times 6\sqrt{3}$) & (13 × 13)-ZLG layer for two different rotational angles. The bond length distribution of the 30° rotated ZLG layer is taken from Fig. 9.1 (shown in grey in Fig. 9.3). Structure (d), rotated by 2.204°, is shown in blue in Fig. 9.3. We applied a Gaussian broadening of 0.002 Å for visualisation purposes only. The average bond length of structure (d) is 1.434 Å, which is 0.012 Å smaller than for the ZLG-layer. In Section 9.1, we demonstrated that the two peak structure can be understood as a result of a mixture of regions with a sp^2-like and sp^3-like hybridisation in the ZLG layer. The bond length of the sp^3-like hybridised C atoms in the ZLG-layer range from 1.468 Å to 1.504 Å. If we compare the two curves in Fig. 9.3, we see that in the bond length range of the sp^3-hybridised C atoms of the ZLG layer are only very

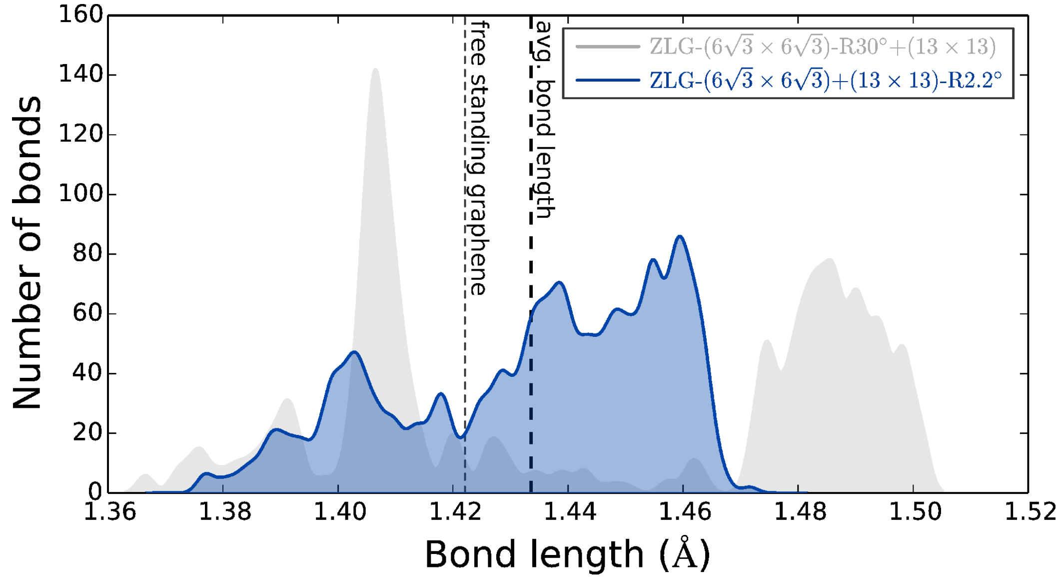

Figure 9.3.: Bond length distribution in the $(6\sqrt{3} \times 6\sqrt{3})$ & (13×13)-ZLG layer for two different rotational angles. The bond length distribution for the ZLG layer in the 30° rotated structure from Fig. 9.1 is shown in grey and the ZLG structure rotated by 2.204° in blue. A Gaussian broadening of 0.002 Å was applied for visualisation purposes only. The two vertical lines indicate the bond length of free-standing graphene in the optimised structure on a PBE+vdW level and the average bond length in the ZLG layer rotated by 2.204°.

few C-C bonds of structure (d). Indeed, the maximum C-C bond length in structure (d) is 1.472 Å, indicating that the C-C bonds with sp^3 characteristic are compressed. Most bonds of structure (d) are between the two peaks of the ZLG structure. From the analysis shown in Fig. 9.3, we conclude that the surface energy of structure (d) is increased by the compression of the sp^3-like hybridised C-C bonds and the stretching of the sp^2-like hybridised C-C bonds. The difference in the bond length distribution originates in the detailed bonding situation determined by the position of the Si dangling bonds. However, also the electronic structure of the specific arrangement will play a role in the stabilisation of one structure over the other.

Finally, we discuss the influence of artificially strained approximant phases on electronically relevant properties, such as the formation energies of defects. To calculate the defect formation energy, we substract from the surface energy (Eq. 4.9) of the system including the defect (γ_{def}) the surface energy of the defect free surface (γ_{ZLG}) and account for additional C atoms or C vacancies by the carbon chemical potential $\mu_{\text{C}}^{\text{Graphite}}$ (Eq. 4.15)

$$\Delta G = \frac{1}{N_{\text{def}}} \left(\gamma_{\text{def}} - \gamma_{\text{ZLG}} - N_{\text{C}} \mu_{\text{C}}^{\text{Graphite}} \right), \tag{9.2}$$

where N_{C} is the number of substituted or vacant C atoms and N_{def} the number of defects in the slab. For negative defect formation energies (ΔG) the defect is stable and for positive ΔG the formation of the defect is unlikely.

As an example, we consider a specific class of C-rich hexagon-pentagon-heptagon (H5,6,7) defects suggested as an equilibrium feature of the ZLG phase in Ref. [256]. The defects consist of three carbon heptagons and pentagons surrounding one carbon hexagon. The central hexagon is rotated by 30° with respect to the graphene lattice. This defect incoporates two additional carbon atoms (N_{C} =2) , lowering the average C-C bond length in the ZLG. Qi *et al.* suggested two different defect positions, “hollow” and “top”, shown in Fig. 9.4.

In Figure 9.4 the H(5,6,7) defect is shown for both positions in the approximated 3×3 and in the $(6\sqrt{3} \times 6\sqrt{3})$-R30° ZLG phase. The 3×3 is a supercell of the approximated $(\sqrt{3} \times \sqrt{3})$-R30° ZLG phase with a massively strained carbon layer (see Tab. 9.1). All four phases were fully relaxed using the same procedure as described above. Indeed, both defects would be more stable than the hypothetical $(\sqrt{3} \times \sqrt{3})$-R30° ZLG approximant when included in a (3×3) arrangement as done in Ref. [256]: Using Eq. 9.2 gives $\Delta G = -1.75$ eV per defect for the hollow and $\Delta G = -2.93$ eV per defect for the top position. However, the same defects are unstable when included into and compared to the correct $(6\sqrt{3} \times 6\sqrt{3})$-R30° ZLG phase: $\Delta G = +5.28$ eV per defect for the hollow and $\Delta G = +5.27$ eV for the top site, again at the chemical potential limit for graphite. The formation energy of the H(5,6,7) defect in the $(6\sqrt{3} \times 6\sqrt{3})$-R30° ZLG phase is too high to make the formation of these defects likely. The formation of a H(5,6,7) defect introduces two additional C atoms, lowering the overall strain of the C-C bonds in the approximated $(\sqrt{3} \times \sqrt{3})$-R30° ZLG phase, which leads to a stabilisation of the defect. This example illustrates the importance of a careful interpretation of any results obtained by using an approximated interface structure.

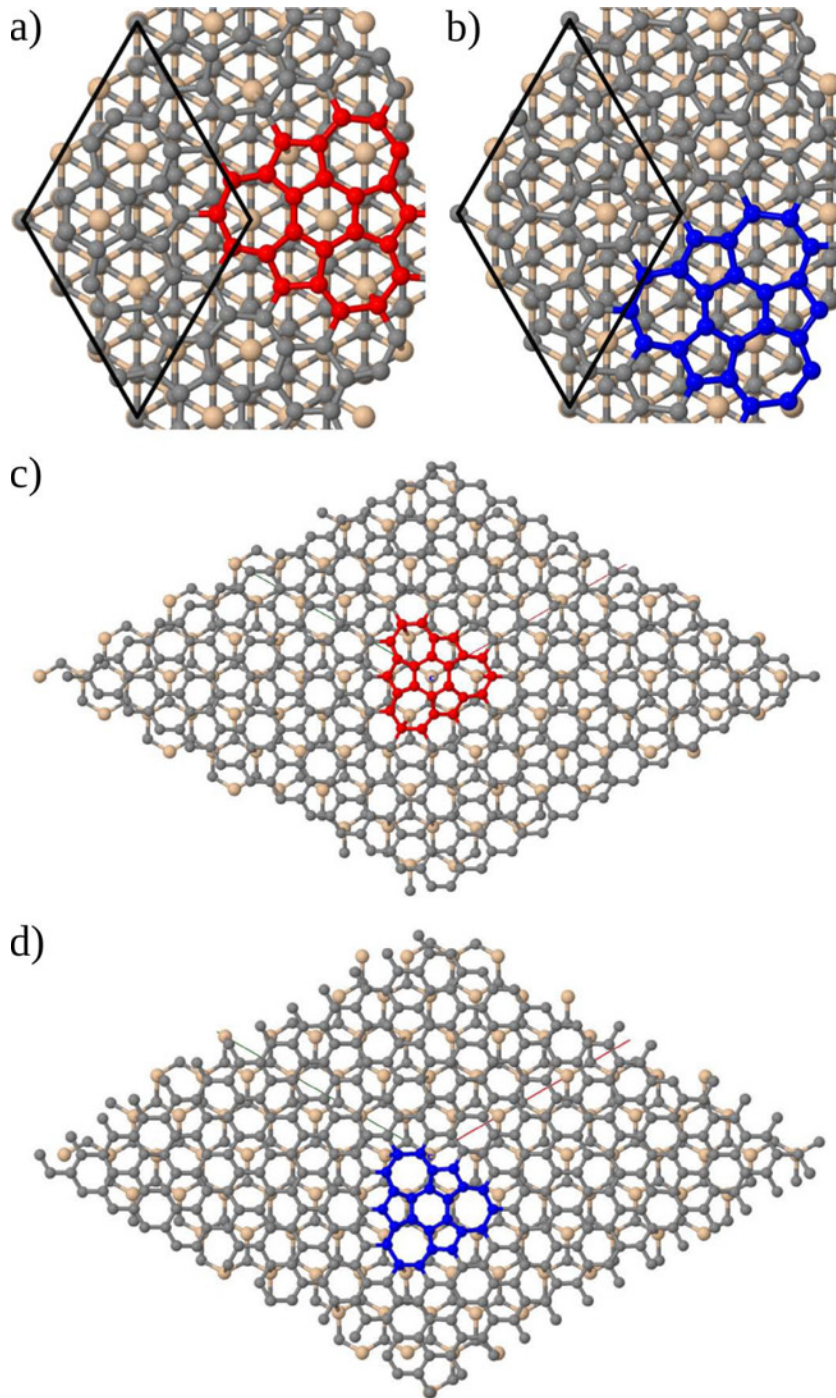

Figure 9.4.: The hexagon-pentagon-heptagon (H5,6,7) defect in the zero-layer graphene shown in the approximated 3×3 cell (insert a and b) and in the $(6\sqrt{3} \times 6\sqrt{3})$-R30° ZLG phase. The defect was placed in two different positions. In inset a and c the defect is placed at the "hollow" position with a silicon atom of the underlying SiC bilayer in the middle of the central hexagon and at the "top" position.

9.3. Defect Induced Strain in Graphene

Schumann *et al.* [284] demonstarted the feasibility of growing nano-crystalline graphene films on $(6\sqrt{3} \times 6\sqrt{3})$-R30° ZLG phase using MBE as an alternative method for graphene synthesis. In a combined experimental and theoretical study, we investigated the strain observed in nano-crystalline graphene grown by MBE, published in Ref. [284]. Our experimental collaborators investigated the structural quality of the MBE grown graphene films, by AFM, XPS, Raman spectroscopy and GID. XPS and Raman spectroscopy indicate that the ZLG-layer persists throughout the growth process. They demonstrated that grown carbon films indeed consist of planar sp^2-bonded carbon by XPS measurements. The appearance of an intense D peak in Raman spectroscopy, a characteristic feature in the Raman spectra of defects in graphene, reveal that the MBE-grown carbon films possesses a nano-crystalline and partially defective structure.

From the Raman spectra they estimated the average lateral size of the graphene domains to be at the order of 15-20 nm. GID measurements show that the graphene domains have the same in-plane orientation and are aligned to the substrate. Interestingly, the lattice parameter of the nano-crystalline graphene films is contracted by 0.45% in comparison to the lattice parameter of graphite (2.461 Å [132]). They measured the lattice parameter of the graphene films to be 2.450 Å. The origin of the observed contraction is unclear. We here list three potential reasons:

i The linear thermal expansion coefficients of graphene and SiC are very different in their low temperature behaviour [87, 266]. While the lattice parameter of graphene decreases [221] the volume of SiC expands [193, 196, 317] for increased temperatures. These qualitatively different behaviour was related to the contraction of the MLG lattice parameter [87, 266]. Based on this difference, Ferralis *et al.* [87] estimated that a compressive strain in graphene of up to 0.8% can arise upon sample cooling down to room temperature.

ii The strong corrugation in the ZLG as discussed in Sec. 9.1 could contribute to the apparent contraction of the (2D projected) lattice parameter of the uppermost nano-crystalline graphene, despite the existent epitaxial relation between them. Indeed, in Sec. 8.2 we found a corrugation of the MLG films of 0.41Å.

iii The presence of defects and grain boundaries in the nano-crystalline film could also lead to a lateral contraction of graphene. The strong

D peak in the Raman spectra would allow for the presence of zero- or one-dimensional defects in the films.

Strain up to 0.4% has been inferred by Raman spectroscopy for the epitaxially grown MLG [281]. A similar contraction was directly linked to substrate thermal contraction in a recent study of near-perfect CVD-grown graphene on Ir(111) [132]. However, the contraction observed by the GID measurements extends to a smaller lattice parameter than that found in Ref. [281] and Ref. [132]. For a perfect free-standing graphene layer, the observed contraction would most likely induce the formation of wrinkles/nano-fins for strain relief. Schumann *et al.* [284] performed an AFM analysis and did not observe such wrinkles in the MBE grown graphene films.

To estimate the possible contributions of (ii) and (iii), we performed DFT calculations of isolated graphene sheets. In Table 6.1, we found for the infinite periodic flat graphene sheet a lattice parameter of a = 2.463 Å (PBE+vdW). The calculated value for MLG layer on SiC is practically the same (within 0.1%, see Tab. 9.1). For straight PBE without vdW corrections the in-plane lattice parameter of graphene is slightly affected leading to an increase of 0.004 Å (see Tab. 6.1). Beyond the original vdW correction of Tkatchenko and Scheffler [326], the strength of effective interatomic *C*6 coefficients that describe the vdW interaction in carbon-based nanostructures may vary considerably with the structure [107] and could significantly change out-of plane interactions with a graphene sheet (Sec. 6.2). However, their effect will still be small on the energy scale of interest for the in-plane lattice parameter, which is dominated by the covalent interactions that are described by the PBE functional itself.

First we address point (ii), the influence of the substrate-induced corrugation. In Sec. 8.2, we found that the corrugation of the ZLG-layer induces a corrugation in the MLG-layer of 0.41 Å (Fig. 8.5). The MBE-grown graphene on the ZLG should show the same approximate corrugation. If this corrugation led to significant stress in the plane, a perfect graphene sheet with the same (fixed) z corrugation should experience the same stress and should thus contract. Our collaborator Volker Blum relaxed all in-plane coordinates and lattice parameters of such a corrugated graphene plane with fixed z corrugation. However, he found a calculated contraction of less than 0.05%, leading to a surface area that corresponds to an effective graphene lattice parameter of a = 2.462 Å.

Finally, we address the potential impact of different types of defects on the in-plane lattice parameter (point (iii) above). We first address one dimensional defect types (domain boundaries). Figure 9.5 shows the development

of the effective lattice parameter of finite-size hexagonal graphene flakes as a function of flake size. The effective lattice parameter is calculated by fully relaxing the flat graphene flakes, then calculating the average of all C-C nearest-neighbour bond distances in the flake and converting this value to the equivalent lattice parameter of a perfect honeycomb mesh. We considered two different types of flakes: One type with a H-saturated boundary (inset in Fig. 9.5) and those without H atoms at the boundary. The effective lattice parameter for small flakes is significantly contracted in either case. To approach the GID-observed lattice parameter of 2.450 Å by this effect alone, the equivalent saturated flakes would have to be extremely small (less than 0.8 nm in diameter). The equivalent unsaturated flakes, however, could be significantly larger: about 2 nm even if they were perfect otherwise. With increasing flake size, the net contraction decreases rapidly for larger sizes. However, the graphene domain size was estimated to be at the order of 15-20 nm.

Localised zero-dimensional (point-like) defects can also lead to strain and corrugation in graphene sheets [47, 274]. In close collaboration with Volker Blum, we investigate the influence of point-like defects on the average in-plane lattice parameter. We used three different defect types: monovacancies, divacancies and Stone-Wales defects in three different periodic supercell arrangements (for a recent review, consider, e.g. [47]). Figure 9.6 shows the three defect types. The monovacancy and 5-8-5 divacancy defects are shown in a (10×10) graphene unit cell and the Stone-Wales defect in a (7×7) unit cell. To give a quantitative prediction on how the graphene defects influence strain, corrugation and net area change of a periodic graphene sheet (Tab. 9.2), we fully relaxed the atomic structure and unit cell (residual forces and stresses below 0.001 eV/Å) of the three defect types in different supercell (*SC*) arrangements using PBE+vdW.

In graphene, the perhaps most studied point defect type are monovacancies (e.g. [274, 265, 6] and references therein). In a recent, exhaustive study Santos *et al.* [274] addressed the relation between theoretically imposed isotropic strain and monovacancy properties such as corrugation and spin polarisation.

The following anaysis of the different defect types in graphene was carried out by Volker Blum, published in a the joined publication Ref. [284]. He considered only the fully relaxed, stress-free local optimum structures as calculated by DFT on the level of PBE+vdW. Table 9.2 includes the calculated data for monovacancies in three different supercell arrangements with and without spin polarisation. For the structures without including spin polarisation monovacancies would be associated with significant strain and

Defect	Supercell	a_{eff} [Å]	Δz [Å]	ΔA_{defect} [Å^2]
monovacancy	5×5	2.447	0.741	-1.72
	7×7	2.455	0.800	-1.78
	10×10	2.459	0.856	-1.88
	spin-polarised (ferro- or paramagnetic)			
	5×5	2.453	<0.01	-1.06
	7×7	2.458	0.197	-1.11
	10×10	2.461	0.055	-0.98
divacancy	5×5	2.417	1.023	-4.94
	7×7	2.431	1.566	-6.82
	10×10	2.443	1.888	-8.46
	flat (meta stable)			
	7×7	2.447	<0.02	-3.42
Stone-Wales defect	7×7	2.469	0.00	+0.54

Table 9.2.: PBE+vdW calculated effective lateral lattice parameter a_{eff} (in Å), the top-to-bottom corrugation Δz (in Å) and the effective area lost (gained) per defect, ΔA_{defect} (in Å^2) of different defect types and periodicities in an ideal, free-standing graphene sheet. (Table published in Ref. [284])

corrugations of perfect graphene sheets (see Tab. 9.2). The picture changes for monovacancies calculated with the inclusion of spin polarisation. In DFT on the level of PBE+vdW monovacancies are paramagnetic defects that carry a significant local moment. This leads to a slight reduction of the compressive strain compared to a perfect graphene sheet, and thus also to a reduction of the overall distortion (buckling of the monovacancy and corrugation of the sheet). Even with the highest concentration considered in Tab. 9.2 (2% of monovacancies modeled by a (5×5) supercell), monovacancies alone would not yet lead to the full strain seen in the GID experiments.

The next defect type in graphene, we considered is the divacancy. In fact, divacancies in graphene are thermodynamically more stable than monovacancies [47], a tendency that is even enhanced by compressive strain

[48]. Volker Blum obtained the results for the divacancies with corrugation shown in Fig 9.6 by starting from the fully relaxed, non-spinpolarised monovacancy geometries and removing the most strongly buckled atom (in z direction) in the monovacancy.

As can be seen in the Tab. 9.2 and the structure of the (10×10) divacancy defect in Fig. 9.6, this procedure leads to very significant strains and buckling in a free-standing graphene sheet. The sheet curvatures seen at the defect locations follow the trend described in the literature [47]. It is also obvious that such defects could easily explain the GID-observed lateral lattice parameter reduction even for relatively low defect concentrations ((10×10) case). In fact, significant corrugations of this kind are seen in atomically resolved STM images of defects generated in Highly Ordered Pyrolytic Graphite by ion implantation (e.g. Fig. 1 in Ref. [203]). However, even if a divacancy were completely flat, the associated strain would still be significant. For comparison, Tab. 9.2 also includes the case of a flat, (7×7) periodic divacancy, which is a local structure optimum about 0.1 eV higher in energy than the corrugated divacancy arrangement. The compression of the lattice parameter for the defect densities of the divacancies included in Tab. 9.2 compresses the latttice parameter to much compared to the 2.450 Å measured by GID experiments.

Finally, we also include the case of the Stone-Wales defect, which results from the rotation of a single C-C bond, but the number of C atoms remains unchanged. Here, a slight expansion, not compression, of the overall lattice parameter would result (Tab. 9.2).

We here used idealised theoretical defects and boundaries as approximations to the experimental reality of MBE-grown nano-crystalline graphene films. Assuming that the growth process leads to defective graphene films, such that the defects influence the characteristic of such films, the morphology of the MBE-grown graphene films would most likely consists of a combination of the defect types considered in this section, as well as others. It thus seems qualitatively plausible that the strain induced by defects may indeed significantly contribute to the overall lattice parameter contraction that was observed in GID. However, to achieve large-scale homogeneous electronic properties of epitaxially MBE-grown graphene films it will be important to eliminate the potential for metastable defects.

9.4. Summary

In summary, a detailed analysis of the ZLG layer revealed the origin of the increased lattice parameter of the ZLG layer observed in GID measurements [283]. The mixture of sp^2 and sp^3-like hybridisation of the carbon atoms in the ZLG layer leads to a double peak structure in the bond length distribution. The first peak corresponds to the sp^2-like hybridised carbon atoms and the second one to the sp^3-like hybridised carbon atoms, leading to an overall increase of the average in-plane C-C bond length.

We compared different interface models for the ZLG structure. Care has to be taken when using smaller approximated interface structure to the experimentally observed $6\sqrt{3}$-ZLG interface. By comparing the ZLG structure with a $(6\sqrt{3} \times 6\sqrt{3})$ SiC supercell and a (13×13)-R2.2° C layer, we found that the specific bonding situation at the interface plays a crucial role in stabilising the SiC-graphene interface. The differences in strain and the detailed position of the Si-C bonds at the substrate/graphene interface, can for example misleadingly stabilise defects. We calculated the hexagon-pentagon-heptagon (H5,6,7) defect as suggested by Qi *et al.* [256] in the ZLG using the approximated $\sqrt{3}$-ZLG cell and the $6\sqrt{3}$-ZLG phase. We found that the defects calculated in the $\sqrt{3}$-ZLG would be energetically stable, the same defects calculated in the $6\sqrt{3}$-ZLG are energetically unfavourable.

To shed some light on the observed lattice contraction in MBE-grown nanocrystalline graphene, we derived reference values for the lattice parameter contraction expected from a possible substrate-induced corrugation. To evaluate the influence of domain boundaries, we calculated the C-C bond length of finite carbon flakes (hydrogen-saturated or unsaturated). However, both the corrugation and the domain boundary effects were too small to solely explain the observed lattice corrugation. Finally, we calculated the change of the average in-plane lattice parameter for graphene sheets with monovacancies, divacancies and Stone-Wales defects in periodic supercell arrangements. The calculations demonstrate that a lattice parameter contraction will arise from all defects except for the Stone-Wales defect. The largest contraction is associated with the divacancy, which also induces a significant buckling in free-standing graphene sheets. A low concentration of defects is thus one possible explanation for the observed contraction.

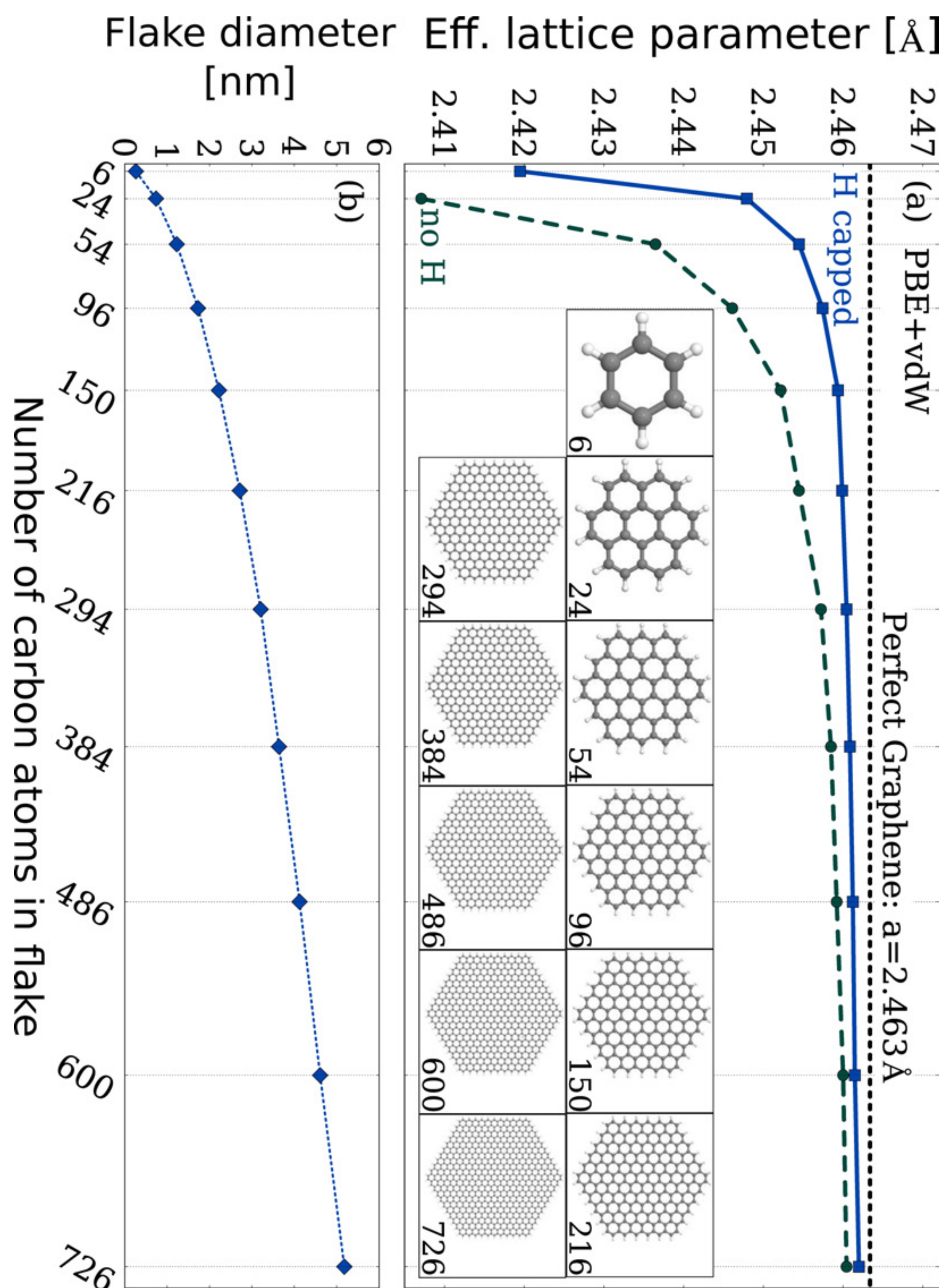

Figure 9.5.: (a) Calculated (PBE+vdW) effective lattice parameter (average C-C bond length) in a series of fully relaxed graphene flakes of finite size with (squares) and without (circles) hydrogen termination at the edges. The hydrogen terminated flakes are shown in the inset. The lattice parameter of a flat, strainfree, periodic graphene sheet calculated in PBE+vdW is indicated by a dashed line. (b) Diameter (maximum C-C distance) of the flakes used in (a). (Figure published in Ref. [284])

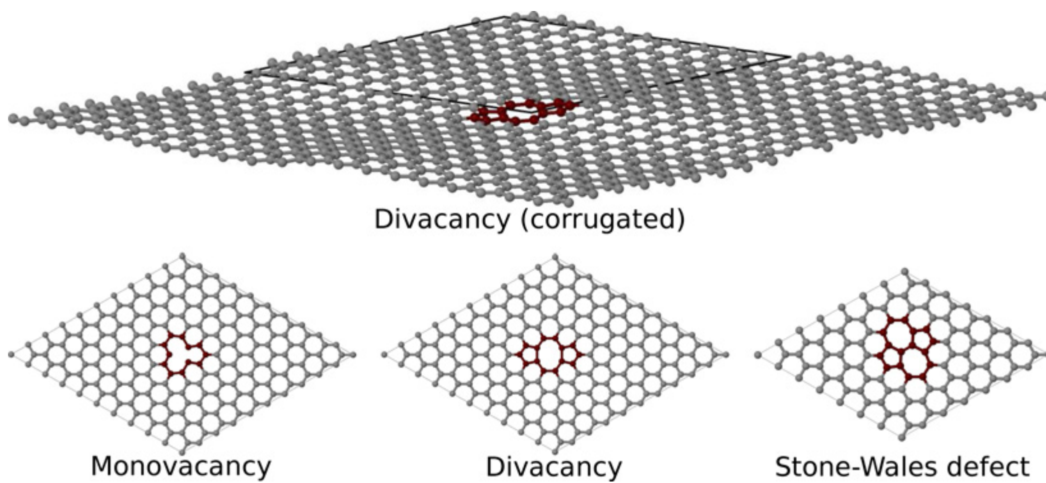

Figure 9.6.: Top: calculated fully relaxed (atomic postion and unit cell) structure of a graphene sheet with a (10×10) periodic arrangement of a 5-8-5 divacancy defects (atoms highlighted in red). The in-plane unit cell is marked by black lines. Bottom from left to right: fully relaxed monovacancy and 5-8-5 divacancy defects in a (10×10) unit cell and Stone-Wales defect in a (7×7) unit cell.

10 Thermodynamic Equilibrium Conditions of Graphene Films on SiC

In Chapter 8, we introduced the Si-rich $(\sqrt{3} \times \sqrt{3})$-R30° and (3×3) reconstructions (Sec. 8.1) and the C-rich phases ZLG, MLG and BLG (Sec. 8.2). In this chapter, we will examine the thermodynamic phase stability of these different phases using the *ab initio* atomistic thermodynamics formalism as presented in Ch. 4. The results presented in this chapter were published in 2014 Nemec *et al.* [227].

The surface energies (γ from Eq. 4.9) of the known surface phases of SiC (Si face) are shown as a function of $\Delta\mu_C = \mu_C - E_C^{bulk}$ in Fig. 10.1a for PBE+vdW. In the surface diagram in Fig. 10.1a, we included seven different surface reconstructions:

(1×1) SiC-(1×1) calculated in a SiC-$(\sqrt{3} \times \sqrt{3})$-R30° cell (see Fig. 8.1)

$(\sqrt{3} \times \sqrt{3})$ SiC-$(\sqrt{3} \times \sqrt{3})$-R30° & Si adatom (see Sec. 8.1.1)

(3×3) SiC-(3×3) & 9 atomic Si ad-layer and 4 atomic Si ad-cluster (see Sec. 8.1.2)

(ZLG) SiC-$(6\sqrt{3} \times 6\sqrt{3})$-R30° & 1 (13×13) C layer (see Sec. 8.2)

(MLG) SiC-$(6\sqrt{3} \times 6\sqrt{3})$-R30° & 2 AB-stacked (13×13) C layer (see Sec. 8.2)

(BLG) SiC-$(6\sqrt{3} \times 6\sqrt{3})$-R30° & 3 ABA-stacked (13×13) C layer (see Sec. 8.2)

(3LG) SiC-$(6\sqrt{3} \times 6\sqrt{3})$-R30° & 4 ABAB-stacked (13×13) C layer

The most stable phase for a given value of $\Delta\mu_C$ is that with the lowest surface energy. Going through Fig. 10.1a from left to right, we first find the expected broad stability range of the very Si-rich (3×3) reconstruction (13 atomic Si surface structure, see Sec. 8.1.2), followed by the $(\sqrt{3} \times \sqrt{3})$-R30° Si adatom structure (see Sec. 8.1.1). In the C-rich regime, just before the C-rich limit (bulk graphite) is reached, the C-rich phases stabilise. First the ZLG crosses the $(\sqrt{3} \times \sqrt{3})$ reconstruction and then the MLG, and even for a very narrow stability range the BLG phase. The 3LG crosses the BLG within

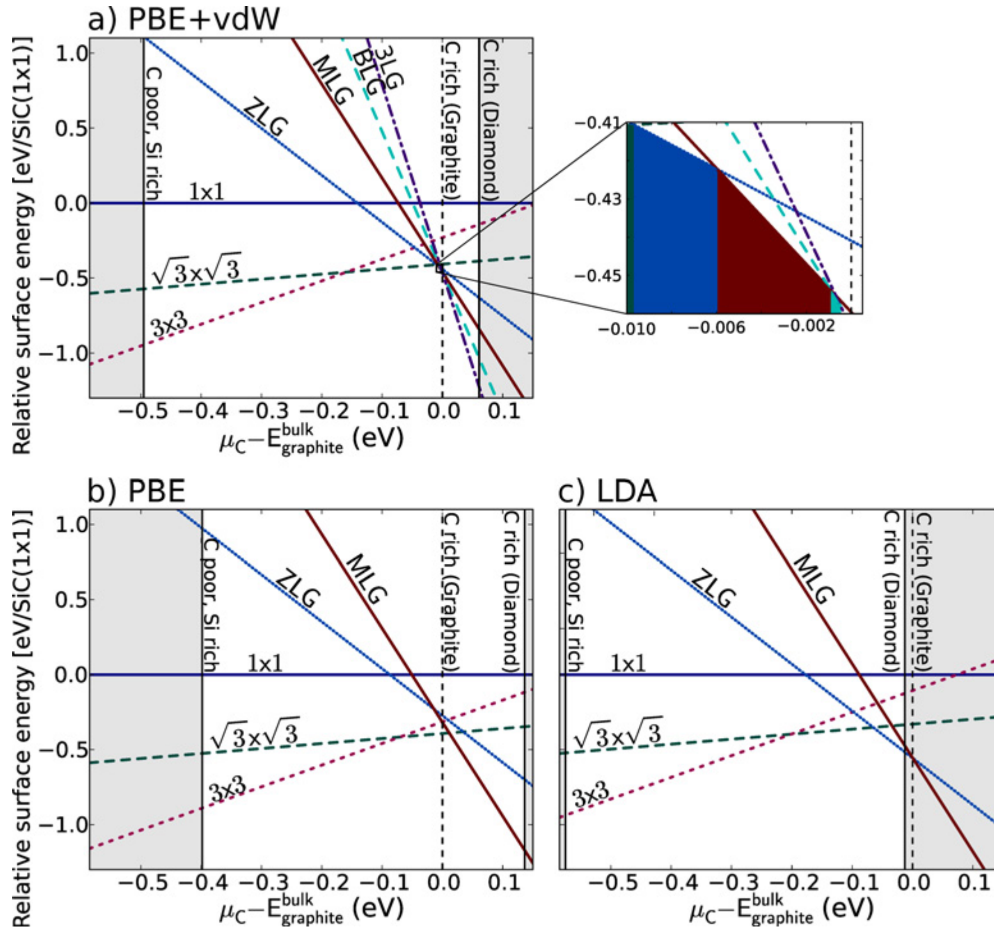

Figure 10.1.: Comparison of the surface energies for five different reconstructions of the 3C-SiC(111) Si side, relative to the bulk-terminated (1×1) phase (always unstable), as a function of the C chemical potential within the allowed ranges (given by diamond Si, diamond C or graphite C, respectively). (a) PBE+vdW, (b) PBE,(c) LDA. The shaded areas indicate chemical potential values outside the strict thermodynamic stability limits of Eq. 4.15. (Data published in Ref. Nemec *et al.* [227])

1 meV of bulk graphite. The respective stability ranges of the C chemical potential are very narrow for the different C-rich phases are small (inset of Fig. 10.1a: 4 meV, 5 meV and $<$1 meV for ZLG, MLG and BLG, respectively at the chemical potential axis). As pointed out in Sec. 4.2 narrow chemical potential ranges do not necessarily correspond to narrow experimental conditions.

The differences in γ between the C-rich phases are also rather small (a few tens of meV per (1×1) SiC surface unit cell), which necessitates the calculation of highly accurate total energies. We ensured the convergence with respect to the basis set size, the sampling in real and reciprocal space and the number of SiC-bilayers included to represent the substrate (see

Appendix B).

As already discussed in Ch. 4, one can further include the much smaller (p, T) dependence of the solid phases by focusing on Gibbs free energies $G(T, p)$ (see Eq. 4.1) in the QHA instead of E to e.g. capture small temperature-dependent surface strain effects. However, quantifying this T dependence precisely would necessitate accurate phonon calculations for structure sizes of the order of ~2,000 atoms, a task that is computationally prohibitive at present. ZPC are small for the bulk phases (see Tab. 7.2). However, there is the possibility of small contributions of finite T for the surface phases [266]. We keep them in mind when interpreting our calculated results below.

The primary approximations that we cannot systematically improve in our calculations originate from the exchange-correlation functional used. Standard approximations to the exchange-correlation functionals cannot capture correlation effects [14] rendering all discussed surface phases metallic. However, in experiment a small band gap of approximately 300 meV was observed in scanning tunnelling spectroscopy (STS) measurements of the ZLG layer [270, 109]. A more advanced treatment might suppress the metallicity, shifting the surface energetics towards lower energies, most likely maintaining the relative energy differences between the graphene phases while the crossing point between the Si adatom phase and the ZLG phase could change.

We evaluated the influence of different density functionals for the related bulk phases in Part. II. In Figures 10.1 b & c), we show how the surface energies would be affected by different density-functional treatments. We have thus recomputed the surface phase diagram up to the MLG phase for the PBE and LDA functionals.

The results for the plain PBE functional, which lacks long-range vdW interactions are shown in Fig. 10.1 b). In Chapter 6.2 and Sec. 8.2, we already discussed the importance of the inclusion of long-range vdW interactions and demonstarted that plain PBE fails to describe the interplanar bonding between the graphene layers. As expected, the absence of vdW tails in the plain PBE functional changes the phase diagram drastically. Due to the overstabilisation of graphite (130 meV/atom Sec. 6.1), its stability line moves significantly further to the left, as does the crossover point between ZLG and MLG. As a result, *neither* ZLG nor MLG become stable over the competing Si-rich $(\sqrt{3} \times \sqrt{3})$-R30° phase in PBE, in outright contradiction to experiment [329].

In the LDA-derived phase diagram shown in Fig. 10.1 c), the most significant change compared to PBE+vdW is the apparent incorrect stability hierarchy of graphite vs. diamond (see Ch. 6 and Appendix A). If we focus on the graphite line, we find that the ZLG-MLG crossover point is almost exactly on that line. In LDA, the net interlayer bonding between the first graphene layer and the ZLG phase is thus the same as that in bulk graphite. As a result, the ZLG phase in LDA has a broader stability range than in PBE+vdW. The MLG phase would only be a (very) near-equilibrium phase in LDA. Still, even taking LDA at face value implies the existence of T-p conditions very close to equilibrium for MLG, making the experimental search for such conditions promising. The key message of Fig. 10.1 is thus that equilibrium or near-equilibrium chemical potential ranges for ZLG, MLG, and even BLG, corresponding to specific T/p conditions in experiment exist.

The actual growth process proceeds by Si out-diffusion from underneath already formed graphene planes. Yet, the external Si reservoir background pressure still matters in equilibrium: As long as the diffusion path to the outside remains open, so does the inward diffusion path, and near-equilibrium with the reservoir gas can be achieved. During intermediate stages of the formation of a new graphene plane [230], such diffusion paths must be available. This finding proves the potential for much better growth control for each phase than what could be expected if each phase were just a necessary (but not thermodynamically stable) kinetic intermediate. Achieving true *reversibility* for actual MLG may be hard, since the reverse growth process require to disassemble a fully formed graphene plane which is kinetically difficult [329, 124]. However, the active *forward* growth process from MLG to BLG under Si out-diffusion should still be limitable by appropriate T/p conditions. A macroscopically homogeneous surface very close to pure-phase MLG should thus be achievable in principle.

Next, we bring our results in the context of some specific growth-related observations. For epitaxial graphene growth in ultrahigh vacuum (UHV), the background pressures of Si and C are low and ill-defined leading to a coexistence phases with different number of graphene layer [82]. Emtsev *et al.* [82] achieved much more homogeneous graphene growth by introducing an argon atmosphere, although MLG/BLG phase areas still coexist. A uniform background partial pressure of Si, however, will not be strictly guaranteed. The observed thermodynamic ZLG stability and improved growth of MLG by controlling a disilane (Si_2H_8) reservoir [329] is fully consistent with our findings. The use of a confined cavity to control the Si flux away from the sample reportedly yields excellent wafer-size films [67]. Maintaining a controlled Si partial pressure at constant temperature is most likely the important step for large-scale growth of high quality graphene.

The bulk projected band structure is a very helpful tool to analyse surface systems built from only a few unit cells. However, when studying the interface between two materials with different lattice parameters, such as SiC and graphene, a coincidence structure has to be found. These resulting structures can easily become several hundreds of unit cells large. The corresponding Brillouin zone of the supercell (SCBZ) then becomes very small and the resulting band structure hard to interpret.

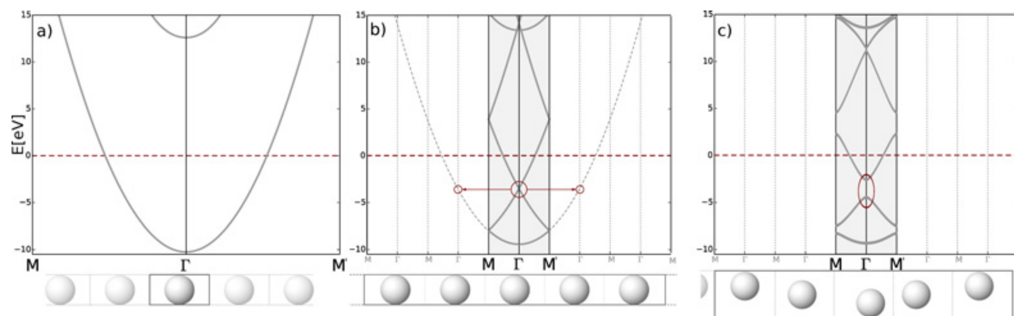

Figure 11.1.: a: Linear hydrogen chain with one hydrogen atom (H) in the unit cell and its band structure. b: supercell of the linear hydrogen chain with 5 times the one-atomic unit cell. The band structure is folded at the edges of the reduced Brillouin zone of the supercell. The band structure corresponding to the actual one-atomic unit cell is plotted with dashed lines. c: the hydrogen atoms in the 5 atomic chain are moved away from their periodic position. The corresponding band structure is perturbed, preventing the straight forward reversal of the band folding.

In Figure 11.1, we demonstrated how a *SC* influences the band structure using a linear hydrogen chain as an example. We assume a periodic one-dimensional chain of hydrogen atoms, shown in Fig. 11.1 a). The band structure for the one-atomic unit cell is plotted from the zone edge (M) to the Γ-point to the other M-point (M′). The bands of the linear hydrogen chain with one atom in the unit cell show the typical parabolic behaviour. Next, the hydrogen atom is repeated five times in a perfect chain. The supercell (*SC*) contains five hydrogen primitive cells (*PC*s) and the band structure is plotted in Fig. 11.1 b). The bands of the *SC* are folded at the zone edges of the smaller SCBZ. Comparing Fig. 11.1 a and b), it becomes apparent that the Brillouin zone of the supercell (SCBZ) is reduced to one-fifth compared to the Brillouin zone of the primitive cell (PCBZ). For example the band structure plot for the five-atomic hydrogen chain *SC* (Fig. 11.1 b) shows six states at the Γ-point with two occupied states crossing at the Γ-point of the PCBZ(circled in red). A comparison of the band structure of the one-atomic and the perfectly periodic five-atomic hydrogen chain (Fig. 11.1 a

and b), allows to lift the crossing by ordering the states of the folded *SC* band structure into the PCBZ as indicated by red circles in Fig. 11.1 b). In the extended PCBZ, it becomes clear that this crossing is an artifact of the zone folding, because the eigenvalue is actually located at the neighbouring PCBZ. In such a situation it is desirable to represent the band structure or spectral function of the *SC* in an extended BZ by exploiting the additional translational symmetry. In the third example, the atoms in the five-atomic chain are moved away from their periodic position (see Fig. 11.1 c). The band crossing at the Γ-point of the SCBZ (circeled in red) is lifted, preventing the straight forward reversal of the folding operation. Although, the band structure of the perturbed hydrogen chain shows a close resemblance with the unperturbed one, it is unclear how to unfold the band structure into the PCBZ of the one-atomic hydrogen chain. In the following, we present a way to unfold the band structure of a supercell into that of a chosen unit cell.

Many different approaches have been proposed to map the band structure of a *SC* onto a different unit cell and have been implemented in a range of electronic structure codes [189, 37, 36, 176, 253, 254, 4, 187, 84, 147, 3].

For the band structure of a periodically repeated primitive cell spanning a perfect supercell, exact methods based on the Bloch's theorem [31] exist to map the eigenstates from a *SC* calculation onto a unit cell. For example, in the tight-binding community an exact method has been proposed for unfolding the band structure of a perfect *SC* into bulk dispersion curves [37] with an extension to imperfect *SC*s [36] or to imaginary bands [3].

Facing the challenge of investigating the electronic band structure of alloys, Popescu and Zunger developed an unfolding method within the plane-wave DFT framework [253, 254]. To unfold the spectral function of functionalised carbon nanotubes [189] or bulk structures with impurities [176], the spectral function is represented in Wannier functions. Farjam adapted the unfolding formalism from Lee *et al.* [189] for the density-fuctional-based tight-binding scheme to visualise the influence of point defects on the electronic structure of graphene [84]. Allen *et al.* [4] and Huang *et al.* [147] presented the unfolding formalism in a mathematical generalised notation and applied it to tight-binding band structures and phonon dispersions.

Lee *et al.* [187] unfolded the band structure using a basis of linear combination of atomic orbitals (LCAO). It was developed independently of the unfolding routine presented in this work. There is one major conceptual difference between the unfolding formalism from Lee *et al.* [187] and this work: The formalism presented by Lee *et al.* [187] (as well as the work by

Ku *et al.* [176]) is built upon the concept of a connection between the *SC* and a *conceptual normal cell*. In the case of a perfectly periodic *SC* the conceptual normal cell is identical to the *PC*. The relationship between the conceptual normal cell and *SC* coordinates is given by what Ku *et al.* refer to as "the map". This "map" consists of two pieces of information: First, a (3×3) integer matrix, the so-called $\mathcal{N}$, which expresses the *SC* lattice vectors in terms of the *PC* lattice vectors. Second, a list of *SC* orbitals and their corresponding *PC* lattice vectors and conceptual normal cell orbitals. In a perfectly periodic *SC* the assignment of *SC* orbitals to their corresponding *PC* lattice vectors is trivial. However, as soon as the periodicity in the *SC* is broken for example by a defect, substitution, structural distortion or an interface the identification of such a conceptual normal cell is not clear and their is no unique mapping. As this "map" plays a fundamental role in their algorithm, the unfolded band structure depends on the chosen conceptual normal cell.

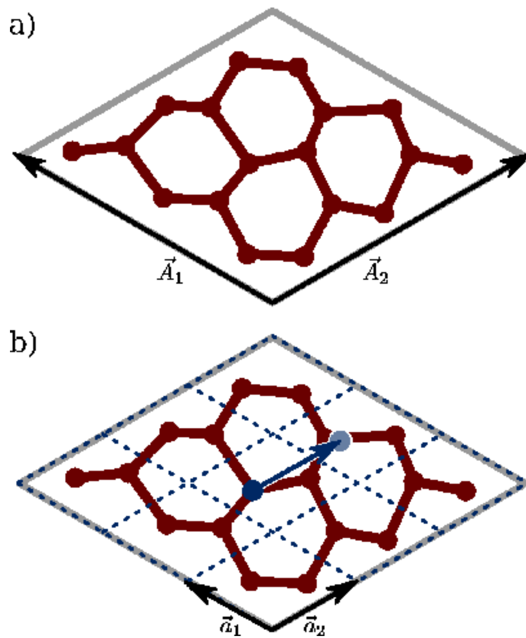

Figure 11.2.: a) shows 18 atoms arranged in a perturbed hexagonal lattice, the unit cell and the lattice vectors $\mathbf{A}_1$ and $\mathbf{A}_2$. b): the structure from a) is presented as a (3×3) supercell. The nine primitive unit cells are indicated by blue lines and the primitive lattice vectors $\mathbf{a}_1$ and $\mathbf{a}_2$ by black arrows. The blue atom in the central unit cell can be shifted to its periodic image by a lattice vector translation.

In this work we exploit Bloch's theorem to unveil hidden translational symmetries in a *SC* calculation by specifying an arbitrary supercell matrix ($\mathcal{N}$). The formalism does not require the knowledge of any symmetry in the system. Before, we introduce the formal unfolding formalism, we discuss the basic underlying idea.

Any wave function can be unfolded by projecting onto a system with shorter real space translation vectors corresponding to a higher translational symmetry. For any projection, we can determine the unfolding spectral weight. The unfolding spectral weight gives the probability of a state p to exist at $\mathbf{K}$ and takes a value between 0 and 1. For the spectral weight, we can distinguish three different cases. First, the assumed translational symmetry corresponds exactly to the periodicity of the wave function. Then the spectral weight will be one for one point

in the BZ (see example Fig. 11.1 b). Second, the wave function does not resembles the assumed translational symmetry. Then, the resulting projection will be noisy and no point in the BZ accentuated. The third case is the range in between. Here, the wave function is approximately periodic and the spectral weight will be close to 1 or close to 0.

Figure 11.2 a) shows 18 atoms forming a perturbed hexagonal lattice. The lattice in Fig. 11.2 a) can also be seen as a 3×3 *SC* with 2 atoms in the *PC*, shown in Fig. 11.2 b). The *SC* is spanned by the unit cell vectors $\mathbf{A}_1$ and $\mathbf{A}_2$. In the example sketched in Fig. 11.2, the supercell matrix ($\mathcal{N}$) is a 2×2 matrix with the diagonal elements equal 3. In FHI-aims the wave function of the system is expanded into numeric atom-centered orbitals (NAOs). A set of NAOs is localised on every atom (see Sec. 2.5). We can use Bloch's theorem to define an operator that projects out all the contributions of the wave function corresponding to the translational symmetry given by $\mathcal{N}$. Apart from the information available from the full system in Fig. 11.2 a) the only additional requirement is the translation operator (marked in blue in Fig. 11.2 b) defined by $\mathcal{N}$. The projector then translates a basis element localised at an atom in the *SC* by the translation vector (e.g. $\mathbf{a}_2$ indicated by an arrow in Fig. 11.2 b). To determine the projection weight in one k-point the basis element has to be translated to every *PC* determined by $\mathcal{N}$.

11.1. The Brillouin Zone (BZ)

Just for the moment, we assume a perfect *SC* built from N_C *PC*s and determine the connection between the *PC* and the *SC* lattice of the same crystal in real and reciprocal space.

We consider a bulk crystal with a primitive cell (*PC*) described by real space lattice vectors $\mathbf{a}_i$, where the integer i denotes the spatial direction. The corresponding unit cell in reciprocal space is shown in Fig. 11.3. The BZ of the conventional unit cell contains a mesh of k-points (shaded in grey and the k-points are shown in purple) and is spanned by the reciprocal lattice vectors $\mathbf{b}_j$. The real space lattice vectors and the reciprocal lattice vectors are connected by the relation

$$\mathbf{a}_i \cdot \mathbf{b}_j = 2\pi\delta_{ij}. \tag{11.1}$$

The *SC* lattice vectors are generated by integer multiples of the primitive

lattice vectors $\mathbf{a}_i$.

$$\mathbf{A}_i = \sum_j \mathcal{N}_{ij}\mathbf{a}_j, \tag{11.2}$$

where $\mathcal{N}_{ij}$ are the integer entries of the invertible, (3×3) supercell matrix $(\mathcal{N})$. The inverse of $\mathcal{N}$ is calculated using integer vector and matrix operations only. Using the transposed inverse of the supercell matrix $(\mathcal{N}^{-1})^T$, the reciprocal lattice vectors can be obtained by

$$\mathbf{B}_j = \sum_i \mathcal{N}_{ji}^{-1}\mathbf{b}_i. \tag{11.3}$$

The $\mathbf{B}_j$ span the BZ of the *SC* (indicated in blue in Fig. 11.3).

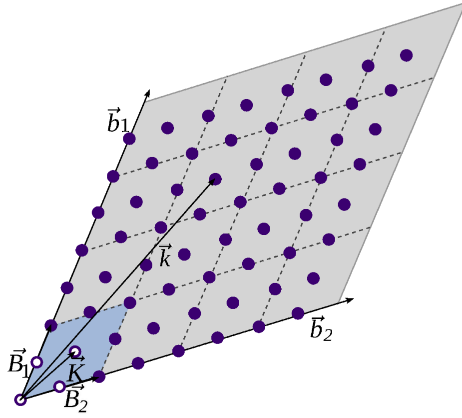

Figure 11.3.: Sketch of a 2-dimensional unit cell in reciprocal space: The grey area indicates the first BZ with the reciprocal lattice vectors $\mathbf{b}_i$ of the conventional unit cell (in this example 64 k-points ($\mathbf{k}$) (purple points)) and the SCBZ of a 4×4 supercell with lattice vectors $\mathbf{B}_i$ and four k-points ($\mathbf{K}$) (white points).

All calculation in the BZ are evaluated on a grid of k-points defined by M_j: The BZ of the *SC* contains M_j k-points in the direction of the reciprocal lattice vector $\mathbf{B}_j$ (shown as white points in Fig. 11.3). This gives $N_k = \prod_j M_j$ k-points in total. The K-vector pointing to one of these points is

$$\mathbf{K} = \sum_{j=1} \frac{m_j}{M_j}\mathbf{B}_j, \tag{11.4}$$

where the integer $m_j = 0, \ldots, M_j - 1$ is the index of the k-point along the direction j. On the other hand, the reciprocal representation of the *SC* is periodically repeated. A K-vector in one BZ is connected to the same point in a periodic repetition by a reciprocal lattice vector

$$\mathbf{G}_n = \sum_{j=1}^{3} n_j\mathbf{B}_j. \tag{11.5}$$

Within the PCBZ, there are N_C different reciprocal lattice vector $\mathbf{G}_n$. Any k-point in the PCBZ can be uniquely written as a sum of a SCBZ vector $\mathbf{K}$ and lattice vector $\mathbf{G}_n$

$$\mathbf{K} + \mathbf{G}_n = \sum_{j=1}^{3} \frac{m_j\mathbf{B}_j}{M_j} + n_j\mathbf{B}_j = \sum_{ij}^{3} \frac{m_j + M_j n_j}{M_j}\mathcal{N}_{ji}^{-1}\mathbf{b}_i = \mathbf{k}. \tag{11.6}$$

For any $\mathbf{k}$, a vector of integers ($p_j = m_j + M_j n_j$) can be found to express $\mathbf{k}$ in terms of reciprocal lattice vectors $\mathbf{b}$. [1]

From these basic considerations, we can draw some helpful conclusions: The folded SCBZ can be repeated to span the unfolded PCBZ corresponding to the primitive unit cell. Therefore, every $\mathbf{K}$ in the folded SCBZ has a copy in all periodically repeated PCBZ. With Eq. 11.6 each $\mathbf{k}$ in the unfolded PCBZ can be determined by an integer operation in terms of the reciprocal lattice vectors $\mathbf{B}$. This facilitates a numerically accurate and easy assignment of the k-path in the unfolded BZ.

11.1.1. The Wave Function

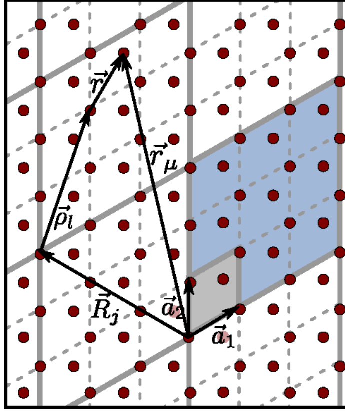

Figure 11.4.: The real-space *SC* containing 3×3 *PC* is shaded in blue. The lattice vector $\mathbf{R}_j$ points to a periodic copy of the *SC*. The *PC* with lattice vectors $\mathbf{a}_{1,2}$ is shaded in grey. The lattice vector ρ_l points to a periodic copy of the *PC*. Each *PC* contains two atoms (red circle) with atomic position $\mathbf{r}_\mu$.

Before we introduce the actual unfolding routine, we include some notational preliminaries:

First, we introduce the wave function of the supercell (shaded in blue in Fig. 11.4). The wave function (eigenvector) $\phi^{\mathbf{K}p}$ of the eigenstate with band index (p) at SCBZ K-point ($\mathbf{K}$) with energy $\varepsilon^{\mathbf{K}p}$ of a *SC* calculation is a Bloch function

$$\begin{aligned}\phi^{\mathbf{K}p}(\mathbf{r}+\mathbf{R}) &= \langle \mathbf{r}+\mathbf{R}|\phi^{p}(\mathbf{K})\rangle \\ &= e^{i\mathbf{K}\cdot\mathbf{R}}\phi^{\mathbf{K}p}(\mathbf{r})\end{aligned} \tag{11.7}$$

for any *SC* lattice vector $\mathbf{R} = \sum_{i=1} n_i \mathbf{A}_i$. The eigenvector $|\phi^p(\mathbf{K})\rangle$ can be expanded in atomic basis functions

$$|\phi^p(\mathbf{K})\rangle = \sum_{\mu}^{N_{\text{basis}}} C_\mu^p(\mathbf{K})|\mathbf{K},\mu\rangle \tag{11.8}$$

where μ is the index of an orbital in the *SC* and N_{basis} the total number of basis functions. $|\mathbf{K},\mu\rangle$ is the basis function in reciprocal space with

$$|\mathbf{K},\mu\rangle = \frac{1}{\sqrt{N_S}}\sum_{j}^{N_S} e^{i\mathbf{K}\cdot\mathbf{R}_j}|\mathbf{R}_j,\mu\rangle, \tag{11.9}$$

[1] For example, applying Eq. 11.6 to the BZ shown in Fig. 11.3 the wave vector $\mathbf{K}$ becomes $\mathbf{K} = \frac{1}{2}\mathbf{B}_1 + \frac{1}{2}\mathbf{B}_2$ and $\mathbf{k} = \frac{6}{2\cdot 4}\mathbf{b}_1 + \frac{4}{2\cdot 4}\mathbf{b}_2$.

where N_S is the number of SCs included in the crystal, $\mathbf{R}_j$ is the lattice vector pointing to the jth periodic copy of the SC and $|\mathbf{R}_j, \mu\rangle$ are the atomic basis functions in real space (Eq. 2.27) in cell j and orbital μ.

11.2. The Unfolding Projector

Unfolding the states $|\phi^p(\mathbf{K})\rangle$ in Eq. 11.8 into the PCBZ corresponds to a projection onto Bloch states of higher periodicity given by the supercell matrix ($\mathcal{N}$). We can thus project the component of a SC eigenvector at $\mathbf{K}$ into the nth reciprocal PC given by the reciprocal lattice vector $\mathbf{G}_n$ (Eq. 11.5) by a projector $P_n(\mathbf{K})$. This projection measures how close a state is to a Bloch state with higher periodicity. To express an unfolding projector, we require a basis of the same periodicity defined by $\mathcal{N}$. In general the SC is not an exact copy of N_C PCs and the wave function Eq. 11.8 does not necessarily have the required periodicity. We extend the basis $|\mathbf{K}, \mu\rangle$ by adding periodic copies of each basis function with

$$\hat{T}(\rho_l)|\mathbf{K}, \mu\rangle =: |\mathbf{K}, \mu, l\rangle, \tag{11.10}$$

where $\hat{T}(\rho_l)$ is a translation operator that translates the basis function $|\mathbf{K}, \mu\rangle$ into the lth PC by the lattice vector $\rho_l = \sum_i n_i \mathbf{a}_i$.

The unfolding projector $P_n(\mathbf{K})$ has to fulfil three constraints:

1. $P_n(\mathbf{K})$ has to be invariant under PC lattice translations – $P_n(\mathbf{K})$ is a **periodic** operator.

2. once the projector acted on a state any additional application must not change the result beyond the initial application – $P_n(\mathbf{K})$ is an **idempotent** operator.

3. in a perfectly periodic SC, $P_n(\mathbf{K})$ projects a state fully in one reciprocal unit cell $\mathbf{G}_n$ only. Any state with any Bloch symmetry has a unique decomposition into N_C functions of higher PC translational symmetry. This has to be true for any arbitrary division in subcells that span the SC by lattice vector translations. The sum of $P_n(\mathbf{K})$ over all possible N_C SCBZ is one – $P_n(\mathbf{K})$ **sums to one**.

Definition 11.2.1. *The unfolding projector $P_n(\mathbf{K})$ is defined by:*

$$P_n(\mathbf{K})|\mathbf{K},\mu\rangle := \frac{1}{N_C}\sum_{l}^{N_C} e^{-i\mathbf{G}_n\cdot\rho_l}|\mathbf{K},\mu,l\rangle$$

a. Periodicity

$$P_n(\mathbf{K})|\mathbf{K},\mu,l\rangle = e^{i\mathbf{G}_n\cdot\rho_l}P_n(\mathbf{K})|\mathbf{K},\mu\rangle$$

where ρ_l is a PC lattice vector (see Fig. 11.4).

b. Idempotency

$$P_n(\mathbf{K})^2 = P_n(\mathbf{K})$$

c. Sum-to-one

$$\sum_n P_n(\mathbf{K}) = 1$$

In the following, we show that the unfolding projector defined by Def. 11.2.1 satisfies the three conditions.

a. Periodicity $P_n(\mathbf{K})|\mathbf{K},\mu,l\rangle = e^{i\mathbf{G}_n\cdot\rho_l}P_n(\mathbf{K})|\mathbf{K},\mu\rangle$

$$e^{i\mathbf{G}_n\cdot\rho_{l'}}P_n(\mathbf{K})|\mathbf{K},\mu\rangle = \frac{1}{N_C}\sum_{l}^{N_C} e^{i\mathbf{G}_n\cdot(\rho_{l'}-\rho_l)}|\mathbf{K},\mu,l\rangle$$

By construction $|\mathbf{K},\mu,l\rangle$ is a Bloch function, so that

$$e^{i\mathbf{G}_n\cdot\rho_{l'}}|\mathbf{K},\mu,l\rangle = |\mathbf{K},\mu,l+l'\rangle,$$

where $\rho_{l'}$ and ρ_l are both lattice vectors, so that the sum of both is again a lattice vector. Inserting it into the Eq. 11.2 gives

$$\frac{1}{N_C}\sum_{l}^{N_C} e^{-i\mathbf{G}_n\cdot\rho_l}|\mathbf{K},\mu,l+l'\rangle = P_n(\mathbf{K})|\mathbf{K},\mu,l'\rangle$$

b. Idempotency $P_n(\mathbf{K})^2 = P_n(\mathbf{K})$

$$P_n(\mathbf{K})P_n(\mathbf{K})|\mathbf{K},\mu\rangle = \frac{1}{N_C}\sum_{l}^{N_C} e^{-i\mathbf{G}_n\cdot\rho_l} P_n(\mathbf{K})|\mathbf{K},\mu,l\rangle$$

Inserting Eq. 11.2.1 for $P_n(\mathbf{K})$

$$= \frac{1}{N_C^2}\sum_{l,l'}^{N_C} e^{-i\mathbf{G}_n\cdot(\rho_l+\rho_{l'})}|\mathbf{K},\mu,l'\rangle$$

$$= \frac{1}{N_C^2}\sum_{l'}^{N_C} N_C e^{-i\mathbf{G}_n\cdot\rho_{l'}}|\mathbf{K},\mu,l'\rangle$$

Wich is the definition of $P_n(\mathbf{K})$ (Def. 11.2.1)

$$= P_n(\mathbf{K})|\mathbf{K},\mu\rangle.$$

c. Sum-to-one $\sum_n^{N_C} P_n(\mathbf{K}) = 1$

$$\sum_{n}^{N_C} P_n(\mathbf{K})|\mathbf{K},\mu\rangle = \frac{1}{N_C}\sum_{l}^{N_C}\sum_{n}^{N_C} e^{-i\mathbf{G}_n\cdot\rho_l}|\mathbf{K},l,\mu\rangle$$

applying the basic rules of Fourier transformation to the sum over n phase factors

$$= \frac{1}{N_C}\sum_{l}^{N_C} N_C\delta_{l,0}|\mathbf{K},l,\mu\rangle$$

$$= |\mathbf{K},\mu\rangle.$$

Here Eq. 11.10 was used for $l = 0$

$$|\mathbf{K},l=0,\mu\rangle = \hat{T}(\rho_{l=0})|\mathbf{K},\mu\rangle = |\mathbf{K},\mu\rangle.$$

The unfolding projector defined by Def. 11.2.1 satisfies the conditions *a*-*c*. Therefore it can be used to uniquely determine the spectral weight in the PCBZ.

As a final step the projector $P_n(\mathbf{K})$ is applied to the eigenvector $|\phi^p(\mathbf{K}\rangle$ to calculate the unfolded spectral weight $w_n^{\mathbf{K}p}$ of the state p in the PCBZ n at $\mathbf{K}$.

$$w_n^{\mathbf{K}p} = \langle\phi^p(\mathbf{K})|P_n(\mathbf{K})|\phi^p(\mathbf{K})\rangle \tag{11.11}$$

Inserting Eq. 11.8 for the SC eigenvector $|\phi^p(\mathbf{K})\rangle$ gives

$$\begin{aligned} w_n^{\mathbf{K}p} &= \sum_{\mu,\mu'}^{N_{\text{basis}}} \langle \mathbf{K}, \mu' | C_{\mu'}^{*p}(\mathbf{K}) P_n(\mathbf{K}) C_{\mu}^{p}(\mathbf{K}) | \mathbf{K}, \mu \rangle \\ &= \frac{1}{N_C} \sum_{l}^{N_C} \sum_{\mu,\mu'}^{N_{\text{basis}}} C_{\mu'}^{*p}(\mathbf{K}) C_{\mu}^{p}(\mathbf{K}) e^{-i\mathbf{G}_n \cdot \rho_l} \langle \mathbf{K}, \mu' | \mathbf{K}, \mu, l \rangle \end{aligned} \tag{11.12}$$

In an orthonormal basis, the object $\langle \mathbf{K}, \mu' | \mathbf{K}, \mu, l \rangle$ would be a unity matrix $\delta_{\mu',\mu l}$ and the work would be done. However, a numeric atom-centered orbital-basis is non-orthogonal. Using Eq. 11.9 and Eq. 11.10 the matrix element $\langle \mathbf{K}, \mu' | \mathbf{K}, \mu, l \rangle$ becomes

$$\begin{aligned} \langle \mathbf{K}, \mu' | \mathbf{K}, \mu, l \rangle &= \frac{1}{N_S} \sum_{j,j'}^{N_S} e^{i\mathbf{K}(\mathbf{R}_{j'} - \mathbf{R}_j)} \langle \mathbf{R}_{j'} \mu' | \hat{T}(\rho_l) | \mathbf{R}_j \mu \rangle \\ &= [S(\mathbf{K})]_{\mu';\mu l}. \end{aligned} \tag{11.13}$$

$[S(\mathbf{K})]_{\mu';\mu l}$ is the overlap matrix element of the basis function μ' located in the SC j' and the basis function μ translated by a PC unit cell vector ρ_l. In an exactly PC-periodic system, the translation operator $\hat{T}(\rho_l)$ translates the basis function μ to an exact copy of μ. In that case, the $(N_{\text{basis}} \times N_{\text{basis}})$ overlap matrix used in the DFT calculation already contains all matrix elements $[S(\mathbf{K})]_{\mu';\mu l}$. The remaining task is to assign every μ to a primitive cell l. However, in the case of a perturbed system, for example due to structure relaxation or defects, $\hat{T}(\rho_l)$ translates an orbital μ to an empty site and the overlap matrix $[S(\mathbf{K})]$ is an $(N_{\text{basis}} \times N_C N_{\text{basis}})$ object. The missing matrix elements would have to be calculated. However in practice, we introduce the first approximation by setting the overlap

$$[S(\mathbf{K})]_{\mu;\mu' l'} \approx [S(\mathbf{K})]_{\mu;\mu'}, \tag{11.14}$$

where in the overlap matrix $[S(\mathbf{K})]_{\mu;\mu'}$, μ' can be assigned to a PC l'. This approximation allows us to use the overlap matrix as calculated in the FHI-aims-code. For two atoms far apart, the overlap is small and the change in the overlap matrix element due to changes in the atomic position should be minor. However, for neighbouring PC the overlap between basis functions can still be sizeable. Here, the approximation only holds for small changes in the geometry.

The unfolding spectral weight gives the probability of a state to exist at $\mathbf{K}$. The sum of all spectral weights of a state p over the SCBZ is

$$\sum_{n}^{N_c} w_n^{\mathbf{K}p} = 1. \tag{11.15}$$

The normalisation is ensured by the **sum-to-one** constraint of the unfolding projector and the Eigenvector norm

$$\sum_{\mu,\mu'}^{N_{\text{basis}}} C_{\mu}^{*p}(\mathbf{K})\,[S(\mathbf{K})]_{\mu;\mu'}\,C_{\mu'}^{p}(\mathbf{K}) = 1. \tag{11.16}$$

The unfolding formalism is exact and allows the mapping of any band structure onto a Brillouin zone. By defining a supercell matrix one imposes an underlying periodicity on the system. Only states corresponding to the periodicity defined by $\mathcal{N}$ will show a band dispersion in the extended Brillouin zone.

11.3. The Hydrogen Chain: Practical Aspects of the Band Structure Unfolding

In the following we discuss some practical details on the basis of a few examples shown in Fig. 11.5.

Example a: Figure 11.5a shows a perfectly periodic 10-atom hydrogen chain. In this example the band structure can be unfolded exactly. In the PCBZ the spectral weight, Eq. 11.12, is either zero or one.

Example b: Figure 11.5b shows a distorted geometry with broken translational symmetry. The overall shape of the band structure is very similar to that of example a, but close to the Γ point the effect of the distortion can be seen. In this example, the difference between an atom in the PC l at position ρ_l and an atom at position $\rho_{l'}$ in the l'th PC is not a lattice vector of the PC. The spectral weight reflects the strength of the symmetry breaking by reaching a value between zero and one. However, for very strong distorted geometry, where the displacement is at the order of a lattice translation the approximation to the overlap matrix Eq. 11.14 would break down. In this case, all overlap matrix elements $[S(\mathbf{K})]_{\mu;\mu'l'}$ would need to be calculated explicitly.

Example c: In this example the hydrogen chain is perfectly periodic except

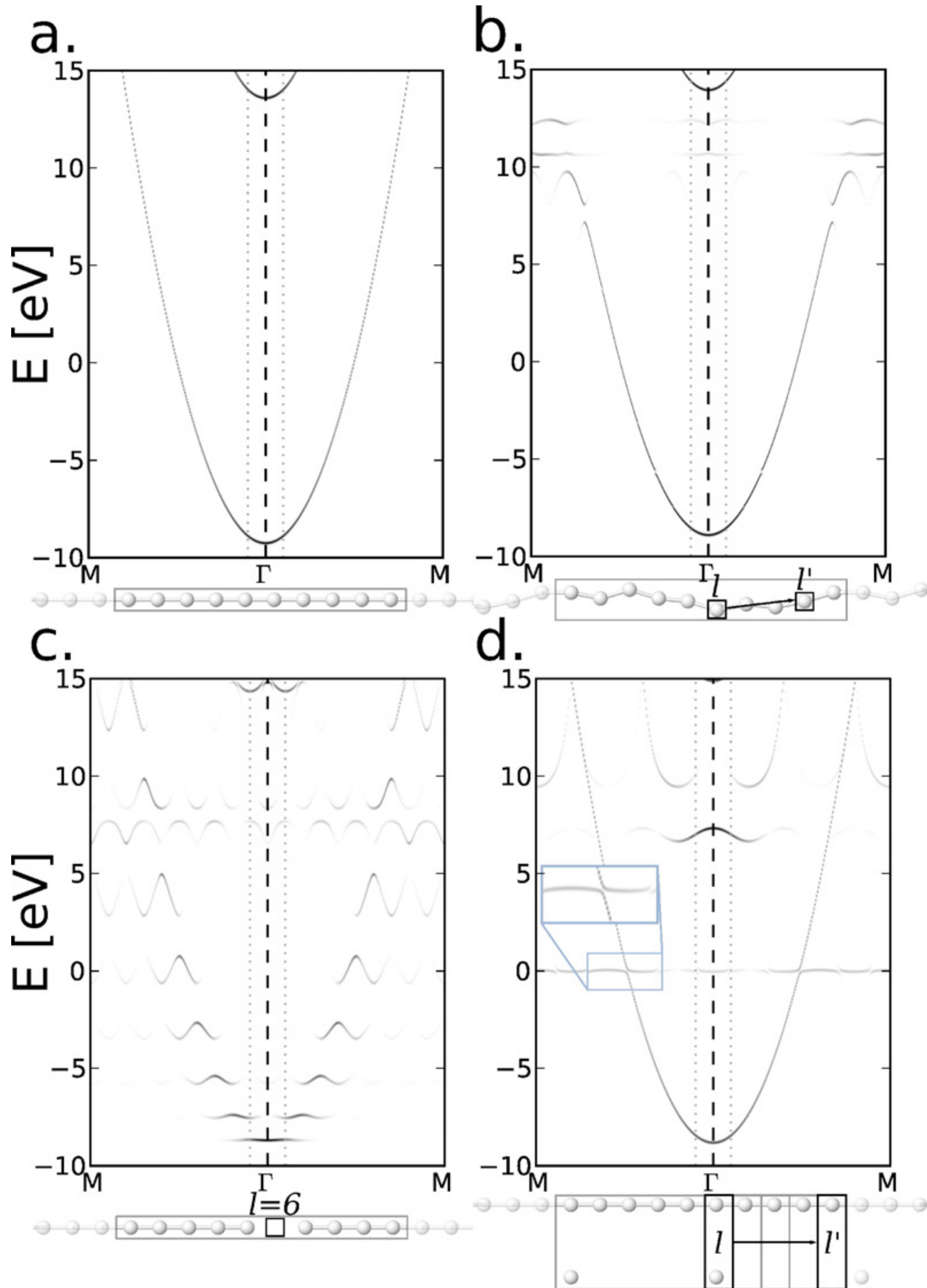

Figure 11.5.: The unfolded band structures of four different 10-atom hydrogen chains are plotted along the PCBZ path M to Γ to M. Dashed lines indicate the SCBZ. The corresponding atomic structure is shown at the bottom. a.: A perfectly periodic hydrogen chain, b.: a hydrogen chain with geometric distortions, c.: a defect in the PC $l = 6$ in an otherwise perfectly periodic chain and d.: two chains with different periodicity.

for one defect in the $PC\ l = 6$. Part of the original hydrogen band can still be observed, but the symmetry breaking is clearly seen in Fig. 11.5c by small gap openings. To evaluate Eq. 11.12, the overlap matrix of atom μ' in $PC\ l'$ and atom μ in $PC\ l = 6$ is required, but the overlap is not calculated within FHI-aims, because in the $PC\ l = 6$ contains no basis functions. This can be circumvent by introducing a ghost atom that consists of the same basis functions but without any mass or charge.

Example d: The system contains two hydrogen chains, a 10-atomic and a 2-atomic one separated by 2.5 Å. It is not clear how $\mathcal{N}$ should be chosen. We are interested in the effect of the additional chain on the 10-atomic hydrogen chain, therefore

$$\mathcal{N} = \begin{bmatrix} 10 & 0 & 0 \\ 0 & 1 & 0 \\ 0 & 0 & 1 \end{bmatrix}. \tag{11.17}$$

Figure 11.5d shows the unfolded band structure. The band originating from the 10-atomic hydrogen experiences a small gap opening at the Fermi level. The second 5-atomic chain is too far away for any chemical bonding between the chains, which is reflected by the almost undisturbed band, but introduces a periodic potential. Additional states appear in particular some very weak states at the Fermi level. What cannot conclusively be determined from the plot is which states originate from which chain. In this system we face a similar problem as in example c. We need to calculate the overlap of the two atoms in $PC\ l$ and l', as depicted in Fig. 11.5d. The $PC\ l'$ contains just one atom, as a consequence the overlap between the basis function in l and l' is not fully available. In this particular system, ghost atoms can again be used to unfold the combined system. However, in general the full $(N_{\text{basis}} \times N_C N_{\text{basis}})$ overlap matrix defined in Eq. 11.13 is required to unfold an interface system formed by two subsystems with different periodicities.

In summary, the unfolding procedure introduced in this section facilitates the unfolding of the band structure of an arbitrary system by imposing a translational symmetry. However, because of the overlap matrix $[S(\mathbf{K})]_{\mu';\mu l}$ Eq. 11.13 a first approximation was introduced, see Example 11.3b. For small displacements of atoms in the PC the changes of the respective overlap matrix element are smalss, such that the approximation holds. As shown in Example 11.3c there is a workaround by introducing mass- and chargeless basis functions at the position of "missing atoms". For interface systems this workaround is only applicable in a few special cases.

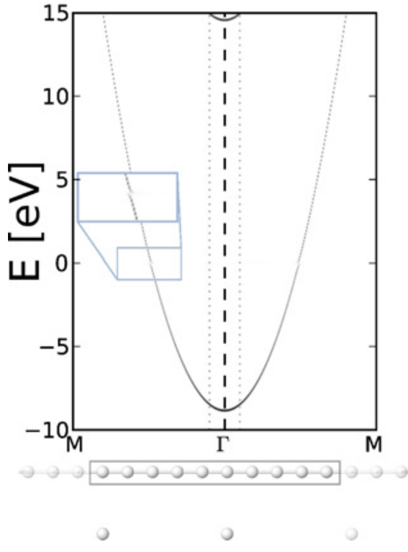

Figure 11.6.: The unfolded band structure of the two chain system introduced in Example 11.3d. The band structure is projected on the 10-atomic chain marked by a grey box.

For an interface system formed by two subsystems with different periodicities, we are generally interested in the band structure projected on the subsystem of interest. In a LCAO basis a straight forward projection is given by a Mulliken partitioning [222]. In Eq. 11.12 the sum over basis functions μ should than run over all basis functions μ_s located in the subsystem and not over all basis functions. In essence the projection splits the eigenvector C^p in two parts:

1. Eigenvector entries belonging to the subsytem $C^p_{\mu'_s}$
2. Eigenvector entries belonging to the rest $C^p_{\mu'_r}$

If the sum over basis functions in Eq. 11.16 is split into these two contributions

$$\sum_{\mu_s,\mu'_s}^{N^{\text{proj}}_{\text{basis}}} C^{*p}_{\mu_s}(\mathbf{K})\,[S(\mathbf{K})]_{\mu_s;\mu'_s}\,C^p_{\mu'_s}(\mathbf{K}) + \sum_{\mu_r,\mu'_r}^{N^{rest}_{\text{basis}}} C^{*p}_{\mu_r}(\mathbf{K})\,[S(\mathbf{K})]_{\mu_r;\mu'_r}\,C^p_{\mu'_r}(\mathbf{K}) \neq 1. \tag{11.18}$$

the eigenvector is no longer normalised, because the contribution from the off-diagonal blocks $C^{*p}_{\mu_s}\,[S]_{\mu_s;\mu_r}\,C^p_{\mu_r}$ and $C^{*p}_{\mu'_r}\,[S]_{\mu'_r;\mu'_s}\,C^p_{\mu'_s}$ is not included in the sum. As a result, the eigenvector norm in Eq. 11.16 has to be introduced

explicitly by a rescaling factor N^p_{sub} such that

$$\frac{1}{N^p_{\text{sub}}} \sum_{\mu_s,\mu'_s}^{N^{\text{proj}}_{\text{basis}}} C^{*p}_{\mu_s}(\mathbf{K}) \left[S(\mathbf{K})\right]_{\mu_s;\mu'_s} C^p_{\mu'_s}(\mathbf{K}) \equiv 1 \tag{11.19}$$

the weight normalisation (Eq. 11.15) is ensured. In analog to Eq. 11.19 a normalisation factor for the rest N^p_{rest} can be calculated. With

$$1 - (N^p_{\text{sub}} + N^p_{\text{rest}}) = J^p \tag{11.20}$$

we can then determine how strongly the subsystem and the rest are coupled for a state p. For a combined system in which the two subsystems are infinitely separated, the overlap matrix becomes a block matrix and the coupling coefficient $J^p = 0$. When interpreting J^p one has to keep in mind that J^p strongly depends on the chosen basis set used for the projection and there is no well defined upper limit of J^p in cases of strong coupling. However, it can be used to visualise general trends within one system.

In Figure 11.6 the band structure of the system introduced in Example 11.3d is shown. The two subsystems are well separated, the overlap matrix is close to a block matrix and the coupling coefficients are very small. For the band structure plotted in Fig. 11.6 the maximal coupling coefficient is $J^p = 0.038$ for the state $p = 5$ meV and the k-point at which the band touches the Fermi level. At this very point the projected band structure shows a very small gap opening at the Fermi level in an otherwise undisturbed band.

In Section 8.2, we discussed the atomic structure of epitaxial graphene, MLG and the interface, the ZLG, structure on the Si side of SiC. The atomic composition of theses two structures differ by the number of hexagonal carbon layers. We found that the ZLG consitsts of a mixture of sp^3 hybridised bonds to the substrate and in-plane sp^2-like bonds, while the MLG is a sp^2 bonded graphene layer. ARPES measurements Ref. [83] and DFT (LDA) calculations of the $(6\sqrt{3}\times6\sqrt{3})$-R30° commensurate supercell Ref. [166] showed qualitatively different electronic structure originating from the specific bonding situation of the top carbon layer.

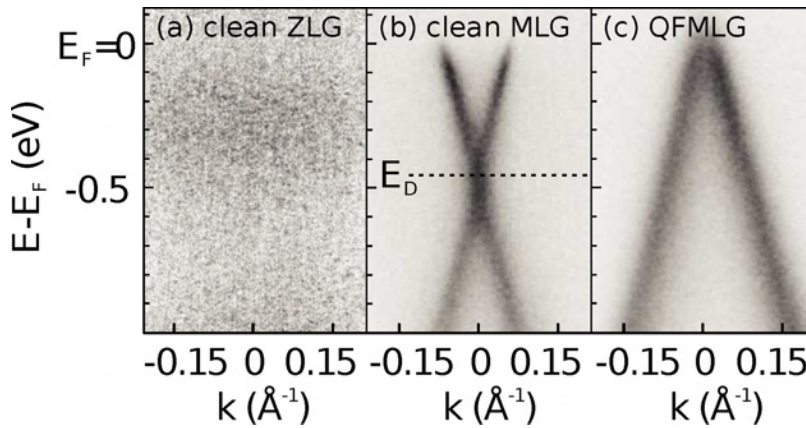

Figure 12.1.: Figure taken from Ref. [263]: Dispersion of the π-bands of graphene grown on 6H-SiC(0001) measured with ARPES perpendicular to the $\overline{\Gamma K}$-direction of the graphene Brillouin zone for (a) an as-grown ZLG (Ref. [263] Fig. 15 a); (b) an as-grown MLG (Ref. [263] Fig. 15 e); (c) after hydrogen intercalation (Ref. [263] Fig. 15 b).

Figure 12.1 (taken from Ref. [263]) shows the dispersion of the π-bands of ZLG, MLG and QFMLG grown on 6H-SiC(0001) measured with ARPES perpendicular to the $\overline{\Gamma K}$-direction of the graphene Brillouin zone. For the ZLG layer the characteristic graphene π and π^* states with their linear dispersion at the K-point in the BZ are not present (see Fig. 12.1 a) [214, 334, 263]. However, the in-plane σ bonds are already observed in ARPES [35, 81, 83]. Only with the MLG layer π and π^* band appear, Fig. 12.1 b) [83, 34, 263]. In epitaxial graphene the Dirac point is shifted under the Fermi level showing a n-type doping [83, 35, 238, 263]. When the ZLG surface is intercalated by hydrogen (H) QFMLG forms. QFMLG is undoped if grown on 3C-SiC (see Fig. 12.1 c) [96].

The origin of the doping and the effect of charge transfer is not yet fully understood. Improving the understanding of the SiC-graphene interface

and its influence on the electronic structure of MLG and few-layer graphene is the aim of this chapter.

In this chapter, we discuss the electronic structure of epitaxial graphene on the Si side of SiC. For calculating the electronic structure, we use the all-electron, localised basis code FHI-aims. For the approximation to the exchange-correlation functional, we use PBE and the hybrid functional HSE06 (ω =0.207Å^{-1}, α =0.25). The atomic structure was introduced in Ch. 8 (all structures were optimised using PBE+vdW).

12.1. The Electronic Structure of Epitaxial Graphene

First, we discuss the electronic structure of the competing C-rich surface phases introduced in Sec. 8.2 in the approximated ($\sqrt{3} \times \sqrt{3}$) 3C-SiC unit cell covered by a strained 2×2 graphene cell (see Tab. 9.1) [214, 215, 334, 335, 243]. There are three Si atoms in the top SiC layer of the 3C-SiC $\sqrt{3} \times \sqrt{3}$ unit cell; two of them are covalently bound to the 2×2 ZLG layer and one Si atom is right underneath the midpoint of a carbon hexagon of the ZLG layer. This structure closely resembles the configuration at the center of the experimentally observed ($6\sqrt{3}\times6\sqrt{3}$)-R30° commensurate supercell (see Fig. 8.4). In the following, we will refere to the C-rich phases in the ($\sqrt{3} \times \sqrt{3}$) unit cell using the abbreviated form, $\sqrt{3}$-ZLG, $\sqrt{3}$-MLG and $\sqrt{3}$-BLG.

In Section 7.2, we found that HSE06 improves the description of the cohesive properties of SiC polytypes, in specific the valence band width and band-gap, over PBE, so we used the hybrid functional HSE06 to calculate the electronic structure. A comparison between the HSE06 and PBE DOS of the $\sqrt{3}$-MLG structure can be found in Appendix F. For the bulk projected states the 3C-SiC unit cell was chosen such that the three SiC-bilayers are stacked along the z-axis. In the x-y-plane a $\sqrt{3} \times \sqrt{3}$ cell was chosen. For the bulk projected DOS the bulk states were multiplied by two to equal the six SiC bilayers in the slab calculation.

Figure 12.2 shows the calculated bulk projected band structure (see Sec. 5) and DOS of the $\sqrt{3}$-ZLG, $\sqrt{3}$-MLG and $\sqrt{3}$-BLG phases.

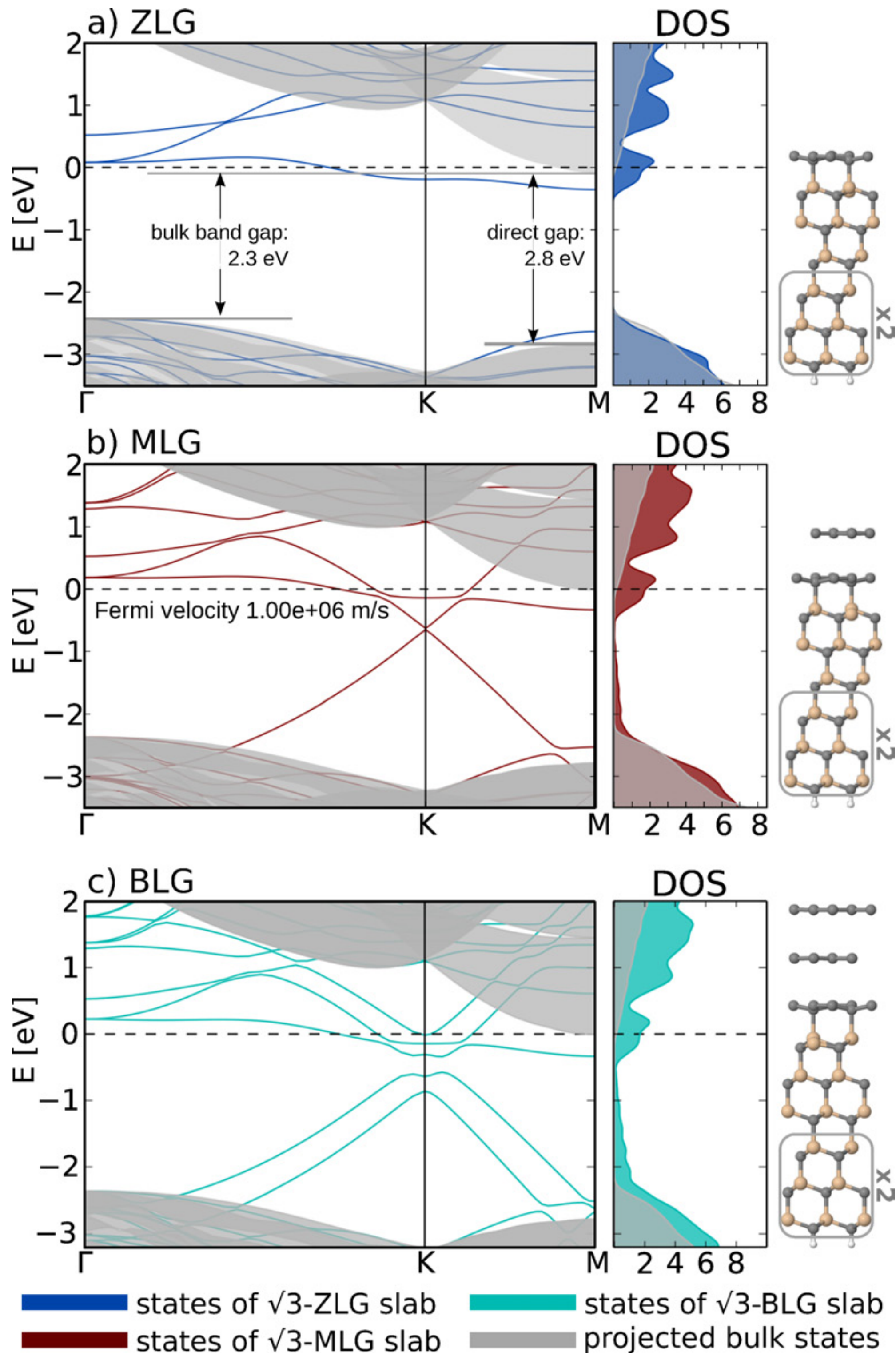

Figure 12.2.: The surface projected Kohn-Sham band structure and DOS of the (a) ZLG, (b) MLG, and (c) BLG calculated in the $(\sqrt{3} \times \sqrt{(3)})$ approximate unit cell using the HSE06 hybrid functional.

The bulk projected band structure, DOS and the geometric structure of the $\sqrt{3}$-ZLG phase are shown in Fig. 12.2 a). The direct and indirect band gap of bulk 3C-SiC are drawn into the band structure plot (for more details about the 3C-SiC bulk properties see Sec. 7.2). There is a single band at the Fermi level giving rise to a peak in the DOS. In the case of the 3C-SiC polytype the conduction band minimum (CBm) reaches into the Fermi level (see Fig. 12.2 a-c). This is different for hexagonal polytypes, where the CBm is well above the Fermi level [243]. The $\sqrt{3}$-ZLG layer contains a mixture of sp^2 and sp^3 hybridised orbitals, therefore the π bands with their linear dispersion close to the K-point characteristic for graphene are missing.

However, experimental studies of the ZLG suggest a small band gap around the Fermi level of 300 meV in STS [270, 109]. We tested the influence of spin-polarisation in separate calculations for $\sqrt{3}$-ZLG (not shown here). In a non-spin-polarised calculation every state is occupied by two electrons. In a surface with one dangling bond the structure is by necessity metallic. Introducing spin-polarisation allows the surface to open a gap. We compared the spin-polarised and non-spin-polarised band structure and DOS, but we could not find a change in the electronic structure or a gap opening, which agrees well with a DFT study of the $\sqrt{3}$-ZLG structure using LDA [215]. For the SiC/graphene hybrid structures included in this section the non-spin-polarised calculation gives the same result as the spin-polarised one.

The $\sqrt{3}$-MLG layer forms on top of the $\sqrt{3}$-ZLG interface. In the band structure Fig. 12.2 b) the Dirac point is shifted by -0.64 eV (-0.62 eV using LDA Pankratov *et al.* [243]) leading to n-type doping similar to the experimental value of -0.4 eV [83, 35, 238, 96]. The energy difference between E_D and the CBm is 0.63 eV. The Fermi velocity is the slope of the graphene π band at the Fermi level. For the $\sqrt{3}$-MLG layer, we found $1.00 \cdot 10^6$ m/s (PBE: $0.84 \cdot 10^6$ m/s; Experiment: $0.90 \cdot 10^6$ m/s [96]). A flat surface band appears at the Fermi level, similar to the one observed in the band structure of the $\sqrt{3}$-ZLG phase.

For the AB stacked $\sqrt{3}$-BLG (Fig. 12.2 c), we find a n-type doping of the $\sqrt{3}$-BLG layer, in agreement with experiment [238, 263]. Between the bilayer graphene related π bands a Kohn-Sham gap opens by 0.33 eV (PBE: 0.25 eV; 0.12 eV in experiment using the 6H-SiC polytype as substrate [263]). As for the $\sqrt{3}$-ZLG and $\sqrt{3}$-MLG there is a flat surface band at the Fermi level.

A possible explanation for the surface band at the Fermi level could be that the absence of the band gap in the simulated band structure is due to the approximated $\sqrt{3}$-ZLG structure. In Figure 12.3, we compare the DOS of

the $\sqrt{3}$-ZLG and the $6\sqrt{3}$-ZLG phase. Because of the increased system size, we will use the PBE exchange-correlation functional instead of the hybrid functional HSE06. In addition, we show in Fig. 12.3 the projected DOS of all Si atoms in the simulation cell (beige) and of the single Si dangling bond (pink) in the $\sqrt{3}$-ZLG and 19 dangling bonds in the $6\sqrt{3}$-ZLG structure as introduced in Sec. 9.2.

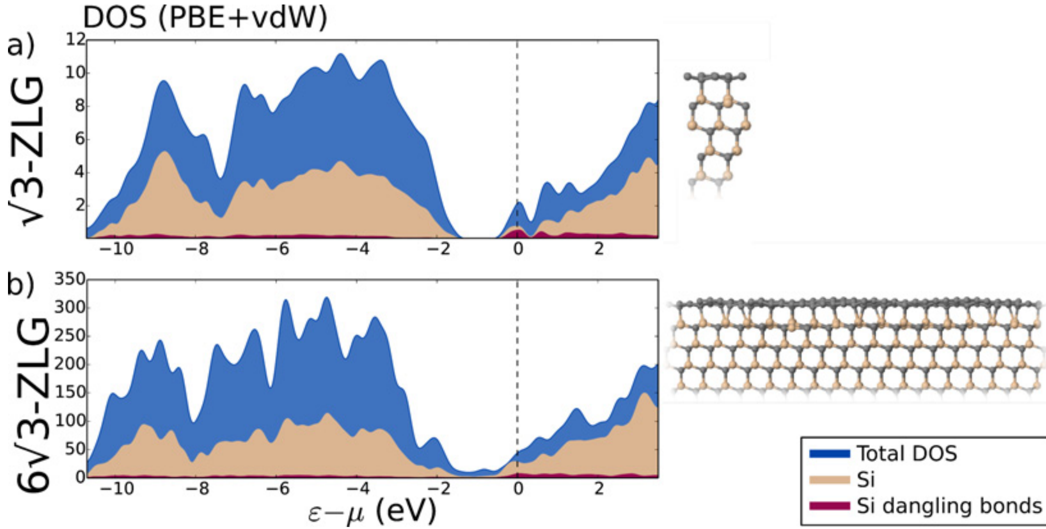

Figure 12.3.: Comparison between the DOS of the $\sqrt{3}$-ZLG and $6\sqrt{3}$-ZLG surface calculated using PBE exchange-correlation functional. The full DOS is shown in blue, the projected DOS of all Si atoms in the slab (beige) and of the Si dangling bonds (pink). On the right are shown images of the geometric structure optimised using PBE+vdW.

We first discuss the DOS of the $\sqrt{3}$-ZLG structure in Fig. 12.3 a). In the $\sqrt{3}$-ZLG structure the surface band (see Fig. 12.2 a) leads to a pronounced peak in the DOS at the Fermi level. The peak at the Fermi level cannot fully be contributed to the Si related states (shown in beige in Fig. 12.3 a). However, the projected DOS of the Si dangling bonds (shown in pink in Fig. 12.3 a), gives a clear peak at the Fermi level. Between the peak at the Fermi level and the SiC bulk states the DOS shows a gap (for comparison see Fig. 12.2 a).

In the case of the $6\sqrt{3}$-ZLG phase, the picture changes. Here, also the DOS close to the Fermi level increases. The states at the Fermi level are domiated by Si states (shown in beige in Fig. 12.3 b), but the contribution to the Si states originating from the Si dangling bonds is minor (shown in pink in Fig. 12.3 b). In the case of the $6\sqrt{3}$-ZLG the projected DOS of the Si dangling bonds does not show a clear peak like in the $\sqrt{3}$-ZLG structure.

In a LDA based DFT study by Kim *et al.* [166] the simulated ARPES spectra

of the ZLG layer on 4H-SiC shows several flat bands at the Fermi energy originating from the interface [166]. However, Kim *et al.* [166] did not show a DOS to allow for a detailed comparison.

However, the LDA as well as PBE are known to severely underestimate band gaps [209]. In the case of the ZLG layer the experimentally observed gap is of the order of 300 meV. To clarify the electronic structure of the interface close to the Fermi level a simulated band structure accounting for spin-polarisation on a dense k-grid at least on the level of HSE would be desirable, but, at the moment prohibited by the computational costs for system sizes of $\sim$2000 atoms.

12.2. The Influence of Doping and Corrugation on the Electronic Structure

For epitaxial graphene grown on SiC, we found in Sec. 8.2 that the MLG layer is corrugated. The corrugation is passed on to the MLG layer by the substrate/graphene interface structure. In Section 12.1, we found by evaluating the band structure of $\sqrt{3}$-ZLG, -MLG and -BLG structures that epitaxial mono- and bi-layer graphene are n-type doped. Electronic states originating from the interface could affect device operation through electrostatic screening even without directly contributing to electron transport. In addition, doping the graphene by charge transfer from the substrate or a possible symmetry breaking caused by the corrugation could affect electron transport [219, 19].

The interplay of saturated and unsaturated Si atoms at the interface causes a charge redistribution in the $6\sqrt{3}$-ZLG carbon layer (Fig. 12.8). We calculated the change in the electron density at the interface between the ZLG surface and the MLG layer, to evaluate how the charge redistribution in the ZLG-layer effects the MLG-layer.

We calculated the electron density $n(\mathbf{r})$ of a 3C-SiC slab with a reduced layer thickness (4 SiC bilayers instead of 6). The electron density of the MLG layer $n_{\mathrm{G}}(\mathbf{r})$, the substrate including the ZLG layer in the substrate reference electron density $n_{\mathrm{sub}}(\mathbf{r})$ and the full system n_{full} are calculated in isolation from each other. The electron density is represented on an evenly distributed grid ($260 \times 260 \times 350$) for all three systems. The electron density

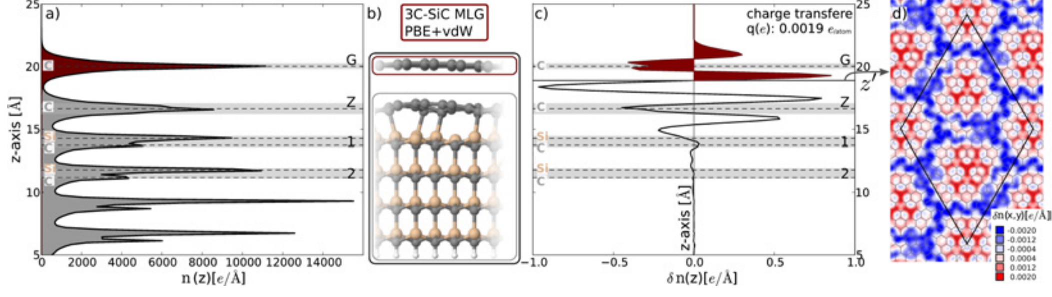

Figure 12.4.: The electron density of the $6\sqrt{3}$-MLG phase. Panel (a) shows the full electron density n_{full} of the MLG surface integrated over the x-y-plane along the z-axis (solid black line), the electron density of the substrate (filled in grey) n_{sub} and the graphene layer n_{G}. The average atomic layer position is indicated by dashed lines. Panel (b) displays a cutout of the atomic surface structure. The boxes indicate the structures calculated in isolation, black the full slab, grey the substrate and red the graphene layer. Panel (c) shows the electron density difference $\Delta n(z)$ (Eq. 12.1 and Eq. 12.2). The charge transfer is calculated by integrating $\Delta n(z)$ from z' to ∞ (integrated area filled in red). Panel (d) shows the charge distribution in the x-y-plane at $z = z'$.

difference $\Delta n(\mathbf{r})$ is given by

$$\Delta n(\mathbf{r}) = n_{\text{full}}(\mathbf{r}) - (n_{\text{G}}(\mathbf{r}) + n_{\text{sub}}(\mathbf{r})). \tag{12.1}$$

The change in the electron density along the z-axis is calculated by integrating over the x-y-plane

$$n(z) = \int dx\, dy\, n(\mathbf{r}). \tag{12.2}$$

In Figure 12.4 a), the electron densities $n(z)$ are shown for the full system n_{full} (outline in black), the substrate n_{sub} filled in grey and the MLG layer n_{G} filled in red. To obtain information about a possible charge transfer from the substrate to the MLG layer, we calculated the electron density difference $\Delta n(\mathbf{r})$ applying Eq. 12.1. Integrating $\Delta n(\mathbf{r})$ using Eq. 12.2 gives the change in the electron density along the z-axis shown in Fig. 12.4 c). Already the second SiC bilayer shows only small changes in the electron density. At the interface between the SiC bilayer and the ZLG layer the electron density redistribution is intensified. We use $\Delta n(z)$ to calculate the charge transfer by integrating $\Delta n(z)$ from the inflection point z' into the vacuum region above the MLG layer marked in red in Fig. 12.4 c). It shows that the MLG layer is negatively charged by an average charge of 0.0019 e^-/atom. Figure 12.4 d) shows $\Delta n(\mathbf{r})$ in the x-y-plane at position $z = z'$ between the substrate and the graphene layer. Figure 12.5 shows $\Delta n(\mathbf{r})$ in the x-y-plane at equidistant z_i heights of 0.3 Å between the MLG-layer and the substrate. The electron density pattern from Fig. 12.4 d) is shown in Fig. 12.5 8. The resulting pattern is very similar for any chosen height. The modulations of the electron density in the MLG layer are governed by the interplay of

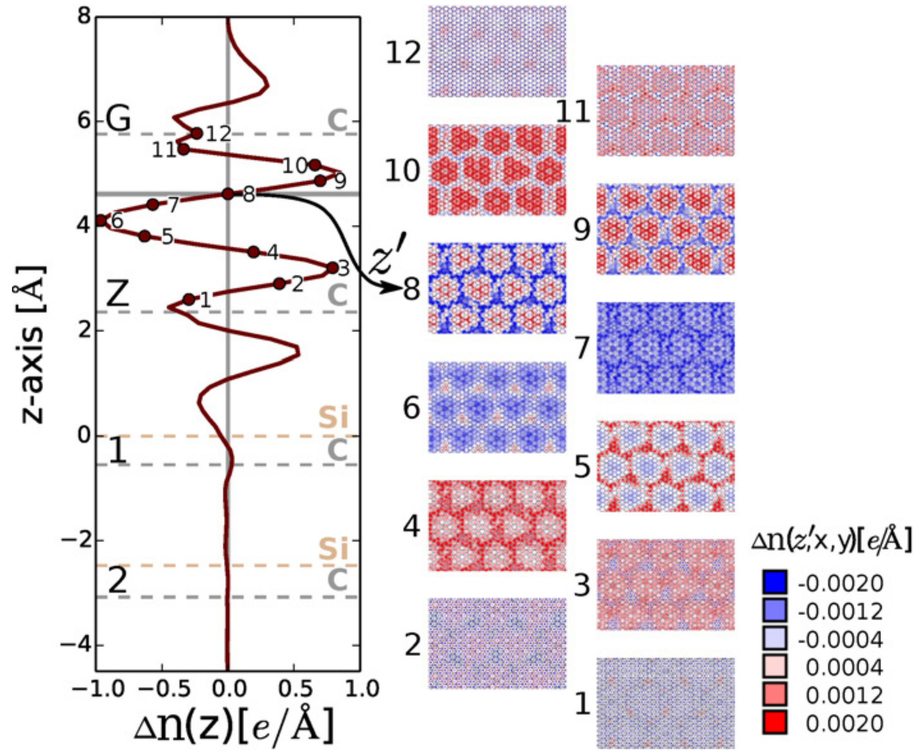

Figure 12.5.: The difference in the electron density given by Eq. 12.1 is shown for the 3C-SiC MLG phase. Eq. 12.2 gives Δn averaged over the x-y-plane and plotted it along z. The position of the Si, C, H, and graphene-layer are indicated by dashed lines. We show $\Delta n(z_i)$ in the x-y-plane at equidistant z_i heights between the MLG-layer and the substrate.

saturated and unsaturated Si bonds to the ZLG layer.

In Section 2.4, we introduced the Hirshfeld charge analysis as a tool to divide the total electron density between different atoms of a system according to the electron density of the electron density of a free neutral atom. In a real system, we have an electron density in the field of positively charged nucleii, which makes any definition of atomic charges arbitrary. Hirshfeld charges show the general tendency to underestimate the charge transfer, e.g. [190]. We calculate the average Hirshfeld charge in the ZLG and MLG layer (shown in Fig. 12.6 a). The average Hirshfeld charge per C atom of the ZLG layer amounts to 0.024 e^-/atom leading to a negatively charged layer. However the charge of a C atom in the ZLG layer underneath the MLG layer is reduced to 0.021 e^-/atom. Evaluating the Hirshfeld charges for the MLG layer, we found a negatively charge per C atom of 0.0015 e^-/atom, which agrees well with the charge transfer of 0.0019 e^-/atom calculated by charge density differences. The charge transfer in the ZLG layer is approximately 10 times larger than in the MLG layer. This finding is not surprising as the

ZLG layer is covalently bonded to the substrate, while the MLG layer is attached to the ZLG layer by weak vdW bonds.

In experiment, the MLG band structure shows a n-type doping. ARPES measurements of the MLG layer show that the graphene Dirac point is shifted by approximately -0.4 eV [83, 35, 238]. From Fig. 6.7, we can estimate that a charge transfer of $\sim$0.005 e^-/atom would be necessary to shift the Dirac point to -0.4 eV. An electron doping of 0.0019 e^-/atom (0.0015 e^-/atom) shifts the Dirac point to -0.25 eV (-0.22 eV) (see Sec. 6.3).

The underestimation of the charge transfer could be an artefact of the approximation to the exchange-correlation functional. To test the influence of the exchange-correlation functional on the charge transfer, we used the $\sqrt{3}$-MLG structure introduced in Sec. 12.1 (see Tab. 12.1).

Hirshfeld charges in e^-/atom			
Layer	$\sqrt{3}$-MLG		$6\sqrt{3}$-MLG
	PBE	HSE06	PBE
MLG	0.0045	0.0079	0.0015
ZLG	0.019	0.012	0.021

Table 12.1.: The Hirshfeld charge per C atom [e^-/atom] in the $\sqrt{3}$-MLG calculated using PBE and HSE06 and for comparison the Hirshfeld charges calculated in the $6\sqrt{3}$-MLG structure using PBE.

In Table 12.1, we list the Hirshfeld charges per C atom calculated in the $\sqrt{3}$-MLG structure using PBE and the hybrid functional HSE06. In addition, we include in Tab. 12.1 the Hirshfeld charges for the $6\sqrt{3}$-MLG structure using PBE. First, we compare the difference in charge transfer between the two different MLG structures. The Hirshfeld charges listed in Tab. 12.1 for the $\sqrt{3}$-MLG-layer amounts to 0.0045 e^-/atom, three times higher than the charge transfer for the $6\sqrt{3}$-MLG-layer using PBE. As a next step, we compare the charge transfer calculated using the two different exchange-correlation functionals PBE and HSE06. The charge transfer to the $\sqrt{3}$-MLG-layer increases by almost a factor two from 0.0045 e^-/atom for PBE to 0.0079 e^-/atom for HSE06. We heere can conclude that the choice of simulation cell ($6\sqrt{3}$-MLG versus $\sqrt{3}$-MLG) has a larger influence on the charge transfer than the functional, at least for the functionals we tested.

However, the change in the charge transfer between HSE06 and PBE is

not large enough to explain the discrepancy between our calculations and the experiment. The difference might not solely originate from the approximation to the exchange-correlation functional, but originates from the experimental setup. In experiment the SiC substrate is nitrogen doped leading to a n-type doping [263]. One can well imagine that during the growth process nitrogen migrates to the SiC surface enhancing the charge transfer at the SiC-graphene interface.

The $6\sqrt{3}$-MLG-layer differs from free-standing graphene due to the interaction with the substrate. Here the graphene-substrate interaction on the level of PBE+vdW leads to a corrugation of 0.41 Å (see Fig. 8.5) and a charge transfer from the substrate to the graphene layer of 0.0019 e^{-}/atom (0.0015 e^{-}/atom, respectively). In the following, we will systematically evaluate the effect of the corrugation and the charge transfer on the electron band structure of the MLG layer.

For a systematic study of the influence of doping and corrugation on the graphene layer, we calculated the Kohn-Sham band structure of an isolated 13×13 graphene cell including the corrugation as calculated in Sec. 8.2 and the charge transfere as given by the Hirshfeld analysis. The band structure of the 13×13 graphene supercell is then folded back into into the graphene BZ applying the formalism introduced in Sec. 11. The bands were unfolded along the high symmetry lines Γ - K - M - Γ in the graphene BZ. First, we calculated the band structure of a perfectly symmetric 13×13 graphene cell and overlaid the unfolded band structure with the bands calculated in the primitive graphene unit cell (Fig. 12.6 b). As expected, we find a perfect agreement for the perfectly periodic graphene cell.

As a next step, we were interested in the influence of the doping. The atom resolved Hirshfeld charges are shown in Fig. 12.6 a). The Hirshfeld charges are unevenly distributed and vary between 0.0038 e^{-}/atom to 0.0091 e^{+}/atom leading to an average Hirshfeld charge of 0.0015 e^{-}/atom. We applied the VCA [336, 278, 261], every C atom was doped according to its Hirshfeld charge calculated in the experimentally observed 3C-SiC-$6\sqrt{3}$-MLG structure. The unfolded Kohn-Sham band structure Fig. 12.6 c) shows the graphene Dirac point shifted by -0.22 eV with respect to the Fermi level. However, signs of symmetry breaking in the graphene band structure caused by the modulation of the Hirshfeld charge in the graphene layer are not visible.

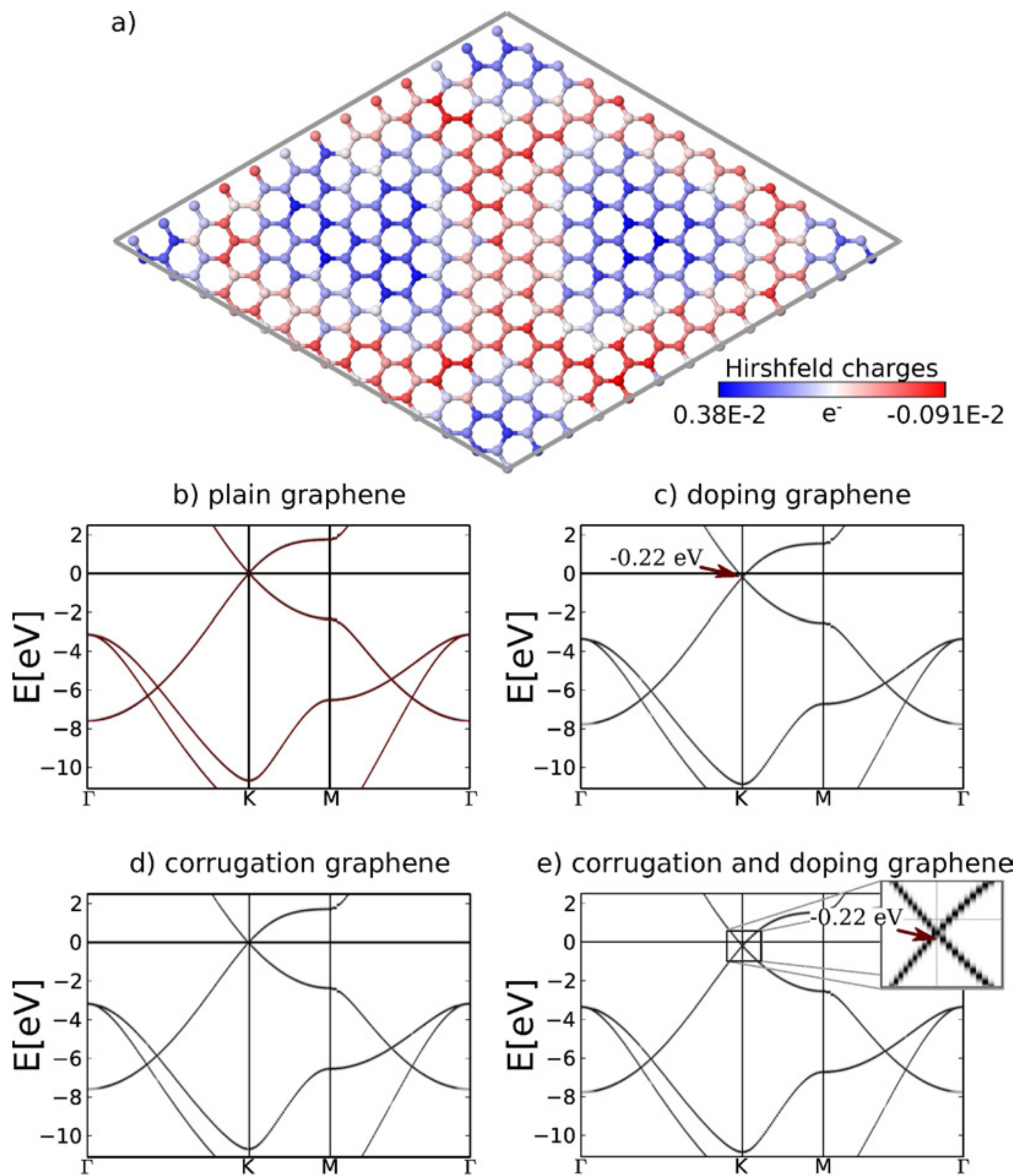

Figure 12.6.: The band structure of a 13×13 graphene cell. Subfigure a) shows the Hirshfeld charge distribution of a MLG layer. b) shows the unfolded band structure of a perfectly periodic 13×13 graphene cell and overlayed in red is the band structure of free-standing graphene in its 1×1 unit cell. c) unfolded band structure of a flat graphene layer doped according to the Hirshfeld charges. The charges lead to a shift of the Dirac point by 0.22 eV. c) the unfolded band structure with the same corrugation as the MLG layer. d) Band structure of a graphene layer which is both corrugated and doped. The region around the Dirac point is enlarged showing the shift of the Dirac point caused by the doping.

Fig. 12.6 d) shows the unfolded band structure of a corrugated graphene layer. We used the exact geometry of the MLG layer from the 3C-SiC-3C-SiC-6$\sqrt{3}$-MLG structure from Sec. 8.2 without the substrate. Likewise the corrugation of graphene layer is to weak to break the symmetry of graphene enough to influence the graphene π bands.

In this analysis, we did not include the effects of the substrate directly. There is still the possibility that electronic states originating from the interface could affect device operation through electrostatic screening. However, the corrugation of the MLG-layer and the inhomogeneous charge redistribution alone do not show a significant change in the electronic band structure and therefore should not affect device operation.

12.3. The Silicon Dangling Bonds and their Effect on the Electronic Structure

3C-SiC has a band gap of 1.44 eV (PBE) and experimental gap of 2.2 eV [204] (see Tab. 7.3). For ZLG the band gap is reduced to 300 meV (STS measurements) [270, 109]. In Section 12.1, we discussed the the DOS close to the Fermi level. However, we could not reproduce the opening of a small band gap.

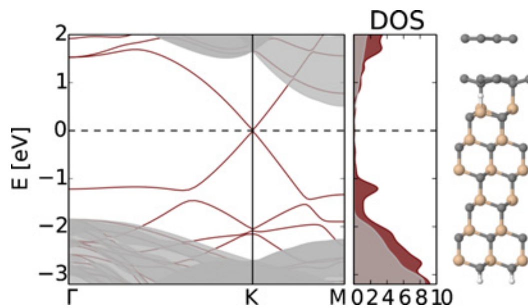

Figure 12.7.: The bulk projected Kohn-Sham band structure and DOS of the $\sqrt{3}$-MLG structure with the Si dangling bond saturated by an H atom. The full band structure and DOS of the slab used in the calculation is shown in red and the 3C-SiC bulk states in grey.

In Chapter 9, we found 19 unsaturated Si atoms – the *Si dangling bonds* – at the interface between the SiC substrate and the ZLG layer. Their influence on the electronic structure and how they effect the graphene electronic properties is not fully understood. It is speculated that the difference in the electronic structure between the ZLG- and MLG layer is due to partial hybridisation of the C atoms in the ZLG layer and the substrate Si atoms [83, 263]. It is conceivable that for the ZLG the observed low DOS in the SiC bulk band gap are caused by the unsaturated Si atoms in the top SiC bilayer.

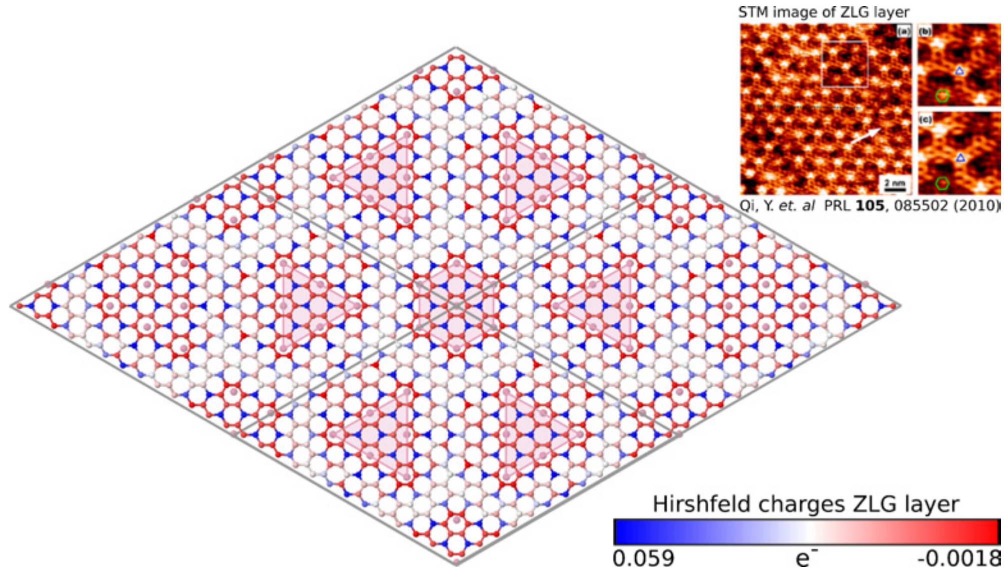

Figure 12.8.: Four times the ZLG layer coloured depending on the Hirshfeld charge of the C atom from blue for electron gain to red for electron loss. The position of the unsaturated Si atoms is shown in pink. The STM image taken from Qi *et al.* [256] is shown for comparison.

To evaluate the influence of the Si dangling bond, we will use the $\sqrt{3}$-ZLG model as introduced in Sec. 12.1. The advantage of this approximated structure over the true $(6\sqrt{3} \times 6\sqrt{3})$-R30° is that the Si dangling bond can be clearly distinguished from the two covalently bounded Si atoms.

In Figure 12.2 the Fermi level was pinned by a flat surface state in all three phases, the $\sqrt{3}$-ZLG, $\sqrt{3}$-MLG and $\sqrt{3}$-BLG. The main suspect is the unsaturated Si dangling bond in the top SiC-bilayer at the interface. To evaluate the origin of the flat surface band, we saturated the Si dangling bonds by one H atom. After optimising the atomic structure, we calculated the band structure and DOS. In the band structure (Fig. 12.7) the Dirac point coincides with the Fermi level, such that the surface is undoped. The 3C-SiC bulk CBm is shifted away from the Fermi level. The energy difference between E_D and the CBm is slightly reduced to 0.51 eV compared to 0.63 eV in the $\sqrt{3}$-MLG (see Sec. 12.1). The surface band at the Fermi level disappeared. From Fig. 12.7, we can conclude that the doping of the MLG layer is induced by the Si dangling bonds at the interface and that it indeed give rise to the flat surface state at the Fermi level.

Using the $\sqrt{3}$-ZLG model, we found that the Fermi level is determined by the interface structure most likely induced by charge transfer from the dangling Si bonds at the interface. We marked the Si dangling bonds underneath the ZLG layer in pink in Fig. 12.8. On the basis of geometric position and bond length differences, we identified the Si dangling bonds

(for a detailed discussion see Appendix E). They form two different types of cluster: two triangular shaped clusters per unit cell and one hexagonal. The hexagonal cluster is centered around the Si atom positioned exactly in the middle of a C hexagon of the ZLG layer (see Fig. 12.8). The dangling bond cluster give rise to the characteristic corrugation of the ZLG layer as discussed in Sec. 9.1.

We can assign every C atom in the ZLG layer a charge by using the Hirshfeld partitioning scheme [142]. The calculated charge partitioning is shown in Fig. 12.8. On average, a C atom in the ZLG layer is negatively charged by 0.024 e^{-}/atom, which is reduced to 0.021 if a additional MLG-layer is adsorbed (see Tab. 12.1). The charge transfer in the ZLG layer is maximal at C atoms with a Si atom right underneath forming a strong covalent bond (shown as blue C atoms in Fig. 12.8). On the other hand, for C hexagons on top of a Si dangling bond the electrons disperse (indicated by red C atoms in Fig. 12.8).

In 2010, Qi *et al.* [256] visualised the ZLG surface using STM with a special iron treated tip. They found two differently shaped patterns in their STM images: one hexagonal and two triangular pattern (the STM image taken by Qi *et al.* [256] is shown in Fig. 12.8). They suggested the presence of C-rich hexagon-pentagon-heptagon (H5,6,7) defects at two different defect positions, "hollow" and "top" (see Fig. 9.4). In Section 9.2, we demonstrated that the formation energy for these defects make their presence at the interface unlikely.

Due to the two different types of cluster formed by the Si dangling bonds, the charge in the ZLG layer is redistributed. The resulting pattern of the Hirshfeld charge map of the ZLG layer looks similar to the pattern seen in STM. It is conceivable that Qi *et al.* [256] actually visualised the Si dangling bonds in their measurements.

12.4. Summary

In conclusion, we used density-functional approximation (DFA) HSE06+vdW and PBE+vdW calculations to evaluate the origin of doping in epitaxial few-layer graphene on the Si face of SiC. The $\sqrt{3}$-approximated interface structure features three Si atoms in the top layer of which two are covalently bonded and one is unsaturated. Because of the clear interface structure the dangling bond can be identified. We evaluated the influence of the dangling bond on the ZLG-layer and few-layer graphene. We found that indeed the

Si dangling bond dopes the ZLG, MLG and BLG by a interface state at the Fermi level. The BLG structure has a Kohn-Sham band gap of 0.33 eV using the HSE06 functional. Saturating the Si dangling bond by a hydrogen atom shifts the graphene Dirac point to the Fermi energy resulting in an undoped epitaxial graphene layer. Evaluating the electron density of MLG we found a doping of 0.0019 e^-/atom (experiment $\sim$0.005 e^-/atom [83, 35, 238]). The doping shifts the Dirac point to -0.22 eV (experiment -0.4 eV). However, the doping as well as the corrugation of the MLG layer hardly disturb the graphene π bands. In the case of the $6\sqrt{3}$-ZLG structure, we found a very low DOS near the Fermi level, which might be to low to be detected experimentally. Evaluating the electron density of the $6\sqrt{3}$-ZLG we found a pattern in the electron density of ZLG similar to the STM images from Qi *et al.* [256]. In the STM image as well as in the electron density plot two differently shaped patterns are found: one hexagonal and two triangular pattern per unit cell. Similar to the patterns visualised in STM measurements by Qi *et al.* [256].

13 The Decoupling of Epitaxial Graphene on SiC by Hydrogen Intercalation

In the previous Chapters, we discussed how the mixture of covalent and non-covalent bonding between the substrate (SiC) and the ZLG-layer influences the atomic structure (see Ch. 8) and the electronic structure (Ch. 12) of the MLG-layer. For future graphene applications, it is desirable to find a substrate for which the interactions are minimised and the extraordinary properties of a single graphene layer are preserved.

In experiment, Riedl *et al.* [262] demonstrated the possibility to decouple graphene from SiC by intercalation of H atoms forming QFMLG. The intercalation process removes the covalent Si-C bonds by saturating the Si atoms in the top SiC-bilayer. The experimental band structure (see Fig. 12.1 c) and core-levels of graphene indicate that indeed the intercalation process reduces the interaction with the substrate substantially [97].

For weakly interacting graphene the sensitivity of ARPES becomes insufficient to assess the interaction with the substrate [153]. An alternative criterion to quantify the interaction strength of graphene with a substrate is its adsorption height. However, for H-intercalated graphene, the adsorption height is not known experimentally. Moreover, it is not clear whether for such a weakly interacting system, this height can be calculated reliably, as it is entirely determined by vdW interactions, which are difficult to treat (see Sec. 2.4).

In this chapter, we present the results from a theoretical and experimental collaborative study of the electronic and structural properties of QFMLG in comparison to MLG on 6H-SiC(0001) [294]. The author of this thesis contributed the calculations and theoretical analysis. We present DFA calculations of QFMLG in the large commensurate $(6\sqrt{3} \times 6\sqrt{3})$-R30° supercell consisting of 6 SiC-bilayers using PBE+vdW. We fully relaxed the top three SiC bilayers and all planes above (residual energy gradients $< 8 \cdot 10^{-3}$ eV/Å). Our experimental collaborators validate this calculations with an accurate experimental height measurement by normal incidence x-ray standing wave (NIXSW) [294].

13.1. The Vertical Graphene-Substrate Distance

To test whether the structure of this predominantly vdW interacting interface can be predicted using DFA and to gain a detailed understanding of how H decouples the graphene layer from the substrate, we performed DFA calculations for the QFMLG on the level of PBE+vdW. The bulk lattice parameters are listed in Tab. 7.2. In experiment and therefore in our calculations we use 6H-SiC as a substrate.

Figure 13.1.: (a) Vertical distances measured by NIXSW on QFMLG. The position of the Bragg planes around the surface are indicated by blue lines [294]. PBE+vdW calculated geometry for (b) QFMLG on 6H-SiC(0001) and histograms of the number of atoms N_a versus the atomic coordinates (z) relative to the topmost Si layer (Gaussian broadening: 0.05 Å). N_a is normalised by N_{SiC}, the number of SiC unit cells. $D_{n,n+1}$ is the distance between the layer n and $n+1$, d_n gives the Si-C distance within the SiC bilayer n, and δ_n the corrugation of the layer n. All values are given in Å. (Figure published in Ref. [294])

The NIXSW method, combining dynamical x-ray diffraction and photoelectron spectroscopy, is a powerful tool for determining the vertical adsorption distances at surfaces with sub-Å accuracy and high chemical sensitivity. Applying these techniques, our collaborators determined the heights of bulk C and bulk Si and graphene C with respect to the bulk-extrapolated SiC(0006) atomic plane. The C^{SiC}_{surf} atoms are located at 0.61 ± 0.04 Å below the bulk-extrapolated Si plane and the Si^{SiC}_{surf} 0.05 ± 0.04 Å above. Thus we obtain an experimental Si-C distance of 0.66 ± 0.06 Å, in agreement with the SiC crystalline structure (Sec. 7.1, Lee *et al.* [186], Wang *et al.* [339]). In the same way, we find the adsorption height z^{ads} of the graphene layer with respect to the topmost Si layer to be 4.22 ± 0.06 Å, as shown in Fig. 13.1 a.

Figure 13.1 shows the measured (panel a) and the calculated (panel b) structure of the QFMLG on 6H-SiC, predicted at the PBE+vdW level. In addition, we include a histogram of the atomic z coordinates relative to the top Si layer normalised by the number of SiC unit cells. For illustration purposes, we broadened the histogram lines using a Gaussian with a width of 0.05 Å. For the QFMLG, we found a bulk-like distance of 1.89 Å between the SiC bilayers. The Si-C distance within the top SiC bilayer (0.62 Å) and the remaining Si-C bilayer distances are practically bulk-like (0.63 Å), in good agreement with the experimental result (0.66 ± 0.06 Å). The distance between the top Si-layer and the graphene layer is $z^{\mathrm{ads}} = 4.16$ Å for 6H-SiC, again in good agreement with the measured 4.22 ± 0.06 Å. Overall, we find excellent agreement between calculation and experiment [294].

Next, we compare the QFMLG (Fig. 13.1 b) with the MLG (Fig. 8.7) structure. The most significant difference between the geometry of these two structures is the significant reduction of the layer corrugation in the QFMLG. For the 6H-SiC-MLG we found a strong corrugation of the top Si-C bilayer (top Si layer 0.78 Å and C layer 0.30 Å), the ZLG-layer (0.86 Å) and the MLG-layer (0.45 Å). In comparison the corrugation of the QFMLG-layer is very small (0.02 Å) and for the H layer and all layers underneath the corrugation is $< 10^{-2}$ Å. This is in agreement with STM results [109] showing no corrugation within the experimental accuracy.

In Section 8.2, we demonstrated that the chosen exchange-correlation functional can have a significant impact on the geometric structure, e.g. in plain PBE the interplanar layer distance between the graphene layer and the ZLG-layer is unphysically expanded. We also tested the influence of the exchange-correlation functional on the geometry and in particular the adsorption height for the QFMLG structure. For our test calculations, we used the approximated $(\sqrt{3} \times \sqrt{3})$-R30° cell introduced in Sec. 9.2 (see Appendix F). For the adsorption height z^{ads}, we found a small difference of 0.01 Å between PBE+vdW and HSE06+MBD. Therefore, we do not expect significant changes of the adsorption height in the $6\sqrt{3}$-QFMLG for higher level functionals, such as HSE06+MBD.

In addition, we found that the influence of the SiC polytype on the atomic structure of the SiC surface reconstructions is small [100, 277, 243]. We compare the structural key parameters of the QFMLG (see Appendix H) and MLG (see Sec. 8.2) on 3C-SiC and 6H-SiC. The interface geometry hardly changes with the polytype, and the same qualitative difference between the QFMLG and MLG phases can be observed for both SiC polytypes.

To evaluate how strong the QFMLG-layer is bound to the substrate, we

calculated the graphene exfoliation energy (E_{XF}). In Sec. 6.2, we discussed the challenge to reliably calculate the graphite interlayer binding energy. We introduced the exfoliation energy (E_{XF}) given by Eq. 6.2, as the energy of an isolated graphene layer adsorbed on a graphite bulk structure. On the level of PBE+vdW, we found a exfoliation energy for graphite of 81 meV/atom. We rewrite Eq. 6.2 to calculate the E_{XF} of a graphene layer adsorbed on any substrate to

$$E_{XF} = \frac{E_{\text{full}} - (E_{\text{sub}} + E_{\text{graphene}})}{N_{\text{atom}}}, \tag{13.1}$$

where E_{full}, E_{graphene} and E_{sub} are DFT total energies for the full system, the graphene layer and the substrate including the hydrogen layer for QFMLG and the ZLG-layer for MLG. N_{atom} is the total number of C atoms in the graphene layer.

Evaluating Eq. 13.1, we found an exfoliation energy for the QFMLG-layer of 59 meV/atom and for the MLG-layer of 89.2 meV/atom. For the QFMLG-layer the exfoliation energy is significantly smaller than the corresponding values for MLG and graphite. The vdW correction may not capture the correct absolut exfoliation energy, however the error should be of the same order in the different structures compared here. We consider only the relative change in the exfoliation energy, therefore it is conceivable that the realtive energy differences are qualitatively correct.

13.2. The Electron Density Maps

To evaluate how the presence of a flat intercalated layer translates into the electronic structure of the graphene layer, we calculate the change of electron density at the interface between the H-terminated SiC surface and the QFMLG-layer. The calculations were performed with a 3C-SiC substrate as it allows us to use a smaller substrate thickness (4 SiC bilayers instead of 6 for 6H-SiC) and renders the calculation more affordable. We found the differences in geometry of the QFMLG to be small between the 3C-SiC and 6H-SiC (see Sec. 13.1 and Appendix H). We assume that the qualitative changes in the electron density would also be small between the two polytypes.

Similar to the electron density investigation in Sec. 12.2 for the MLG-layer, we calculated the electron density $n(\mathbf{r})$ of a 4-bilayer 3C-SiC-QFMLG slab on an evenly distributed grid ($260 \times 260 \times 350$) for the full system $n_{\text{full}}(r)$, the graphene layer alone $n_{\text{G}}(r)$ and the substrate alone $n_{\text{sub}}(r)$ including

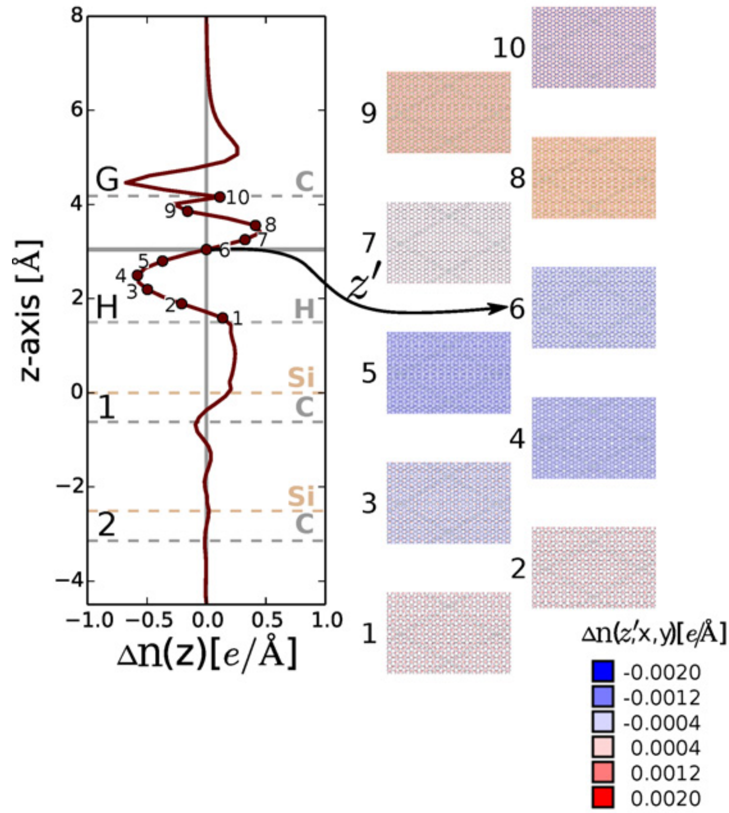

Figure 13.2.: The difference in the electron density given by Eq. 12.1 is shown for the 3C-SiC QFMLG phase. We integrated Δn in the x-y-plane and plotted it along z (Eq. 12.2). The position of the Si, C, H, and graphene-layer are indicated by dashed lines. We show $\Delta n(z_i)$ in the x-y-plane at equidistant z_i heights between the graphene layer and the substrate.

the H layer.

The electron density difference $\Delta n(\mathbf{r})$ was calculated using Eq. 12.1. We obtained the change in the electron density along the z-axis by integrating $\Delta n(\mathbf{r})$ over the x-y-plane (Eq. 12.2). In Figure 13.2 the change in the electron density along the z-axis is shown for the QFMLG. Figure 13.2 shows $\Delta n(\mathbf{r})$ maps in the x-y-plane at equidistant heights of 0.3 Å at the interface region.

In the QFMLG, all Si atoms are saturated by H [33] resulting in negligible variations of the electron density within the x-y-plane independently of the chosen height as seen in Fig. 13.2. On the other hand, we found for the MLG phase that the in-plane electron density is influenced by the interplay of saturated and unsaturated Si bonds in the ZLG-layer (see Sec. 12.2 Fig. 12.5). The modulations in the charge distribution of the QFMLG-layer are very

small at any chosen position z_i in the interface region. This is an additional indication for the improved decoupling of the graphene layer from the substrate and thus prevents its buckling.

13.3. Summary

In conclusion, we showed that our DFA calculations at the level of PBE+vdW provide a valid description of the SiC-graphene interface. In particular, they reproduce quantitatively the NIXSW-measured graphene-Si distances for the QFMLG. From a comparison of the corrugation between the QFMLG (0.02 Å) and the MLG (0.45 Å Fig. 8.7), we can conclude that QFMLG is better suited for device applications than MLG. This is also reflected in the low exfoliation energy E_{XF} calculated for QFMLG.

The QFMLG is a very flat graphene layer with a very homogeneous electron density at the interface. This significant difference between the MLG- and QFMLG-layer translates into a dramatic improvement of electronic devices after H intercalation [137, 198].

So far the focus of this work has been on epitaxial graphene on the Si terminated surface of SiC (Ch. 8 - 13). On the Si side, nearly perfect, MLG films can be grown over large areas [82, 66]. This is very different from the C side, where controlling the layer thickness of the graphene films remains a challenge [213]. In this chapter we will investigate the relative phase stability of the competing surface phases in the thermodynamic range of graphitisation, published in Ref. [228]. Parts of the results presented in this chapter were obtained in close collaboration with Florian Lazarevic and have been discussed in his master thesis Ref. [184].

14.1. The 3C-SiC $(\bar{1}\bar{1}\bar{1})$ Surface Reconstructions

On the C side, during graphene growth, a series of different surface structures have been observed [332, 304, 145, 192, 24, 292, 208, 140, 307, 139]. The two most relevant surfcae phases for this work are the $(2\times2)_C$ and the (3×3) reconstruction. Seubert *et al.* [292] resolved the atomic structure of the $(2\times2)_C$ by quantitative LEED, but the (3×3) reconstruction remains an open puzzle.

14.1.1. The (2 x 2) Si Adatom Phase

The (2×2) cell contains four C atoms in the top Si-C bilayer, so that the bulk truncated surface has four unsaturated bonds. It is the only reconstruction on the C side for which a detailed atomic structure was identified by quantitative LEED [292, 291]. The reconstructed surface consists of a Si adatom on top of a bulk-like C layer (shown in Fig. 14.1). The adatom is at position C in Fig. 7.1, also known as H_3-site. At this position the adatom forms bonds with the three C atoms of the top Si-C-bilayer, reducing the number of dangling bond orbitals at the surface from 4 to 2. The two remaining p_z-like dangling bond orbitals are located on the Si adatom and one on the unsaturated surface C atom.

We performed DFA calculations using different exchange-correlation functionals. The bulk lattice parameter were taken from Tab. 7.2. As before, we use six SiC bilayers and the bottom silicon atoms are H terminated. The

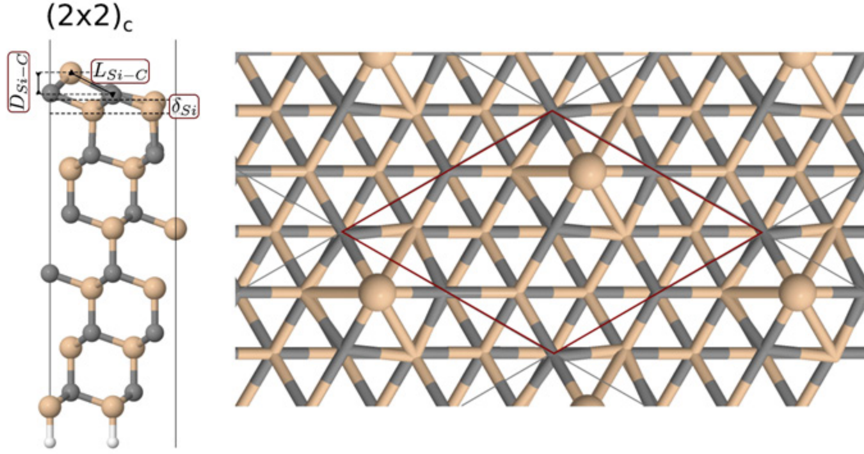

Figure 14.1.: Geometry of the 3C-SiC($\bar{1}\bar{1}\bar{1}$) $(2\times2)_C$ Si adatom structure. The bond length of the adatom with the top C layer ($L_{\text{Si-C}}$), the distance from the surface ($D_{\text{C,Si}}$) and the corrugation of the top Si layer (δ_{Si}) are shown.

top three SiC bilayers and all adatoms or planes above are fully relaxed (residual energy gradients: $8 \cdot 10^{-3}$ eV/Å or below). In Table 14.1, we list the structural key parameter of the 3C-SiC($\bar{1}\bar{1}\bar{1}$) $(2\times2)_C$ Si adatom structure for different exchange-correlation functionals.

3C-SiC($\bar{1}\bar{1}\bar{1}$)		$L_{\text{Si-C}}$	$D_{\text{C,Si}}$	δ_{C}	δ_{Si}
Data from Ref. [184]	LDA	1.90	0.86	0.10	0.32
	PBE	1.91	0.88	0.09	0.33
	PBE+vdW	1.91	0.87	0.09	0.33
This work	HSE	1.87	0.86	0.10	0.33
	HSE+vdW	1.86	0.86	0.09	0.34
	HSE+MBD	1.86	0.85	0.10	0.34
6H-SiC(000$\bar{1}$)					
Exp. data from Ref. [291, 292]		1.94	1.06	0.22	0.2

Table 14.1.: Atomic position of the Si adatom relative to the surface for different exchange-correlation functionals. The bulk lattice parameter were taken from Tab. 7.2. $L_{\text{Si-C}}$ is the bond length between the adatom and the top layer C atoms, $D_{\text{C,Si}}$ is the distance between the adatom and top layer C atoms along the z-axis, and δ_{Si} is the corrugation of the top Si-layer (see Fig. 14.1). (All values in Å)

We include in Tab. 14.1 experimental data from quantitative LEED measurements [292, 291] The structure parameters on the level of LDA, PBE and PBE+vdW were obtained by Florian Lazarevic and have been discussed in his master thesis Ref. [184]. The overall agreement of the structural parameter between the different exchange-correlation functionals listed in this work is very good. However, the theoretical prediction only agrees qualitatively with experiment [292, 291]. One has to keep in mind that the experimental reference data from Ref. [292, 291] corresponds to the 6H-SiC polytype. More importantly Seubert *et al.* [292] found that the $(2\times2)_C$ reconstruction preferes a $S1_{6H}$ stacking order (CACBAB) (see Fig. 8.1). LEED data indicates that the $(2\times2)_C$ reconstruction on the 6H-SiC(000$\bar{1}$) surface stabilises hexagonal stacking at the surface ($S1_{6H}$). For the $\sqrt{3}\times\sqrt{3}$)-R30° adatom reconstruction on the Si terminated surface we found a preferred linear stacking ($S3_{6H}$) (see Sec. 8.1.1 and [304, 308, 309]).

It remains to examine whether the differences in the geometry between experiment and theory originate from the different choice of polytype. In the following, we will use the $(2\times2)_C$ reconstruction as a reference phase.

14.1.2. The (3 x 3) Surface Reconstruction: An Open Puzzle

Over the last two decades, several structural models have been suggested for the (3×3) phase on the C face [192, 145, 139, 71], however, so far it remained an open puzzle. We here summarise the experimentally observed characteristics of the (3×3) reconstruction:

Si-rich:
AES indicates that the stoichiometry of the surface reconstruction is Si-rich [145, 24].

Triagonal adatom structure seen in STM:
The corresponding filled-state STM image is consistent with three adatoms residing at the same height [71, 139].

Semiconducting:
STS shows a semiconducting surface with a band gap of 1.5 eV [140].

We performed DFT calculations using PBE+vdW and HSE06+vdW. In our calculations, we use six SiC bilayers and the bottom silicon atoms are H

terminated. The top three SiC bilayers and all adatoms or planes above are fully relaxed (residual energy gradients: $8 \cdot 10^{-3}$ eV/Å or below).

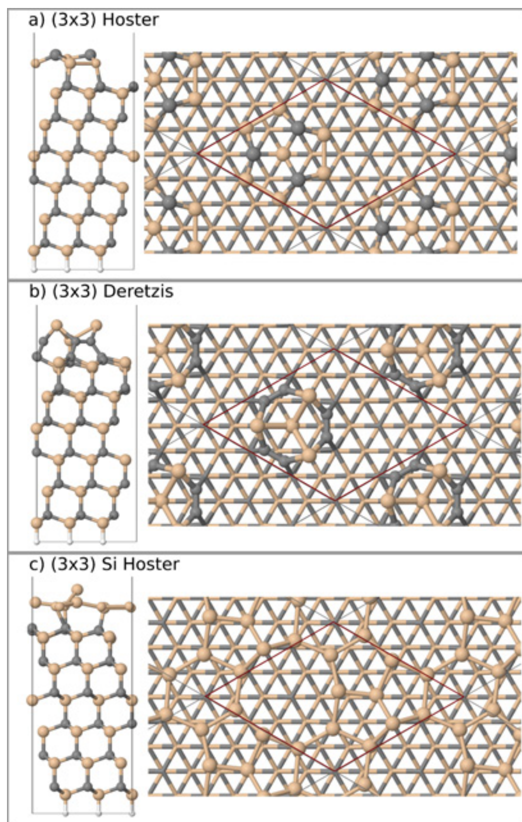

Figure 14.2.: All structural models based on the model proposed by Hoster *et al.* [145] for the (3×3) reconstructions of the 3C-SiC($\bar{1}\bar{1}\bar{1}$) are shown in a side and top view. In the top view the unit cell is marked in red. We include three different chemical compositions: (a) from Hiebel *et al.* [139], (b) from Deretzis and La Magna [71], (c) as a plain Si adatom.

In the following, we discuss the structural model of the (3×3) reconstruction included in our analysis. On the basis of these characteristics various alternative structural models for the (3×3) reconstruction on the C terminated surface have been proposed in the literature [145, 139, 71, 192]. We here briefly discuss the alternative surface reconstructions of the 3C-SiC($\bar{1}\bar{1}\bar{1}$) surface:

We start with a geometric configuration for the (3×3) reconstruction suggested by Hoster, Kulakov, and Bullemer [145][1]. On the basis of STM measurements they constructed a model consisting of an adcluster containing 10 atoms. On top of the truncated SiC surface forms 3 dimers arrange in a hexagon with an additional atom in the middle of the hexagon. The remaining 3 adatoms are adsorbed on top of the hexagon (see Fig. 14.2 a). The unit cell contains five dangling bonds. Two dangling bonds originate from the C atoms of the substrate and three from the top adatoms. Hoster *et al.* [145] did not specify the chemical composition of their model. Several modifications of the chemical composition have been proposed (shown in Fig. 14.2) [71, 139].

Figure 14.2 *a* shows a variation of the model suggested by Ref. [139]. This structure consists of a fractional bilayer with seven Si adatoms bonded to the substrate and three C adatoms.

[1]The structure was first calculated and discussed by Lazarevic [184]. We took the geometries from Ref. [184]. We adapted the structures to the lattice parameters given in Tab. 7.2 and postrelaxed the structure with the numerical settings given in Appendix B

The next structure, labeled *b* in Fig. 14.2, is a carbon rich model suggested by Deretzis and La Magna [71]. It changes of the chemical composition to six C adatoms forming a dimer ring and four Si adatoms. We added a modification with all adatoms chosen to be Si, Fig. 14.2 c) (from Lazarevic [184]).

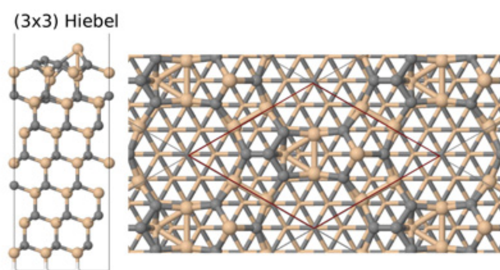

Figure 14.3.: A Si rich structural model for the (3×3) reconstructions shown in a side and top view from Ref. [139]. In the top view the unit cell is marked in red.

A new model was suggested by Hiebel *et al.* [139]. Their model consists of a Si-C-bilayer with a stacking fault of one half of the cell and two adatoms, a Si adatom and on the faulted side a C adatom, shown in Fig. 14.3 (This structure was not included in Ref. [184]).

For the (3×3) reconstruction on the Si- and C-terminated surface Li and Tsong [192] proposed a Si or C-rich tetrahedrally shaped cluster as adatoms. We tested three different chemical combinations shown in Fig. 14.4 (from Lazarevic [184][2]):

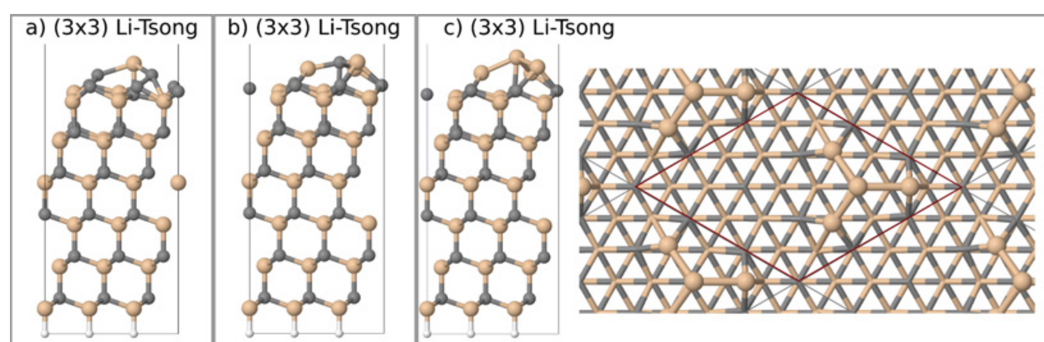

Figure 14.4.: Three different chemical compositions of the tetrahedral adcluster structure suggested by Li and Tsong [192]. In a) the tetrahedron is formed by a Si atom surrounded by three C atoms, b) three C atoms surrounding a Si atom (a) and b) shown in a side view), c) 4 Si atoms form a tetrahedron (side and top view)

The first tetrahedron is formed by a Si atom surrounded by three C atoms (see Fig. 14.4 a). The second one consists of three C atoms surrounding a Si atom (see Fig. 14.4 b) and the last tetrahedron we tested is formed by four Si atoms (see Fig. 14.4 c). For further analysis, we include the most stable cluster formed by four Si atoms shown in Fig. 14.4 c).

[2]The structure was first calculated and discussed by Lazarevic [184]. We took the geometries from Ref. [184]. We adapted the structures to the lattice parameters given in Tab. 7.2 and postrelaxed the structure with the numerical settings given in Appendix B

Next we include models for the (3×3) reconstructions, which were proposed originally for the Si side of SiC.

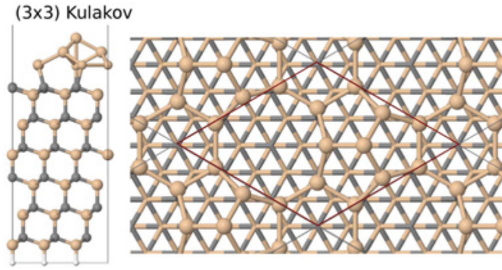

Figure 14.5.: A Si rich structural model for the (3×3) reconstructions adapted from the Si face [177]

First, the Si-rich structure for the 6H-SiC(0001)-(3×3) reconstruction shown in Fig. 14.5 by Kulakov *et al.* [177][3]. In this model dangling bond saturation is optimal with only one out of nine dangling bonds per (3×3) cell remaining.

We base our last model on the *Si twist model* [310, 277][3], known from the 3C-SiC(111)-(3×3) reconstruction (see Sec. 8.1.2). It is a silicon rich surface reconstruction. Figure 14.6 shows its geometry in a side view and from atop. The top bulk C layer is covered by a Si ad-layer forming heterogeneous Si-C bonds. Three Si adatoms form a triangle twisted by 7.7° with respect to the top SiC layer. In comparison, the twist angle on the Si side amounts to 9.3° (see Sec. 8.1.2)). The topmost Si adatom is positioned on top of the triangle.

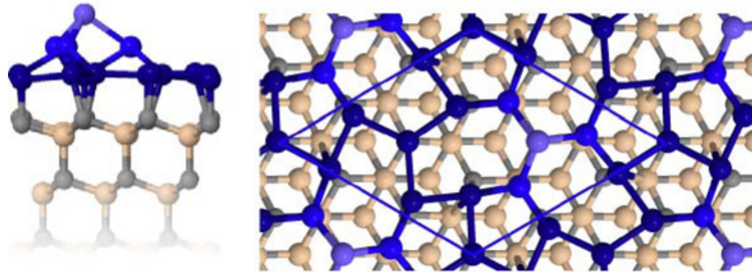

Figure 14.6.: The Si twist model adapted from the 3C-SiC(111)-(3 × 3) reconstruction Sec. 8.1.2. On the left: The Si twist model from a side view. On the right: The Si twist model from a top view. The unit cell is shown in blue. The Si adatoms are coloured depending on their distance to the top Si-C-bilayer: The nine ad-layer Si atoms in dark blue, the three Si adatoms on top of the ad-layer in blue and the top Si adatom in purple. (Figure published in Ref. [228])

In Chapter 4, we showed that for finding the most likely (3×3) reconstruction, a good indicator is a comparison of the respective surface free energies as introduced in Chapter 4. As before, we neglect vibrational and configurational entropy contribution to the free energy, although in the coexistence

[3]The structure was first calculated and discussed by Lazarevic [184]. We took the geometries from Ref. [184]. We adapted the structures to the lattice parameters given in Tab. 7.2 and postrelaxed the structure with the numerical settings given in Appendix B

region they might lead to small shifts.

In Figure 14.7, we show the the relative surface energy γ as a function of $\Delta\mu_C = \mu_C - E_C^{bulk}$ (Eq. 4.9) using PBE+vdW for the $(2\times2)_C$ surface model by Seubert *et al.* [292] (Sec. 14.1.1) and the different models for the SiC-(3×3) reconstruction introduced above. All surface energies are in eV per area of a (1×1) SiC unit cell. In Section 4.2 we found that the chemical potential limits of the C and Si reservoirs are fixed by the requirement that the underlying SiC bulk is stable against decomposition (see also Sec. 4.2 or Ref. [227]). Because of the close competition between the diamond and graphite structure for C (see Appendix A or [23, 347, 348]), we include both limiting phases in our analysis.

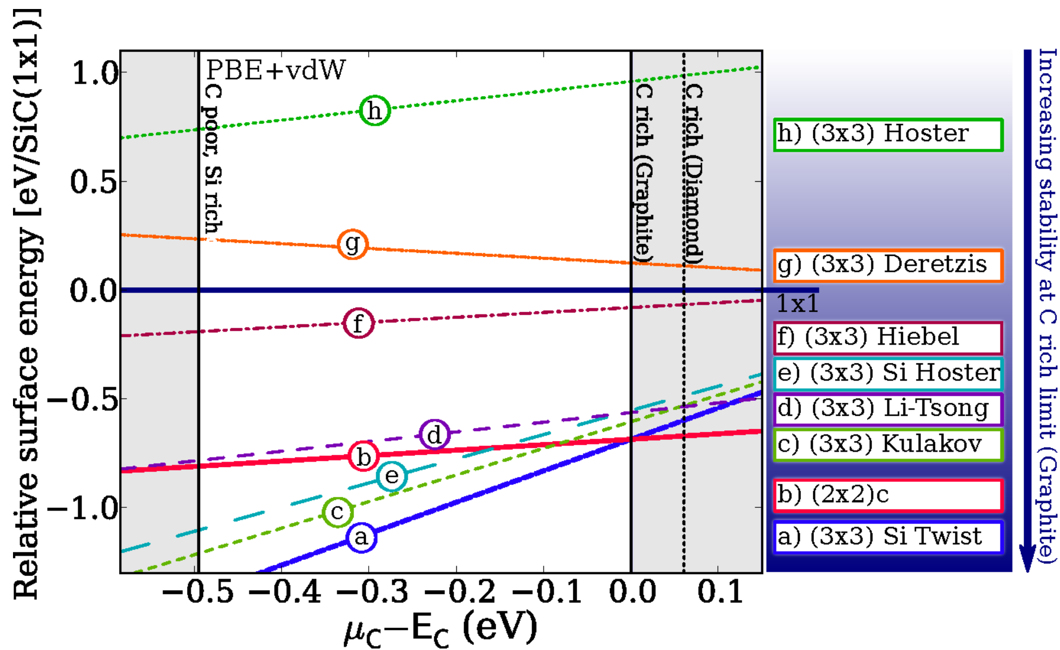

Figure 14.7.: Comparison of the surface energies relative to the bulk terminated (1×1) phase as a function of the C chemical potential within the allowed ranges (given by diamond Si, graphite C and for completeness diamond C, respectively). The shaded areas indicate chemical potential values outside the strict thermodynamic stability limits. Included in the surface energy diagram are structure models as proposed for the C face [(b) [292] Sec. 14.1.1, (d) [192] Fig. 14.4 c), (e) Fig. 14.2 c) and (h) [145] with the chemical composition given by [139] Fig. 14.2 a), (f) [139] Fig. 14.3, (g) [71] Fig. 14.2 b] and models adapted from the Si face [(a) [310] Fig. 14.6 and (c) [177] Fig. 14.5]. In the right panel the different models for the (3×3) reconstructions of the 3C-SiC($\bar{1}\bar{1}\bar{1}$) are ordered by their surface energies in the graphite C limit of the chemical potential with increasing stability from top to bottom. (Figure published in Ref. [228])

The structure with the lowest energy for a given $\Delta\mu_C$ corresponds to the most stable phase. The most stable phase in surface diagram (Fig. 14.7) is the (3×3) Si twist. The four most stable models in the surface diagram (Fig. 14.7)

are structure (a) the (3×3) Si twist with 13 Si adatoms (see Fig. 14.6), (c) (3×3) Kulakov from Ref. [177] with 11 Si adatoms (see Fig. 14.5), (e) (3×3) Si Hoster with 10 Si adatoms (see Fig. 14.2 c) and (d) (3×3) Li-Tsong from Ref. [192] with 4 Si adatoms (Fig. 14.4 c). These four structures have in common that they only include Si atoms in their adatom structures.

The three remaining less favourable structures Fig. 14.7 (f,g and h) include a mixture of Si and C atoms in their reconstructions. A comparison of the different models shown in Fig. 14.7 indicate that Si rich (3×3) reconstructions are energetically preferred. However, we did not include enough structures in our comparison to conclusively show this trend.

14.1.3. The Si Twist Model

In the surface diagram (Fig. 14.7 of Sec. 14.1.2), the Si twist model adapted from the 3C-SiC(111)-(3 × 3) phase (Ref. [310] and Sec. 8.1.2) has the lowest energy of all previously proposed (3×3) models (Sec. 14.1.2). Its formation energy crosses that of the $(2\times2)_C$ phase just at the C-rich limit (graphite) of the chemical potential with a surface energy difference of 0.47 meV in favour of the Si twist reconstruction. To coexist with the $(2\times2)_C$ phase and to be present at the onset of graphite formation, the (3×3) phase has to cross the graphite line very close to the crossing point between the graphite line and the $(2\times2)_C$ phase. The Si twist model shown in Fig. 14.8 satisfies this condition.

In Figure 14.8 I we show the surface energetics of the coexisting phases $(2\times2)_C$ and the Si twist model using the higher level HSE06+vdW functional with fully relaxed structures including spin-polarisation and unit cells (Tab. 7.2). As can be seen, the phase coexistence does not depend on the chosen functional. However, to distinguish between a phase coexistence or a close competition between the two phases, the inclusion of entropy terms would be the next step [86].

In Section 14.1.2 we summarised the experimentally observed characteristics of the (3×3) reconstruction. Next, we will show that Si twist model for the (3×3) reconstruction based on a Si-rich termination well-captures the various surface characteristics:

Si-rich:
In agreement with the AES experiments [145, 24] our model is Si-rich.

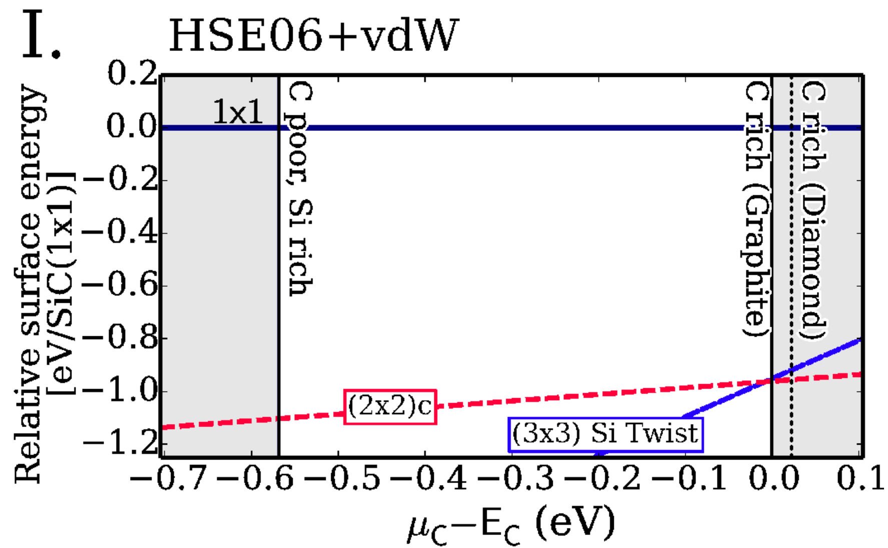

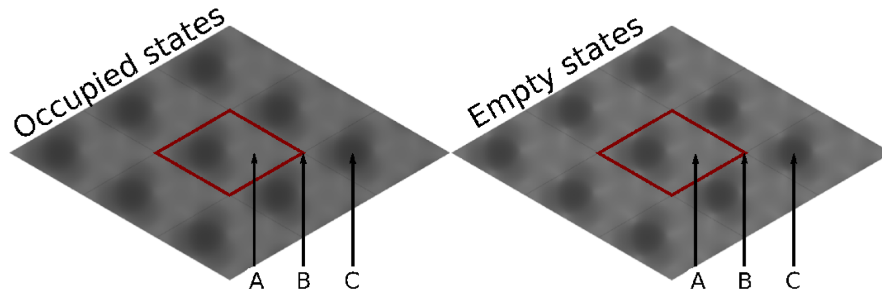

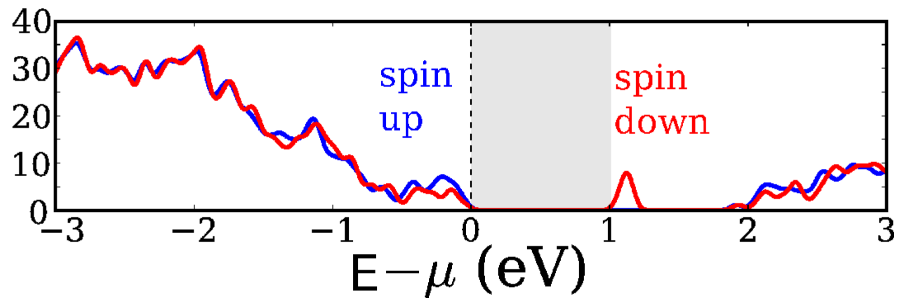

Figure 14.8.: I: The a) and b) phases from Fig. 14.7 calculated using the HSE06+vdW exchange-correlation functional with fully relaxed structures and unit cells (Tab. 7.2). II: Simulated constant current STM images for occupied- and empty-state of the Si twist model (unit cell shown in red). The three points of interest (A, B, C) are marked by arrows and labeled according to Hiebel *et al.* [139]. III: The DOS for the spin-up and spin-down states clearly shows a band gap rendering the surface semiconducting. (Figure published in Ref. [228])

Triagonal adatom structure seen in STM:
The atomic structure includes triangular Si adatom (see Fig. 14.6) consistent with the filled-state STM image [71, 139]. Our simulated STM images Fig. 14.8 (II) reproduce the measured height modulation, [139] but the experimentally observed difference in intensity between occupied and empty-state images is not captured by our simulated images.

Semiconducting:
We performed a spin-polarised calculation of the electronic structure using HSE06. Figure 14.8 (III) shows the DOS for the spin-down (in red) and spin-up (in blue) channel. The DOS clearly demonstrates that the surface is semiconducting in agreement with STS experiment [140], featuring a band gap of 1.12 eV (Exp. 1.5 eV Ref. [140]). In the DOS the spin-down surface state gives rise to a peak in the SiC bulk band gap above the Fermi level. On the other hand the spin-up surface state is in resonance with the SiC bulk states.

The disagreement in the STM images might be an indication that a different structure is observed in the STM measurements. An exhaustive structure search to find a surface model that is even lower in energy than the Si twist model and that reproduces all experimental observations, including the STM images, is desirable. However, if an alternative model were to be found, its surface energy would have to be close to the Si twist model at the graphite line to still coexist with the $(2\times2)_C$ phase. As a result, it would very likely coexist with the Si twist model. The conceptual Si twist model - inspired by the Si side - appears to satisfy the existing experimental constraints well.

14.2. Assessing the Graphene and SiC Interface

In the following, we will use the Si twist model (Sec.14.1.3) as a representative model to shed light on the SiC-graphene interface on the C face. Depending on the specific growth conditions two qualitatively different interface structures are observed. In one case, the first carbon layer is strongly bound to the interface and in the other case it is weakly bound.

For the experimenatly observed strongly bound interface, it is unclear, whether the different groups observe the same structures. Based on their LEED diffraction pattern, Srivastava *et al.* [302] proposed a $(\sqrt{43} \times \sqrt{43})$-

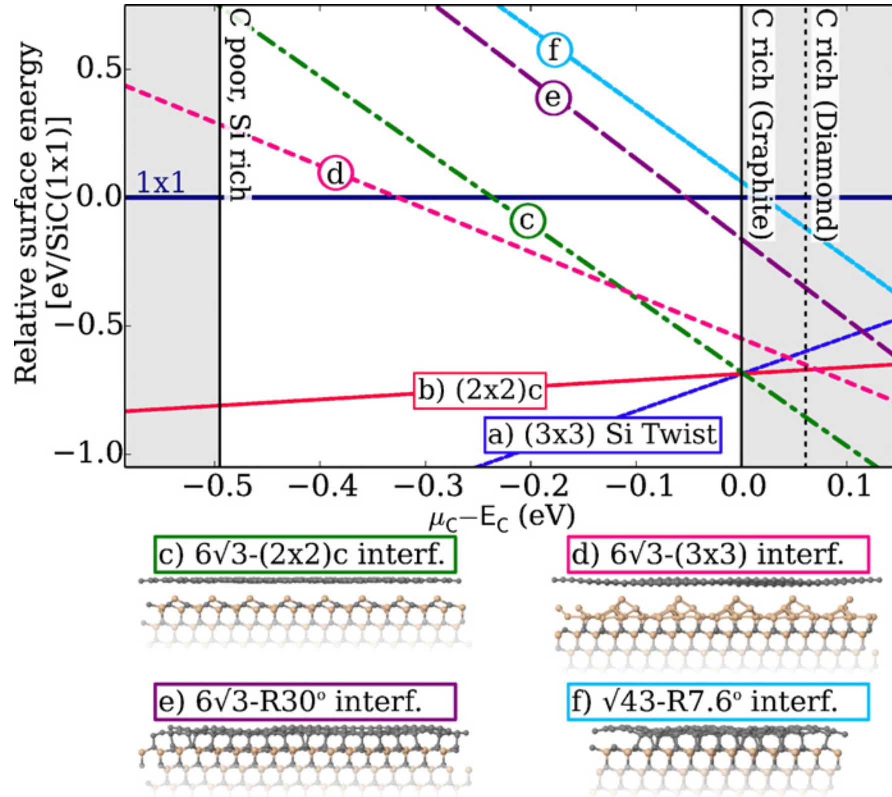

Figure 14.9.: Comparison of the surface energies for four different interface structures of 3C-SiC($\bar{1}\bar{1}\bar{1}$), relative to the bulk-truncated (1×1) phase, as a function of the C chemical potential within the allowed ranges (given by diamond Si, diamond C or graphite C, respectively), using the graphite limit as zero reference. In addition, the known $(2\times2)_C$ reconstruction and the (3×3) Si twist model are shown. (Figure published in Ref. [228])

R±7.6° SiC substrate with a (8×8) carbon mesh rotated by 7.6° with respect to the substrate ('$\sqrt{43}$-R7.6°') [302].

Figure 14.9 shows a surface diagram including the $(2\times2)_C$ (see Sec. 14.1.1) reconstruction and the (3×3) Si twist model (Sec.14.1.2) from Fig.14.7. In addition, we include 4 different SiC-graphene interface structures. Two models represent the weakly bound C layer at the interface (Fig. 14.9 c-d) and two models the strongly bound C layer at the interface shown in Fig. 14.9 e-f.

As a first step, we constructed the strongly bound interface structures. We construct an interface structure similar to the ZLG phase known from the Si face (see Sec. 8.2)- a 6 $\sqrt{3}$-R30°-interface[4], labeled *e* in Fig. 14.9. As a second

[4]The structure was first calculated and discussed by Lazarevic [184]. We took the geometries from Ref. [184]. We adapted the structures to the lattice parameters given in Tab. 7.2 and postrelaxed the structure with the numerical settings given in Appendix B

structure, we included a purely C based model of the $\sqrt{43}$-R 7.6°-interface[5] as described above, labeled f in Fig. 14.9.

As a next step, we built the two weakly bound structures. To model the interface, we limited our study to a 30° rotation between the substrate and the graphene film. This choice was motivated by the LEED study of Hass *et al.* [131], who showed that graphene sheets on the C face appear mainly with a 30° and a ±2.2° rotation. A 30° rotation has also be seen in STM measurements for the graphene covered (2×2) and (3×3) phases [141], from here on called $(2\times2)_G$ (Fig. 14.9 c) and $(3\times3)_G$ (Fig. 14.9 d). We therefore chose a $(6\sqrt{3} \times 6\sqrt{3})$ SiC supercell, covered by a (13×13) graphene cell rotated by 30° with respect to the substrate.

The $(2\times2)_G$-interface covers 27 unit cells of the $(2\times2)_C$ reconstruction. Our model of the graphene covered (3×3) phase consist of the same (13×13) graphene supercell, covering 12 units of the (3×3) Si twist model.

The surface energies for the four different interface structures of the 3C-SiC$(\bar{1}\bar{1}\bar{1})$ surface are shown in the phase diagram in Fig. 14.9. All surface energies are calculated using PBE+vdW for the fully relaxed interface structures. The surface energies are given relative to the bulk-truncated (1×1) phase, as a function of the C chemical potential within the allowed ranges.

The 6 $\sqrt{3}$-R30°-interface crosses the graphite line 0.46 eV above the crossing point of the (3×3) Si twist model, rendering it unstable. In our calculations, the $\sqrt{43}$-R 7.6°-interface is even higher in energy than the $6\sqrt{3}$-R30°-interface. The $\sqrt{43}$-R 7.6°-interface is grown reproducibly and observed in LEED [206, 302, 303], however its detailed atomic structure is unknown [135]. A recent LEED analysis indicates that the experimentally observed $\sqrt{43}$-R 7.6°-interface involves a graphene-like layer witH-intercalated Si atoms between this layer and a hydrogenated SiC C-face surface [85].

The $(2\times2)_G$-interface crosses the $(2\times2)_C$ reconstruction just to the right of the graphite limit at a chemical potential of 2 meV and a surface energy of −0.69 eV. This finding demonstrates that the observed (2×2) LEED pattern underneath the graphene layer is indeed consistent with the well known $(2\times2)_C$ reconstruction. The surface energy difference between $(2\times2)_G$- and the $(3\times3)_G$-interface amounts to 0.13 eV at the graphite line, favouring the $(2\times2)_G$-interface.

[5] The structure was first calculated and discussed by Lazarevic [184]. We took the geometries from Ref. [184]. We adapted the structures to the lattice parameters given in Tab. 7.2 and postrelaxed the structure with the numerical settings given in Appendix B

The two strongly bound interface models, the $6\sqrt{3}$-R30°- and $\sqrt{43}$-R 7.6°-interface have both a comparatively high surface energy compared to the $(2\times2)_C$ reconstruction.

Already in Sec. 14.1.2 for the different models of the (3×3) reconstruction, it seemed that the formation of Si-C bonds with the surface C atoms is energetically favourable. This can be understood in terms of the enthalpy of formation ΔH_f Def. 4.2.2. The enthalpy of formation for SiC is quite large (-0.77 eV in experiment [168], -0.56 eV in DFT-PBE+vdW and -0.59 eV in DFT-HSE06+vdW (Tab. 7.2)), favouring the formation of SiC bonds. This explains why the $(2\times2)_C$ and (3×3) Si twist model are more stable, because they contain a large number of Si-C bonds. Conversely, the $6\sqrt{3}$-R30°- and the $\sqrt{43}$-R 7.6°-interface are made up of energetically less favourable C-C bonds, which increases the surface energy considerably.

To put our results into context, we revisit the growth process. In experiment, growth starts with a clean (3×3) reconstruction. The sample is annealed until the surface is covered by graphene. At this stage, the (3×3) reconstruction is the dominant phase underneath graphene [139]. However, a shift from the SiC (3×3) to the $(2\times2)_C$ surface reconstruction at the SiC-graphene interface can be stimulated by an additional annealing step at a temperature below graphitisation (950C° - 1000C°) leaving the graphene layer unaffected [139]. Graphene growth starts at a point where bulk SiC decomposes. The interface is determined by the momentary stoichiometry at which the sublimation stopped – a coexistences of different phases is observed. The final annealing step shifts the chemical potential into a regime in which SiC bulk decomposition stops and the graphene layer does not disintegrate, but the SiC surface at the interface moves closer to local equilibrium, in agreement with the phase diagram in Fig. 14.9, forming an interface structure between the $(2\times2)_C$ reconstruction and graphene. In our view, the main difference between the Si face and the C face is the fact that Si-terminated phases are more stable on the C face due to the formation of heterogeneous Si-C bonds. The Si-rich phases are thus stable practically up to the graphite line, allowing the surface to form graphene only at the point where bulk SiC itself is no longer stable. This makes MLG growth on the C side more difficult than on the Si face.

14.3. Summary

In summary, we shed new light on the central aspects of the thermodynamically stable phases that govern the onset of graphene formation on SiC($\bar{1}\bar{1}\bar{1}$). We showed that a Si-rich model, represented by the Si twist model, reproduces the experimental observations - Si-rich and semiconducting. We also used the $(2\times2)_C$ and the (3×3) Si twist model as interface structures. We argue that the formation of C face surface MLG is blocked by Si-rich phases in the same chemical potential range in which MLG formation can be thermodynamically controlled on the Si face, making the growth of homogeneous MLG much more difficult on the C face.

Conclusions

Silicon carbide (SiC) is a widely used substrate for epitaxial growth of mono- and few-layer graphene. The exact material properties of graphene depend on their interaction with the substrate. In this work, we applied the *ab initio* atomistic thermodynamic formalism (Ch. 4) to evaluate the interface structure of epitaxial graphene on the silicon (Si) and carbon (C) face of SiC, applying all-electron density-functional theory (DFT) based on Perdew-Burke-Ernzerhof generalised gradient approximation [246] (PBE) and HSE hybrid functional with α=0.25 and ω=0.11 bohr^{-1} [175] (HSE06) including van-der-Waals effects [326]. The C-rich limit of the chemical potential is of particular interest for the thermodynamic evaluation of the combined SiC-graphene surface structures. The limiting structures in the C-rich limit are diamond and graphite. However, the very small difference in binding energy between diamond and graphite (see Ch. 6) necessitate an accurate description of their energetics. This is a challenge for theory in particular the description of the interlayer bonding between graphite sheets. In graphite the atomic bonding is very inhomogeneous. The in-plane bonds are formed by strong sp^2-hybridised C orbitals. The bonding between graphene sheets on the other hand is formed by weak van-der-Waals (vdW) forces. Accurately determining the inter-planar binding energy necessitates the inclusion of long-range vdW effects which is a major and ongoing experimental and theoretical quest (Sec. 6.2).

On the Si-terminated SiC surface, wafer-size, well-ordered areas of graphene form as $(6\sqrt{3} \times 6\sqrt{3})$-R30° $(6\sqrt{3})$ commensurate periodic films [332, 95, 82, 263, 67, 302, 346]. We address how the substrate affects the atomic structure Ch. 8 and the energetics of the different Si-rich reconstructions Ch. 10 and the C-rich surface structures from the first, partially covalently bonded zero-layer graphene (ZLG) via mono-layer graphene (MLG) and bi-layer graphene (BLG), up to three-layer graphene (3LG), a challenge, because of the system sizes up to $\sim$ 2800 atoms and vdW interactions, not accounted for by most standard density functionals. We found narrow *thermodynamic* equilibrium conditions for the ZLG, MLG and even BLG. The equilibrium geometry emerged as a direct prediction, including the significant graphene layer corrugation. The remaining difficulty will be to find the precise Si partial pressure and temperature in experiment, an important step towards equilibrium graphene growth.

In Chapter 9, we compared different approximated interface models of the experimentally observed $6\sqrt{3}$-ZLG structure. We also show that smaller-cell

approximants may miss some geometric features, and could erroneously stabilise hexagon-pentagon-heptagon (H5,6,7) defects due to artificially induced strain. The bonding in the $6\sqrt{3}$-ZLG layer contains a mixture of in-plane sp^2-like and sp^3-like hybridisation of the carbon atoms. The C atoms with sp^3-like hybridisation covalently bind the ZLG layer to the SiC substrate with an increased in-plane C-C bond length (compared to free standing graphene). This explains the increased lattice parameter of the ZLG layer observed in grazing-incidence x-ray diffraction (GID) measurements [283].

Some of the Si atoms in the top SiC bilayer are covalently bonded to the ZLG layer, while others remain unsaturated, the *Si dangling bonds*. We used DFT PBE including van-der-Waals effects [326] (PBE+vdW) and HSE06+vdW calculations to evaluate the influence of the Si dangling bonds on the electronic structure of the C-rich surface phases on 3C-SiC(111) (Ch. 12). Using the $\sqrt{3}$ approximated interface structure, we found that the ZLG, MLG and BLG is doped by the Si dangling bond state at the Fermi level. The doping of the graphene layer can be removed by saturating the Si dangling bond with an H atom. The situation in the $(6\sqrt{3} \times 6\sqrt{3})$-R30° is less clear. In the density of states (DOS) of the $6\sqrt{3}$-ZLG structure, we found a few states close to the Fermi level in good agreement with scanning tunnelling spectroscopy (STS) measurements [270, 109]. A Hirshfeld atomic charge partitioning analysis [142] revealed one hexagonal and two triangular shaped pattern per unit cell similar to those found in scanning tunnelling microscopy (STM) images by Qi *et al.* [256].

A possibility to eliminate the effects of the Si dangling bonds on the epitaxially grown graphene layer is to saturate the Si atoms at the interface by H atoms. Indeed H intercalation of epitaxial graphene on the Si face of SiC decouples the graphene layer from the substrate forming quasi-free-standing mono-layer graphene (QFMLG) [262]. As described in Chapter 13, we found the adsorption height QFMLG layer calculated in the full $(6\sqrt{3} \times 6\sqrt{3})$-R30° unit cell to be in excellent agreement with normal incidence x-ray standing wave (NIXSW) experiments. The corrugation is drastically reduced when compared to the MLG layer and the electron density at the interface is very homogeneous. All these features improve the electronic properties of QFMLG compared to epitaxial MLG.

In contrast to graphene growth on the Si face, experimentally controlling the layer thickness on the C face is significantly more challenging [213]. To refine the growth quality of epitaxial graphene on the C side of SiC and improving the resulting electronic character of these films, it is important to understand the atomic interface structure. A phase mixture of different

surface phases is observed when surface graphitisation first sets in. However, the atomic structure of some of the competing surface phases as well as of the SiC-graphene interface are unknown. We calculated the formation energy of different reconstructions and model systems for the interface and compared the different structures within the thermodynamically allowed range. We showed that the Si-rich *Si twist model* reproduces the experimental observations - Si-rich and semiconducting - of the hitherto unknown 3×3-SiC($\bar{1}\bar{1}\bar{1}$) reconstruction. Its formation energy crosses that of the $(2\times2)_C$ phase just at the carbon rich limit of the chemical potential, which explains the observed phase mixture. We used the $(2\times2)_C$ and the (3×3) *Si twist model* as interface structures. Our results indicate that the formation of an interface structure like the ZLG on the Si-terminated surface is blocked by Si-rich phases. This answers the key question why the graphene growth differs strongly between the C and Si-terminated surface.

In conclusion, graphene films on the Si face of SiC form at least as near-equilibrium phases. The remaining challenge is to find the necessary Si partial pressure and growth temperature and keep them constant close to the surface. This makes the Si-terminated surface an ideal substrate for graphene growth. The ZLG interface structure – which aids the graphene growth – on the other hand leads to a corrugation of the graphene film and influences its electronic structure by states close to the Fermi level originating from the Si dangling bonds. By H intercalation the Si bonds at the SiC-graphene interface are saturated lifting the ZLG layer up forming QFMLG. The QFMLG is flat and undoped featuring a homogeneous charge density at the interface. The same mechanism which leads to graphene growth on the Si face fails on the C face, because here the formation of a regulating interface structure like the ZLG layer is hindered by Si-rich surface reconstructions.

Appendices

A Thermal Expansion and Phase Coexistence

In 1938, the first phase diagram for carbon was constructed on the basis of thermochemical data for temperatures up to 1200 K by Rossini and Jessup [268]. Although both forms of carbon, diamond and graphite, exist in nature, their phase diagram revealed that only graphite is thermodynamically stable at standard conditions for temperature and pressure (normal conditions)[1]. Fortunately, the rate of reversion from diamond to graphite is insignificant under normal conditions and only measurable at temperatures above 1000 K. On the basis of theoretical considerations, Berman and Simon [23] extended the phase line between diamond and graphite to temperatures higher than 1200 K. This linear extrapolation of the form $p = a + bT$, where p is the pressure and T the temperature, is known as the *Berman-Simon line*. Since then, the interest in the phase diagram of carbon continued experimentally [44, 162, 43], as well as theoretically [205, 164, 103, 349, 120].

The following Sections are a brief outline of our results presented in the Master thesis by Florian Lazarevic [184] about the phase coexistence line between graphite and diamond in the temperature range from 0 to 2000 K. Temperature effects are included by calculating the Helmholtz free energy $F(T, V) = E(V) + F^{vib}(T, V)$ (Eq. 4.7), where $E(V)$ is the volume dependent total energy and F^{vib} is the vibrational free energy introduced in Sec. 4.1.

At constant pressure, the equilibrium volume of a material changes with temperature. In Sec. 4.1, we saw that the thermal expansion can be understood in terms of lattice vibrations. We introduced the quasiharmonic approximation (QHA) to calculate the volume dependent potential energy surface. The basic assumption of the QHA is that the anharmonicity is restricted to the change of the volume without any further anharmonicities, so that the lattice dynamics can still be treated within the harmonic approximation (Ch. 3). The equilibrium volume for every temperature is given by minimising $F(T, V)$ with respect to the volume at a fixed T.

The potential energy surface (PES) is sampled by calculating the Helmholtz free energy (Eq. 4.7) for different volumes. Then, the equilibrium volume is calculated by fitting the $F(T, V)$ pairs to the Birch-Murnaghan (B.-M.) equation of states Def. 6.1.1 for every temperature T [223, 27].

[1] The National Institute of Standards and Technology (NIST) defines the standard conditions for temperature as 293.15 K (20°C) and the absolute pressure as 1 atm (101.325 kPa)

Temperature [K]		288	423	573	723	873	973	1073
$V/atom$ [Å^3]	PBE+vdW	8.788	8.802	8.819	8.839	8.864	8.883	8.904
	PBE-D [117] Ref. [349]	8.700	8.722	8.757	8.791	8.817	8.837	8.860
	Exp. Ref. [226]	8.744	8.773	8.808	8.846	8.885	8.912	8.939

Table A.1.: Calculated unit cell volume of graphite in the temperature range between 288 K and 1073 K. For comparison DFT data using vdW Grimme [117] corrected PBE-D (Ref. Yu *et al.* [349]) and experimental data (Ref. Nelson and Riley [226]).

As a next step the thermal expansion of graphite and diamond is calculated within the QHA (Sec. 4.1). To calculate the vibrational free energy, we used the finite displacement method (Ch. 3). We obtained the vibrational free energy for different volumes from phonon calculations for diamond and graphite. In the case of diamond we included 5 different volumes ranging from 5.28 Å^3/atom to 5.95 Å^3/atom. For the phonon calculations, we used a $(3 \times 3 \times 3)$ supercell (*SC*) for diamond. For graphite we calculated the vibrational free energy in a $(5 \times 5 \times 2)$ *SC* for 4 different volumes ranging from 8.10 Å^3/atom to 8.70 Å^3/atom. For each volume we included 5 calculations to optimise the ratio between the lattice parameter a and c to find the minimum Helmholtz free energy.

Figure A.1 shows the fitting results at 4 different temperatures (0 K, 300 K, 700 K and 1500 K) for graphite and diamond. The energy for the chosen volumes are shown in Fig. A.1 as crosses for diamond and squares for graphite. The volumes were chosen close to the ground state equilibrium volume as given in Tab. 6.2.

In the range between 0 K and 2000 K the equilibrium volume and corresponding Helmholtz free energies was obtained by the fitting procedure explained above. For high temperatures > 2000 K the inclusion of anharmonic effects becomes relevant. To include them, we would need to go beyond the QHA. We are interested in the temperature range < 2000 K. To ensure the quality of the data, we only included data with a root mean square fitting error of the B.-M. smaller than 7 meV.

The thermal expansion of graphite and diamond is shown in Fig. A.2. For diamond, we included experimental x-ray data [320]. Our computed thermal expansion shows good agreement with experiment. At 293.15 K Thewlis and Davey measured the diamond lattice constant to be 3.567 Å, our calculated lattice constant at 293.15 K is 3.568 Å.

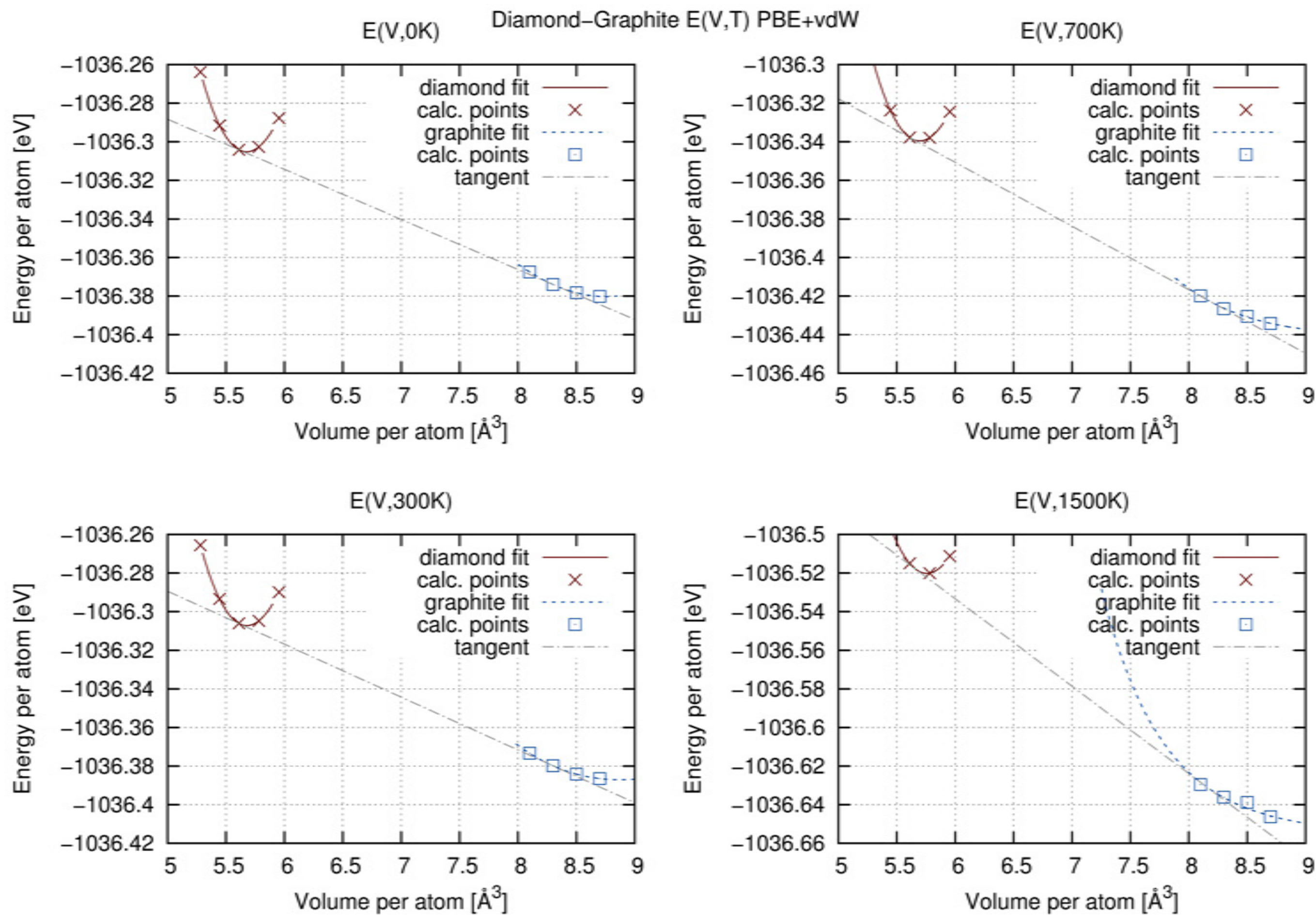

Figure A.1.: Calculated Helmholtz free energies within the BO-approximation as a function of the volume per atom for graphite and diamond at 4 different temperatures (0 K, 700 K, 1500 K and 3000 K) using PBE+vdW. The B.-M. fit is shown as red solid line (blue dashed line) for diamond (graphite). The calculated points used for the fitting are shown as crosses (squares) for diamond (graphite). The phase transition line - a tangent to both curves Eq. A.2 - between graphite and diamond is shown. [Plot taken from Lazarevic [184]]

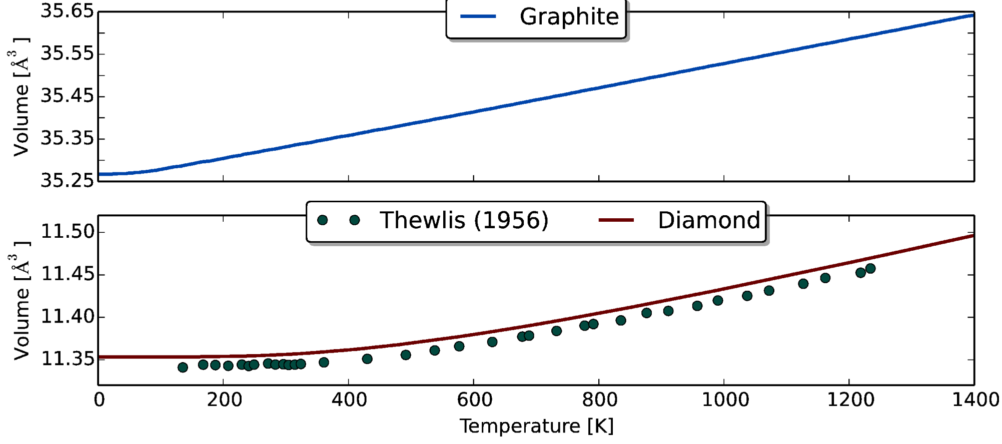

Figure A.2.: The unit cell volume for graphite (top panel) and diamond (bottom panel) for temperatures ranging from 0 K to 1400 K calculated using PBE+vdW. [Data taken from Lazarevic [184]] For comparison, experimental x-ray measurements data from Thewlis and Davey [320] is included for diamond as green circles.

For graphite, we listed the volume per atom for temperatures between 288 K and 1073 K in Tab. A.1. The temperatures were chosen to be the same as listet in Ref. Nelson and Riley [226]. For comparison, we included *ab initio* (*ab initio*) data from Yu *et al.* [349] in the QHA and experimental data from Nelson and Riley [226]. Yu *et al.* used the *abinit*-code, a plane-wave and pseudopotential code, [110] to calculate the temperature dependent volume of graphite using the vdW[117] corrected Perdew-Burke-Ernzerhof generalised gradient approximation [246] (PBE) exchange-correlation functional (PBE-D). They fitted the equation of states to 11 E(V) data points. At each fixed volume they performed a constant-volume optimisation of the cell geometry to get the optimal lattice constant ratio c/a. Nelson and Riley used a x-ray powder method to measure the temperature dependence of the unit-cell dimensions of hexagonal Ceylon graphite. The stacking order of hexagonal Ceylon graphite is ABC [11], while in the theoretical work , this work and Yu *et al.* [349], an AB stacking was used. The largest disagreement between our results and the reference data is at 288 K, here the unit cell volume in this work is 1.0% larger than the value obtained by Yu *et al.* [349] and 0.5% larger than the experimental value [226].

In thermodynamics the pressure for the canonical ensemble is defined as

$$p(V,T) := -\left(\frac{\partial F(V,T)}{\partial V}\right)_T \tag{A.1}$$

This is the negative of the slope of the $F(T = const, V)$ curve at a constant temperature. For a specific temperature, both carbon phases - diamond and graphite - coexist at the pressure given by the common tangent of the

graphite and diamond free energy.

$$\begin{aligned} p_{coex} &= p_{dia} &= p_{gra} \\ -\left(\frac{\partial F}{\partial V}\right)_T &= -\left(\frac{\partial F_{dia}}{\partial V}\right)_T &= -\left(\frac{\partial F_{gra}}{\partial V}\right)_T \end{aligned} \tag{A.2}$$

For every temperature a coexistence pressure can be determined by calculating the common tangent. The obtained $p_{coex}(T)$ curve is called the coexistence line. The coexistence line gives the temperature/ pressure pair at which graphite and diamond coexist. The common tangent is shown in Fig. A.1 for 4 different temperatures. The volumes for graphite were chosen in such a way that the common tangent of graphite and diamond touches the $E(V)$ close to the calculated reference points. Figure A.3 shows the coexistence line in a pressure-temperature phase diagram for different exchange-correlation functionals. At a fixed temperature for pressure lower than p_{coex} graphite is the most stable phase and for pressure higher than p_{coex} diamond becomes more stable.

Experimental data from three different experiments are included in Fig. A.3. Bundy *et al.* [44] measured the coexistence line in a temperature range between 1500 to 2000 K and found that p_{coex} ranges from 4.9 GPa to 6.1 GPa. The second experiment was performed by Kennedy and Kennedy [162], who were able to reduce the error in the pressure determination. In the linear part of the coexistence line, they found for the Berman-Simon line $P = 0.194$ GPa $+ T\, 3.2 \cdot 10^{-3}$ GPa/K. There have been several theoretical attempts to predict the graphite-diamond coexistence line. In 2010, Khaliullin *et al.* [164] studied the graphite-diamond coexistence by employing a neural-network (NN) mapping of the generalised gradient approximation (GGA)-derived *ab initio* potential energy surface. They used the obtained potential to generate molecular-dynamics (MD) trajectories at the cost of force field MD simulations (nanosecond-long trajectories are required to study thermodynamics and mechanism of phases transitions [164]). This allowed them to go beyond the QHA. A comparison of their results with the experimental data [43], shown in Fig. A.3, reveals that the NN overestimates the transition pressure by approximately 3.5 GPa. However, their slope of the Berman-Simon line agrees well with the experimental findings, listed in Tab. A.2. Ghiringhelli *et al.* [103] used a long-range carbon bond order potential (LCBOPI+) to sample the potential free energy surface using MD simulations [103]. In the 1000-2000 K range, the coexistence line predicted by LCBOPI+ lies very close to the experimental line [43] at the onset correctly estimating the 0 K transition pressure. However, the slope in the low-temperature regime deviates from the experimental data [43].

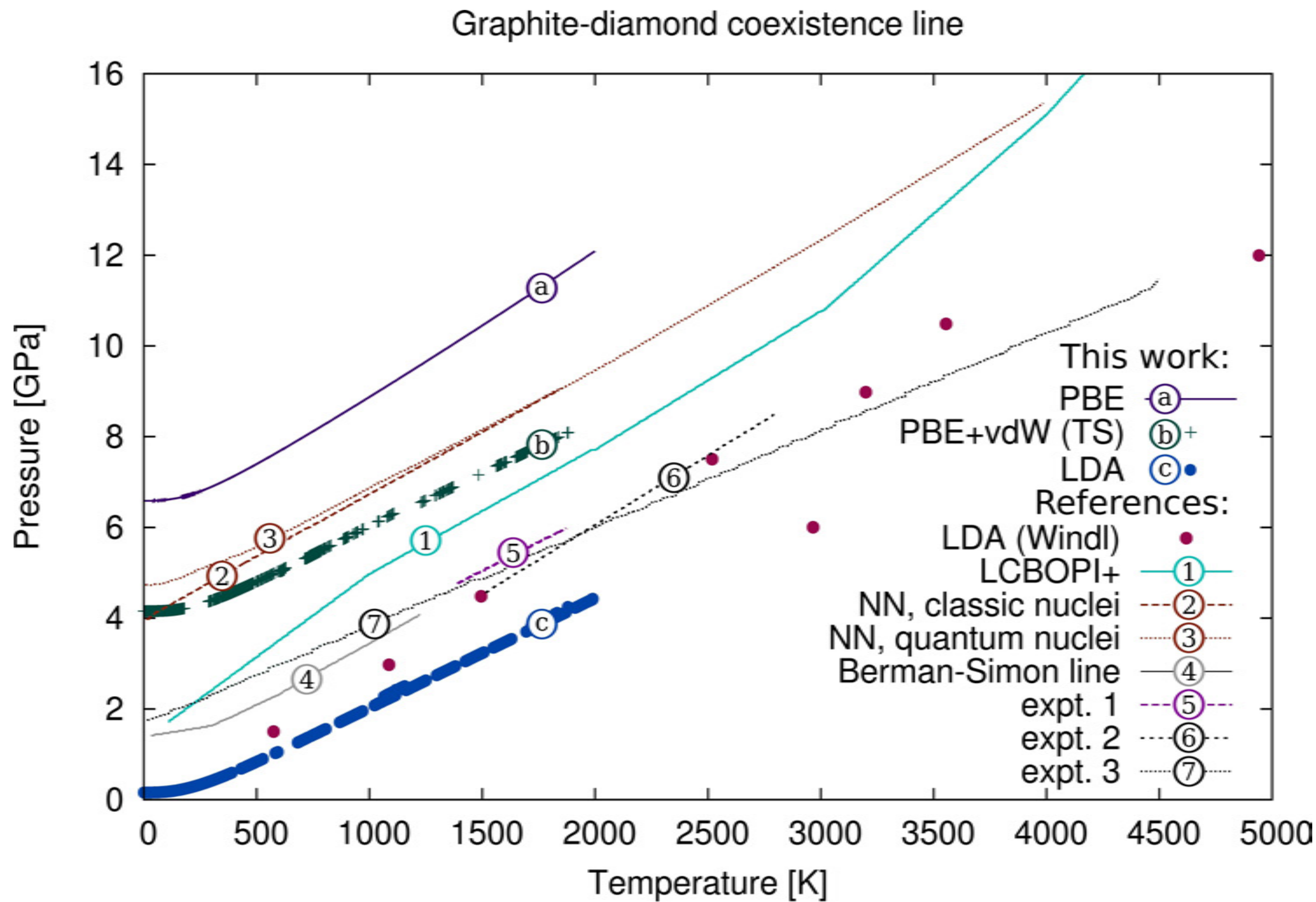

Figure A.3.: The graphite-diamond coexistence line is shown in a pressure-temperature phase diagram for different E_{XC}s;(a) PBE, (b) PBE+vdW and (c) LDA. For comparison previous calculations and experimental data are included in the plot: LDA (Windl) [205] (red), LCBOPI+ data (1) [103], neural-networking classical (2) and quantum nuclei (3) results [164], Bermann-Simon line (4) [23] and experimental data (Exp. 1 (5) [44], Exp. 2 (6) [162] and Exp. 3 (7) [43]). [Plot adapted from Lazarevic [184]]

	Functional				
	LDA	PBE	PBE+vdW		
a [GPa]	-0.37	5.6	3.7		
b [GPa/K]	$2.7 \cdot 10^{-3}$	$3.1 \cdot 10^{-3}$	$2.7 \cdot 10^{-3}$		
$p_{coex}(0K)$ [GPa]	0.2	6.6	4.2		
	References				
	theo.[(a)]	theo.[(b)]	exp.[(c)]	exp.[(d)]	exp.[(e)]
a [GPa]	1.7	3.7	0.19	0.71	1.7
b [GPa/K]	$2.5 \cdot 10^{-3}$	$2.8 \cdot 10^{-3}$	$3.2 \cdot 10^{-3}$	$2.7 \cdot 10^{-3}$	$2.2 \cdot 10^{-3}$
$p_{coex}(0K)$ [GPa]	1.6	4.7			1.8

Table A.2.: For the exchange-correlation functional (LDA, PBE, PBE+vdW) the linear interpolation of the p-T-data in the temperature range between 1000 K and 1500 K, to the Berman-Simon line, $P = a + bT$, where b is the slope in GPa/K. In addition the coexistence pressure p_{coex} at 0 K is given for different functionals. Reference data is given for two theoretical works (a) Yu *et al.* [349], (b) Khaliullin *et al.* [164] and experimental data (c) Kennedy and Kennedy [162], (d) Bundy *et al.* [44] and (e) Bundy *et al.* [43].

First we compare our results obtained with the PBE functional to the experimental data. For PBE, the transition pressure p_{coex} at 1500 K is overestimated by 5.5 GPa. If we include vdW-effects, the overestimation is reduced to 1.9 GPa, while LDA underestimates p_{coex} by 1.7 GPa. The energy difference between graphite and diamond is of the order of a few meV. For an accurate description of the transition pressure the exchange-correlation functional has to capture the E-V curve (Fig. A.1) for graphite and diamond equally good. It necessitates a highly accurate description of the ground state energy of these two systems, which is a challenge for density-functional theory (DFT). The difficulty of DFT functionals to correctly describe the graphite/diamond energetics, in particular the inter-planar bonding of graphite (see Sec. 6.2), leads to the observed systematic shift of the coexistence line in Fig. A.3.

We performed a linear interpolation of the p-T-data by fitting to the Berman-Simon line. The Berman-Simon line is defined as

$$p = a + bT, \tag{A.3}$$

where b is the slope in GPa/K. In experiment, the data is usually fitted in the temperature range from 1000 K to 2000 K. We use the same temperature

range for the fitting. The results are given in Tab. A.2 for different functionals and reference data. The Berman-Simon line shown in Fig. A.3 was obtained from experimental thermodynamic properties of diamond and graphite [23]. Its overall shape is well-captured by our calculations. The 0 K transition pressure, however, varies depending of the used functional.

Regardless of the energy errors introduced by the functional, the onset of the coexistence line at low temperatures is well described. In the linear regime the slope is well captured and in excellent agreement with experiment.

B.1. The Basis Set

The FHI-aims code employs numeric atom-centered basis sets; basic descriptions of their mathematical form and properties as introduced in Sec. 2.5 or in Ref. [32]. The FHI-aims basis sets are defined by numerically determined radial functions Eq. 2.28 corresponding to different angula momentum channels. Each radial function is obtained by solving a radial Schrödinger equation and is subject to a confinement potential $v_{\text{cut}}(r)$ in Eq. 2.28. It ensures that the radial function is strictly zero beyond the confining radius

	C	Si
minimal	[He]+2s2p	[Ne]+3s3p
tier 1	H(2p, 1.7)	H(3d, 4.2)
	H(3d, 6.0)	H(2p, 1.4)
	H(2s,4.9)	H(4f, 6.2)
		Si^{2+}(3s)
tier 2	H(4f, 9.8)	H(3d, 9.0)
	H(3p, 5.2)	H(5g, 9.4)
	H(3s, 4.3)	H(4p, 4.0)
	H(5g, 14.4)	H(1s, 0.65)
	H(3d, 6.2)	
	...	...

Table B.1.: Radial functions used for C and Si. The first line ("minimal") denotes the radial functions of the occupied orbitals of spherically symmetric free atoms as computed in DFT-LDA or -PBE (noble-gas configuration of the core and quantum numbers of the additional valence radial functions). "H(nl, z)" denotes a hydrogen-like basis function for the bare Coulomb potential z/r, including its radial and angular momentum quantum numbers, n and l. X^{2+}(nl) denotes a n, l radial function of a doubly positive free ion of element X. See also Ref. Blum *et al.* [32] for notational details.

r_{cut} and decays smoothly.

What is important for the present purposes is to demonstrate the accurate convergence, up to a few meV at most, of our calculated surface energies with respect to the basis set used. As is typical of atom-centered basis sets (Gaussian-type, Slater-type, numerically tabulated etc.), variational flexibility is achieved by successively adding radial functions for individual angular momentum channels, until convergence is achieved. In practice, the basis functions for individual elements in FHI-aims are grouped in so-called "tiers" or "levels": *tier 1*, *tier 2*, and so forth. In the present work, basis functions for Si and C up to *tier 2* were used. The pertinent radial functions are summarised in Table (B.1), using the exact same notation that was established in Ref. [32].

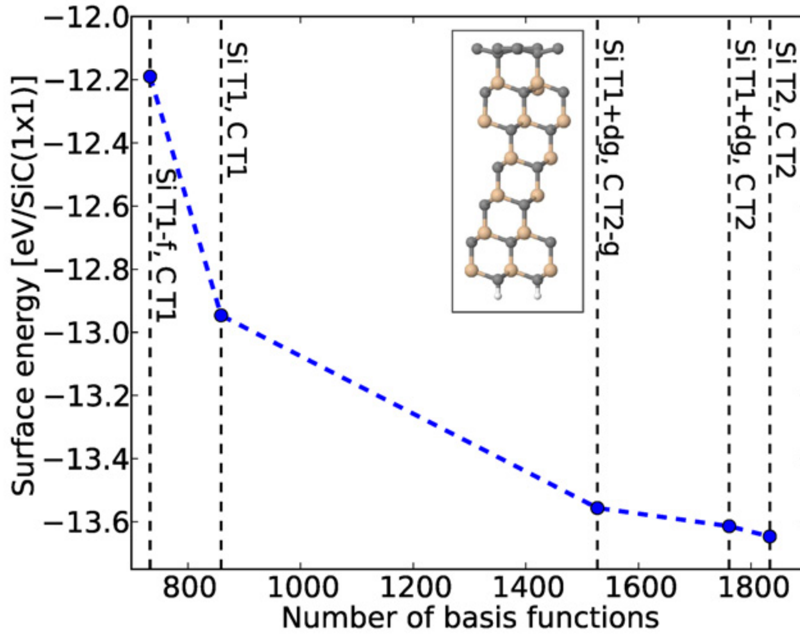

Figure B.1.: Effect of increasing the basis set size on the surface energy of the $\sqrt{3}$ approximant to the ZLG phase at the chemical potential limit of bulk graphite. The PBE+vdW functional was used. In the plot we use T1 (T2) as abbrevation of *tier 1* (*tier 2*) , respectively

The convergence of the calculated surface energies in this work with basis size is exemplified for the $(\sqrt{3} \times \sqrt{3})$-R30° small unit cell approximant [334, 214] to the ZLG phase in Fig. (B.1) including 6 SiC-bilayer. The bottom carbon atoms were saturated by hydrogen. Its geometry was first fully relaxed with FHI-aims *tight* grid settings, a *tier 1+dg* basis set for Si and a *tier 2* basis set for C basis settings. This geometry was then kept fixed

for the convergence tests shown here. What is shown in Fig. (B.1) is the development of the surface energy (Si face and H-terminated C face) with increasing basis size for both C and Si were calculated using

$$\gamma_{\text{Si face}} + \gamma_{\text{C face}} = \frac{1}{A}\left(E^{\text{slab}} - N_{\text{Si}}\mu_{\text{Si}} - N_{\text{C}}\mu_{\text{C}}\right) . \tag{B.1}$$

where N_{Si} and N_{C} denote the number of Si and C atoms in the slab, respectively, and A is the chosen area. The computed surface energy is shown per 1×1 surface area as in all surface energies given in the main text.

The notation in the figure is as follows:

- "T1" and "T2" abbreviate the set of radial functions included in *tier 1* and *tier 2*, respectively (see Table B.1).
- "Si T1-f" denotes the Si *tier 1* basis set, but with the f radial function omitted.
- "C T2-g denotes the set of radial functions for C up to *tier 2*, but omitting the g-type radial function of *tier 2*.
- "Si T1+dg" denotes the radial functions included up to *tier 1* of Si, and additionally the d and g radial functions that are part of *tier 2*. This is also the predefined default basis set for FHI-aims '*tight*' settings for Si.
- "C T2" denotes the radial functions of C up to *tier 2* and is the default choice for '*tight*' settings in FHI-aims.

In short, the plot indicates the required convergence of the surface energy to a few meV/(1×1) surface area if the default FHI-aims '*tight*' settings are used. It is evident that the high-l g-type component for C contributes noticeably to the surface energy.

B.2. Slab Thickness

The convergence of our surface calculations with respect to the number of SiC bilayers is shown in Fig. (B.2) by considering surface energies for the $(\sqrt{3}\times\sqrt{3})$-R30° small unit cell approximant [334, 214]. The zero reference

energy is an unreconstructed six bilayer 1x1 SiC surface. A six bilayer slab is sufficient to accurately represent bulk effects.

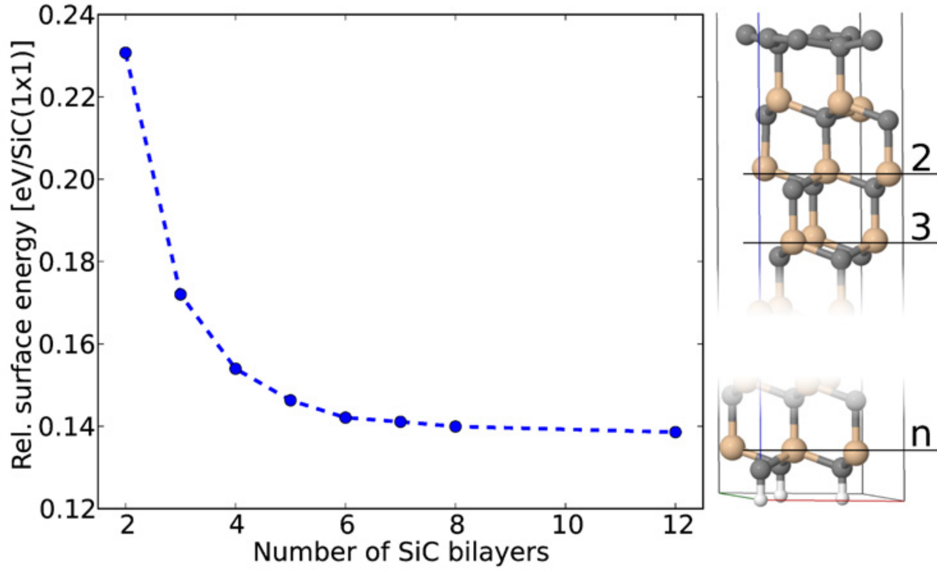

Figure B.2.: Slab thickness dependence of the surface energy of the $(\sqrt{3} \times \sqrt{3})$-R30° approximant to the ZLG phase.

B.3. k-Space Integration Grids

We demonstrate the accuracy of the 2D Brillouin zone (BZ) integrals for our graphene-like surface phases by comparing different k-space integration grids in Table (B.2). The ZLG and mono-layer graphene (MLG) surface energies in the full $(6\sqrt{3}\times6\sqrt{3})$-R30° cell are compared using the Γ-point only and using a 2x2x1 k-space grid. These k-mesh tests were performed in a four bilayer slab, using the PBE including van-der-Waals effects [326] (PBE+vdW) functional, *light* real space integration grids, a *tier1* basis set without the f functions for Si and *tier1* for C. The geometries were kept fixed at the configuration relaxed with a Γ-point only k-space grid. In Table (B.2), the surface energies relative to the unreconstructed 1x1 surface in the graphite limit are listed for the silicon rich $\sqrt{3}$x$\sqrt{3}$ reconstruction, the ZLG and MLG phases. Table (B.2) clearly shows that the surface energies are well converged using the Γ-point only. Hence in this work, all surface energies for the $(6\sqrt{3}\times6\sqrt{3})$-R30° phases were calculated using this k-space integration grid. For all bulk reference energies as well as for the two silicon rich surface reconstructions, the convergence with respect to the k-mesh size has been tested and found to be well converged for grids equivalent to the ZLG phase.

system	k-grid		
	6x6x1	12x12x1	24x24x1
$\sqrt{3}$x$\sqrt{3}$	-0.439	-0.435	-0.436
	1x1x1	2x2x1	
ZLG	-0.426	-0.426	
MLG	-0.454	-0.455	

Table B.2.: Surface energies in [eV/SiC(1x1)] relative to the unreconstructed 3C-SiC(1x1) surface for the chemical potential limit of graphite, four-bilayer SiC slabs. The silicon-rich $\sqrt{3}$x$\sqrt{3}$ reconstruction, ZLG and MLG phases using different k-grids are shown. The PBE+vdW exchange-correlation functional was used.

B.4. The Heyd-Scuseria-Ernzerhof Hybrid Functional Family for 3C-SiC

In this work, we used the HSE [175] for calculating the electronic structure and validating surface energies. In HSE06 the amount of exact exchange is set to $\alpha = 0.25$ and the range-separation parameter $\omega = 0.2\text{Å}^{-1}$. We calculated the band gap and valence band width of 3C-SiC for different values of α. We used with '*tight*' numerical settings as introduced in Sec. B.1 with an 12×12×12 off-Γ k-grid.

As can be seen in Fig. B.3, for fixed (ω) the band gap and valence band width depend practically linearly on the exchange parameter α. We tested the HSE06 with respect to the band gap and band width, the latter being a measure for the cohesive properties of a crystal [257]. The default HSE06 value of $\alpha = 0.25$ captures both the band gap and the band width well and we therefore adopt it for our calculations.

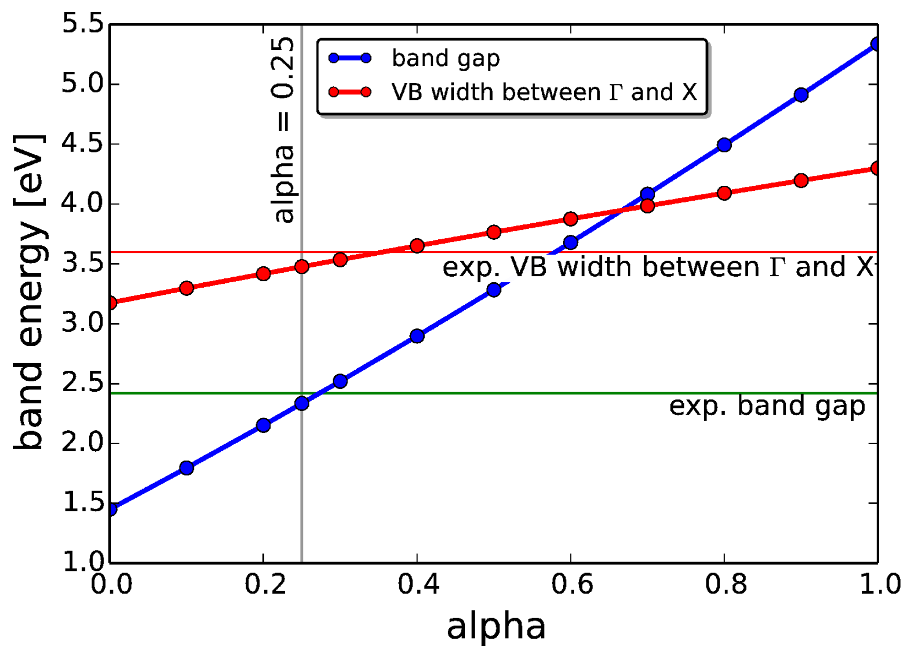

Figure B.3.: The Kohn-Sham band-gap (blue circles) and valence band width along Γ to X (red circles) of 3C-SiC as a function of α. The HSE06 value $\alpha = 0.25$ is marked by a vertical line. The experimental valence band width is shown as horizontal line at 3.6 eV[143] and the exp. band gap at 2.42 eV[148].

C.1. Cubic Silicon Carbide (3C-SiC)

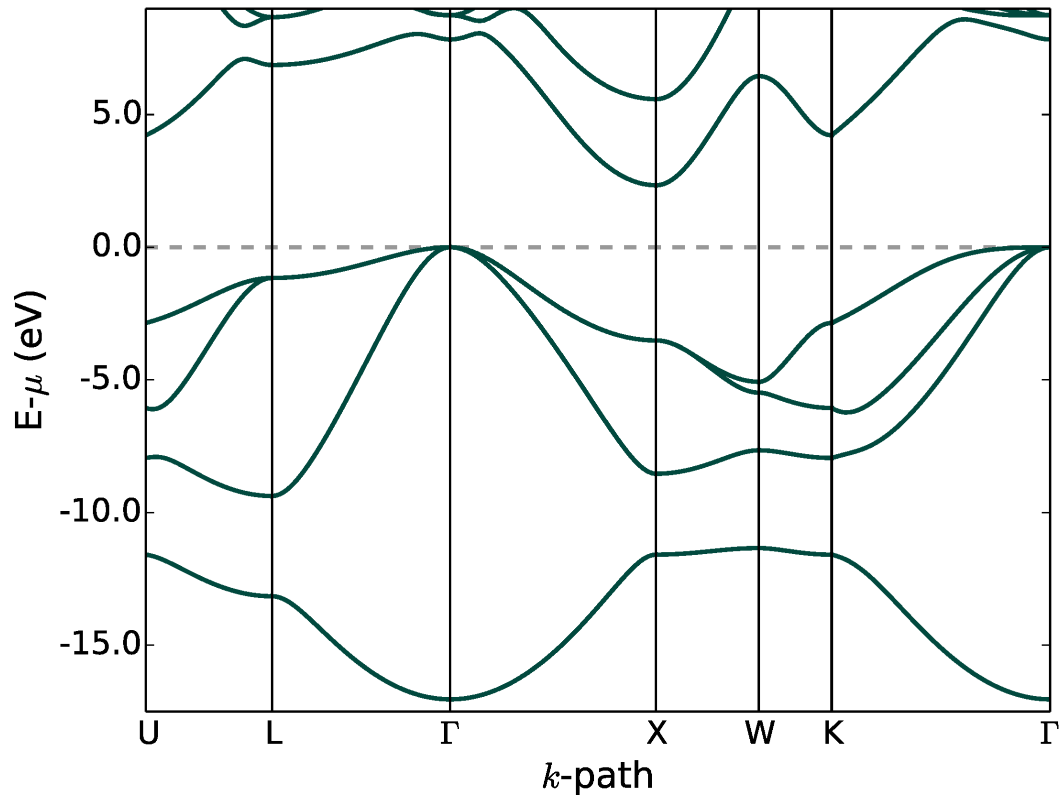

Figure C.1.: The band structure of cubic silicon carbide (3C-SiC) is shown along the high symmetry lines. We used the Heyd-Scuseria-Ernzerhof hybrid functional [138, 175] (HSE). The atomic structure was relaxed including vdW corrections (Tab. 7.2). 3C-SiC has an indirect band gap between Γ and X of 2.33 eV.

C.2. Hexagonal Silicon Carbide 4H-SiC and 6H-SiC

C.2.1. The HSE Band Structure of 4H-SiC

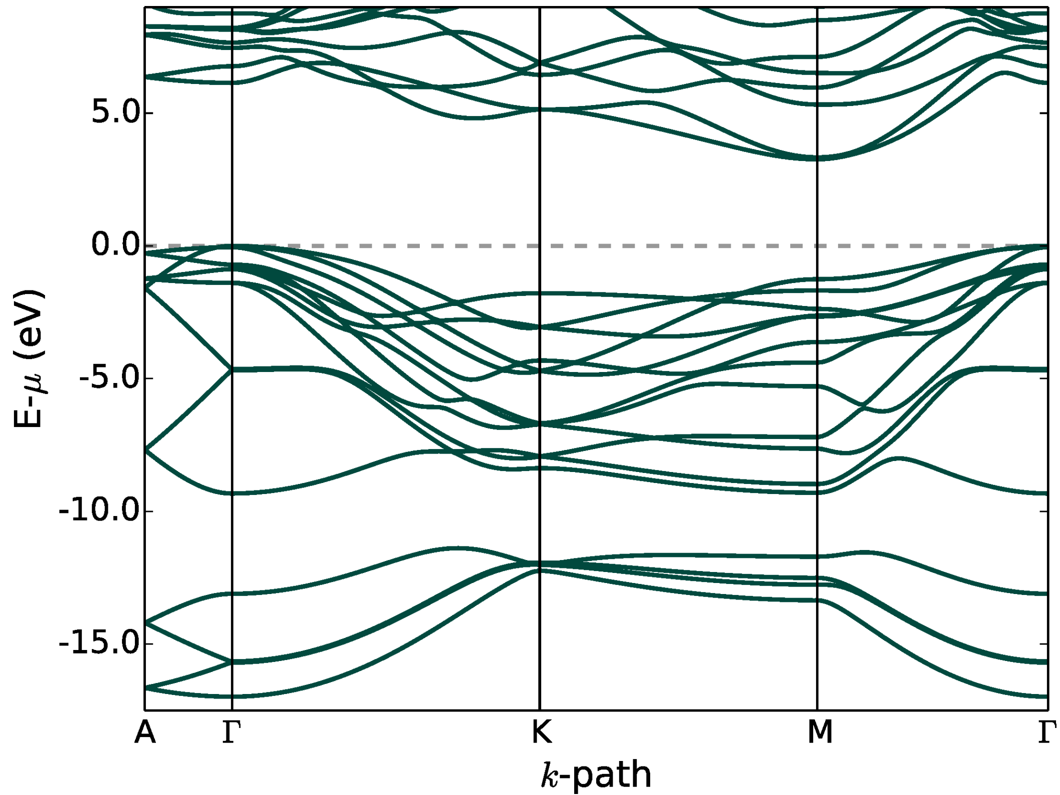

Figure C.2.: The band structure of 4H-SiC is shown along the high symmetry lines. We used the Heyd-Scuseria-Ernzerhof hybrid functional [138, 175] (HSE). The atomic structure was relaxed including vdW corrections (see Tab. 7.2). 4H-SiC has an indirect band gap between Γ and M of 3.26 eV.

C.2.2. The HSE Band Structure of 6H-SiC

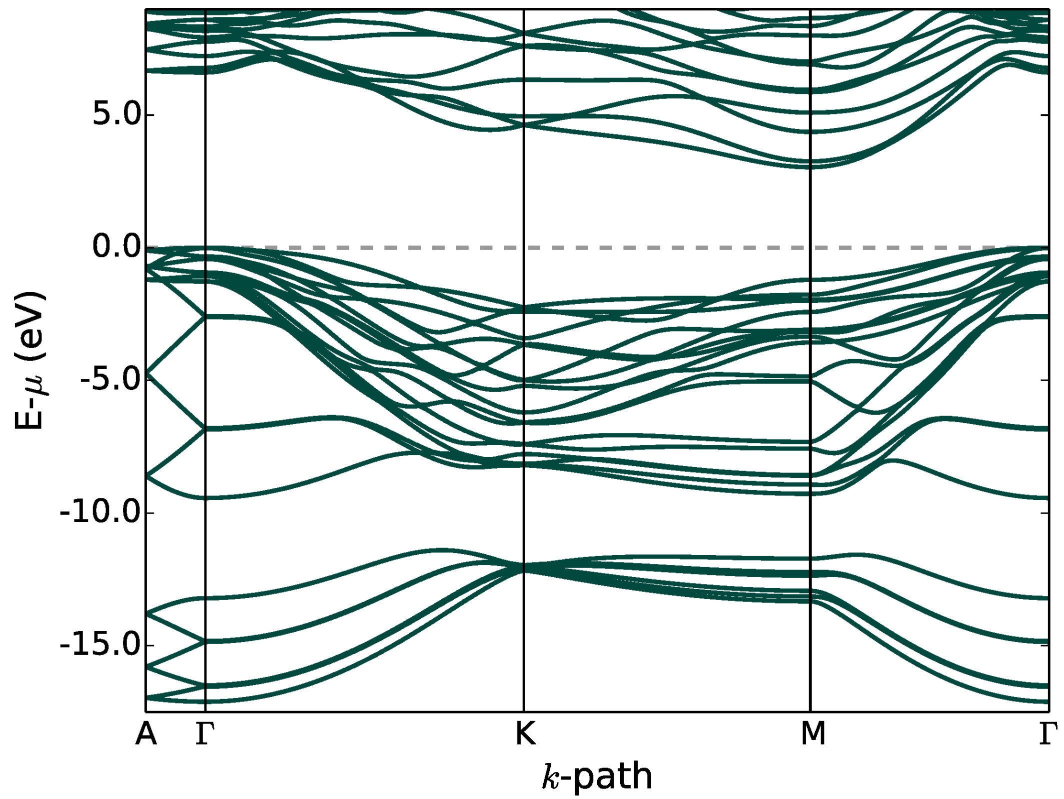

Figure C.3.: The band structure of 6H-SiC is shown along the high symmetry lines. We used the Heyd-Scuseria-Ernzerhof hybrid functional [138, 175] (HSE). The atomic structure was relaxed including vdW corrections (see Tab. 7.2). 6H-SiC has an indirect band gap between Γ and M of 2.92 eV.

All phonon calculations are based on finite difference approach as described in Sec. 3 using the phonopy-code [327].

D.1. The Phonon Band Structure of the Carbon Structures: Graphene, Graphite and Diamond

D.1.1. Graphene

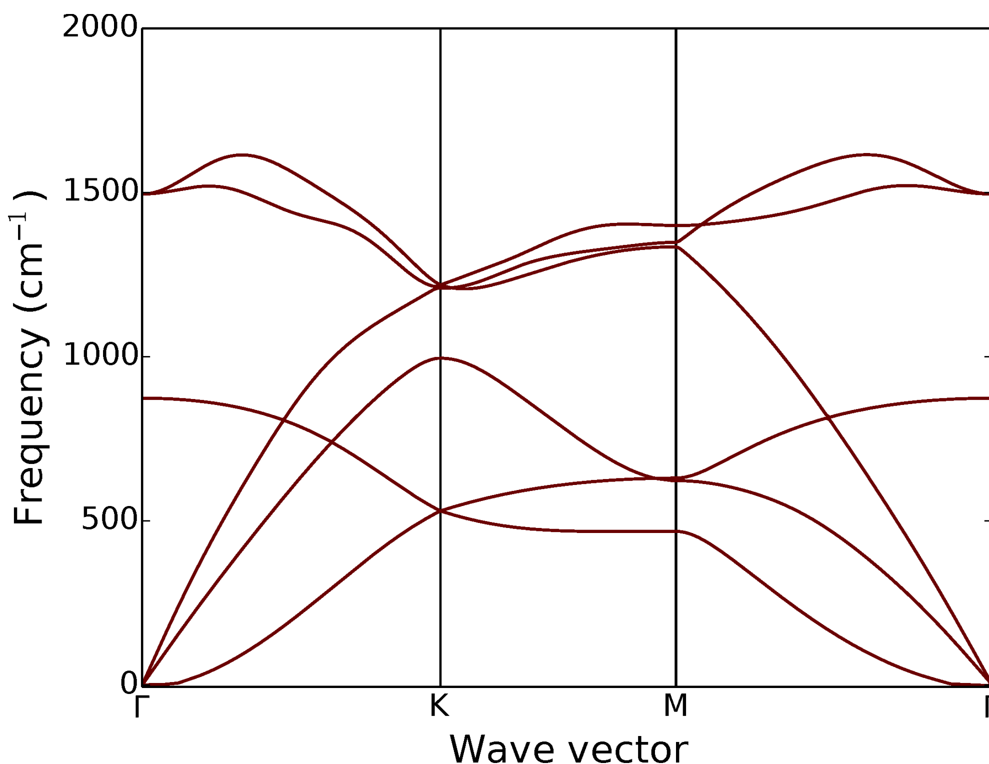

Figure D.1.: Calculated phonon dispersion relation of graphene along the high symmetry lines (PBE+vdW).

We used the finite difference approach to calculating phonon dispersion with a supercell of 6×6 and a finite displacement of 0.008 Å. For an accurate description of the soft accoustic phonon mode near the Γ-point a very dense real space sampling (*really tight* Sec. 2.5) was chosen.

Since the graphene unit cell contains two carbon (C) atoms, A and B, there are six phonon dispersion bands Fig. D.1, three accoustic and three optic phonon branches. The two atomic vibrations perpendicular to the graphene plane correspond to one accoustic and one optic phonon mode. The accoustic one is the lowest phonon branch in the Γ-K direction and the optic one has a phonon frequency of 873 cm^{-1} at the Γ-point. For the remaining 2 accoustic and 2 optic phonon modes the vibrations are in-plane. Near the BZ center (Γ-point) the two optic in-plane phonon modes correspond two vibrations of the two sublattices A and B against each other, the so-called E_{2g} phonon mode. The E_{2g} mode is doubly degenerate in Γ at 1495 cm^{-1} and is a first order Raman active phonon mode [331]. However, within BO approximation (see Sec. 1.2), the Raman G-peak position is independent of Fermi-level in the electronic band structure, in contrast with experiments [251, 62] where a stiffening (a shift to higher frequencies) of the E_{2g} phonon mode is observed with increased electron (hole) doping concentration. The E_{2g} mode within the BO approximation is given by the perturbation of the electronic structure due to the atomic displacement (phonon) and the rearrangement of the Fermi surface as a response. Pisana *et al.* showed that in graphene these two contributions cancel out exactly because of the rigid motion of the Dirac cones, associated with the E_{2g} phonon breaking the BO approximation.

D.1.2. Graphite

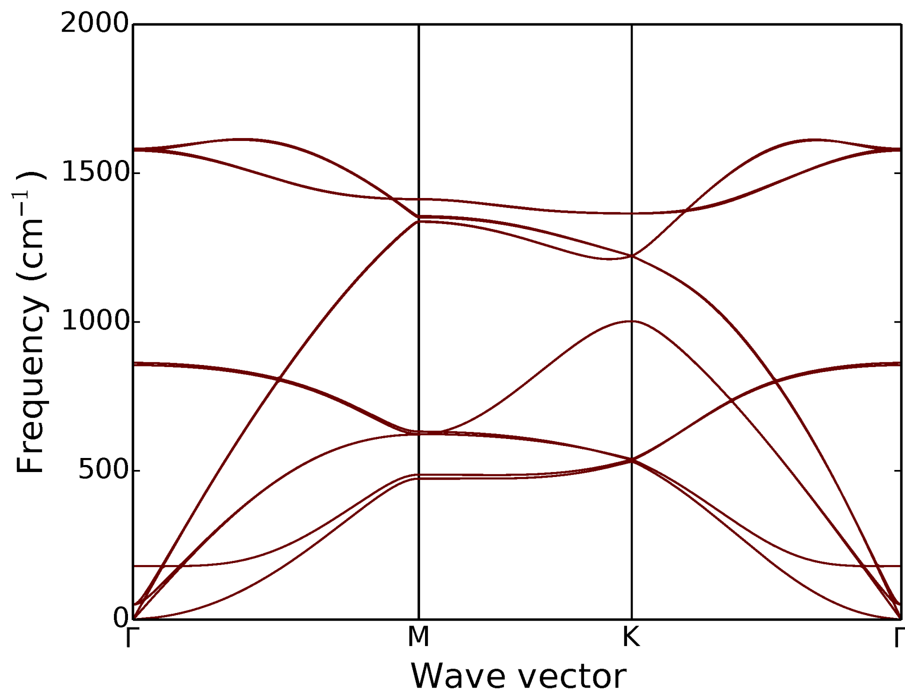

Figure D.2.: Calculated phonon dispersion relation of graphite along the high symmetry lines (PBE+vdW).

We used the finite difference approach to calculating phonon dispersion with a supercell of $5 \times 5 \times 2$ and a finite displacement of 0.005 Å. For an accurate description of the soft accoustic phonon mode near the Γ-point a dense real space sampling (*tight* Sec. 2.5) was chosen.

D.1.3. Diamond

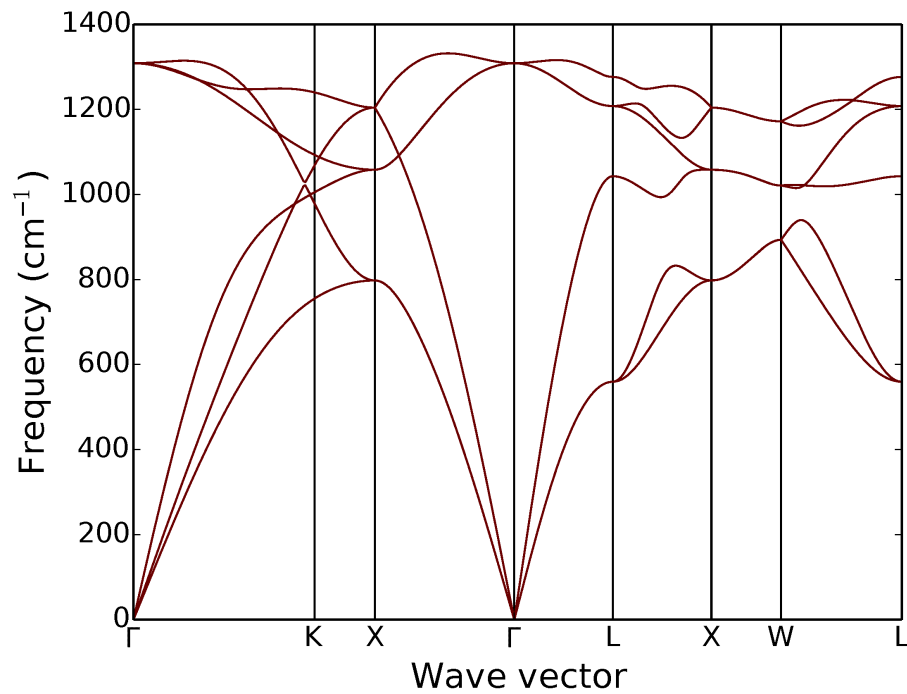

Figure D.3.: Calculated phonon dispersion relation of diamond along the high symmetry lines (PBE+vdW).

We used the finite difference approach to calculating phonon dispersion with a supercell of $3 \times 3 \times 3$ and a finite displacement of 0.001 Å. We chose a dense real space sampling (*tight* Sec. 2.5).

D.2. Phonon Band Structure of Silicon Carbide

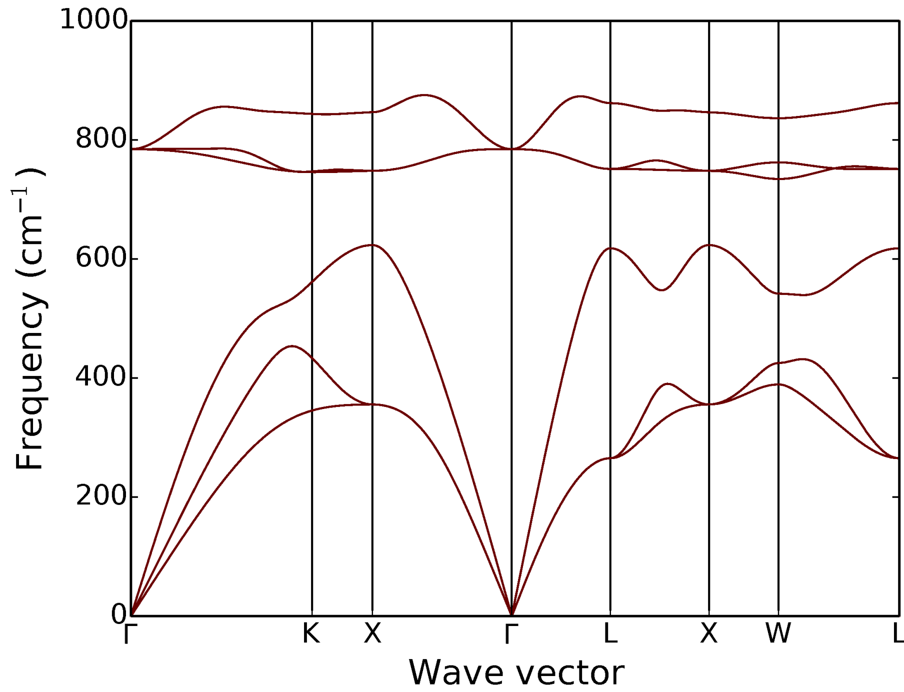

Figure D.4.: Calculated phonon dispersion relation of SiC along the high symmetry lines (PBE+vdW).

We used the finite difference approach to calculating phonon dispersion with a supercell of $3 \times 3 \times 3$ and a finite displacement of 0.001 Å. We chose a dense real space sampling (*tight* Sec. 2.5).

At the SiC-graphene interface on the Si face of SiC some Si atoms in the top SiC bilayer remain unsaturated, the so-called *Si dangling bonds*. To identify the Si dangling bonds, we computed the distance between a top layer Si atom and the closest C atom in the ZLG layer. Figure E.1, shows the Si-C distance for every Si atom in the top SiC bilayer ordered by bond length of the 3C-SiC-ZLG structure calcualted with PBE+vdW. For all structures we evaluated, we found a similar picture. The Si-C bond length of most Si atoms is between the bulk Si-C bond length of 1.89 Åin the case of 3C-SiC and the average Si-ZLG layer distance. The atoms well above the Si-ZLG layer distance ar defined as Si dangling bonds.

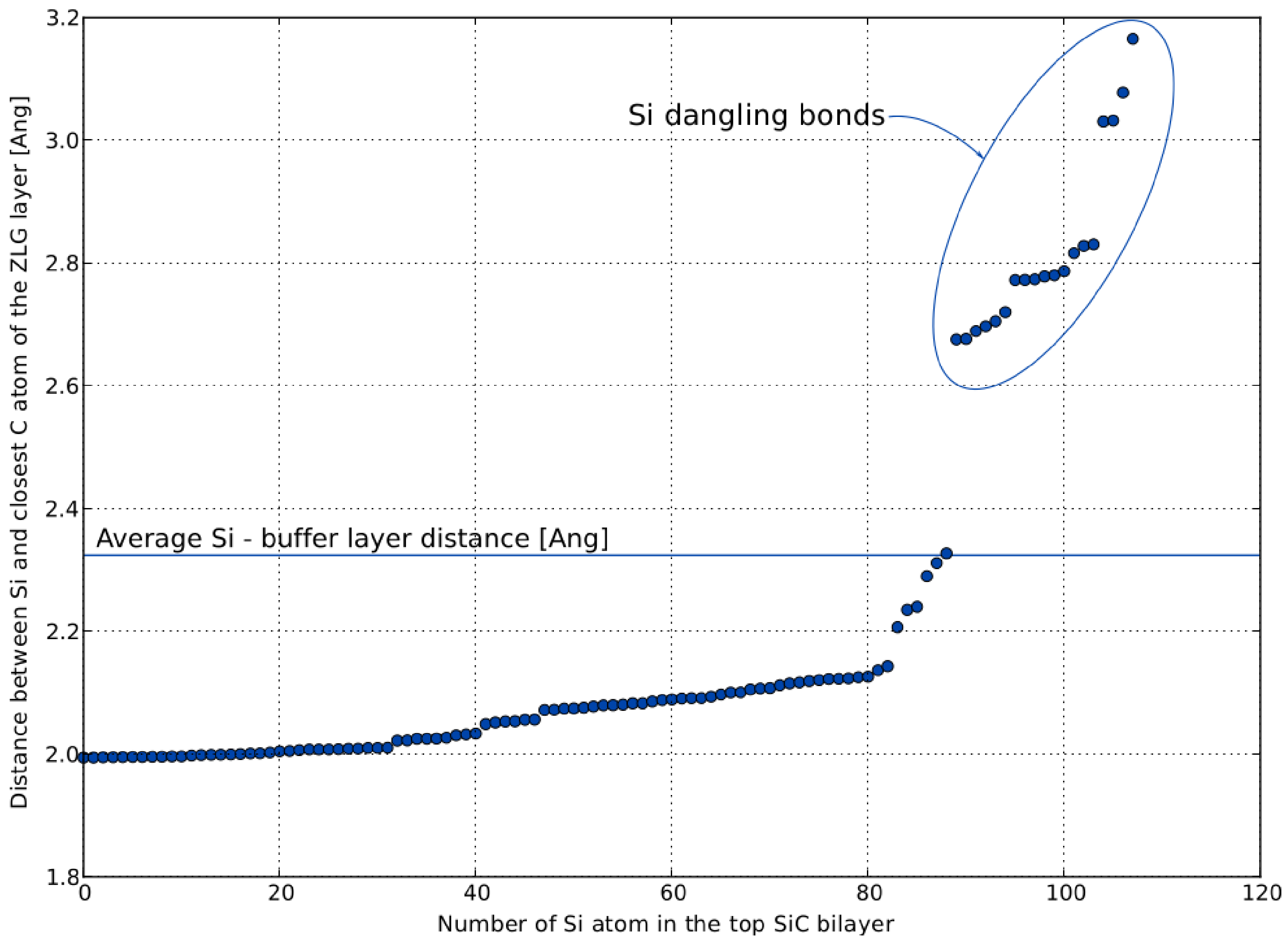

Figure E.1.: The distance between a Si atom of the top SiC bilayer and the closest C atom in the ZLG layer is used to identify the Si dangling bonds.

F Comparing the PBE and HSE06 Density of States of the MLG Phase

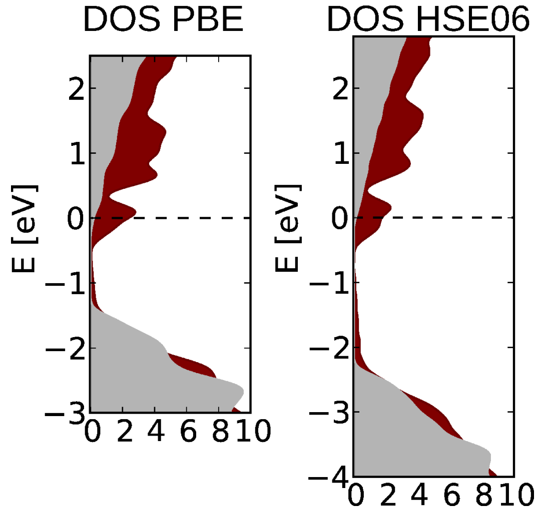

Figure F.1.: The Density of states of the $\sqrt{3}$-MLG structure calculated using the PBE and the HSE06 exchange-correlation functional. Shown in red is the DOS of the slab used in the calculation and in grey is shown the 3C-SiC-bulk projected DOS.

In Chapter 12, we discussed the electronic structure of epitaxial graphene on the 3C-SiC(111) surface. In a small approximated $(\sqrt{3} \times \sqrt{3})$-SiC unit cell with a strained (2×2) graphene layer, we calculated the electronic structure using the hybrid functional HSE06. However, to gain inside into the electronic structure of the experimentally observed $(6\sqrt{3} \times 6\sqrt{3})$R30° structure, we use the PBE approximation to the exchange-correlation functional to render the calculations affordable. In Figure F.1, we compare the DOS of the the $\sqrt{3}$-MLG structure calculated using the PBE and the HSE06 exchange-correlation functional. We used a six bilayer $(\sqrt{3} \times \sqrt{3})$-SiC slab covered by a (2×2)-ZLG and (2×2)-MLG layer. It shows in red the full DOS of the slab used in the calculation and in grey the 3C-SiC-bulk projected DOS. PBE and HSE06 give qualitatively the same result, however, in HSE06 the bulk band gap is larger and the overall spectrum seems to be streched over a larger energy range.

The doping of the $\sqrt{3}$-MLG layer increased with the fraction of exact exchange included in the exchange-correlation functional from PBE, to HSE06 to PBE0, shifting the graphene Dirac point from -0.48 eV (PBE), -0.63 eV (HSE06) to -0.86 eV (PBE0).

F.1. Influence of the DFT Functional

In Appendix B, we included details on the numerical convergence of calculations for similar structures with respect to the number of basis functions

and the grid density in real and reciprocal space. For the $(6\sqrt{3} \times 6\sqrt{3})$ interfaces, we chose the Γ-point for accurate integrations in reciprocal space. The FHI-aims code employs numeric atom-centered basis sets. Basic descriptions of their mathematical form and properties are published in in Ref. [32] or in Sec. 2.5. The basis set and numerical real space grids are of high quality as defined by the *tight* settings including a *tier*1+dg basis set for Si and a *tier*2 basis set for C [32].

To test the influence of the exchange correlation functional on the geometry we used three different exchange correlation functionals, the LDA [249], the Perdew-Burke-Enzerhof generalised gradient approximation (PBE) [247] and the Heyd-Scuseria-Ernzerhof hybrid functional (HSE06)[175]. In HSE06 the amount of exact exchange is set to $\alpha = 0.25$ and a range-separation parameter $\omega = 0.2\text{Å}^{-1}$ is used.

For an accurate description of the different surface phases, in particular hydrogen-graphene bonding in the quasi-free-standing mono-layer graphene (QFMLG) phase, we include long range electron correlations, so-called van der Waals (vdW) effects. Here, we compare the results of two different schemes. The first scheme used in this work is the well established Tkatchenko-Scheffler (TS) [326] method. It is a pairwise approach, where the effective C6 dispersion coefficients are derived from the self-consistent electron density. The second approach is a more recent refinement to the TS scheme incorporating many-body effects [325, 324, 5]. In this scheme, the atoms are modelled as spherical quantum harmonic oscillators, which are coupled through dipole-dipole interactions. The corresponding many-body Hamiltonian is diagonalised to calculate the many-body vdW energies. As a result, this approach accounts for long-range many-body dispersion (MBD) effects employing a range-separated (rs) self-consistent screening (SCS) of polarizabilities and is therefore called MBD@rsSCS (for details see Ref. [5]). To include the long-range tail of dispersion interaction we couple each functional with either the pairwise TS scheme, here refered to as PBE+vdW (HSE06+vdW), or the MBD@rsSCS scheme in this work abbreviated as PBE+MBD (HSE06+MBD).

In Table F.1 we list the layer distance ($D_{n,n+1}$), the Si-C distance within a SiC bilayer (d_n) and the layer corrugation (δ_n), the difference between the highest and lowest atom in the layer, for QFMLG and MLG on 6H-SiC(0001) calculated with different exchange correlation functionals and vdW corrections. We conclude that PBE+vdW, PBE+MBD, HSE06+vdW and HSE06+MBD yield the same results for both phases.

6H-SiC ZLG															
	PBE+vdW			PBE+MBD			LDA			HSE06+vdW			HSE06+MBD		
n	$D_{n,n+1}$	d_n	δ_n Si/C	$D_{n,n+1}$	d_n	δ_n Si/C	$D_{n,n+1}$	d_n	δ_n Si/C	$D_{n,n+1}$	d_n	δ_n Si/C	$D_{n,n+1}$	d_n	δ_n
Z	2.37	—	—/ 0.30	2.35	—	—/ 0.29	2.30	—	—/ 0.37	2.38	—	—/ 0.30	2.37	—	—/ 0.30
1	1.92	0.48	$0.42/<10^{-2}$	1.92	0.51	$0.40/<10^{-2}$	1.91	0.53	$0.31/<10^{-2}$	1.92	0.48	$0.48/<10^{-2}$	1.92	0.48	$0.47/<10^{-2}$
2	1.88	0.61	$<10^{-2}/<10^{-2}$	1.89	0.61	$<10^{-2}/<10^{-2}$	1.88	0.60	$<10^{-2}/<10^{-2}$	1.88	0.61	$<10^{-2}/<10^{-2}$	1.88	0.61	$<10^{-2}/<10^{-2}$
3	1.89	0.62	$<10^{-2}/<10^{-2}$	1.90	0.63	$<10^{-2}/<10^{-2}$	1.88	0.62	$<10^{-2}/<10^{-2}$	1.88	0.62	$<10^{-2}/<10^{-2}$	1.89	0.62	$<10^{-2}/<10^{-2}$

6H-SiC QFMLG															
	PBE+vdW			PBE+MBD			LDA			HSE06+vdW			HSE06+MBD		
n	$D_{n,n+1}$	d_n	δ_n Si/C	$D_{n,n+1}$	d_n	δ_n Si/C	$D_{n,n+1}$	d_n	δ_n Si/C	$D_{n,n+1}$	d_n	δ_n Si/C	$D_{n,n+1}$	d_n	δ_n
G	2.75	—	$—/<10^{-2}$	2.76	—	$—/<10^{-2}$	2.71	—	$—/<10^{-2}$	2.71	—	$—/<10^{-2}$	2.77	—	$—/<10^{-2}$
H	1.50	—	— / —	1.50	—	— / —	1.51	—	— / —	1.49	—	— / —	1.49	—	— / —
1	1.89	0.62	$<10^{-2}/<10^{-2}$	1.89	0.62	$<10^{-2}/<10^{-2}$	1.88	0.61	$<10^{-2}/<10^{-2}$	1.88	0.62	$<10^{-2}/<10^{-2}$	1.88	0.61	$<10^{-2}/<10^{-2}$
2	1.89	0.63	$<10^{-2}/<10^{-2}$	1.89	0.63	$<10^{-2}/<10^{-2}$	1.88	0.63	$<10^{-2}/<10^{-2}$	1.88	0.63	$<10^{-2}/<10^{-2}$	1.88	0.63	$<10^{-2}/<10^{-2}$
3	1.89	0.63	$<10^{-2}/<10^{-2}$	1.89	0.63	$<10^{-2}/<10^{-2}$	1.88	0.62	$<10^{-2}/<10^{-2}$	1.88	0.62	$<10^{-2}/<10^{-2}$	1.88	0.63	$<10^{-2}/<10^{-2}$

Table F.1.: Influence of the functional on the interface structure of 6H-SiC ($\sqrt{3}$-SiC model cell). $D_{n,n+1}$ is the distance between layer n and $n+1$, d_n gives the distance within SiC bilayer n, and δ_n the corrugation of layer n. All distances are given in Å.

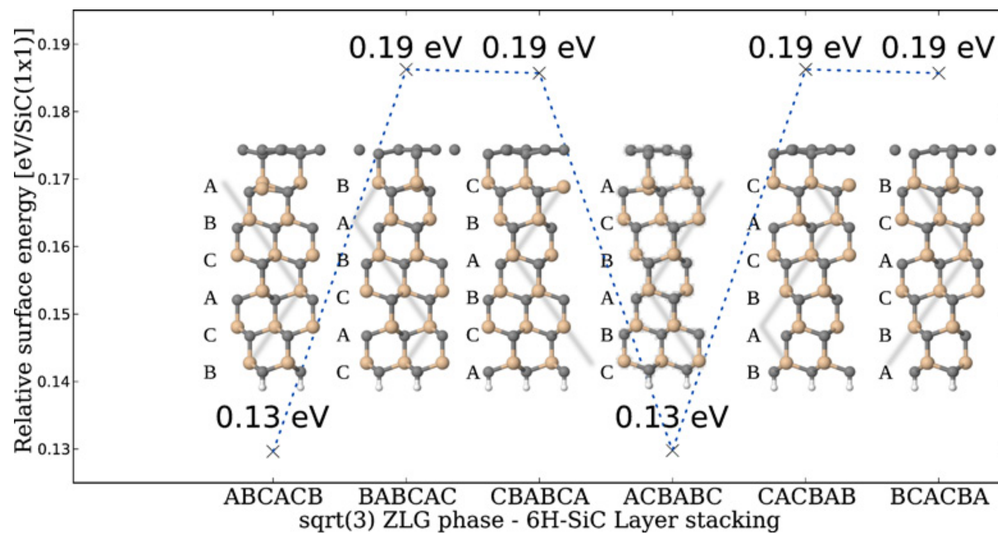

Figure G.1.: The zero-layer graphene (ZLG) of the hexagonal SiC polytype (6H-SiC) using an approximated $\sqrt{3} \times \sqrt{3}$-R30° unit cell and their surface energies are shown for different SiC-bilayer stacking order calculated using PBE+vdW.

For 3C-SiC(111), the stacking order close to the surface is independent of where the surface is cut. However, for the 6H-SiC(0001) this is different as the SiC bilayers are rotated every third layer by 30 degree in the unit cell. The position of the rotation is indicated in Fig. G.1 by a kink in the grey line. We tested the influence of the stacking order for 6H-SiC using an approximated $\sqrt{3} \times \sqrt{3}$-R30° unit cell. The surface energies calculated using PBE+vdW of the 6H-SiC ZLG and the atomic structure are shown in Fig. G.1. We find the lowest surface energy for ABCACB and ACBABC stacked SiC. We therefore use a ABCACB stacked 6H-SiC substrate.

	QFMLG					
	6H-SiC			3C-SiC		
n	$D_{n,n+1}$	d_n	δ_n Si/C	$D_{n,n+1}$	d_n	δ_n Si/C
G	2.66	—	0.02	2.68	—	0.01
H	1.50	—	0.00/0.00	1.50	—	0.00/0.00
1	1.89	0.62	0.00/0.00	1.89	0.62	0.00/0.00
2	1.89	0.63	0.00/0.00	1.89	0.63	0.00/0.00
3	1.89	0.63	0.00/0.00	1.89	0.63	0.00/0.00
	MLG					
	6H-SiC			3C-SiC[227]		
n	$D_{n,n+1}$	d_n	δ_n Si/C	$D_{n,n+1}$	d_n	δ_n Si/C
G	3.40	—	0.45	3.40	—	0.41
Z	2.36	—	0.86	2.36	—	0.82
1	1.92	0.55	0.78/0.30	1.93	0.55	0.74/0.31
2	1.90	0.61	0.21/0.14	1.90	0.61	0.21/0.13
3	1.89	0.62	0.08/0.05	1.89	0.62	0.08/0.05

Table H.1.: Geometry comparison of the layer distance ($D_{n,n+1}$), the Si-C distance within a SiC bilayer (d_n) and the layer corrugation, the difference between the highest and lowest atom in the layer, (δ_n) for two different SiC polytypes, 6H-SiC(0001) and 3C-SiC(111), including the QFMLG and MLG surface structure calculated with PBE+vdW. The data was taken from [227].

To evaluate the influence of the SiC polytype on the geometry, we list the key geometry parameters for the QFMLG and MLG in Tab. H.1 phase for two different polytypes, the 3C-SiC and 6H-SiC. For the QFMLG phase the interface geometries are practically identical. Likewise the interface of the MLG phase shows polytype induced changes that are smaller than 0.04 Å. Therefore, 3C and 6H polytypes can be exchanged without qualitatively changing the result of the calculation. It should be noted that the advantage of 3C is that the number of bilayers one uses in the slab can be smaller than six.

I The 3C-SiC(111)-(3x3) Phase: Details on the Geometry

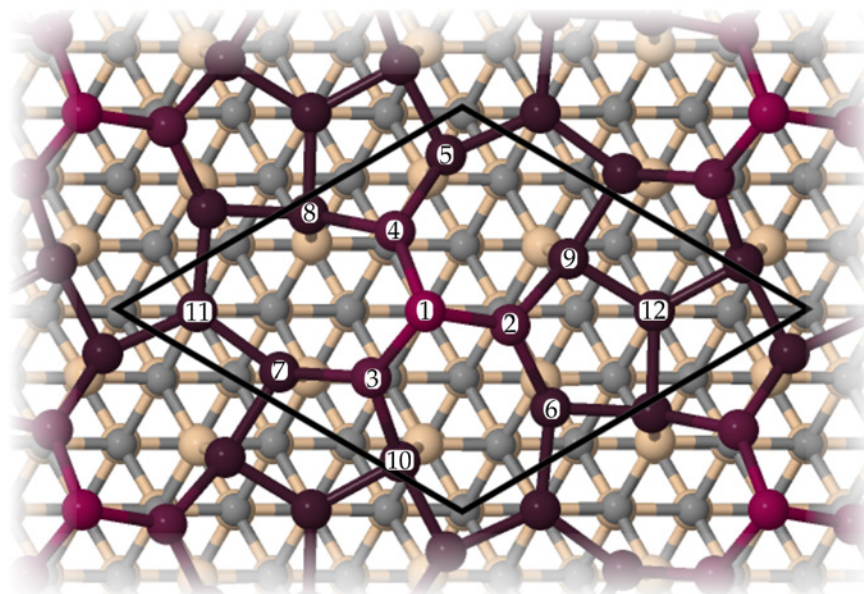

Figure I.1.: Schematic representation of the 3C-SiC(111)-(3×3) reconstruction. The numeration of the Si adatoms in the unit cell (shown in black) is used to mark the atoms according to their appearance in Tab. I.1.

In Sec. 8.1.2, the 3C-SiC(111)-(3×3) reconstruction was introduced. We performed DFT calculations including structure realxation for the Si rich (3×3) reconstruction. We here include details of the calculation using the generalised gradient approximation to the exchange-correlation functional including long-range dispersion effects using the well established Tkatchenko-Scheffler [326] method (PBE+vdW). The bulk lattice parameter are listed in Tab.7.2. Each slab consists of six SiC-bilayers and the bottom C bonds are saturated by hydrogen. The top three SiC-bilayers and all atoms above are fully relaxed (residual energy gradients: $8 \cdot 10^{-3}$ eV/Å or below).

Figure I.1 shows a schematic top few of the 3C-SiC(111)-(3×3) reconstruction. The structure consists of a silicon (Si) adatom (atom 1), a trimer (atoms 2-4) and a Si-adlayer (atoms 5-13). The trimer is slightly rotated with respect to its bulk position by an twist angle of 9.3° in excellent agreement with Ref. [306].

In Table I.1, we list the structural displacement of the Si adatoms with respect to their symmetric bulk position and the total displacement in the

Atom id		This work (PBE+vdW)			J. Schardt Ref. [276]		
		x [Å]	y [Å]	Δxy [Å]	x [Å]	y [Å]	Δxy [Å]
1	Top Atom	0.00	0.00	0.00	0.00	0.00	0.00
2		0.00	0.37	0.37	0.01	0.38	0.38
3		-0.33	-0.19	0.38	-0.33	-0.19	0.38
4	Trimer	0.33	-0.19	0.38	0.33	-0.19	0.38
5	Sublayer	0.70	-0.26	0.75	0.71	-0.24	0.74
6		-0.13	0.73	0.74	-0.14	0.73	0.74
7		-0.57	-0.48	0.75	-0.56	-0.49	0.74
8		0.31	-0.66	0.73	0.31	-0.67	0.74
9		0.42	0.60	0.73	0.43	0.61	0.74
10		-0.73	0.06	0.73	-0.74	0.07	0.74
11		0.00	0.00	0.00	0.00	0.00	0.00
12		0.00	0.00	0.00	0.00	0.00	0.00
13		0.00	0.00	0.00	0.00	0.00	0.00

Table I.1.: The displacement of the adatoms with respect to their symmetric bulk position. The surface structure was calculated using PBE+vdW for the approximantion to the exchange-correlation functional (E_{XC}). The LEED optimised geometric structure from Schardt [276] is included for comparison.

xy-plane (Δxy). The overall agreement between our calculation and the experimental structure obtained from quantitative LEED measurements is very good.

J The History of Graphite Interlayer Binding Energy

The history of the graphite binding energy (E_b) for different experiments and level of theory.

Year	Reference	E_b meV/atom		Method
1954	Girifalco [105]	42	exp.	Heat of wetting experiments
1956	Girifalco and Lad [106]	43±5	exp./ theo.	Lattice summation and experiment [105]
1998	Benedict *et al.* [17]	35^{+15}_{-10}	exp.	Collapsed carbon-nanotube structure
2004	Zacharia *et al.* [350]	52±5	exp.	Thermal desorption experiments of polyaromatic hydrocarbons
2012	Liu *et al.* [201]	31±2	exp.	Directly measurement of the interlayer binding energy
2013	Gould *et al.* [113]	44±3	exp./ theo.	[201] with improved fitting
1952	Brennan [39]	173	theo.	LCAO+vdW
1983	DiVincenzo *et al.* [74]	110	theo.	DFT+Thomas Fermi
1987	Jansen and Freeman [151]	82	theo.	All-electron augmented plane wave
1992	Schabel and Martins [275]	24	theo.	DFT (LDA)
1994	Charlier *et al.* [54]	20	theo.	DFT (LDA)
2003	Rydberg *et al.* [271]	24	theo.	DFT PBE+ vdW correction
2003	Telling and Heggie [318]	35	theo.	DFT (LDA)
2004	Hasegawa and Nishidate [127]	27	theo.	DFT (LDA)

2005	Zhechkov *et al.* [352]	38.5	theo.	Density-functional-based tight binding (DFTB)
2006	Dappe *et al.* [60]	66±6	theo.	DFT with perturbation theory based vdWcorrection
2006	Donchev [76]	55	theo.	Quantum mechanical polarisable force field (QMPFF)
2006	Ortmann *et al.* [240]	83.5	theo.	DFT PBE+ vdW correction
2007	Grimme *et al.* [119]	66	theo.	All-electron DFT (PBE-D)
2007	Hasegawa *et al.* [128]	60.4	theo.	DFT+semi-empirical correction
2007	Ziambaras *et al.* [354]	53	theo.	DFT PBE+ vdW correction
2008	Barone *et al.* [7]	54	theo.	DFT PBE+semi-empirical addition of dispersive forces
2008	Gould *et al.* [114]	59.7	theo.	DFT PBE+ vdW correction
2008	Kerber *et al.* [163]	57	theo.	DFT PBE+D vdW corrected
2008	Kleis *et al.* [167]	50	theo.	DFT PBE vdW-DF
2008	Silvestrelli [297]	61	theo.	DFT PBE+ vdW correction
2009	Spanu *et al.* [299]	56	theo.	QMC - not corrected for finite size effects
2010	Cooper [59]	59	theo.	DFT vdW corrected exchange-correlation functional
2010	Grimme *et al.* [118]	66	theo.	DFT+D vdW corrected

2010	Lebègue *et al.* [185]	48	theo.	RPA-DFT
2010	Liu and Goddard [200]	43	theo.	DFT-low gradient (DFT-lg) formula including ZPE
2010	Madsen *et al.* [207]	41	theo.	DFT meta-GGA (M06-L)
2010	Podeszwa [252]	45.3	theo.	[SAPT(DFT)] extrapolated from binding energy of polycyclic aromatic hydrocarbons
2012	Dappe *et al.* [61]	70±5	theo.	Combined local orbital DFT and second order perturbation theory
2012	Graziano *et al.* [115]	56	theo.	DFT optimised PBE vdW (optPBE-vdW) including ZPE
2012	Kim *et al.* [165]	59	theo.	DFT PBE+ vdW correction
2013	Brandenburg *et al.* [38]	43	theo.	DFT-D3 basis set superposition error corrected
2013	Bučko *et al.* [42]	55	theo.	DFT PBE (TS + SCS) vdW correction
2013	Chen *et al.* [56]	55.15	theo.	DFT PBE+ vdWinterlayer potential
2013	Gould *et al.* [112]	48	theo.	DFT PBE+ vdW correction
2013	Strutyński *et al.* [314]	40	theo.	Parameterisated DFT-D
2013	Sabatini *et al.* [272]	39	theo.	DFT rVV10 functional (vdW correction)

2013	Silvestrelli [298]	37	theo.	DFT PBE many body dispersion correction
2013	Thrower *et al.* [323]	58	theo.	DFT optB88-vdW functional
2013	Olsen and Thygesen [239]	62	theo.	RPA-DFT
2014	Ambrosetti *et al.* [5]	50	theo.	DFT PBE0+MBD@rsSCS
2014	Berland and Hyldgaard [22]	66	theo.	DFT vdW corrected exchange-correlation functional
2014	Bučko *et al.* [45]	81	theo.	DFT PBE+TS with iterative Hirshfeld charges
2014	Hamada [123]	60	theo.	DFT PBE+ vdW correction

Basic Theory

ab initio *ab initio*. is derived from the two Latin words *ab* (“ from ”) and *initio* (“ beginning”). It can be translated to “from the beginning”. p. 7

FHI-aims Fritz Haber Institute *ab initio molecular simulations* p. 6

B.-M. Birch-Murnaghan p. 46

BO Born-Oppenheimer p. 10

BZ Brillouin zone p. 30

CBm conduction band minimum p. 125

DFA density-functional approximation p. v

DFT density-functional theory p. 6

DOS density of states p. 66

E_B binding energy. The binding energy is the energy to stetch the graphite bulk structure along the axis perpendicular to the carbon planes until the individual layers are seperated to infinity. p. 50

E_D Dirac point p. 59

E_{XC} exchange-correlation functional p. 18

E_{XF} exfoliation energy. The exfoliation energy is the energy to remove a single carbon layer from the graphite bulk structure. p. 51

GGA generalised gradient approximation p. 21

HSE Heyd-Scuseria-Ernzerhof hybrid functional [138, 175] p. 6

HSE06 HSE hybrid functional with α=0.25 and ω=0.11 bohr^{-1} [175] p. 23

HSE06+MBD HSE06 including van-der-Waals effects with full many-body treatment (MBD@rsSCS) [325, 324, 5] p. 57

HSE06+vdW HSE06 including van-der-Waals effects [326] p. 46

$\varphi_i(\mathbf{r})$ Kohn-Sham orbital p. 17

LCAO linear combination of atomic orbitals p. 108

LDA local-density approximation p. 20

LJ Lennard-Jones. The Lennard-Jones potential is a mathematical model used to approximate the interaction between a pair of neutral atoms or molecules. It has the form $V_{\mathrm{LJ}} = 4\varepsilon\left[\left(\frac{\sigma}{r}\right)^{12} - 2\left(\frac{\sigma}{r}\right)^{6}\right]$, where ε is the depth of the potential well, σ is the distance at which the intermolecular potential between the two particles is zero and r is the distance between the two particles. p. 55

MBD@rsSCS long-range many-body dispersion (MBD) effects employing a range-separated (rs) self-consistent screening (SCS) of polarisabilities [324, 5] p. 25

NAO numeric atom-centered orbital p. 26

PBE Perdew-Burke-Ernzerhof generalised gradient approximation [246] p. 6

PBE+MBD PBE including van-der-Waals effects with full many-body treatment (MBD@rsSCS) [325, 324, 5] p. 56

PBE+vdW PBE including van-der-Waals effects [326] p. 6

PCBZ Brillouin zone of the primitive cell p. 107

PC primitive cell p. 107

PES potential energy surface p. 46

phonon-DOS phonon density of states p. 30

QHA quasiharmonic approximation p. 34

QMC quantum Monte Carlo p. 21

RPA random phase approximation p. 56

SCBZ Brillouin zone of the supercell p. 107

SC supercell p. 31

$\mathcal{N}$ supercell matrix p. 89

γ surface free energy p. 35

VCA virtual-crystal approximation p. 59

vdW van-der-Waals p. 6

ZPC zero-point vibrational correction p. 46

A Few Common Symbols

$n(\mathbf{r})$ electron density p. 20

$n_0(\mathbf{r})$ ground state density p. 15

$\mathcal{E}_0$ ground state energy p. 13

$\Psi_0(\{\mathbf{r}_i\})$ ground state wave function p. 15

Ψ_0 ground state wave function p. 12

$\hat{\mathcal{H}}$ many-body Hamiltonian p. 11

$\hat{\mathcal{H}}^e$ electronic Hamiltonian p. 13

$n_{KS}(\mathbf{r})$ Kohn-Sham density p. 19

$V^{\textbf{ext}}$ external potential p. 13

Experimental Techniques

AES Auger electron spectroscopy p. 77

AFM atomic force microscopy p. 55

ARPES angle-resolved photoemission spectroscopy p. 74

ELS electron-energy loss spectroscopy p. 77

GID grazing-incidence x-ray diffraction p. 85

LEED low-energy electron diffraction p. 4

MBE molecular beam epitaxy p. 5

NIXSW normal incidence x-ray standing wave p. 137

STM scanning tunnelling microscopy p. 74

STS scanning tunnelling spectroscopy p. 105

TEM transmission electron microscopy p. 54

XPS x-ray photoemission spectroscopy p. 81

Materials and Surface Reconstructions

3C-SiC cubic silicon carbide p. 7

3LG three-layer graphene p. 80

4H-SiC hexagonal silicon carbide p. 7

6H-SiC hexagonal silicon carbide p. 7

BLG bi-layer graphene p. 4

C carbon p. 5

DAS dimer ad-atom stacking fault p. 78

H hydrogen p. 40

MLG mono-layer graphene p. v

QFMLG quasi-free-standing mono-layer graphene p. v

Si silicon p. 36

SiC silicon carbide p. 13

ZLG zero-layer graphene. Also called “buffer layer”. p. v

Miscellaneous

LED light emitting diode p. 61

UHV ultrahigh vacuum p. 4

List of Figures

0.1 Schematic illustration of the graphene growth on the Si-side of SiC. On the Si-side, epitaxial graphene growth starts with a clean Si-terminated surface. At temperatures above 1000 K first a carbon interface layer forms [263], the so-called zero-layer graphene (ZLG). Increased temperature and growth time lead to the formation of monolayer graphene (MLG) and bilayer graphene (BLG). 3

2.1 The interacting system is mapped to a non-interacting auxiliary system. 17
2.2 The effective potential v_{eff} of the many-body system depends on Kohn-Sham density ($n_{KS}(\mathbf{r})$), which we are searching, which depends on the Kohn-Sham orbital ($\varphi_i(\mathbf{r})$), which in turn depends on v_{eff} 19
2.3 The radial function $u_j(r)$ of the 3s orbital for a free silicon atom is plotted along radius r. Also shown are the free-atom like potential $v_j(r)$ and the steeply increasing confining potential $v_{\mathrm{cut}}(r)$. The dotted line indicates the confining radius r_{cut}. 27

5.1 (a) shows a periodic cubic silicon carbide (3C-SiC) crystal. In (b) the periodicity is broken by inserting a vacuum region along the z-axis. The bottom C atoms of the slab are terminated by H atoms. In all surface calculations periodic boundary conditions are applied. Hence the surface slab is periodically repeated along the z-direction as shown in (c). . 39
5.2 A projected bulk band structure is illustrated schematically. For wave vectors $\mathbf{k}_\perp$ perpendicular to the surface bulk states appear. For different $\mathbf{k}_\perp$ the band energies between the lowest and highest values correspond to regions of bulk states. These bulk states are shaded in grey in the band structure along wave vectors parallel to the surface $\mathbf{k}_\parallel$. Outside the shaded bulk regions surface states can occur. (Figure courtesy of Johan M. Carlsson International Max-Planck Research School *"Theoretical Methods for Surface Science Part I"* (Presentation)) 40

6.1 Shows five different carbon structures. The two commonly known three dimensional carbon crystals: a. diamond and b. graphite. A single layer of graphite forms graphene a sp^2 bonded two-dimensional structure, labeled c. d. shows an example of a carbon nanotube and e. the Buckminster-Fullerene - C60, also-called Buckyball. 44
6.2 Number of publications per year as given in a Web-of-Science search for the keywords 'graphene', 'silicon carbide' and both keywords together [321]. 45
6.3 The interlayer binding energy sketch for three different types of binding: *a.) exfoliation energy, b.) binding energy, c.) cleavage energy*. In (a) and (b), the layer of interest is marked by a box. The scissor and dashed line for the exfoliation (a) and cleavage (c) cases illustrates how the crystal is cut. 51
6.4 History of the graphite interlayer binding energy (meV/atom) since the first experiment in 1954 [106]. The experimental values [106, 17, 350, 201, 113] are given as crosses and the theoretical values as filled circles. The colour of each circle depends on the experimental work cited in the publication. Girifalco and Lad [106] gave the binding energy in units of ergs/cm^2, their value of 260 ergs/cm^2 was erroneously converted to 23 meV/atom (shown in light green) instead of the correct 42 meV/atom (dark green). A full list of references and binding energies is given in Appendix J 53
6.5 Binding energy E_B of graphite as a function of the interplanar distance d using LDA, PBE, HSE06 and two different vdW correction schemes (TS [326] and MBD [325, 324, 5]). The symbols mark E_B at the equilibrium interlayer distance. The vertical line marks the experimental lattice spacing of $c_0 = 6.694$Å [226]. For comparison E_B values from RPA@PBE calculations ((1) Lebègue *et al.* [185], (2) Olsen *et al.* [239]) and from experiment ((3) Girifalco *et al.* [106], (4) Benedict *et al.* [17], (5) Zacharia *et al.* [350], (6) and (7) Liu *et al.* [201, 113]) are included. 54
6.6 Subfigure (a) shows the graphene Brillouin zone (shaded in grey) and the high symmetry points Γ, M and K (marked by blue points). (b) The band dispersion of graphene on the level of PBE. The k-path is chosen along the high symmetry lines of the graphene Brillouin zone as indicated by arrows in Subfigure (a). 59
6.7 The position of the graphene Dirac point with respect to the Fermi level for doping in the range of $\pm$ 0.005 e^-/atom on the level of PBE. PBE+vdW lattice parameter were used (Tab. 6.1). 60

7.1 The white spheres represent a hexagonal structure. The possible stacking positions of a closed hexagonal structure are marked as A, B, and C. A SiC-bilayer overlayers the hexagonal structure. The primitive unit cell of the SiC-bilayer is shown. 62
7.2 The atomic structure of three different SiC polytypes are shown, cubic silicon carbide (3C-SiC) (left), and two hexagonal structures 4H-SiC (middle) and 6H-SiC (right). The atoms in the black box mark the unit cell. The stacking sequence of the SiC-bilayers is shown for every polytype and indicated by a grey line in the structure. 3C-SiC is also shown in its zinc blende structure (bottom, left). The distance $d_{n,n-1}$ between two bilayers and the distance D_n between a Si and C atoms within a SiC bilayer are shown. 63
7.3 Density of states (DOS) around the band gap for 3C-SiC: The top panel shows the experimental species projected DOS (C solid line and Si dashed line) measured by soft x-ray spectroscopy with a band gap of 2.2 eV [204]. The middle panel shows the calculated species projected DOS using the HSE06 exchange-correlation functional with a band gap of 2.33 eV. In the bottom panel the calculated total Kohn-Sham DOS using the HSE06 exchange-correlation functional is compared to the total DOS calculated with PBE. The theoretical magnitude of the peaks in the spectra depends on the number of basis functions included in the calculation. 67
7.4 Plot of the band structure of 3C-SiC from Γ to X. The band structure (solid line) is calculated using HSE06 exchange-correlation functional and the vdW corrected lattice parameter (HSE06+vdW from Tab. 7.2). The shaded area (in grey) marks the band gap of 2.33 eV. In addition, experimental photoemission data is included (filled cicle) and parameterised bands (dashed line) taken from Ref. [143]. 68
7.5 Shows the Density of states (DOS) of the valence band for 3C-SiC. The top panel shows the experimental DOS measured by photoemission spectroscopy with a band width of 11.3 eV [296]. The calculated DOS using the HSE06 exchange-correlation functional with a band width of 9.3 eV is shown in the middle panel and using PBE with a band width of 8.4 eV in the bottom panel. 69

8.1 The surface termination of 3C-SiC and 6H-SiC is shown for a clean surface. In 6H-SiC every third Si-C bilayer is rotated by 30° indicated by a kink in the grey line. This rotation in the stacking order leads to different surface terminations $\mathrm{S}n_{6\mathrm{H}}$ and $\mathrm{S}^*n_{6\mathrm{H}}$ where n runs from one to three. 73

8.2 Geometry of the 3C-SiC(111) ($\sqrt{3} \times \sqrt{3}$)-R30° Si adatom structure. The bond length of the adatom with the top Si atom ($L_{\text{Si-Si}}$), the distance from the surface ($D_{1_{\text{Si}},\text{Si}}$) and the corrugation of the top C layer ($\delta_{1_{\text{C}}}$) are shown. 75
8.3 The twist model of the 3C-SiC(111)-(3×3) reconstruction. On the left: The twist model from a side view. The layer distance between the substrate and the Si-ad-layer $D_{1_{\text{Si}},\text{Si}_3}$, as well as the distance between the ad-layer and the Si-trimer $D_{\text{Si}_3,\text{Si}_2}$ and trimer-Si-adatom $D_{\text{Si}_2,\text{Si}_1}$ are indicated by arrows. On the right: The twist model from a top view. The unit cell is shown in black. 77
8.4 Top view of the relaxed ZLG structure using PBE+vdW. The unit cell in the x-y-plane is indicate by a grey rhombus. The C atoms in the ZLG layer are coloured according to their z-coordinate (the colour scale reaches from yellow for atoms close to the substrate to blue for atoms away from it). The top Si-C bilayer is shown as well, here the z-coordinate scales from black to white, where black indicates that the atom is pushed towards bulk SiC. The ZLG hexagons furthest away from the substrate form a hexagonal pattern (marked in grey). The Si atom of the top Si-C bilayer in the middle of a ZLG carbon ring has the minimum z-coordinate (in the middle of the unit cell marked in light green). 80
8.5 Geometry and key geometric parameters determined by DFT-PBE+vdW for the three phases (a) ZLG, (b) MLG and (c) bi-layer graphene (BLG) on the Si face of 3C-SiC(111) and histograms of the number of atoms (N_a) versus the atomic coordinates (z) relative to the topmost Si layer (Gaussian broadening: 0.05 Å). N_a is normalised by N_{SiC}, the number of SiC unit cells. All values are given in Å. (Data published in Nemec *et al.* [227]) 82
8.6 Histogramm of the number of atoms N_a versus the atomic coordinates (z) relative to the topmost Si layer (Gaussian broadening: 0.05 Å). The key geometric parameter of the MLG on the Si face of 3C-SiC(111) at the level of a) LDA and b) PBE. All values are given in Å. 83
8.7 MLG on 6H-SiC(0001) and histogram of the number of atoms N_a versus the atomic coordinates (z) relative to the topmost Si layer (Gaussian broadening: 0.05 Å). N_a is normalised by N_{SiC}, the number of SiC unit cells. $D_{n,n+1}$ is the distance between the layer n and $n+1$, d_n gives the Si-C distance within the SiC bilayer n, and δ_n the corrugation of the layer n. All values are given in Å. (Figure published in Ref. [294]) . . 84

9.1 a) Top view of the ZLG layer and the top SiC bilayer fully relaxed using PBE+vdW. The carbon atoms of the ZLG layer are coloured according to their vertical distance from the average height of the Si-layer ranging from black being close to the Si layer to white for C atoms away from the Si-layer. The bonds between the ZLG C atoms are coloured from blue to red for increasing bond length. b) Bond length distribution in the ZLG layer. A Gaussian broadening of 0.002 Å was applied for visualisation purposes only. The two vertical lines indicate the bond length of free-standing graphene in the optimised structure on a PBE+vdW level and the average bond length in the ZLG layer. 87
9.2 Comparison of the surface energies for six different smaller-cell approximant models of the 3C-SiC(111) ZLG phase, relative to the bulk-terminated (1×1) phase, as a function of the C chemical potential within the allowed ranges using PBE+vdW. The Si rich (3×3) and $(\sqrt{3} \times \sqrt{3})$ reconstructions as well as the $(6\sqrt{3} \times 6\sqrt{3})$-R30° ZLG phase from Fig. 10.1 are included for comparison. The shaded areas indicate chemical potential values outside the strict thermodynamic stability limits of Eq. 4.15. 88
9.3 Bond length distribution in the $(6\sqrt{3} \times 6\sqrt{3})$ & (13×13)-ZLG layer for two different rotational angles. The bond length distribution for the ZLG layer in the 30° rotated structure from Fig. 9.1 is shown in grey and the ZLG structure rotated by 2.204° in blue. A Gaussian broadening of 0.002 Å was applied for visualisation purposes only. The two vertical lines indicate the bond length of free-standing graphene in the optimised structure on a PBE+vdW level and the average bond length in the ZLG layer rotated by 2.204°. 92
9.4 The hexagon-pentagon-heptagon (H5,6,7) defect in the zero-layer graphene shown in the approximated 3×3 cell (insert a and b) and in the $(6\sqrt{3} \times 6\sqrt{3})$-R30° ZLG phase. The defect was placed in two different positions. In inset a and c the defect is placed at the “hollow” position with a silicon atom of the underlying SiC bilayer in the middle of the central hexagon and at the “top” position. 94

9.5 (a) Calculated (PBE+vdW) effective lattice parameter (average C-C bond length) in a series of fully relaxed graphene flakes of finite size with (squares) and without (circles) hydrogen termination at the edges. The hydrogen terminated flakes are shown in the inset. The lattice parameter of a flat, strainfree, periodic graphene sheet calculated in PBE+vdW is indicated by a dashed line. (b) Diameter (maximum C-C distance) of the flakes used in (a). (Figure published in Ref. [284]) 101
9.6 Top: calculated fully relaxed (atomic postion and unit cell) structure of a graphene sheet with a (10×10) periodic arrangement of a 5-8-5 divacancy defects (atoms highlighted in red). The in-plane unit cell is marked by black lines. Bottom from left to right: fully relaxed monovacancy and 5-8-5 divacancy defects in a (10×10) unit cell and Stone-Wales defect in a (7×7) unit cell. 102

10.1 Comparison of the surface energies for five different reconstructions of the 3C-SiC(111) Si side, relative to the bulk-terminated (1×1) phase (always unstable), as a function of the C chemical potential within the allowed ranges (given by diamond Si, diamond C or graphite C, respectively). (a) PBE+vdW, (b) PBE,(c) LDA. The shaded areas indicate chemical potential values outside the strict thermodynamic stability limits of Eq. 4.15. (Data published in Ref. Nemec *et al.* [227]) 104

11.1 a: Linear hydrogen chain with one hydrogen atom (H) in the unit cell and its band structure. b: supercell of the linear hydrogen chain with 5 times the one-atomic unit cell. The band structure is folded at the edges of the reduced Brillouin zone of the supercell. The band structure corresponding to the actual one-atomic unit cell is plotted with dashed lines. c: the hydrogen atoms in the 5 atomic chain are moved away from their periodic position. The corresponding band structure is perturbed, preventing the straight forward reversal of the band folding. 107
11.2 a) shows 18 atoms arranged in a perturbed hexagonal lattice, the unit cell and the lattice vectors $\mathbf{A}_1$ and $\mathbf{A}_2$. b): the structure from a) is presented as a (3×3) supercell. The nine primitive unit cells are indicated by blue lines and the primitive lattice vectors $\mathbf{a}_1$ and $\mathbf{a}_2$ by black arrows. The blue atom in the central unit cell can be shifted to its periodic image by a lattice vector translation. 109

11.3 Sketch of a 2-dimensional unit cell in reciprocal space: The grey area indicates the first BZ with the reciprocal lattice vectors $\mathbf{b}_i$ of the conventional unit cell (in this example 64 k-points ($\mathbf{k}$) (purple points)) and the SCBZ of a 4×4 supercell with lattice vectors $\mathbf{B}_i$ and four k-points ($\mathbf{K}$) (white points). . 111
11.4 The real-space SC containing 3×3 primitive cell (PC) is shaded in blue. The lattice vector $\mathbf{R}_j$ points to a periodic copy of the SC. The PC with lattice vectors $\mathbf{a}_{1,2}$ is shaded in grey. The lattice vector ρ_l points to a periodic copy of the PC. Each PC contains two atoms (red circle) with atomic position $\mathbf{r}_\mu$. 112
11.5 The unfolded band structures of four different 10-atom hydrogen chains are plotted along the Brillouin zone of the primitive cell (PCBZ) path M to Γ to M. Dashed lines indicate the SCBZ. The corresponding atomic structure is shown at the bottom. a.: A perfectly periodic hydrogen chain, b.: a hydrogen chain with geometric distortions, c.: a defect in the PC $l = 6$ in an otherwise perfectly periodic chain and d.: two chains with different periodicity. 118
11.6 The unfolded band structure of the two chain system introduced in Example 11.3d. The band structure is projected on the 10-atomic chain marked by a grey box. 120

12.1 Figure taken from Ref. [263]: Dispersion of the π-bands of graphene grown on 6H-SiC(0001) measured with angle-resolved photoemission spectroscopy (ARPES) perpendicular to the $\overline{\Gamma K}$-direction of the graphene Brillouin zone for (a) an as-grown ZLG (Ref. [263] Fig. 15 a); (b) an as-grown MLG (Ref. [263] Fig. 15 e); (c) after hydrogen intercalation (Ref. [263] Fig. 15 b). 122
12.2 The surface projected Kohn-Sham band structure and DOS of the (a) ZLG, (b) MLG, and (c) BLG calculated in the ($\sqrt{3} \times \sqrt(3)$) approximate unit cell using the HSE06 hybrid functional. 124
12.3 Comparison between the DOS of the $\sqrt{3}$-ZLG and $6\sqrt{3}$-ZLG surface calculated using PBE exchange-correlation functional. The full DOS is shown in blue, the projected DOS of all Si atoms in the slab (beige) and of the Si dangling bonds (pink). On the right are shown images of the geometric structure optimised using PBE+vdW. 126

12.4 The electron density of the $6\sqrt{3}$-MLG phase. Panel (a) shows the full electron density n_{full} of the MLG surface integrated over the x-y-plane along the z-axis (solid black line), the electron density of the substrate (filled in grey) n_{sub} and the graphene layer n_{G}. The average atomic layer position is indicated by dashed lines. Panel (b) displays a cutout of the atomic surface structure. The boxes indicate the structures calculated in isolation, black the full slab, grey the substrate and red the graphene layer. Panel (c) shows the electron density difference $\Delta n(z)$ (Eq. 12.1 and Eq. 12.2). The charge transfer is calculated by integrating $\Delta n(z)$ from z' to ∞ (integrated area filled in red). Panel (d) shows the charge distribution in the x-y-plane at $z = z'$. 128
12.5 The difference in the electron density given by Eq. 12.1 is shown for the 3C-SiC MLG phase. Eq. 12.2 gives Δn averaged over the x-y-plane and plotted it along z. The position of the Si, C, H, and graphene-layer are indicated by dashed lines. We show $\Delta n(z_i)$ in the x-y-plane at equidistant z_i heights between the MLG-layer and the substrate. 129
12.6 The band structure of a 13×13 graphene cell. Subfigure a) shows the Hirshfeld charge distribution of a MLG layer. b) shows the unfolded band structure of a perfectly periodic 13×13 graphene cell and overlayed in red is the band structure of free-standing graphene in its 1×1 unit cell. c) unfolded band structure of a flat graphene layer doped according to the Hirshfeld charges. The charges lead to a shift of the Dirac point by 0.22 eV. c) the unfolded band structure with the same corrugation as the MLG layer. d) Band structure of a graphene layer which is both corrugated and doped. The region around the Dirac point is enlarged showing the shift of the Dirac point caused by the doping. 132
12.7 The bulk projected Kohn-Sham band structure and DOS of the $\sqrt{3}$-MLG structure with the Si dangling bond saturated by an H atom. The full band structure and DOS of the slab used in the calculation is shown in red and the 3C-SiC bulk states in grey. 133
12.8 Four times the ZLG layer coloured depending on the Hirshfeld charge of the C atom from blue for electron gain to red for electron loss. The position of the unsaturated Si atoms is shown in pink. The scanning tunnelling microscopy (STM) image taken from Qi *et al.* [256] is shown for comparison. . . 134

13.1 (a) Vertical distances measured by normal incidence x-ray standing wave (NIXSW) on QFMLG. The position of the Bragg planes around the surface are indicated by blue lines [294]. PBE+vdW calculated geometry for (b) QFMLG on 6H-SiC(0001) and histograms of the number of atoms N_a versus the atomic coordinates (z) relative to the topmost Si layer (Gaussian broadening: 0.05 Å). N_a is normalised by N_{SiC}, the number of SiC unit cells. $D_{n,n+1}$ is the distance between the layer n and $n+1$, d_n gives the Si-C distance within the SiC bilayer n, and δ_n the corrugation of the layer n. All values are given in Å. (Figure published in Ref. [294]) 138
13.2 The difference in the electron density given by Eq. 12.1 is shown for the 3C-SiC QFMLG phase. We integrated Δn in the x-y-plane and plotted it along z (Eq. 12.2). The position of the Si, C, H, and graphene-layer are indicated by dashed lines. We show $\Delta n(z_i)$ in the x-y-plane at equidistant z_i heights between the graphene layer and the substrate. 141

14.1 Geometry of the 3C-SiC($\bar{1}\bar{1}\bar{1}$) $(2\times2)_C$ Si adatom structure. The bond length of the adatom with the top C layer ($L_{\text{Si-C}}$), the distance from the surface ($D_{\text{C,Si}}$) and the corrugation of the top Si layer (δ_{Si}) are shown. 144
14.2 All structural models based on the model proposed by Hoster *et al.* [145] for the (3×3) reconstructions of the 3C-SiC($\bar{1}\bar{1}\bar{1}$) are shown in a side and top view. In the top view the unit cell is marked in red. We include three different chemical compositions: (a) from Hiebel *et al.* [139], (b) from Deretzis and La Magna [71], (c) as a plain Si adatom. 146
14.3 A Si rich structural model for the (3×3) reconstructions shown in a side and top view from Ref. [139]. In the top view the unit cell is marked in red. 147
14.4 Three different chemical compositions of the tetrahedral ad-cluster structure suggested by Li and Tsong [192]. In a) the tetrahedron is formed by a Si atom surrounded by three C atoms, b) three C atoms surrounding a Si atom (a) and b) shown in a side view), c) 4 Si atoms form a tetrahedron (side and top view) 147
14.5 A Si rich structural model for the (3×3) reconstructions adapted from the Si face [177] 148

14.6 The Si twist model adapted from the 3C-SiC(111)-(3×3) reconstruction Sec. 8.1.2. On the left: The Si twist model from a side view. On the right: The Si twist model from a top view. The unit cell is shown in blue. The Si adatoms are coloured depending on their distance to the top Si-C-bilayer: The nine ad-layer Si atoms in dark blue, the three Si adatoms on top of the ad-layer in blue and the top Si adatom in purple. (Figure published in Ref. [228]) 148
14.7 Comparison of the surface energies relative to the bulk terminated (1×1) phase as a function of the C chemical potential within the allowed ranges (given by diamond Si, graphite C and for completeness diamond C, respectively). The shaded areas indicate chemical potential values outside the strict thermodynamic stability limits. Included in the surface energy diagram are structure models as proposed for the C face [(b) [292] Sec. 14.1.1, (d) [192] Fig. 14.4 c), (e) Fig. 14.2 c) and (h) [145] with the chemical composition given by [139] Fig. 14.2 a), (f) [139] Fig. 14.3, (g) [71] Fig. 14.2 b] and models adapted from the Si face [(a) [310] Fig. 14.6 and (c) [177] Fig. 14.5]. In the right panel the different models for the (3×3) reconstructions of the 3C-SiC($\bar{1}\bar{1}\bar{1}$) are ordered by their surface energies in the graphite C limit of the chemical potential with increasing stability from top to bottom. (Figure published in Ref. [228]) 149
14.8 I: The a) and b) phases from Fig. 14.7 calculated using the HSE06+vdW exchange-correlation functional with fully relaxed structures and unit cells (Tab. 7.2). II: Simulated constant current STM images for occupied- and empty-state of the Si twist model (unit cell shown in red). The three points of interest (A, B, C) are marked by arrows and labeled according to Hiebel *et al.* [139]. III: The DOS for the spin-up and spin-down states clearly shows a band gap rendering the surface semiconducting. (Figure published in Ref. [228]) . . 151
14.9 Comparison of the surface energies for four different interface structures of 3C-SiC($\bar{1}\bar{1}\bar{1}$), relative to the bulk-truncated (1×1) phase, as a function of the C chemical potential within the allowed ranges (given by diamond Si, diamond C or graphite C, respectively), using the graphite limit as zero reference. In addition, the known $(2\times2)_C$ reconstruction and the (3×3) Si twist model are shown. (Figure published in Ref. [228]) . . . 153

A.1 Calculated Helmholtz free energies within the BO-approximation as a function of the volume per atom for graphite and diamond at 4 different temperatures (0 K, 700 K, 1500 K and 3000 K) using PBE+vdW. The B.-M. fit is shown as red solid line (blue dashed line) for diamond (graphite). The calculated points used for the fitting are shown as crosses (squares) for diamond (graphite). The phase transition line - a tangent to both curves Eq. A.2 - between graphite and diamond is shown. [Plot taken from Lazarevic [184]] III
A.2 The unit cell volume for graphite (top panel) and diamond (bottom panel) for temperatures ranging from 0 K to 1400 K calculated using PBE+vdW. [Data taken from Lazarevic [184]] For comparison, experimental x-ray measurements data from Thewlis and Davey [320] is included for diamond as green circles. IV
A.3 The graphite-diamond coexistence line is shown in a pressure-temperature phase diagram for different E_{XC}s;(a) PBE, (b) PBE+vdW and (c) LDA. For comparison previous calculations and experimental data are included in the plot: LDA (Windl) [205] (red), LCBOPI+ data (1) [103], neural-networking classical (2) and quantum nuclei (3) results [164], Bermann-Simon line (4) [23] and experimental data (Exp. 1 (5) [44], Exp. 2 (6) [162] and Exp. 3 (7) [43]). [Plot adapted from Lazarevic [184]] VI

B.1 Effect of increasing the basis set size on the surface energy of the $\sqrt{3}$ approximant to the ZLG phase at the chemical potential limit of bulk graphite. The PBE+vdW functional was used. In the plot we use T1 (T2) as abbrevation of *tier 1* (*tier 2*) , respectively X
B.2 Slab thickness dependence of the surface energy of the ($\sqrt{3} \times \sqrt{3}$)-R30° approximant to the ZLG phase. XII
B.3 The Kohn-Sham band-gap (blue circles) and valence band width along Γ to X (red circles) of 3C-SiC as a function of α. The HSE06 value $\alpha = 0.25$ is marked by a vertical line. The experimental valence band width is shown as horizontal line at 3.6 eV[143] and the exp. band gap at 2.42 eV[148]. XIV

C.1 The band structure of cubic silicon carbide (3C-SiC) is shown along the high symmetry lines. We used the Heyd-Scuseria-Ernzerhof hybrid functional [138, 175] (HSE). The atomic structure was relaxed including vdW corrections (Tab. 7.2). 3C-SiC has an indirect band gap between Γ and X of 2.33 eV. XV

C.2 The band structure of 4H-SiC is shown along the high symmetry lines. We used the Heyd-Scuseria-Ernzerhof hybrid functional [138, 175] (HSE). The atomic structure was relaxed including vdW corrections (see Tab. 7.2). 4H-SiC has an indirect band gap between Γ and M of 3.26 eV. XVI
C.3 The band structure of 6H-SiC is shown along the high symmetry lines. We used the Heyd-Scuseria-Ernzerhof hybrid functional [138, 175] (HSE). The atomic structure was relaxed including vdW corrections (see Tab. 7.2). 6H-SiC has an indirect band gap between Γ and M of 2.92 eV. XVII

D.1 Calculated phonon dispersion relation of graphene along the high symmetry lines (PBE+vdW). XVIII
D.2 Calculated phonon dispersion relation of graphite along the high symmetry lines (PBE+vdW). XX
D.3 Calculated phonon dispersion relation of diamond along the high symmetry lines (PBE+vdW). XXI
D.4 Calculated phonon dispersion relation of SiC along the high symmetry lines (PBE+vdW). XXII

E.1 The distance between a Si atom of the top SiC bilayer and the closest C atom in the ZLG layer is used to identify the Si dangling bonds. XXIV

F.1 The Density of states of the $\sqrt{3}$-MLG structure calculated using the PBE and the HSE06 exchange-correlation functional. Shown in red is the DOS of the slab used in the calculation and in grey is shown the 3C-SiC-bulk projected DOS. XXV

G.1 The zero-layer graphene (ZLG) of the hexagonal SiC polytype (6H-SiC) using an approximated $\sqrt{3} \times \sqrt{3}$-R30° unit cell and their surface energies are shown for different SiC-bilayer stacking order calculated using PBE+vdW. XXVIII

I.1 Schematic representation of the 3C-SiC(111)-(3×3) reconstruction. The numeration of the Si adatoms in the unit cell (shown in black) is used to mark the atoms according to their appearance in Tab. I.1. XXX

List of Tables

6.1 The structural and cohesive properties of diamond, graphite and graphene are listed for different exchange-correlation functionals (LDA, PBE, HSE06 and vdW corrected PBE+vdW and HSE06+vdW): The lattice parameters a_0 [Å] and for graphite c_0 [Å] calculated by minimising the energy with the help of analytic forces and stress tensor as implemented in the FHI-aims-code [169]. The cohesive energy E_{coh} [eV] as obtained in this work. Reference data from experiment is included. "PES" refers to results computed based on the Born-Oppenheimer potential energy surface without any corrections. 47
6.2 Calculated ground state lattice parameter a_0 and c_0, unit cell volume per atom and cohesive energies for diamond and graphite using Def. 6.1.1. "PES" refers to results computed based on the Born-Oppenheimer potential energy surface without any corrections. We also include ZPC lattice parameters. (Data taken from Master thesis by Florian Lazarevic [184]) 49

7.1 The distance $d_{n,n-1}$ between two SiC-bilayer and the distance D_n between the Si and C sublayer with in SiC-bilayer are listed for 3C-SiC, 4H-SiC and 6H-SiC calculated for different exchange-correlation functionals (LDA, PBE, HSE and vdW corrected PBE+vdW and HSE06+vdW). 63

7.2 The structural and cohesive properties of 3C-SiC, 4H-SiC and 6H-SiC are listed for different exchange-correlation functionals (LDA, PBE, HSE06 and vdW corrected PBE+vdW and HSE06+vdW): The lattice parameters a_0 [Å], and for the two hexagonal polytypes c_0 [Å/n] where n is the number of SiC bilayers, the bulk modulus B_0 [Mbar], cohesive energy E_{coh} [eV], and enthalpy of formation ΔH_f [eV] as obtained in this work. Reference data from experiment and theory is included. The theoretical reference data was calulated using DFT codes based on pseudopotentials with a plane-wave basis (PSP-PW) [15, 244, 157, 355, 126] or Gaussian basis (PSP-G) [12] in the LDA. "PES" refers to results computed based on the Born-Oppenheimer potential energy surface without any corrections. We also include zero-point vibrational correction (ZPC) lattice parameters and bulk moduli. 65
7.3 The direct and indirect band gap and the valence band width are listed for 3C-SiC, 4H-SiC and 6H-SiC calculated for different exchange-correlation functionals (PBE, LDA, HSE06). We used the geometries given in Tab. 7.2 for PBE, HSE06 the vdW corrected values were chosen. 70

8.1 Atomic position of the Si adatom relative to the surface for different exchange-correlation functionals. The bulk lattice parameter were taken from Tab. 7.2. For 6H-SiC we chose a ABCACB stacking order (see Appendix G). $L_{\text{Si-Si}}$ is the bond length between the adatom and the top layer Si atoms, $D_{1_{\text{Si}},\text{Si}}$ is the distance between the adatom and top layer Si atoms along the z-axis, and δ_{1_C} is the corrugation of the top C-layer (see Fig. 8.2). (All values in Å) 76
8.2 Layer distances of the Si adatom structure relative to the surface for different exchange-correlation functionals (LDA and PBE+vdW) of the 3C-SiC(111)-(3×3) reconstruction. For comparison, the layer distances obtained from quantitative LEED measurements are included [276]. (All values in Å) . . 78

9.1 Parameters of the simulated ZLG-3C-SiC(111) interface structures in different commensurate supercells: the 3C-SiC and ZLG periodicity, the rotation angle (α), the number of surface Si atoms ($\text{N}_{\text{SiC}}^{\text{surf}}$) and C atoms in the ZLG (N_{ZLG}), the number of unsaturated Si bonds ($\text{N}_{\text{Si}}^{\text{DB}}$) (see Appendix E), the corrugation of the ZLG layer (δ_C), the strain in the carbon layer, and the relative surface energy at the carbon rich graphite-limit ($\gamma|_{\mu_C=E_{\text{graphite}}^{\text{bulk}}}$). 90

9.2 PBE+vdW calculated effective lateral lattice parameter a_{eff} (in Å), the top-to-bottom corrugation Δz (in Å) and the effective area lost (gained) per defect, ΔA_{defect} (in Å^2) of different defect types and periodicities in an ideal, free-standing graphene sheet. (Table published in Ref. [284]) 98

12.1 The Hirshfeld charge per C atom [e^-/atom] in the $\sqrt{3}$-MLG calculated using PBE and HSE06 and for comparison the Hirshfeld charges calculated in the $6\sqrt{3}$-MLG structure using PBE. 130

14.1 Atomic position of the Si adatom relative to the surface for different exchange-correlation functionals. The bulk lattice parameter were taken from Tab. 7.2. $L_{\text{Si-C}}$ is the bond length between the adatom and the top layer C atoms, $D_{\text{C,Si}}$ is the distance between the adatom and top layer C atoms along the z-axis, and δ_{Si} is the corrugation of the top Si-layer (see Fig. 14.1). (All values in Å) 144

A.1 Calculated unit cell volume of graphite in the temperature range between 288 K and 1073 K. For comparison DFT data using vdW Grimme [117] corrected PBE-D (Ref. Yu *et al.* [349]) and experimental data (Ref. Nelson and Riley [226]). . II

A.2 For the exchange-correlation functional (LDA, PBE, PBE+vdW) the linear interpolation of the p-T-data in the temperature range between 1000 K and 1500 K, to the Berman-Simon line, $P = a + bT$, where b is the slope in GPa/K. In addition the coexistence pressure p_{coex} at 0 K is given for different functionals. Reference data is given for two theoretical works (a) Yu *et al.* [349], (b) Khaliullin *et al.* [164] and experimental data (c) Kennedy and Kennedy [162], (d) Bundy *et al.* [44] and (e) Bundy *et al.* [43]. VII

B.1 Radial functions used for C and Si. The first line ("minimal") denotes the radial functions of the occupied orbitals of spherically symmetric free atoms as computed in DFT-LDA or -PBE (noble-gas configuration of the core and quantum numbers of the additional valence radial functions). "H(nl, z)" denotes a hydrogen-like basis function for the bare Coulomb potential z/r, including its radial and angular momentum quantum numbers, n and l. X^{2+}(nl) denotes a n, l radial function of a doubly positive free ion of element X. See also Ref. Blum *et al.* [32] for notational details. IX

B.2 Surface energies in [eV/SiC(1x1)] relative to the unreconstructed 3C-SiC(1x1) surface for the chemical potential limit of graphite, four-bilayer SiC slabs. The silicon-rich $\sqrt{3}$x$\sqrt{3}$ reconstruction, ZLG and MLG phases using different k-grids are shown. The PBE+vdW exchange-correlation functional was used. XIII

F.1 Influence of the functional on the interface structure of 6H-SiC ($\sqrt{3}$-SiC model cell). $D_{n,n+1}$ is the distance between layer n and $n+1$, d_n gives the distance within SiC bilayer n, and δ_n the corrugation of layer n. All distances are given in Å. . . XXVII

H.1 Geometry comparison of the layer distance ($D_{n,n+1}$), the Si-C distance within a SiC bilayer (d_n) and the layer corrugation, the difference between the highest and lowest atom in the layer, (δ_n) for two different SiC polytypes, 6H-SiC(0001) and 3C-SiC(111), including the QFMLG and MLG surface structure calculated with PBE+vdW. The data was taken from [227]. XXIX

I.1 The displacement of the adatoms with respect to their symmetric bulk position. The surface structure was calculated using PBE+vdW for the approximantion to the exchange-correlation functional (E_{XC}). The LEED optimised geometric structure from Schardt [276] is included for comparison. . . XXXI

[1] *Silicon carbide (SiC) lattice parameters*. In O. Madelung, U. Rössler, and M. Schulz, editors, *Group IV Elements, IV-IV and III-V Compounds. Part a - Lattice Properties*, vol. 41A1a of *Landolt-Börnstein - Group III Condensed Matter*, (p. 1-13). Springer Berlin Heidelberg (2001).
[ISBN 9783540640707].
[doi:10.1007/10551045_253]. 7.1

[2] Acheson, E. G. *Production of Artificial Crystaline Garbonaceous Materials* (February 1893). US Patent 492,767.
http://www.google.com/patents/US492767 7

[3] Ajoy, A., Murali, K. V. R. M., and Karmalkar, S. *Brillouin zone unfolding of complex bands in a nearest neighbour tight binding scheme*. *Journal of Physics: Condensed Matter*, vol. 24 (5) : 055504 (2012).
[doi:10.1088/0953-8984/24/5/055504]. 11

[4] Allen, P. B., Berlijn, T., Casavant, D. A., and Soler, J. M. *Recovering hidden Bloch character: Unfolding electrons, phonons, and slabs*. *Physical Reviews B*, vol. 87 : 085322 (February 2013).
[doi:10.1103/PhysRevB.87.085322]. 11

[5] Ambrosetti, A., Reilly, A. M., DiStasio, R. A., and Tkatchenko, A. *Long-range correlation energy calculated from coupled atomic response functions*. *The Journal of Chemical Physics*, vol. 140 (18) : 18A508 (2014).
[doi:10.1063/1.4865104]. 2.4, 6.2, 6.5, 6.2, 7.1, F.1, J.1, J

[6] Araujo, P. T., Terrones, M., and Dresselhaus, M. S. *Defects and impurities in graphene-like materials*. *Materials Today*, vol. 15 (3) : 98 - 109 (2012). ISSN 1369-7021.
[doi:10.1016/S1369-7021(12)70045-7]. 9.3

[7] Barone, V., Casarin, M., Forrer, D., Pavone, M., Sambi, M., and Vittadini, A. *Role and effective treatment of dispersive forces in materials: Polyethylene and graphite crystals as test cases*. *J. Comput. Chem.*, vol. 30 : 934 (2008).
[doi:10.1002/jcc.21112]. 6.2, J.1

[8] Baroni, S., Giannozzi, P., and Testa, A. *Green's-Function Approach to Linear Response in Solids*. *Phys. Rev. Lett.*, vol. 58 (18) : 1861–1864 (May

1987).
[doi:10.1103/PhysRevLett.58.1861]. 2

[9] Baskin, Y. and Meyer, L. *Phys. Rev.*, vol. 100 : 544 (1955). 8.2, 8.2

[10] Bassett, W. A., Weathers, M. S., Wu, T.-C., and Holmquist, T. *Compressibility of SiC up to 68.4 GPa*. *Journal of Applied Physics*, vol. 74 (6) : 3824-3826 (1993).
[doi:10.1063/1.354476]. 7.1

[11] Batsanov, S. S. and Batsanov, A. S. *Introduction to Structural Chemistry*. SpringerLink : Bücher. Springer (2012).
[ISBN 9789400747715].
http://books.google.de/books?id=YiHHkIA7K4MC A

[12] Baumeier, B., Krüger, P., and Pollmann, J. *Self-interaction-corrected pseudopotentials for silicon carbide*. *Phys. Rev. B*, vol. 73 (19) : 195205 (May 2006).
[doi:10.1103/PhysRevB.73.195205]. 7.1, 7.2, J

[13] Bechstedt, F. *Principles of Surface Physics*. Advanced Texts in Physics. Springer, Heidelberg, 1 ed. (2003).
[ISBN 978-3-642-55466-7].
[doi:10.1007/978-3-642-55466-7]. 1

[14] Bechstedt, F. and Furthmüller, J. *Electron correlation effects on SiC(111) and SiC(0001) surfaces*. *J. Phys.: Condens. Matter*, vol. 16 (17) : S1721–S1732 (2004).
[doi:10.1088/0953-8984/16/17/014]. 10

[15] Bechstedt, F., Käckell, P., *et al.* *Polytypism and Properties of Silicon Carbide*. *physica status solidi (b)*, vol. 202 (1) : 35–62 (1997). ISSN 1521-3951.
[doi:10.1002/1521-3951(199707)202:1<35::AID-PSSB35>3.0.CO;2-8]. 7.1, 7.2, J

[16] Becke, A. D. *A new mixing of Hartree-Fock and local density-functional theories*. *The Journal of Chemical Physics*, vol. 98 (2) : 1372-1377 (1993).
[doi:10.1063/1.464304]. 2.3.3

[17] Benedict, L. X., Chopra, N. G., Cohen, M. L., Zettl, A., Louie, S. G., and Crespi, V. H. *Microscopic determination of the interlayer binding energy in graphite*. *Chem. Phys. Lett.*, vol. 286 (5-6) : 490–496 (April

1998).
[doi:10.1016/S0009-2614(97)01466-8]. 6.2, 6.4, 6.2, 6.5, 6.2, J.1, J

[18] Berger, C., Song, Z., *et al.* *Ultrathin epitaxial graphite: 2D electron gas properties and a route toward graphene-based nanoelectronics*. *J. Phys. Chem. B*, vol. 108 (52) : 19912–19916 (December 2004).
[doi:10.1021/jp040650f]. (document), 7, III

[19] Berger, C., Song, Z., *et al.* *Electronic confinement and coherence in patterned epitaxial graphene*. *Science*, vol. 312 (5777) : 1191 (May 2006).
[doi:10.1126/science.1125925]. (document), III, 9.2, 12.2

[20] Berger, C., Song, Z., *et al.* *Electronic confinement and coherence in patterned epitaxial graphene*. *Science*, vol. 312 (5777) : 1191 (May 2006).
[doi:10.1126/science.1125925]. 7

[21] Berger, C., Veuillen, J., *et al.* *Electronic properties of epitaxial graphene*. *Int. J. Nanotechnol.*, vol. 7 (4) : 383–402 (2010). (document), III, 8.2

[22] Berland, K. and Hyldgaard, P. *Exchange functional that tests the robustness of the plasmon description of the van der Waals density functional*. *Physical Review B*, vol. 89 : 035412 (January 2014).
[doi:10.1103/PhysRevB.89.035412]. 6.2, J.1

[23] Berman, R. and Simon, F. *On the Graphite-Diamond Equilibrium*. *Z. f. Elektrochem.: Ber. Bunsenges. Phys. Chem.*, vol. 59 : 333-338 (1955). 4.2, 6.1, 14.1.2, A, A.3, A, J

[24] Bernhardt, J., Nerding, M., Starke, U., and Heinz, K. *Stable surface reconstructions on 6H-SiC(000$\bar{1}$*. *Materials Science and Engineering: B*, vol. 61 – 62 (0) : 207 – 211 (1999).
[doi:10.1016/S0921-5107(98)00503-0]. (document), 14.1, 14.1.2, 14.1.3

[25] Bernhardt, J., Schardt, J., Starke, U., and Heinz, K. *Epitaxially ideal oxide-semiconductor interfaces: Silicate adlayers on hexagonal (0001) and (000-1) SiC surfaces*. *Applied Physics Letters*, vol. 74 (8) : 1084-1086 (1999).
[doi:10.1063/1.123489]. (document)

[26] Bhatnagar, M. and Baliga, B. *Comparison of 6H-SiC, 3C-SiC, and Si for power devices*. *Electron Devices, IEEE Transactions on*, vol. 40 (3) :

645-655 (March 1993).
[doi:10.1109/16.199372]. 7

[27] Birch, F. *Finite Elastic Strain of Cubic Crystals*. *Physical Review*, vol. 71 : 809–824 (June 1947).
[doi:10.1103/PhysRev.71.809]. 6.1, A

[28] Björkman, T., Gulans, A., Krasheninnikov, A. V., and Nieminen, R. M. *Are we van der Waals ready?* *Journal of Physics: Condensed Matter*, vol. 24 (42) : 424218 (2012).
[doi:10.1088/0953-8984/24/42/424218]. 6.2

[29] Björkman, T., Gulans, A., Krasheninnikov, A. V., and Nieminen, R. M. *van der Waals Bonding in Layered Compounds from Advanced Density-Functional First-Principles Calculations*. *Physical Review Letters*, vol. 108 : 235502 (June 2012).
[doi:10.1103/PhysRevLett.108.235502]. 6.2

[30] Blaha, P., Schwarz, K., Sorantin, P., and Trickey, S. *Full-potential, linearized augmented plane wave programs for crystalline systems*. *Computer Physics Communications*, vol. 59 (2) : 399 - 415 (1990).
[doi:10.1016/0010-4655(90)90187-6]. 2.5

[31] Bloch, F. *Über die Quantenmechanik der Elektronen in Kristallgittern*. *Zeitschrift fÃ$\frac{1}{4}$r Physik*, vol. 52 (7-8) : 555-600 (1929). ISSN 0044-3328.
[doi:10.1007/BF01339455]. 11

[32] Blum, V., Gehrke, R., *et al.* *Ab initio molecular simulations with numeric atom-centered orbitals*. *Comp. Phys. Commun.*, vol. 180 (11) : 2175–2196 (2009).
[doi:10.1016/j.cpc.2009.06.022]. 2.5, 2.5, 2.5, 6.1, B.1, B.1, F.1, J

[33] Bocquet, F. C., Bisson, R., Themlin, J.-M., Layet, J.-M., and Angot, T. *Reversible hydrogenation of deuterium-intercalated quasi-free-standing graphene on SiC(0001)*. *Physical Review B*, vol. 85 (20) : 201401 (2012).
[doi:10.1103/PhysRevB.85.201401]. 13.2

[34] Bostwick, A., McChesney, J., Ohta, T., Rotenberg, E., Seyller, T., and Horn, K. *Experimental studies of the electronic structure of graphene*. *Progress in Surface Science*, vol. 84 (11) : 380–413 (2009).
[doi:10.1016/j.progsurf.2009.08.002]. 12

[35] Bostwick, A., Ohta, T., Seyller, T., Horn, K., and Rotenberg, E. *Quasiparticle dynamics in graphene*. *Nature Physics*, vol. 3 (1) : 36–40 (2007). [doi:10.1038/nphys477]. (document), 6.3, 12, 12.1, 12.2, 12.4

[36] Boykin, T. B., Kharche, N., Klimeck, G., and Korkusinski, M. *Approximate bandstructures of semiconductor alloys from tight-binding supercell calculations*. *Journal of Physics: Condensed Matter*, vol. 19 (3) : 036203 (2007).
[doi:10.1088/0953-8984/19/3/036203]. 11

[37] Boykin, T. B. and Klimeck, G. *Practical application of zone-folding concepts in tight-binding calculations*. *Phys. Rev. B*, vol. 71 : 115215 (March 2005).
[doi:10.1103/PhysRevB.71.115215].
http://link.aps.org/doi/10.1103/PhysRevB.71.115215 11

[38] Brandenburg, J. G., Alessio, M., Civalleri, B., Peintinger, M. F., Bredow, T., and Grimme, S. *Geometrical Correction for the Inter- and Intramolecular Basis Set Superposition Error in Periodic Density Functional Theory Calculations*. *The Journal of Physical Chemistry A*, vol. 117 (38) : 9282-9292 (2013).
[doi:10.1021/jp406658y]. 6.2, J.1

[39] Brennan, R. O. *The Interlayer Binding in Graphite*. *J. Chem. Phys.*, vol. 20 : 40 (1952).
[doi:10.1063/1.1700193]. J.1

[40] Brewer, L. *Cohesive energies of the elements* (January 1975).
[doi:10.2172/7187973]. 6.1, 6.1

[41] Brown, M. G. *Atom hybridization and bond properties. Some carbon-containing bonds*. *Trans. Faraday Soc.*, vol. 55 : 694-701 (1959).
[doi:10.1039/TF9595500694]. 9.1

[42] Bučko, T. c. v., Lebègue, S., Hafner, J., and Ángyán, J. G. *Tkatchenko-Scheffler van der Waals correction method with and without self-consistent screening applied to solids*. *Phys. Rev. B*, vol. 87 : 064110 (February 2013).
[doi:10.1103/PhysRevB.87.064110]. 6.2, J.1

[43] Bundy, F., Bassett, W., Weathers, M., Hemley, R., Mao, H., and Goncharov, A. *The pressure-temperature phase and transformation diagram for carbon; updated through 1994*. *Carbon*, vol. 34 (2) : 141 - 153 (1996).
[doi:10.1016/0008-6223(96)00170-4]. A, A, A.3, A.2, J

[44] Bundy, F. P., Bovenkerk, H. P., Strong, H. M., and Wentorf Jr, R. H. *Diamond-Graphite Equilibrium Line from Growth and Graphitization of Diamond*. *The Journal of Chemical Physics*, vol. 35 (2) : 383 - 391 (August 1961). ISSN 0021-9606.
[doi:10.1063/1.1731938]. A, A, A.3, A.2, J

[45] Bučko, T., Lebègue, S., Ángyán, J. G., and Hafner, J. *Extending the applicability of the Tkatchenko-Scheffler dispersion correction via iterative Hirshfeld partitioning*. *The Journal of Chemical Physics*, vol. 141 (3) : 034114 (2014).
[doi:10.1063/1.4890003]. 6.2, J.1

[46] Capelle, K. *A bird's-eye view of density-functional theory*. *eprint arXiv* (November 2002).
[arxiv:cond-mat/0211443]. I

[47] Carlsson, J. M. *Simulations of the Structural and Chemical Properties of Nanoporous Carbon*, vol. 3 of *Carbon Materials: Chemistry and Physics*. Springer Netherlands (2010).
[ISBN 978-1-4020-9717-1].
[doi:10.1007/978-1-4020-9718-8_4]. 9.3, 9.3

[48] Carlsson, J. M. (2013). Private communication. 9.3

[49] Casady, J. B. and Johnson, R. W. *Status of silicon carbide (SiC) as a wide-bandgap semiconductor for high-temperature applications: A review*. *Solid-State Electronics*, vol. 39 (10) : 1409 - 1422 (October 1996).
[doi:10.1016/0038-1101(96)00045-7]. 7

[50] Castro Neto, A. H., Guinea, F., Peres, N. M. R., Novoselov, K. S., and Geim, A. K. *The electronic properties of graphene*. *Rev. Mod. Phys.*, vol. 81 : 109–162 (January 2009).
[doi:10.1103/RevModPhys.81.109]. (document), 6, 6.3

[51] Casula, M., Filippi, C., and Sorella, S. *Diffusion Monte Carlo Method with Lattice Regularization*. *Physical Review Letters*, vol. 95 : 100201 (September 2005).
[doi:10.1103/PhysRevLett.95.100201]. 6.2

[52] Ceperley, D. M. and Alder, B. J. *Ground State of the Electron Gas by a Stochastic Method*. *Phys. Rev. Lett.*, vol. 45 (7) : 566–569 (August 1980).
[doi:10.1103/PhysRevLett.45.566]. 2.3.1

[53] Chakarova-Käck, S. D., Schröder, E., Lundqvist, B. I., and Langreth, D. C. *Application of van der Waals Density Functional to an Extended System: Adsorption of Benzene and Naphthalene on Graphite*. *Phys. Rev. Lett.*, vol. 96 : 146107 (April 2006).
[doi:10.1103/PhysRevLett.96.146107]. 6.2

[54] Charlier, J. C., Gonze, X., and Michenaud, J. P. *First-principles study of the stacking effect on the electronic properties of graphite(s)*. *Carbon*, vol. 32 : 289–299 (1994).
[doi:10.1016/0008-6223(94)90192-9]. 6.2, J.1

[55] Chen, W., Xu, H., *et al.* *Atomic structure of the 6H-SiC(0001) nanomesh*. *Surf. Sci.*, vol. 596 : 176 - 186 (2005).
[doi:10.1016/j.susc.2005.09.013]. 8.2, 8.2, 9.2

[56] Chen, X., Tian, F., Persson, C., Duan, W., and Chen, N.-x. *Interlayer interactions in graphites*. *Scientific Report*, vol. 3 (November 2013).
[doi:10.1038/srep03046]. J.1

[57] Cheung, R. *Silicon Carbide Micro Electromechanical Systems for Harsh Environments*. Imperial College Press (2006).
[ISBN 9781860946240]. II, 7

[58] Clark, S., Segall, M., *et al.* *First principles methods using CASTEP*. *Zeitschrift für Kristallographie*, vol. 220 (5-6) : 567–570 (2005).
[doi:10.1524/zkri.220.5.567.65075]. 2.5

[59] Cooper, V. R. *Van der Waals density functional: An appropriate exchange functional*. *Physical Review B*, vol. 81 : 161104 (April 2010).
[doi:10.1103/PhysRevB.81.161104]. 6.2, J.1

[60] Dappe, Y. J., Basanta, M. A., Flores, F., and Ortega, J. *Weak chemical interaction and van der Waals forces between graphene layers: A combined density functional and intermolecular perturbation theory approach*. *Physical Review B*, vol. 74 : 205434 (2006).
[doi:10.1103/PhysRevB.74.205434]. J.1

[61] Dappe, Y. J., Bolcatto, P. G., Ortega, J., and Flores, F. *Dynamical screening of the van der Waals interaction between graphene layers*. *Journal of Physics: Condensed Matter*, vol. 24 (42) : 424208 (2012).
[doi:10.1088/0953-8984/24/42/424208]. J.1

[62] Das, A., Pisana, S., *et al.* *Monitoring dopants by Raman scattering in an*

electrochemically top-gated graphene transistor. *Nature Nanotechnology*, vol. 3 (4) : 210 - 215 (April 2008). ISSN 1748-3387.
[doi:10.1038/nnano.2008.67]. D.1.1

[63] Davis, S. G., Anthrop, D. F., and Searcy, A. W. *Vapor Pressure of Silicon and the Dissociation Pressure of Silicon Carbide*. *The Journal of Chemical Physics*, vol. 34 (2) : 659-664 (1961).
[doi:10.1063/1.1701004"]. 7.1

[64] De Heer, W., Berger, C., and Wu, X. *Epitaxial graphene*. *Solid State Communications*, vol. 143 : 92–100 (2007). (document), 7, III

[65] De Heer, W., Seyller, T., Berger, C., Stroscio, J., and Moon, J. *Epitaxial Graphenes on Silicon Carbide*. *MRS Bulletin*, vol. 35 (4) : 296 – 305 (2010).
[doi:10.1557/mrs2010.552]. (document), 8.2

[66] de Heer, W. A. *Epitaxial graphene: A new electronic material for the 21st century*. *MRS Bulletin*, vol. 36 : 632–639 (August 2011).
[doi:10.1557/mrs.2011.158]. 14

[67] de Heer, W. A., Berger, C., *et al.* *Large area and structured epitaxial graphene produced by confinement controlled sublimation of silicon carbide*. *Proc. Nat. Acad. Sci.*, vol. 108 : 16900 (2011). (document), 4.2, 10, 14.3

[68] de Lima, L. H., de Siervo, A., *et al.* *Atomic surface structure of graphene and its buffer layer on SiC(0001): A chemical-specific photoelectron diffraction approach*. *Physical Review B*, vol. 87 : 081403(R) (February 2013).
[doi:10.1103/PhysRevB.87.081403]. 8.2

[69] Delley, B. *An all-electron numerical method for solving the local density functional for polyatomic molecules*. *The Journal of Chemical Physics*, vol. 92 (1) : 508-517 (1990).
[doi:10.1063/1.458452]. 2.5

[70] Delley, B. *From molecules to solids with the DMol3 approach*. *The Journal of Chemical Physics*, vol. 113 (18) : 7756-7764 (2000).
[doi:10.1063/1.1316015]. 2.5

[71] Deretzis, I. and La Magna, A. *A density functional theory study of epitaxial graphene on the* (3×3)*-reconstructed C-face of SiC*. *Applied Physics Letters*, vol. 102 (2013).

[doi:10.1063/1.4794176]. (document), 14.1.2, 14.2, 14.1.2, 14.7, 14.1.3, J

[72] Dion, M., Rydberg, H., Schr
"oder, E., Langreth, D., and Lundqvist, B. *Van der Waals density functional for general geometries*. *Phys. Rev. Lett.*, vol. 92 (24) : 246401 (June 2004).
[doi:10.1103/PhysRevLett.92.246401]. 6.2

[73] Dirac, P. A. M. *Note on Exchange Phenomena in the Thomas Atom*. *Mathematical Proceedings of the Cambridge Philosophical Society*, vol. 26 : 376–385 (7 1930). ISSN 1469-8064.
[doi:10.1017/S0305004100016108]. 2.3.1, 2.3.1

[74] DiVincenzo, D. P., Mele, E. J., and Holzwarth, N. A. W. *Density-functional study of interplanar binding in graphite*. *Physical Review B*, vol. 27 (4) : 2458–2469 (February 1983).
[doi:10.1103/PhysRevB.27.2458]. J.1

[75] Dobson, J. F., White, A., and Rubio, A. *Asymptotics of the Dispersion Interaction: Analytic Benchmarks for van der Waals Energy Functionals*. *Phys. Rev. Lett.*, vol. 96 : 073201 (February 2006).
[doi:10.1103/PhysRevLett.96.073201]. 6.2

[76] Donchev, A. G. *Ab initio quantum force field for simulations of nanostructures*. *Phys. Rev. B*, vol. 74 : 235401 (2006).
[doi:10.1103/PhysRevB.74.235401]. J.1

[77] Dove, M. T. *Introduction to Lattice Dynamics*. Cambridge Topics in Mineral Physics and Chemistry. Cambridge University Press (1993).
[ISBN 0-521-39293-4].
[doi:10.2277/0521392934]. 3

[78] Dovesi, R., Orlando, R., *et al.* *CRYSTAL14: A program for the ab initio investigation of crystalline solids*. *International Journal of Quantum Chemistry*, vol. 114 (19) : 1287–1317 (2014).
[doi:10.1002/qua.24658]. 2.5

[79] Elias, D. C., Gorbachev, R. V., *et al.* *Dirac cones reshaped by interaction effects in suspended graphene*. *Nature Physics*, vol. 7 (9) : 701–704 (July 2011).
[doi:doi:10.1038/nphys2049]. 6.3

[80] Emery, J. D., Detlefs, B., *et al. Chemically Resolved Interface Structure of Epitaxial Graphene on SiC(0001)*. *Phys. Rev. Lett.*, vol. 111 (21) : 215501 (2013).
[doi:10.1103/PhysRevLett.111.215501]. 8.2, 8.2

[81] Emtsev, K., Seyller, T., *et al. Initial stages of the graphite-SiC (0001) interface formation studied by photoelectron spectroscopy*. In *Materials Science Forum*, vol. 556, (p. 525–528). Trans Tech Publ, scientific.net (September 2007).
[doi:10.4028/www.scientific.net/MSF.556-557.525]. 12

[82] Emtsev, K. V., Bostwick, A., *et al. Towards wafer-size graphene layers by atmospheric pressure graphitization of silicon carbide*. *Nature Materials*, vol. 8 (3) : 203–207 (February 2009).
[doi:10.1038/nmat2382]. (document), a, 7, III, 8.2, 10, 14, 14.3

[83] Emtsev, K. V., Speck, F., Seyller, T., Ley, L., and Riley, J. D. *Interaction, growth, and ordering of epitaxial graphene on SiC {0001} surfaces: A comparative photoelectron spectroscopy study*. *Phys. Rev. B*, vol. 77 (15) : 155303 (2008).
[doi:10.1103/PhysRevB.77.155303]. (document), b, III, 8, 8.2, 9.2, 9.2, 12, 12, 12.1, 12.2, 12.3, 12.4

[84] Farjam, M. *Visualizing the influence of point defects on the electronic band structure of graphene*. *Journal of Physics: Condensed Matter*, vol. 26 (15) : 155502 (2014).
[doi:10.1088/0953-8984/26/15/155502]. 11

[85] Feenstra, R. M. (2014). Private communication. 14.2

[86] Feibelman, P. J. and Alavi, A. *Entropy of H2O Wetting Layers*. *The Journal of Physical Chemistry B*, vol. 108 (38) : 14362-14367 (2004).
[doi:10.1021/jp049934q]. 14.1.3

[87] Ferralis, N., Maboudian, R., and Carraro, C. *Evidence of Structural Strain in Epitaxial Graphene Layers on 6H-SiC(0001)*. *Physical Review Letters*, vol. 101 : 156801 (October 2008).
[doi:10.1103/PhysRevLett.101.156801]. 9, 9.1, i

[88] Ferralis, N., Maboudian, R., and Carraro, C. *Determination of substrate pinning in epitaxial and supported graphene layers via Raman scattering*. *Phys. Rev. B*, vol. 83 : 081410 (February 2011).
[doi:10.1103/PhysRevB.83.081410]. 9.1

[89] Feynman, R. P. *Forces in Molecules*. *Phys. Rev.*, vol. 56 (4) : 340–343 (August 1939).
[doi:10.1103/PhysRev.56.340]. 2.5

[90] Filippi, C., Gonze, X., and Umrigar, C. J. *Generalized Gradient Approximations to Density Functional Theory: Comparison with Exact Results*, vol. 4 of *Theoretical and Computational Chemistry*, chap. 8, (p. 295–326). Elsevier Science (1996).
[ISBN 0-444-82404-9]. 2.3.2

[91] Fiori, G. and Iannaccone, G. *Multiscale Modeling for Graphene-Based Nanoscale Transistors*. *Proceedings of the IEEE*, vol. 101 (7) : 1653–1669 (2013).
[doi:10.1109/JPROC.2013.2259451]. (document)

[92] First, P., De Heer, W., Seyller, T., Berger, C., Stroscio, J., and Moon, J. *Epitaxial graphenes on silicon carbide*. *MRS Bulletin*, vol. 35 (4) : 296–305 (2010).
[doi:10.1557/mrs2010.552]. (document)

[93] Fissel, A., Schröter, B., and Richter, W. *Low-temperature growth of SiC thin films on Si and 6H-SiC by solid-source molecular beam epitaxy*. *Applied Physics Letters*, vol. 66 (23) : 3182-3184 (1995).
[doi:10.1063/1.113716]. 8.1.2

[94] Forbeaux, I., Themlin, J. M., Charrier, A., Thibaudau, F., and Debever, J. M. *Solid-state graphitization mechanisms of silicon carbide 6H-SiC polar faces*. *Applied Surf. Sci.*, (p. 406 - 412) (2000).
[doi:DOI: 10.1016/S0169-4332(00)00224-5]. a

[95] Forbeaux, I., Themlin, J.-M., and Debever, J.-M. *Heteroepitaxial graphite on* $6H-\mathrm{SiC}(0001):$ *Interface formation through conduction-band electronic structure*. *Phys. Rev. B*, vol. 58 : 16396–16406 (December 1998).
[doi:10.1103/PhysRevB.58.16396]. (document), III, 8, 8.2, 9.2, 14.3

[96] Forti, S., Emtsev, K. V., Coletti, C., Zakharov, A. A., Riedl, C., and Starke, U. *Large-area homogeneous quasifree standing epitaxial graphene on SiC(0001): Electronic and structural characterization*. *Physical Review B*, vol. 84 : 125449 (September 2011).
[doi:10.1103/PhysRevB.84.125449]. 12, 12.1

[97] Forti, S. and Starke, U. *Epitaxial graphene on SiC: from carrier density*

engineering to quasi-free standing graphene by atomic intercalation. *Journal of Physics D: Applied Physics*, vol. 47 (9) : 094013 (March 2014).
[doi:10.1088/0022-3727/47/9/094013]. (document), 13

[98] Frisch, M. J., Trucks, G. W., *et al.* *Gaussian09 Revision D.01* (2009). Gaussian Inc. Wallingford CT 2009.
http://www.gaussian.com/index.htm 2.5

[99] Furthmüller, J., Bechstedt, F., Husken, H., Schroter, B., and Richter, W. *Si-rich SiC (111)/(0001) 3 x 3 and sqrt (3) x sqrt (3) surfaces: A Mott-Hubbard picture*. *Physical Review B*, vol. 58 (20) : 13712 (November 1998).
[doi:10.1103/PhysRevB.58.13712]. 8.1.1, 8.1.1

[100] Furthmüller, J., Käckell, P., *et al.* *Model of the epitaxial growth of SiC-polytypes under surface-stabilized conditons*. *Journal of Electronic Materials*, vol. 27 (7) : 848–852 (1998).
[doi:10.1007/s11664-998-0108-1]. 8.1.1, 13.1

[101] Gehrke, R. *First-principles basin-hopping for the structure determination of atomic clusters*. Ph.D. thesis (????). 2.5

[102] Geim, A. and Novoselov, K. *The rise of graphene*. *Nature materials*, vol. 6 (3) : 183–191 (2007).
[doi:10.1038/nmat1849]. (document), 6

[103] Ghiringhelli, L. M., Los, J. H., Meijer, E. J., Fasolino, A., and Frenkel, D. *Modeling the Phase Diagram of Carbon*. *Phys. Rev. Lett.*, vol. 94 : 145701 (April 2005).
[doi:10.1103/PhysRevLett.94.145701]. 6.1, A, A, A.3, J

[104] Giannozzi, P., Baroni, S., *et al.* *QUANTUM ESPRESSO: a modular and open-source software project for quantum simulations of materials*. *Journal of Physics: Condensed Matter*, vol. 21 (39) : 395502 (2009).
[doi:10.1088/0953-8984/21/39/395502]. 2.5

[105] Girifalco, L. A. (1954). (Girifalco, PhD thesis 1954, cited in L. A. Girifalco and R. A. Lad, J. Chem. Phys. 25, 693 (1956).). J.1

[106] Girifalco, L. A. and Lad, R. A. *Energy of Cohesion, Compressibility, and the Potential Energy Functions of the Graphite System*. *J. Chem. Phys.*, vol. 25 : 693 (1956).
[doi:10.1063/1.1743030]. 6.2, 6.4, 6.2, 6.5, 6.2, J.1, J

[107] Gobre, V. V. and Tkatchenko, A. *Scaling laws for van der Waals interactions in nanostructured materials*. *Nature Communincation*, vol. 4 (August 2013).
[doi:10.1038/ncomms3341]. 9.3

[108] Goldberg, Y., Levinshtein, M. E., and Rumyantsev, S. L. *Properties of Advanced Semiconductor Materials GaN, AlN, SiC, BN, SiC, SiGe*. John Wiley & Sons, Inc., New York (2001).
[ISBN 9780471358275]. 7.1

[109] Goler, S., Coletti, C., *et al.* *Revealing the atomic structure of the buffer layer between SiC(0001) and epitaxial graphene*. *Carbon*, vol. 51 : 249–254 (2013).
[doi:10.1016/j.carbon.2012.08.050]. (document), 8.2, 8.2, 9.1, 10, 12.1, 12.3, 13.1, 14.3

[110] Gonze, X., Beuken, J. M., *et al.* *First-Principles Computation of Material Properties: the ABINIT Software Project*. *Computational Materials Science*, vol. 25 (3) : 478–492 (2002).
[doi:10.1016/S0927-0256(02)00325-7]. 2.5, A

[111] Gonze, X. and Lee, C. *Dynamical Matrices, Born Effective Charges, Dielectric Permittivity Tensors, and Interatomic Force Constants from Density-Functional Perturbation Theory*. *Phys. Rev. B*, vol. 55 (16) : 10355–10368 (1997).
[doi:10.1103/PhysRevB.55.10355]. 2

[112] Gould, T., Lebégue, S., and Dobson, J. F. *Dispersion corrections in graphenic systems: a simple and effective model of binding*. *Journal of Physics: Condensed Matter*, vol. 25 (44) : 445010 (2013).
[doi:10.1088/0953-8984/25/44/445010]. J.1

[113] Gould, T., Liu, Z., Liu, J. Z., Dobson, J. F., Zheng, Q., and LebÃ¨gue, S. *Binding and interlayer force in the near-contact region of two graphite slabs: Experiment and theory*. *The Journal of Chemical Physics*, vol. 139 (22) : 224704 (2013).
[doi:10.1063/1.4839615]. 6.4, 6.2, 6.5, 6.2, J.1, J

[114] Gould, T., Simpkins, K., and Dobson, J. F. *A theoretical and semiemprical correction to the long-range dispersion power law of stretched graphite*. *Physical Review B*, vol. 77 : 165134 (2008).
[doi:10.1103/PhysRevB.77.165134].
[arxiv:0801.4426]. 6.2, J.1

[115] Graziano, G., Klimes, J., Fernandez-Alonso, F., and Michaelides, A. *Improved description of soft layered materials with van der Waals density functional theory*. *Journal of Physics: Condensed Matter*, vol. 24 (42) : 424216 (2012).
[doi:10.1088/0953-8984/24/42/424216]. 6.2, 6.2, J.1

[116] Grimme, S. *Accurate Description of van der Waals Complexes by Density Functional Theory Including Empirical Corrections*. *Journal of Computational Chemistry*, vol. 25 (12) : 1463–1473 (2004).
[doi:10.1002/jcc.20078]. 2.4, 6.2, 6.2

[117] Grimme, S. *Semiempirical GGA-type density functional constructed with a long-range dispersion correction*. *Journal of Computational Chemistry*, vol. 27 (15) : 1787–1799 (2006).
[doi:10.1002/jcc.20495]. 2.4, 6.2, 6.2, A, A.1, A, J

[118] Grimme, S., Antony, J., Ehrlich, S., and Krieg, H. *A consistent and accurate ab initio parametrization of density functional dispersion correction (DFT-D) for the 94 elements H-Pu*. *The Journal of Chemical Physics*, vol. 132 (15) : 154104 (2010).
[doi:10.1063/1.3382344]. 6.2, J.1

[119] Grimme, S., Mück-Lichtenfeld, C., and Antony, J. *Noncovalent Interactions between Graphene Sheets and in Multishell (Hyper)Fullerenes*. *The Journal of Physical Chemistry C*, vol. 111 (30) : 11199-11207 (2007).
[doi:10.1021/jp0720791]. 6.2, J.1

[120] Grochala, W. *Diamond: Electronic Ground State of Carbon at Temperatures Approaching 0K*. *ANGEWANDTE CHEMIE-INTERNATIONAL EDITION*, vol. 53 (14) : 3680-3683 (APR 1 2014). ISSN 1433-7851.
[doi:10.1002/anie.201400131]. A

[121] Gulans, A., Kontur, S., *et al.* *EXCITING: a full-potential all-electron package implementing density-functional theory and many-body perturbation theory*. *Journal of Physics: Condensed Matter*, vol. 26 (36) : 363202 (2014).
[doi:10.1088/0953-8984/26/36/363202]. 2.5

[122] Guo, Z., Dong, R., *et al.* *Record Maximum Oscillation Frequency in C-Face Epitaxial Graphene Transistors*. *Nano Letters*, vol. 13 (3) : 942-947 (2013).
[doi:10.1021/nl303587r]. (document)

[123] Hamada, I. *van der Waals density functional made accurate*. *Physical*

Review B, vol. 89 : 121103 (Mar 2014).
[doi:10.1103/PhysRevB.89.121103]. J.1

[124] Hannon, J. B. (2012). Private communication. (document), 10

[125] Hannon, J. B., Copel, M., and Tromp, R. M. *Direct Measurement of the Growth Mode of Graphene on SiC (0001) and SiCð000 1Þ*. *Phys. Rev. Lett.*, vol. 107 (16) : 166101 (October 2011).
[doi:10.1103/PhysRevLett.107.166101]. 8.2

[126] Harl, J. and Kresse, G. *Accurate Bulk Properties from Approximate Many-Body Techniques*. *Phys. Rev. Lett.*, vol. 103 : 056401 (July 2009).
[doi:10.1103/PhysRevLett.103.056401]. 7.1, 7.1, 7.2, J

[127] Hasegawa, M. and Nishidate, K. *Semiempirical approach to the energetics of interlayer binding in graphite*. *Physical Review B*, vol. 70 : 205431 (2004).
[doi:10.1103/PhysRevB.70.205431]. 6.2, J.1

[128] Hasegawa, M., Nishidate, K., and Iyetomi, H. *Energetics of interlayer binding in graphite: The semiempirical approach revisited*. *Physical Review B*, vol. 76 (11) : 115424 (September 2007).
[doi:10.1103/PhysRevB.76.115424]. 6.2, J.1

[129] Hass, J., de Heer, W. A., and Conrad, E. H. *The growth and morphology of epitaxial multilayer graphene*. *J. Phys.: Condens. Matter*, vol. 20 (32) : 323202 (2008).
[doi:10.1088/0953-8984/20/32/323202]. a

[130] Hass, J., Feng, R., *et al.* *Highly ordered graphene for two dimensional electronics*. *Applied Physics Letters*, vol. 89 (14) : 143106 (2006).
[doi:10.1063/1.2358299]. (document)

[131] Hass, J., Varchon, F., *et al.* *Why Multilayer Graphene on 4H-SiC(0001Â¯) Behaves Like a Single Sheet of Graphene*. *Physical Review Letters*, vol. 100 (12) (March 2008).
[doi:10.1103/PhysRevLett.100.125504]. (document), 9.2, 14.2

[132] Hattab, H., N'Diaye, A. T., *et al.* *Interplay of Wrinkles, Strain, and Lattice Parameter in Graphene on Iridium*. *Nano Letters*, vol. 12 (2) : 678-682 (2012).
[doi:10.1021/nl203530t]. 9.3, 9.3

[133] Havu, V., Blum, V., Havu, P., and Scheffler, M. *Efficient O (N) integration for all-electron electronic structure calculation using numeric basis functions*. *J. Comp. Phys.*, vol. 228 (22) : 8367–8379 (2009).
[doi:10.1016/j.jcp.2009.08.008]. 2.5, 6.1

[134] Haynes, W. *CRC Handbook of Chemistry and Physics, 95th Edition*. CRC Handbook of Chemistry and Physics. Taylor & Francis, 95 ed. (2015).
[ISBN 9781482208672].
http://www.hbcpnetbase.com/ 7.1, 7.1

[135] He, G., Srivastava, N., and Feenstra, R. *Formation of a Buffer Layer for Graphene on C-Face SiC0001*. *Journal of Electronic Materials*, vol. 43 : 1-9 (2013).
[doi:10.1007/s11664-013-2901-8]. 14.2

[136] Hellmann, H. *Zur Rolle der kinetischen Elektronenenergie fÃ$\frac{1}{4}$r die zwischenatomaren Kräfte*. *Zeitschrift für Physik*, vol. 85 (3-4) : 180-190 (1933).
[doi:10.1007/BF01342053]. 2.5

[137] Hertel, S., Waldmann, D., *et al.* *Tailoring the graphene/silicon carbide interface for monolithic wafer-scale electronics*. *Nature Comm.*, vol. 3 : 957 (2012).
[doi:10.1038/ncomms1955]. (document), 13.3

[138] Heyd, J., Scuseria, G. E., and Ernzerhof, M. *Hybrid functionals based on a screened Coulomb potential*. *The Journal of Chemical Physics*, vol. 118 (18) : 8207-8215 (2003).
[doi:10.1063/1.1564060]. (document), 2.3.3, 2.3.3, 2.3.3, 6.1, C.1, C.2, C.3, J

[139] Hiebel, F., Magaud, L., Mallet, P., and Veuillen, J.-Y. *Structure and stability of the interface between graphene and 6H-SiC*$(000\bar{1})$ *(3 × 3): an STM and ab initio study*. *Journal of Physics D: Applied Physics*, vol. 45 (15) : 154003 (2012).
[doi:10.1088/0022-3727/45/15/154003]. (document), 14.1, 14.1.2, 14.2, 14.1.2, 14.3, 14.1.2, 14.7, 14.8, 14.1.3, 14.2, J

[140] Hiebel, F., Mallet, P., Magaud, L., and Veuillen, J.-Y. *Atomic and electronic structure of monolayer graphene on 6H-SiC*$(000\bar{1})$ *: A scanning tunneling microscopy study*. *Phys. Rev. B*, vol. 80 (23) : 235429 (December 2009).
[doi:10.1103/PhysRevB.80.235429]. (document), 14.1, 14.1.2, 14.1.3

[141] Hiebel, F., Mallet, P., Varchon, F., Magaud, L., and Veuillen, J.-Y. *Graphene-substrate interaction on 6H-SiC$(000\bar{1})$: A scanning tunneling microscopy study*. *Phys. Rev. B*, vol. 78 : 153412 (Oct 2008). [doi:10.1103/PhysRevB.78.153412]. (document), b, III, 14.2

[142] Hirshfeld, F. *Atom Fragments for Describing Molecular Charge-Densities*. *Theoretica Chimica Acta*, vol. 44 : 129 - 138 (1977). [doi:10.1007/BF00549096]. 2.4, 12.3, 14.3

[143] Hoechst, H., Tang, M., Johnson, B. C., Meese, J. M., Zajac, G. W., and Fleisch, T. H. *The electronic structure of cubic SiC grown by chemical vapor deposition on Si(100)*. *Journal of Vacuum Science & Technology A*, vol. 5 (4) : 1640-1643 (1987). [doi:10.1116/1.574537]. 7.2, 7.4, B.3, J

[144] Hohenberg, P., Kohn, W., Rajagopal, A. K., and Callaway, J. *Inhomogeneous Electron Gas*. *Phys. Rev.*, vol. 136 : B864-B871 (November 1964). [doi:10.1103/PhysRev.136.B864]. 2.1, 2.1, 2.1

[145] Hoster, H. E., Kulakov, M. A., and Bullemer, B. *Morphology and atomic structure of the SiC$(000\bar{1})$3 x 3 surface reconstruction*. *Surface Science*, vol. 382 (1–3) : L658 – L665 (1997). [doi:10.1016/S0039-6028(97)00084-8]. (document), 14.1, 14.1.2, 14.2, 14.1.2, 14.7, 14.1.3, J

[146] Hu, Y., Ruan, M., *et al.* *Structured epitaxial graphene: growth and properties*. *Journal of Physics D: Applied Physics*, vol. 45 (15) : 154010 (2012). (document)

[147] Huang, H., Zheng, F., Zhang, P., Wu, J., Gu, B.-L., and Duan, W. *A general group theoretical method to unfold band structures and its application*. *New Journal of Physics*, vol. 16 (3) : 033034 (2014). [doi:10.1088/1367-2630/16/3/033034]. 11

[148] Humphreys, R., Bimberg, D., and Choyke, W. *Wavelength modulated absorption in SiC*. *Solid State Communications*, vol. 39 (1) : 163 - 167 (1981). ISSN 0038-1098. [doi:10.1016/0038-1098(81)91070-X]. 7.2, B.3, J

[149] Iijima, S. *Helical microtubules of graphitic carbon*. *Nature*, vol. 354 : 56 – 58 (November 1991). [doi:10.1038/354056a0]. 6

[150] Janak, J. F. *Proof that $\frac{\partial E}{\partial n_i} = \epsilon$ in density-functional theory*. *Physical Review B*, vol. 18 : 7165–7168 (December 1978).
[doi:10.1103/PhysRevB.18.7165]. 2.2

[151] Jansen, H. J. F. and Freeman, A. J. *Structural and electronic properties of graphite via an all-electron total-energy local-density approach*. *Physical Review B*, vol. 35 (15) : 8207–8214 (May 1987).
[doi:10.1103/PhysRevB.35.8207]. J.1

[152] Ji, S.-H., Hannon, J. B., Tromp, R. M., Perebeinos, V., Tersoff, J., and Ross, F. M. *Atomic-Scale transport in epitaxial graphene*. *Nature Materials* (2011).
[doi:10.1038/NMAT3170]. (document)

[153] Johannsen, J. C., Ulstrup, S., *et al.* *Electron-phonon coupling in quasi-free-standing graphene*. *Journal of Physics: Condensed Matter*, vol. 25 (9) : 094001 (2013).
[doi:10.1088/0953-8984/25/9/094001]. 13

[154] Johansson, L., Owman, F., Mårtensson, P., Persson, C., and Lindefelt, U. *Electronic structure of 6H-SiC (0001)*. *Phys. Rev. B*, vol. 53 (20) : 13803–13807 (May 1996).
[doi:10.1103/PhysRevB.53.13803]. 7.2, 8.1.1

[155] Junquera, J., Paz, O., Sànchez-Portal, D., and Artacho, E. *Numerical Atomic Orbitals for Linear-Scaling Calculations*. *Phys. Rev. B*, vol. 64 (23) : 235111 (November 2001).
[doi:10.1103/PhysRevB.64.235111]. 2.5

[156] Käckell, P., Furthmüller, J., and Bechstedt, F. *Polytypism and surface structure of SiC*. *Diamond and Related Materials*, vol. 6 (10) : 1346 - 1348 (1997). ISSN 0925-9635.
[doi:10.1016/S0925-9635(97)00089-7]. Proceeding of the 1st European Conference on Silicon Carbide and Related Materials (ECSCRM 1996). 8.1.1, 8.1.1

[157] Käckell, P., Wenzien, B., and Bechstedt, F. *Influence of atomic relaxations on the structural properties of SiC polytypes from ab initio calculations*. *Phys. Rev. B*, vol. 50 : 17037–17046 (December 1994).
[doi:10.1103/PhysRevB.50.17037]. 7.1, 7.2, J

[158] Kaplan, R. *Surface structure and composition of β- and 6H-SiC*. *Surf. Sci.*, vol. 215 (1-2) : 111 - 134 (1989). ISSN 0039-6028.

[doi:10.1016/0039-6028(89)90704-8]. (document), 8, 8.1.2, 8.1.2

[159] Karch, K., Pavone, P., Windl, W., Strauch, D., and Bechstedt, F. *Ab initio calculation of structural, lattice dynamical, and thermal properties of cubic silicon carbide*. *International Journal of Quantum Chemistry*, vol. 56 (6) : 801–817 (December 1995).
[doi:10.1002/qua.560560617]. 7

[160] Katsnelson, M. I., Novoselov, K. S., and Geim, A. K. *Chiral tunnelling and the Klein paradox in graphene*. *Nature Physics*, vol. 2 (9) : 620–625 (2006).
[doi:10.1038/nphys384]. (document)

[161] Kedzierski, J., Hsu, P.-L., *et al*. *Epitaxial Graphene Transistors on SiC Substrates*. *Electron Devices, IEEE Transactions on*, vol. 55 (8) : 2078-2085 (Aug 2008). ISSN 0018-9383.
[doi:10.1109/TED.2008.926593]. (document)

[162] Kennedy, C. S. and Kennedy, G. C. *The equilibrium boundary between graphite and diamond*. *Journal of Geophysical Research*, vol. 81 (14) : 2467–2470 (1976).
[doi:10.1029/JB081i014p02467]. A, A, A.3, A.2, J

[163] Kerber, T., Sierka, M., and Sauer, J. *Application of semiempirical long-range dispersion corrections to periodic systems in density functional theory*. *Journal of Computational Chemistry*, vol. 29 (13) : 2088–2097 (2008). ISSN 1096-987X.
[doi:10.1002/jcc.21069]. J.1

[164] Khaliullin, R. Z., Eshet, H., Kühne, T. D., Behler, J., and Parrinello, M. *Graphite-diamond phase coexistence study employing a neural-network mapping of the ab initio potential energy surface*. *Physical Review B*, vol. 81 : 100103 (March 2010).
[doi:10.1103/PhysRevB.81.100103]. 6.1, A, A, A.3, A.2, J

[165] Kim, H., Choi, J.-M., and Goddard, W. A. *Universal Correction of Density Functional Theory to Include London Dispersion (up to Lr, Element 103)*. *The Journal of Physical Chemistry Letters*, vol. 3 (3) : 360-363 (2012).
[doi:10.1021/jz2016395]. J.1

[166] Kim, S., Ihm, J., Choi, H. J., and Son, Y. W. *Origin of anomalous electronic structures of epitaxial graphene on silicon carbide*. *Phys. Rev. Lett.*, vol.

100 (17) : 176802 (May 2008).
[doi:10.1103/PhysRevLett.100.176802]. 8.2, 8.2, 12, 12.1

[167] Kleis, J., Schröder, E., and Hyldgaard, P. *Nature and strength of bonding in a crystal of semiconducting nanotubes: van der Waals density functional calculations and analytical results*. *Phys. Rev. B*, vol. 77 : 205422 (May 2008).
[doi:10.1103/PhysRevB.77.205422]. 6.2, J.1

[168] Kleykamp, H. *Gibbs energy of formation of SiC: A contribution to the thermodynamic stability of the modifications*. *Ber. Bunsenges. phys. Chem.*, vol. 102 (9) : 1231–1234 (1998).
[doi:10.1002/bbpc.19981020928]. 7.1, 7.1, 14.2

[169] Knuth, F., Carbogno, C., Atalla, V., Blum, V., and Scheffler, M. *All-electron formalism for total energy strain derivatives and stress tensor components for numeric atom-centered orbitals*. *Computer Physics Communications*, vol. 190 (0) : 33 - 50 (2015). ISSN 0010-4655.
[doi:10.1016/j.cpc.2015.01.003]. 6.1, 6.1, J

[170] Kohanoff, J. *Electronic Structure Calculations For Solids And Molecules: Theory And Computational Methods*. Cambridge University Press (2006).
[ISBN 0-521-81591-6]. I

[171] Kohn, W. and Sham, L. J. *Self-Consistent Equations Including Exchange And Correlation Effects*. *Phys. Rev.*, vol. 140 : 1133–1138 (1965).
[doi:10.1103/PhysRev.140.A1133]. 2.2, 2.3.1, 5

[172] Korth, M. and Grimme, S. *Mindless DFT Benchmarking*. *Journal of Chemical Theory and Computation*, vol. 5 (4) : 993-1003 (2009).
[doi:10.1021/ct800511q]. 2.3.2

[173] Kresse, G. and Furthmüller, J. *Efficient iterative schemes for ab initio total-energy calculations using a plane-wave basis set*. *Phys. Rev. B*, vol. 54 : 11169–11186 (October 1996).
[doi:10.1103/PhysRevB.54.11169]. 2.5

[174] Kroto, H. W., Heath, J. R., O'Brien, S. C., Curl, R. F., and Smalley, R. E. *C60: Buckminsterfullerene*. *Nature*, vol. 318 : 162 – 163 (November 1985).
[doi:10.1038/318162a0]. 6

[175] Krukau, A. V., Vydrov, O. A., Izmaylov, A. F., and Scuseria, G. E. *Influence of the exchange screening parameter on the performance of screened hybrid functionals*. *The Journal of Chemical Physics*, vol. 125 (22) : 224106 (2006).
[doi:10.1063/1.2404663]. (document), 2.3.3, 2.3.3, 2.3.3, 6.1, 7.2, 14.3, B.4, C.1, C.2, C.3, F.1, J

[176] Ku, W., Berlijn, T., and Lee, C.-C. *Unfolding First-Principles Band Structures*. *Physical Reviews Letters*, vol. 104 : 216401 (May 2010).
[doi:10.1103/PhysRevLett.104.216401]. 11

[177] Kulakov, M., Henn, G., and Bullemer, B. *SiC(0001)3 x 3-Si surface reconstruction a new insight with a {STM}*. *Surface Science*, vol. 346 (1–3) : 49 – 54 (1996).
[doi:10.1016/0039-6028(95)00919-1]. 14.5, 14.1.2, 14.7, 14.1.2, J

[178] Kulakov, M. A., Henn, G., and Bullemer, B. *SiC(0001)3 x 3-Si surface reconstruction a new insight with a STM*. *Surface Science*, vol. 346 (1–3) : 49 – 54 (February 1996).
[doi:10.1016/0039-6028(95)00919-1]. 8.1.2

[179] La Via, F., Camarda, M., and La Magna, A. *Mechanisms of growth and defect properties of epitaxial SiC*. *Applied Physics Reviews*, vol. 1 (3) : 031301 (2014).
[doi:10.1063/1.4890974]. 8.1.1

[180] Lambrecht, W., Limpijumnong, S., Rashkeev, S., and Segall, B. *Electronic band structure of SiC polytypes: a discussion of theory and experiment*. *phys. stat. sol. (b)*, vol. 202 (1) : 5–33 (July 1997).
[doi:10.1002/1521-3951(199707)202:1<5::AID-PSSB5>3.0.CO;2-L]. 7.1

[181] Lambrecht, W. R. L., Segall, B., *et al. Calculated and measured uv reflectivity of SiC polytypes*. *Physical Review B*, vol. 50 : 10722–10726 (October 1994).
[doi:10.1103/PhysRevB.50.10722]. 7.2

[182] Langreth, D. C., Dion, M., Rydberg, H., Schröder, E., Hyldgaard, P., and Lundqvist, B. I. *Van der Waals density functional theory with applications*. *International Journal of Quantum Chemistry*, vol. 101 (5) : 599–610 (October 2005).
[doi:10.1002/qua.20315]. 6.2, 6.2

[183] Lauffer, P., Emtsev, K. V., *et al.* *Atomic and electronic structure of few-layer graphene on SiC(0001) studied with scanning tunneling microscopy and spectroscopy*. *Physical Review B*, vol. 77 : 155426 (April 2008). [doi:10.1103/PhysRevB.77.155426]. 8.2

[184] Lazarevic, F. *First-Principles Prediction of Phase Stability of Electronic Materials*. Master's thesis, Technische Universität Berlin (May 2013). 6.1, 6.2, 14, 14.1.1, 14.1.1, 1, 14.1.2, 14.1.2, 2, 3, 4, 5, A, A.1, A.2, A.3, J

[185] Lebègue, S., Harl, J., Gould, T., Ángyán, J. G., Kresse, G., and Dobson, J. F. *Cohesive Properties and Asymptotics of the Dispersion Interaction in Graphite by the Random Phase Approximation*. *Physical Review Letters*, vol. 105 : 196401 (November 2010). [doi:10.1103/PhysRevLett.105.196401]. 6.5, 6.2, J.1, J

[186] Lee, B., Han, S., and Kim, Y.-S. *First-principles study of preferential sites of hydrogen incorporated in epitaxial graphene on 6H-SiC(0001)*. *Physical Review B*, vol. 81 (7) : 075432 (2010). [doi:10.1103/PhysRevB.81.075432]. 13.1

[187] Lee, C.-C., Yamada-Takamura, Y., and Ozaki, T. *Unfolding method for first-principles LCAO electronic structure calculations*. *Journal of Physics: Condensed Matter*, vol. 25 (34) : 345501 (2013). [doi:10.1088/0953-8984/25/34/345501]. 11

[188] Lee, K., Murray, É. D., Kong, L., Lundqvist, B. I., and Langreth, D. C. *Higher-accuracy van der Waals density functional*. *Phys. Rev. B*, vol. 82 (8) : 081101 (August 2010). [doi:10.1103/PhysRevB.82.081101]. 6.2

[189] Lee, Y.-S., Nardelli, M. B., and Marzari, N. *Band Structure and Quantum Conductance of Nanostructures from Maximally Localized Wannier Functions: The Case of Functionalized Carbon Nanotubes*. *Physical Reviews Letters*, vol. 95 : 076804 (August 2005). [doi:10.1103/PhysRevLett.95.076804]. 11

[190] Leenaerts, O., Partoens, B., and Peeters, F. M. *Paramagnetic adsorbates on graphene: A charge transfer analysis*. *Applied Physics Letters*, vol. 92 (24) : 243125 (2008). [doi:10.1063/1.2949753]. 12.2

[191] Levy, M. *Electron Densities in Search Of Hamiltonians*. *Phys. Rev. A*,

vol. 26 (3) : 1200–1208 (1982).
[doi:10.1103/PhysRevA.26.1200]. 2.1

[192] Li, L. and Tsong, I. S. T. *Atomic structures of 6H-SiC(0001) and (000$\bar{1}$ surfaces*. *Surface Science*, vol. 351 (1 – 3) : 141 – 148 (May 1996).
[doi:10.1016/0039-6028(95)01355-5]. (document), 8.1.2, 8.2, 14.1, 14.1.2, 14.1.2, 14.1.2, 14.4, 14.7, 14.1.2, J

[193] Li, Z. and Bradt, R. *Thermal expansion of the cubic (3C) polytype of SiC*. *Journal of Materials Science*, vol. 21 (12) : 4366-4368 (1986). ISSN 0022-2461.
[doi:10.1007/BF01106557]. i

[194] Li, Z. and Bradt, R. C. *Thermal expansion of the cubic (3C) polytype of SiC*. *Journal of Materials Science*, vol. 21 : 4366-4368 (1986). 10.1007/BF01106557. 7

[195] Li, Z. and Bradt, R. C. *Thermal Expansion of the Hexagonal (6H) Polytype of Silicon Carbide*. *Journal of the American Ceramic Society*, vol. 69 (12) : 863–866 (1986). ISSN 1551-2916.
[doi:10.1111/j.1151-2916.1986.tb07385.x]. 7, 7.1, 8.2

[196] Li, Z. and Bradt, R. C. *Thermal Expansion of the Hexagonal (6H) Polytype of Silicon Carbide*. *Journal of the American Ceramic Society*, vol. 69 (12) : 863–866 (1986). ISSN 1551-2916.
[doi:10.1111/j.1151-2916.1986.tb07385.x]. i

[197] Lin, Y., Valdes-Garcia, A., *et al. Wafer-Scale Graphene Integrated Circuit*. *Science*, vol. 332 (6035) : 1294 (2011).
[doi:10.1126/science.1204428]. (document)

[198] Liu, F.-H., Lo, S.-T., *et al. Hot carriers in epitaxial graphene sheets with and without hydrogen intercalation: role of substrate coupling*. *Nanoscale*, vol. 6 (18) : 10562–10568 (2014).
[doi:10.1039/C4NR02980A]. 13.3

[199] Liu, X., Li, L., Li, Q., Li, Y., and Lu, F. *Optical and mechanical properties of C, Si, Ge, and 3C-SiC determined by first-principles theory using Heyd-Scuseria-Ernzerhof functional*. *Materials Science in Semiconductor Processing*, vol. 16 (6) : 1369 - 1376 (2013). ISSN 1369-8001.
[doi:10.1016/j.mssp.2013.04.017]. 7.2

[200] Liu, Y. and Goddard, W. A. *First-Principles-Based Dispersion Augmented*

Density Functional Theory: From Molecules to Crystals. *The Journal of Physical Chemistry Letters*, vol. 1 (17) : 2550-2555 (2010). [doi:10.1021/jz100615g]. 6.2, J.1

[201] Liu, Z., Liu, J. Z., Cheng, Y., Li, Z., Wang, L., and Zheng, Q. *Interlayer binding energy of graphite: A mesoscopic determination from deformation*. *Phys. Rev. B*, vol. 85 : 205418 (May 2012). [doi:10.1103/PhysRevB.85.205418]. 6.2, 6.4, 6.2, 6.5, 6.2, J.1, J

[202] Lu, W., Boeckl, J. J., and Mitchell, W. C. *A critical review of growth of low-dimensional carbon nanostructures on SiC(0001): impact of growth environment*. *J. Phys. D: Appl. Phys.*, vol. 43 : 374004 (2010). 4.2

[203] Lucchese, M., Stavale, F., *et al.* *Quantifying ion-induced defects and Raman relaxation length in graphene*. *Carbon*, vol. 48 (5) : 1592 - 1597 (2010). ISSN 0008-6223. [doi:10.1016/j.carbon.2009.12.057]. 9.3

[204] Lüning, J., Eisebitt, S., Rubensson, J.-E., Ellmers, C., and Eberhardt, W. *Electronic structure of silicon carbide polytypes studied by soft x-ray spectroscopy*. *Physical Review B*, vol. 59 : 10573–10582 (April 1999). [doi:10.1103/PhysRevB.59.10573]. 7.2, 7.2, 7.3, 7.2, 7.2, 12.3, J

[205] Luo, W. and Windl, W. *First principles study of the structure and stability of carbynes*. *Carbon*, vol. 47 (2) : 367 - 383 (2009). ISSN 0008-6223. [doi:10.1016/j.carbon.2008.10.017]. A, A.3, J

[206] Luxmi, Srivastava, N., He, G., Feenstra, R. M., and Fisher, P. J. *Comparison of graphene formation on C-face and Si-face SiC 0001 surfaces*. *Phys. Rev. B*, vol. 82 (23) : 235406 (December 2010). [doi:10.1103/PhysRevB.82.235406]. 14.2

[207] Madsen, G. K. H., Ferrighi, L., and Hammer, B. *Treatment of Layered Structures Using a Semilocal meta-GGA Density Functional*. *The Journal of Physical Chemistry Letters*, vol. 1 (2) : 515-519 (2010). [doi:10.1021/jz9002422]. 6.2, J.1

[208] Magaud, L., Hiebel, F., Varchon, F., Mallet, P., and Veuillen, J.-Y. *Graphene on the C-terminated SiC* $(000\bar{1})$ *surface: An ab initio study*. *Phys. Rev. B*, vol. 79 : 161405 (April 2009). [doi:10.1103/PhysRevB.79.161405]. (document), 14.1

[209] Marsman, M., Paier, J., Stroppa, A., and Kresse, G. *Hybrid function-*

als applied to extended systems. *Journal of Physics: Condensed Matter*, vol. 20 (6) : 064201 (February 2008).
[doi:10.1088/0953-8984/20/6/064201]. 12.1

[210] Mårtensson, P., Owman, F., and Johansson, L. I. *Morphology, Atomic and Electronic Structure of 6H-SiC(0001) Surfaces*. *physica status solidi (b)*, vol. 202 (1) : 501–528 (1997). ISSN 1521-3951.
[doi:10.1002/1521-3951(199707)202:1<501::AID-PSSB501>3.0.CO;2-H]. 8.2, 9.2

[211] Martin, R. M. *Electronic Structure: Basic Theory And Practical Methods: Basic Theory And Practical Density Functional Approaches Vol 1*. Cambridge University Press, new ed ed. (2004).
[ISBN 0-521-78285-6]. I

[212] Masri, P. *Silicon carbide and silicon carbide-based structures: The physics of epitaxy*. *Surface Science Reports*, vol. 48 (1-4) : 1 - 51 (2002). ISSN 0167-5729.
[doi:10.1016/S0167-5729(02)00099-7]. 7.2

[213] Mathieu, C., Barrett, N., *et al. Microscopic correlation between chemical and electronic states in epitaxial graphene on SiC*$(000\bar{1})$. *Phys. Rev. B*, vol. 83 : 235436 (Jun 2011).
[doi:10.1103/PhysRevB.83.235436]. (document), a, III, 14, 14.3

[214] Mattausch, A. and Pankratov, O. *Ab initio study of graphene on SiC*. *Phys. Rev. Lett.*, vol. 99 (7) : 076802 (August 2007).
[doi:10.1103/PhysRevLett.99.076802]. 9.2, 9.2, 9.2, 12, 12.1, B.1, B.2

[215] Mattausch, A. and Pankratov, O. *Density functional study of graphene overlayers on SiC*. *phys. stat. sol. (b)*, vol. 245 (7) : 1425–1435 (2008).
[doi:10.1002/pssb.200844031]. 9.2, 12.1, 12.1

[216] Mimura, H., Matsumoto, T., and Kanemitsu, Y. *Blue electroluminescence from porous silicon carbide*. *Applied Physics Letters*, vol. 65 (26) : 3350-3352 (October 1994).
[doi:10.1063/1.112388]. 7

[217] Ming, F. and Zangwill, A. *Model for the epitaxial growth of graphene on 6H-SiC (0001)*. *Phys. Rev. B*, vol. 84 (11) : 115459 (2011).
[doi:10.1103/PhysRevB.84.115459]. (document)

[218] Moreau, E., Godey, S., *et al.* *High-resolution angle-resolved photoemission spectroscopy study of monolayer and bilayer graphene on the C-face of SiC*. *Phys. Rev. B*, vol. 88 : 075406 (Aug 2013).
[doi:10.1103/PhysRevB.88.075406]. (document)

[219] Morozov, S. V., Novoselov, K. S., *et al.* *Strong Suppression of Weak Localization in Graphene*. *Physical Review Letters*, vol. 97 : 016801 (July 2006).
[doi:10.1103/PhysRevLett.97.016801]. 12.2

[220] Mostaani, E., Drummond, N., and Fal´ko, V. *Quantum Monte Carlo Calculation of the Binding Energy of Bilayer Graphene*. *submitted to Phys. Rev. Lett.* (2015). 1, 6.2

[221] Mounet, N. and Marzari, N. *First-principles determination of the structural, vibrational and thermodynamic properties of diamond, graphite, and derivatives*. *Physical Review B*, vol. 71 : 205214 (May 2005).
[doi:10.1103/PhysRevB.71.205214]. 6.1, i

[222] Mulliken, R. S. *Electronic Population Analysis on LCAO-MO Molecular Wave Functions. II. Overlap Populations, Bond Orders and Covalent Bond Energies*. *The Journal of Chemical Physics*, vol. 23 (10) : 1841–1846 (October 1955).
[doi:10.1063/1.1740589]. 11.3

[223] Murnaghan, F. D. *The Compressibility of Media under Extreme Pressures*. *Proc. Nat. Acad. Sci.s of the United States of America*, vol. 30 (9) : 244–247 (1944). 6.1, A

[224] Nakamura, D., Gunjishima, I., *et al.* *Ultrahigh-quality silicon carbide single crystals*. *Nature*, vol. 430 : 1009–1012 (August 2004).
[doi:10.1038/nature02810]. 7, 7.1

[225] Nath, K. and Anderson, A. B. *An ased band theory: Lattice constants, atomization energies, and bulk moduli for C(gr), C(di), Si, α-SiC, and β-SiC*. *Solid State Communications*, vol. 66 (3) : 277-280 (April 1988).
[doi:10.1016/0038-1098(88)90562-5].
Choyke, W.J.: J. Mat. Res. Bull., vol. 5 (4): p. 141 (1969). 7.1

[226] Nelson, J. B. and Riley, D. P. *The Thermal Expansion of Graphite from 15°C to 800°C: Part I. Experimental*. *Proceedings of the Physical Society*, vol. 57 (6) : 477-486 (1945).
[doi:10.1088/0959-5309/57/6/303]. 6.1, 6.5, 6.2, 9.1, A, A.1, A, J

[227] Nemec, L., Blum, V., Rinke, P., and Scheffler, M. *Thermodynamic Equilibrium Conditions of Graphene Films on SiC*. *Phys. Rev. Lett.*, vol. 111 : 065502 (August 2013).
[doi:10.1103/PhysRevLett.111.065502]. (document), 8.2, 8.5, 10, 10.1, 14.1.2, H, H.1, J

[228] Nemec, L., Lazarevic, F., Rinke, P., Scheffler, M., and Blum, V. *Why graphene growth is very different on the C face than on the Si face of SiC: Insights from surface equilibria and the (3×3)-3C-SiC($\bar{1}\bar{1}\bar{1}$) reconstruction*. *accepted at Phys. Rev. B: Rapid Comm.* (2015). (document), 14, 14.6, 14.7, 14.8, 14.9, J

[229] Ni, Z. H., Chen, W., *et al.* *Raman spectroscopy of epitaxial graphene on a SiC substrate*. *Physical Review B*, vol. 77 : 115416 (March 2008).
[doi:10.1103/PhysRevB.77.115416]. 9, 9.1

[230] Norimatsu, W. and Kusunoki, M. *Chem. Phys. Lett.*, vol. 468 : 52 (2009). 8.2, 10

[231] Norimatsu, W. and Kusunoki, M. *Structural features of epitaxial graphene on SiC {0001} surfaces*. *Journal of Physics D: Applied Physics*, vol. 47 (9) : 094017 (2014).
[doi:10.1088/0022-3727/47/9/094017]. (document)

[232] Northrup, J. E. and Neugebauer, J. *Theory of the adatom-induced reconstruction of the SiC(0001)$\sqrt{3} \times \sqrt{3}$ surface*. *Phys. Rev. B*, vol. 52 (24) : R17001–R17004 (December 1995).
[doi:10.1103/PhysRevB.52.R17001]. 8.1.1, 8.1.1

[233] Novoselov, K. *Graphene: The Magic of Flat Carbon*. *Electrochemical Society Interface*, vol. 20 (1) : 45 (2011).
[doi:10.1149/1.3119522]. 6

[234] Novoselov, K. S., Fal'ko, V. I., Colombo, L., Gellert, P. R., Schwab, M. G., and Kim, K. *A roadmap for graphene*. *Nature*, vol. 490 (7419) : 192 – 200 (2012).
[doi:10.1038/nature11458]. 6

[235] Novoselov, K. S., Geim, A. K., *et al.* *Electric Field Effect in Atomically Thin Carbon Films*. *Science*, vol. 306 (5696) : 666-669 (October 2004).
[doi:10.1126/science.1102896]. (document), 6

[236] Novoselov, K. S., Geim, A. K., *et al.* *Two-dimensional gas of massless*

Dirac fermions in graphene. *Nature*, vol. 438 (7065) : 197–200 (November 2005). ISSN 0028-0836.
[doi:10.1038/nature04233]. (document)

[237] Oda, T., Zhang, Y., and Weber, W. J. *Optimization of a hybrid exchange-correlation functional for silicon carbides*. *Chemical Physics Letters*, vol. 579 : 58 - 63 (2013). ISSN 0009-2614.
[doi:10.1016/j.cplett.2013.06.030]. 7.2, 7.2

[238] Ohta, T., Bostwick, A., Seyller, T., Horn, K., and Rotenberg, E. *Controlling the electronic structure of bilayer graphene*. *Science*, vol. 313 (5789) : 951 (2006).
[doi:10.1126/science.1130681]. 7, 8.2, 12, 12.1, 12.2, 12.4

[239] Olsen, T. and Thygesen, K. S. *Random phase approximation applied to solids, molecules, and graphene-metal interfaces: From van der Waals to covalent bonding*. *Physical Review B*, vol. 87 : 075111 (February 2013).
[doi:10.1103/PhysRevB.87.075111]. 6.5, 6.2, J.1, J

[240] Ortmann, F., Bechstedt, F., and Schmidt, W. G. *Semiempirical van der Waals correction to the density functional description of solids and molecular structures*. *Physical Review B*, vol. 73 (20) : 205101 (May 2006).
[doi:10.1103/PhysRevB.73.205101]. J.1

[241] Owman, F. and Mårtensson, P. *{STM} study of the SiC(0001)* $\sqrt{3} \times \sqrt{3}$ *surface*. *Surface Science*, vol. 330 (1) : L639 - L645 (1995). ISSN 0039-6028.
[doi:10.1016/0039-6028(95)00427-0]. 8.1.1

[242] Pankratov, O., Hensel, S., and Bockstedte, M. *Electron spectrum of epitaxial graphene monolayers*. *Phys. Rev. B*, vol. 82 (12) : 121416 (September 2010).
[doi:10.1103/PhysRevB.82.121416]. 9.2, 9.2

[243] Pankratov, O., Hensel, S., Götzfried, P., and Bockstedte, M. *Graphene on cubic and hexagonal SiC: A comparative theoretical study*. *Phys. Rev. B*, vol. 86 : 155432 (Oct 2012).
[doi:10.1103/PhysRevB.86.155432]. 8.1.1, 9.2, 12.1, 12.1, 13.1

[244] Park, C. H., Cheong, B.-H., Lee, K.-H., and Chang, K. J. *Structural and electronic properties of cubic, 2H, 4H, and 6H SiC*. *Phys. Rev. B*, vol. 49 : 4485–4493 (February 1994).
[doi:10.1103/PhysRevB.49.4485]. 7.1, 7.2, J

[245] Parlinski, K., Li, Z. Q., and Kawazoe, Y. *First-Principles Determination of the Soft Mode in Cubic ZrO_2*. *Phys. Rev. Lett.*, vol. 78 (21) : 4063–4066 (May 1997).
[doi:10.1103/PhysRevLett.78.4063]. 3

[246] Perdew, J. P., Burke, K., and Ernzerhof, M. *Generalized Gradient Approximation Made Simple*. *Phys. Rev. Lett.*, vol. 77 (18) : 3865–3868 (October 1996).
[doi:10.1103/PhysRevLett.77.3865]. (document), 2.3.2, 6.1, 14.3, A, J

[247] Perdew, J. P., Burke, K., and Ernzerhof, M. *Generalized Gradient Approximation Made Simple (vol 77, Pg 3865, 1996)*. *Phys. Rev. Lett.*, vol. 78 (7) : 1396 (February 1997).
[doi:10.1103/PhysRevLett.78.1396]. F.1

[248] Perdew, J. P., Ernzerhof, M., and Burke, K. *Rationale for mixing exact exchange with density functional approximations*. *The Journal of Chemical Physics*, vol. 105 (22) : 9982-9985 (1996).
[doi:10.1063/1.472933]. 2.3.3

[249] Perdew, J. P. and Wang, Y. *Accurate and Simple Analytic Representation of the Electron-Gas Correlation Energy*. *Phys. Rev. B*, vol. 45 (23) : 13244–13249 (June 1992).
[doi:10.1103/PhysRevB.45.13244]. 6.1, F.1

[250] Pierson, H. O. *Handbook of carbon, graphite, diamond, and fullerenes: properties, processing, and applications*. Materials science and process technology series. Noyes Publications (1993).
[ISBN 9780815513391]. 6, 6.1

[251] Pisana, S., Lazzeri, M., *et al. Breakdown of the adiabatic Born-Oppenheimer approximation in graphene*. *Nature Materials*, vol. 6 (3) : 198–201 (March 2007). ISSN 1476-1122.
[doi:10.1038/nmat1846]. D.1.1

[252] Podeszwa, R. *Interactions of graphene sheets deduced from properties of polycyclic aromatic hydrocarbons*. *The Journal of Chemical Physics*, vol. 132 (4) : 044704 (2010).
[doi:10.1063/1.3300064]. J.1

[253] Popescu, V. and Zunger, A. *Effective Band Structure of Random Alloys*.

Physical Reviews Letters, vol. 104 : 236403 (June 2010).
[doi:10.1103/PhysRevLett.104.236403]. 11

[254] Popescu, V. and Zunger, A. *Extracting E versus* **k** *effective band structure from supercell calculations on alloys and impurities*. *Physical Reviews B*, vol. 85 : 085201 (February 2012).
[doi:10.1103/PhysRevB.85.085201]. 11

[255] Pulay, P. *Ab Initio Calculation of Force Constants and Equilibrium Geometries in Polyatomic Molecules. I. Theory*. *Molecular Physics*, vol. 100 (1) : 57–62 (February 1969).
[doi:10.1080/0026897011008888]. 2.5

[256] Qi, Y., Rhim, S. H., Sun, G. F., Weinert, M., and Li, L. *Epitaxial graphene on SiC (0001): More than just honeycombs*. *Phys. Rev. Lett.*, vol. 105 (8) : 085502 (2010).
[doi:10.1103/PhysRevLett.105.085502]. 8.2, 9.2, 9.2, 9.4, 12.8, 12.3, 12.4, 14.3, J

[257] Ramprasad, R., Zhu, H., Rinke, P., and Scheffler, M. *New Perspective on Formation Energies and Energy Levels of Point Defects in Nonmetals*. *Physical Review Letters*, vol. 108 : 066404 (February 2012).
[doi:10.1103/PhysRevLett.108.066404]. 7.2, B.4

[258] Ramsdell, L. S. *The Crystal Structure of α-SiC, Type-IV*. *American Mineralogist*, vol. 29 (11-12) : 431-442 (1944). ISSN 0003-004X. 7.1

[259] Reuter, K. and Scheffler, M. *Composition, structure, and stability of RuO2 (110) as a function of oxygen pressure*. *Phys. Rev. B*, vol. 65 (3) : 035406 (December 2001).
[doi:10.1103/PhysRevB.65.035406]. (document), 4, 4.2

[260] Reuter, K., Stampf, C., and Scheffler, M. *Ab Initio Atomistic Thermodynamics and Statistical Mechanics of Surface Properties and Functions*. Springer Netherlands (2005).
[ISBN 978-1-4020-3287-5]. (document), 4

[261] Richter, N. A., Sicolo, S., Levchenko, S. V., Sauer, J., and Scheffler, M. *Concentration of Vacancies at Metal-Oxide Surfaces: Case Study of MgO(100)*. *Physical Review Letters*, vol. 111 : 045502 (July 2013).
[doi:10.1103/PhysRevLett.111.045502]. 6.3, 6.3, 12.2

[262] Riedl, C., Coletti, C., Iwasaki, T., Zakharov, A. A., and Starke, U.

Quasi-Free-Standing Epitaxial Graphene on SiC Obtained by Hydrogen Intercalation. *Phys. Rev. Lett.*, vol. 103 (24) : 246804 (December 2009). [doi:10.1103/PhysRevLett.103.246804]. 8.2, 13, 14.3

[263] Riedl, C., Coletti, C., and Starke, U. *Structural and electronic properties of epitaxial graphene on SiC(0 0 0 1): a review of growth, characterization, transfer doping and hydrogen intercalation*. *J. Phys. D: Appl. Phys.*, vol. 43 (37) : 374009 (2010). [doi:10.1088/0022-3727/43/37/374009]. (document), 0.1, 7, III, 8.2, 8.2, 8.2, 9.2, 12.1, 12, 12.1, 12.2, 12.3, 14.3, J

[264] Riedl, C., Starke, U., Bernhardt, J., Franke, M., and Heinz, K. *Structural properties of the graphene-SiC(0001) interface as a key for the preparation of homogeneous large-terrace graphene surfaces*. *Phys. Rev. B*, vol. 76 (24) : 245406 (December 2007). [doi:10.1103/PhysRevB.76.245406]. (document), III, 8, 8.2, 9.2

[265] Robertson, A. W., Montanari, B., *et al.* *Structural Reconstruction of the Graphene Monovacancy*. *ACS Nano*, vol. 7 (5) : 4495-4502 (2013). [doi:10.1021/nn401113r]. 9.3

[266] Roehrl, J., Hundhausen, M., Emtsev, K., Seyller, T., Graupner, R., and Ley, L. *Raman spectra of epitaxial graphene on SiC (0001)*. *Appl. Phys. Lett.*, vol. 92 (20) : 201918–201918 (March 2008). [doi:10.1063/1.2929746]. 9.1, i, 10

[267] Rohlfing, M. and Pollmann, J. *U Parameter of the Mott-Hubbard Insulator 6H-SiC (0001)-($\sqrt{3} \times \sqrt{3}$) R30°: An Ab Initio Calculation*. *Phys. Rev. Lett.*, vol. 84 (1) : 135–138 (2000). 8.1.1

[268] Rossini, F. D. and Jessup, R. S. *Heat and free energy of formation of carbon dioxide, and of the transition between graphite and diamond*. *Journal of research of the national bureau of standards*, vol. 21 : 491 - 513 (october 1938). [doi:10.6028/jres.021.028]. A

[269] Ruan, M., Hu, Y., *et al.* *Epitaxial graphene on silicon carbide: Introduction to structured graphene*. *MRS Bulletin*, vol. 37 : 1138–1147 (12 2012). [doi:10.1557/mrs.2012.231]. (document)

[270] Rutter, G., Guisinger, N., *et al.* *Imaging the interface of epitaxial graphene with silicon carbide via scanning tunneling microscopy*. *Phys. Rev. B*,

vol. 76 (23) : 235416 (December 2007).
[doi:10.1103/PhysRevB.76.235416]. 10, 12.1, 12.3, 14.3

[271] Rydberg, H., Dion, M., *et al.* *Van der Waals density functional for layered structures*. *Phys. Rev. Lett.*, vol. 91 (12) : 126402 (September 2003).
[doi:10.1103/PhysRevLett.91.126402]. 6.2, 6.2, J.1

[272] Sabatini, R., Gorni, T., and de Gironcoli, S. *Nonlocal van der Waals density functional made simple and efficient*. *Physical Review B*, vol. 87 : 041108 (January 2013).
[doi:10.1103/PhysRevB.87.041108]. 6.2, J.1

[273] Sabisch, M., Krüger, P., and Pollmann, J. *Ab initio calculations of structural and electronic properties of 6H-SiC(0001) surfaces*. *Phys. Rev. B*, vol. 55 (16) : 10561–10570 (April 1997).
[doi:10.1103/PhysRevB.55.10561]. 8.1.1, 8.1.1

[274] Santos, E. J. G., Riikonen, S., Sánchez-Portal, D., and Ayuela, A. *Magnetism of Single Vacancies in Rippled Graphene*. *The Journal of Physical Chemistry C*, vol. 116 (13) : 7602-7606 (2012).
[doi:10.1021/jp300861m]. 9.3, 9.3

[275] Schabel, M. C. and Martins, J. L. *Energetics of interplanar binding in graphite*. *Physical Review B*, vol. 46 : 7185–7188 (1992).
[doi:10.1103/PhysRevB.46.7185]. 6.2, J.1

[276] Schardt, J. *Komplexe Oberflächenstrukturen von Siliziumkarbid*. Ph.D. thesis (June 1999). (document), 8.1.1, 8.1.1, 8.1.2, 8.2, 8.1.2, I, I.1, J

[277] Schardt, J., Bernhardt, J., Starke, U., and Heinz, K. *Crystallography of the* (3×3) *surface reconstruction of 3C-SiC(111), 4H-SiC(0001), and 6H-SiC(0001) surfaces retrieved by low-energy electron diffraction*. *Phys. Rev. B*, vol. 62 (15) : 10335–10344 (2000).
[doi:10.1103/PhysRevB.62.10335]. 8.1.1, 13.1, 14.1.2

[278] Scheffler, M. *Lattice relaxations at substitutional impurities in semiconductors*. *Physica B+C*, vol. 146 (1-2) : 176 - 186 (1987). ISSN 0378-4363.
[doi:10.1016/0378-4363(87)90060-X]. 6.3, 12.2

[279] Scheffler, M. *Thermodynamic Aspects of Bulk and Surface Defects–First-Principle Calculations*. *Studies in Surface Science and Catalysis*, vol. 40 : 115–122 (1988).

http://th.fhi-berlin.mpg.de/site/uploads/Publications/Phys-of-Sol-Surfaces-1987-1988.pdf (document), 4

[280] Scheffler, M. and Dabrowski, J. *Parameter-free calculations of total energies, interatomic forces and vibrational entropies of defects in semiconductors*. *Philosophical Magazine A*, vol. 58 (1) : 107-121 (1988). [doi:10.1080/01418618808205178]. (document), 4

[281] Schmidt, D. A., Ohta, T., and Beechem, T. E. *Strain and charge carrier coupling in epitaxial graphene*. *Physical Review B*, vol. 84 : 235422 (December 2011). [doi:10.1103/PhysRevB.84.235422]. 9.1, 9.3

[282] Schubert, E. *Light-emitting Diodes*. Cambridge University Press (2003). [ISBN 0-521-82330-2]. 7

[283] Schumann, T., Dubslaff, M., Oliveira, M. H., Hanke, M., Lopes, J. M. J., and Riechert, H. *Effect of buffer layer coupling on the lattice parameter of epitaxial graphene on SiC(0001)*. *Phys. Rev. B*, vol. 90 : 041403 (Jul 2014). [doi:10.1103/PhysRevB.90.041403]. 9.1, 9.4, 14.3

[284] Schumann, T., Dubslaff, M., *et al.* *Structural investigation of nanocrystalline graphene grown on* $(6\sqrt{3}\times 6\sqrt{3})R30^{\circ}$*-reconstructed SiC surfaces by molecular beam epitaxy*. *New Journal of Physics*, vol. 15 (12) : 123034 (December 2013). [doi:10.1088/1367-2630/15/12/123034]. (document), 9.3, 9.3, 9.3, 9.2, 9.5, J

[285] Schwabl, F. *Eine Einführung*. Springer-Lehrbuch. Springer, Berlin, 7. aufl. ed. (2007). [ISBN 3-540-73674-3]. 1.1, 1.2

[286] Schwarz, K. and Blaha, P. *Solid state calculations using {WIEN2k}*. *Computational Materials Science*, vol. 28 (2) : 259 - 273 (2003). [doi:10.1016/S0927-0256(03)00112-5]. 2.5

[287] Schwierz, F. *Graphene transistors*. *Nature Nano*, vol. 5 (7) : 487 – 496 (2010). [doi:10.1038/nnano.2010.89]. (document), 6

[288] Sclauzero, G. and Pasquarello, A. *Stability and charge transfer at the interface between SiC (0001) and epitaxial graphene*. *Microelectronic En-*

gineering, vol. 88 (7) : 1478–1481 (April 2011).
[doi:10.1016/j.mee.2011.03.138]. 9.2, 9.2

[289] Sclauzero, G. and Pasquarello, A. *Carbon rehybridization at the graphene/SiC(0001) interface: Effect on stability and atomic-scale corrugation*. *Phys. Rev. B*, vol. 85 : 161405(R) (2012).
[doi:10.1103/PhysRevB.85.161405]. 9.2, 9.2

[290] Sclauzero, G. and Pasquarello, A. *Low-strain interface models for epitaxial graphene on SiC(0001)*. *Diamond Rel. Materials*, vol. 23 : 178–183 (2012).
[doi:10.1016/j.diamond.2011.11.001]. 9, 9.2, 9.2

[291] Seubert, A. *Holographische Methoden in der Oberflächenkristallographie mit Beugung langsamer Elektronen*. Ph.D. thesis (July 2002). 8.1.1, 14.1.1, 14.1.1

[292] Seubert, A., Bernhardt, J., Nerding, M., Starke, U., and Heinz, K. *In situ surface phases and silicon-adatom geometry of the (2x2)C structure on 6H-SiC(000$\bar{1}$*. *Surface Science*, vol. 454 – 456 (0) : 45 – 48 (2000).
[doi:10.1016/S0039-6028(00)00091-1]. (document), 14.1, 14.1.1, 14.1.1, 14.1.2, 14.7, J

[293] Seyller, T., Bostwick, A., *et al. Epitaxial graphene: a new material*. *phys. stat. sol. (b)*, vol. 245 (7) : 1436–1446 (2008).
[doi:10.1002/pssb.200844143]. 8.2

[294] Sforzini, J., Nemec, L., *et al. Approaching Truly Freestanding Graphene: The Structure of Hydrogen-Intercalated Graphene on 6H-SiC(0001)*. *Phys. Rev. Lett.*, vol. 114 : 106804 (March 2015).
[doi:10.1103/PhysRevLett.114.106804]. (document), 8.7, 13, 13.1, 13.1, J

[295] Shaffer, P. T. B. *Refractive Index, Dispersion, and Birefringence of Silicon Carbide Polytypes*. *Appl. Opt.*, vol. 10 (5) : 1034–1036 (May 1971).
[doi:10.1364/AO.10.001034]. 7

[296] Shek, M. L., Miyano, K. E., Dong, Q.-Y., Callcott, T. A., and Ederer, D. L. *Preliminary soft x-ray studies of β-SiC*. *Journal of Vacuum Science & Technology A*, vol. 12 (4) : 1079-1084 (1994).
[doi:10.1116/1.579288]. 7.2, 7.5, 7.2, J

[297] Silvestrelli, P. L. *Van der Waals interactions in DFT made easy by Wannier*

functions. *Physical Review Lett.*, vol. 100 (5) : 053002 (February 2008).
[doi:10.1103/PhysRevLett.100.053002].
[arxiv:0708.4269]. J.1

[298] Silvestrelli, P. L. *Van der Waals interactions in density functional theory by combining the quantum harmonic oscillator-model with localized Wannier functions*. *The Journal of Chemical Physics*, vol. 139 (5) : 054106 (2013).
[doi:10.1063/1.4816964]. J.1

[299] Spanu, L., Sorella, S., and Galli, G. *Nature and Strength of Interlayer Binding in Graphite*. *Phys. Rev. Lett.*, vol. 103 : 196401 (November 2009).
[doi:10.1103/PhysRevLett.103.196401]. 6.2, J.1

[300] SpringerMaterials. *Material Phases Data System (MPDS)* (????). Dataset ID: ppp_032206.
http://materials.springer.com/isp/physical-property/docs/ppp_032206 1

[301] Sprinkle, M., Siegel, D., *et al.* *First Direct Observation of a Nearly Ideal Graphene Band Structure*. *Physical Review Letters*, vol. 103 : 226803 (November 2009).
[doi:10.1103/PhysRevLett.103.226803]. (document)

[302] Srivastava, N., He, G., Luxmi, and Feenstra, R. M. *Interface structure of graphene on SiC(000$\bar{1}$)*. *Phys. Rev. B*, vol. 85 (4) : 041404 (January 2012).
[doi:10.1103/PhysRevB.85.041404]. (document), a, 4.2, III, 14.2, 14.2, 14.3

[303] Srivastava, N., He, G., Luxmi, Mende, P. C., Feenstra, R. M., and Sun, Y. *Graphene formed on SiC under various environments: comparison of Si-face and C-face*. *J. Phys. D: Appl. Phys.*, vol. 45 : 154001 (2012). 14.2

[304] Starke, U. *Atomic Structure of Hexagonal SiC Surfaces*. *physica status solidi (b)*, vol. 202 (1) : 475–499 (1997). ISSN 1521-3951.
[doi:10.1002/1521-3951(199707)202:1<475::AID-PSSB475>3.0.CO;2-E]. (document), 8.1.1, 14.1, 14.1.1

[305] Starke, U., Bernhardt, J., Schardt, J., and Heinz, K. *SiC surface reconstruction: Relevancy of atomic structure for growth technology*. *Surface Review and Letters*, vol. 6 (6) : 1129–1142 (1999).
[doi:10.1142/S0218625X99001256]. 8.1.1, 8.1.1, 8.1.1

[306] Starke, U., Franke, M., Bernhardt, J., Schardt, J., Reuter, K., and Heinz, K. *Large Unit Cell Superstructures on Hexagonal SiC-Sufaces Studied by LEED, AES and STM*. *Materials Science Forum*, (p. 321–326) (1998). [doi:10.4028/www.scientific.net/MSF.264-268.321]. 8.1.2, I

[307] Starke, U. and Riedl, C. *Epitaxial graphene on SiC(0001) and* SiC$(000\bar{1})$ *: from surface reconstructions to carbon electronics*. *J. Phys.: Condens. Matter*, vol. 21 (13) : 134016 (2009). [doi:10.1088/0953-8984/21/13/134016]. (document), b, 8.2, 8.2, 9.2, 14.1

[308] Starke, U., Schardt, J., Bernhardt, J., Franke, M., and Heinz, K. *Stacking Transformation from Hexagonal to Cubic SiC Induced by Surface Reconstruction: A Seed for Heterostructure Growth*. *Phys. Rev. Lett.*, vol. 82 (10) : 2107–2110 (March 1999). [doi:10.1103/PhysRevLett.82.2107]. (document), 8, 14.1.1

[309] Starke, U., Schardt, J., and Franke, M. *Morphology, bond saturation and reconstruction of hexagonal SiC surfaces*. *Applied Physics A*, vol. 65 (6) : 587-596 (1997). ISSN 0947-8396. 8.1.2, 14.1.1

[310] Starke, U., Schardt, J., *et al.* *Novel Reconstruction Mechanism for Dangling-Bond Minimization: Combined Method Surface Structure Determination of SiC*(111)- (3×3). *Phys. Rev. Lett.*, vol. 80 (4) : 758–761 (January 1998). [doi:10.1103/PhysRevLett.80.758]. (document), 8, 8.1.2, 14.1.2, 14.7, 14.1.3, J

[311] Staroverov, V. N., Scuseria, G. E., Tao, J., and Perdew, J. P. *Tests of a ladder of density functionals for bulk solids and surfaces*. *Physical Review B*, vol. 69 : 075102 (February 2004). [doi:10.1103/PhysRevB.69.075102]. 2.3.2

[312] Staroverov, V. N., Scuseria, G. E., Tao, J., and Perdew, J. P. *Erratum: Tests of a ladder of density functionals for bulk solids and surfaces [Phys. Rev. B 69 075102 (2004)]*. *Physical Review B*, vol. 78 : 239907 (December 2008). [doi:10.1103/PhysRevB.78.239907]. 2.3.2

[313] Strössner, K., Cardona, M., and Choyke, W. *High pressure X-ray investigations on 3C-SiC*. *Solid State Communications*, vol. 63 (2) : 113 - 114 (1987). ISSN 0038-1098. [doi:10.1016/0038-1098(87)91176-8]. 1, 7.1

[314] Strutyński, K., Melle-Franco, M., and Gomes, J. A. N. F. *New Parameterization Scheme of DFT-D for Graphitic Materials*. *The Journal of Physical Chemistry A*, vol. 117 (13) : 2844-2853 (2013).
[doi:10.1021/jp312239n]. J.1

[315] Tanabe, S., Takamura, M., Harada, Y., Kageshima, H., and Hibino, H. *Effects of hydrogen intercalation on transport properties of quasi-free-standing monolayer graphene Effects of hydrogen intercalation on transport properties of quasi-free-standing monolayer graphene SiC(0001)*. *Japanese Journal of Applied Physics*, vol. 53 (04EN01) (2014).
[doi:10.7567/JJAP.53.04EN01]. (document)

[316] Tanaka, S., Kern, R. S., and Davis, R. F. *Effects of gas flow ratio on silicon carbide thin film growth mode and polytype formation during gas-source molecular beam epitaxy*. *Applied Physics Letters*, vol. 65 (22) : 2851-2853 (1994).
[doi:10.1063/1.112513]. 8.1.2

[317] Taylor, T. A. and Jones, R. M. *Silicon Carbide, a High Temperature Semiconductor* (????). 7.1, i

[318] Telling, R. H. and Heggie, M. I. *Stacking fault and dislocation glide on the basal plane of graphite*. *Philos. Mag. Lett.*, vol. 83 : 411–421 (2003).
[doi:10.1080/0950083031000137839]. 6.2, J.1

[319] Themlin, J.-M., Forbeaux, I., Langlais, V., Belkhir, H., and Debever, J.-M. *Unoccupied surface state on the ($\sqrt{3} \times \sqrt{3}$)-R30° of 6H-SiC(0001)*. *EPL (Europhysics Letters)*, vol. 39 (1) : 61 (1997).
[doi:10.1209/epl/i1997-00314-9]. 8.1.1

[320] Thewlis, J. and Davey, A. R. *XL. Thermal expansion of diamond*. *Philosophical Magazine*, vol. 1 (5) : 409-414 (1956).
[doi:10.1080/14786435608238119]. A, A.2, J

[321] Thomson Reuters, C. *Web of Science* (2014).
http://www.webofknowledge.com 6.2, J

[322] Thonhauser, T., Cooper, V. R., Li, S., Puzder, A., Hyldgaard, P., and Langreth, D. C. *Van der Waals density functional: Self-consistent potential and the nature of the van der Waals bond*. *Physical Review B*, vol. 76 : 125112 (September 2007).
[doi:10.1103/PhysRevB.76.125112]. 6.2

[323] Thrower, J. D., Friis, E. E., *et al.* *Interaction between Coronene and Graphite from Temperature-Programmed Desorption and DFT-vdW Calculations: Importance of Entropic Effects and Insights into Graphite Interlayer Binding*. *The Journal of Physical Chemistry C*, vol. 117 (26) : 13520-13529 (2013). [doi:10.1021/jp404240h]. 6.2, J.1

[324] Tkatchenko, A., Ambrosetti, A., and DiStasio, R. A. *Interatomic Methods for the Dispersion Energy Derived from the Adiabatic Connection Fluctuation-Dissipation Theorem*. *The Journal of Chemical Physics*, vol. 138 (7) : 074106 (2013). [doi:10.1063/1.4789814]. 2.4, 6.2, 6.5, 6.2, 7.1, F.1, J

[325] Tkatchenko, A., DiStasio, R. A., Car, R., and Scheffler, M. *Accurate and Efficient Method for Many-Body van der Waals Interactions*. *Phys. Rev. Lett.*, vol. 108 : 236402 (June 2012). [doi:10.1103/PhysRevLett.108.236402]. 2.4, 6.2, 6.5, 6.2, 7.1, F.1, J

[326] Tkatchenko, A. and Scheffler, M. *Accurate Molecular Van Der Waals Interactions from Ground-State Electron Density and Free-Atom Reference Data*. *Phys. Rev. Lett.*, vol. 102 (7) : 073005 (February 2009). [doi:10.1103/PhysRevLett.102.073005]. (document), 2.4, 2.4, 6.2, 6.5, 6.2, 7.1, 8, 9.3, 14.3, B.3, F.1, I, J

[327] Togo, A., Oba, F., and Tanaka, I. *First-principles calculations of the ferroelastic transition between rutile-type and CaCl2-type SiO2 at high pressures*. *Physical Review B*, vol. 78 : 134106 (October 2008). 1, D

[328] Tran, F., Laskowski, R., Blaha, P., and Schwarz, K. *Performance on molecules, surfaces, and solids of the Wu-Cohen GGA exchange-correlation energy functional*. *Physical Review B*, vol. 75 : 115131 (March 2007). [doi:10.1103/PhysRevB.75.115131]. 2.3.2

[329] Tromp, R. M. and Hannon, J. B. *Thermodynamics and kinetics of graphene growth on SiC (0001)*. *Phys. Rev. Lett.*, vol. 102 (10) : 106104 (March 2009). [doi:10.1103/PhysRevLett.102.106104]. (document), 4.2, 10

[330] Trucano, P. and Chen, R. *Structure of graphite by neutron diffraction*. *Nature*, vol. 258 : 136–137 (November 1975). [doi:10.1038/258136a0]. 6.1

[331] Tuinstra, F. and Koenig, J. L. *Raman Spectrum of Graphite*. *The Journal*

of Chemical Physics, vol. 53 (3) (1970). D.1.1

[332] Van Bommel, A., Crombeen, J., and Van Tooren, A. *LEED and Auger electron observations of the SiC (0001) surface*. *Surf. Sci.*, vol. 48 (2) : 463–472 (October 1975).
[doi:10.1016/0039-6028(75)90419-7]. (document), III, 8, 8.1.1, 8.2, 14.1, 14.3

[333] Van Noorden, R. *Moving towards a graphene world*. *Nature*, vol. 442 (7100) : 228 – 229 (2006).
[doi:10.1038/442228a]. 6

[334] Varchon, F., Feng, R., *et al.* *Electronic structure of epitaxial graphene layers on SiC: effect of the substrate*. *Phys. Rev. Lett.*, vol. 99 (12) : 126805 (2007).
[doi:10.1103/PhysRevLett.99.126805]. (document), a, III, 8.2, 9.2, 9.2, 9.2, 12, 12.1, B.1, B.2

[335] Varchon, F., Mallet, P., Veuillen, J.-Y., and Magaud, L. *Ripples in epitaxial graphene on the Si-terminated SiC(0001) surface*. *Phys. Rev. B*, vol. 77 (23) : 235412 (June 2008).
[doi:10.1103/PhysRevB.77.235412]. 8.2, 8.2, 9.2, 12.1

[336] Vegard, L. *Die Konstitution der Mischkristalle und die Raumfüllung der Atome*. *Zeitschrift fÃ¼r Physik*, vol. 5 (1) : 17-26 (1921). ISSN 0044-3328.
[doi:10.1007/BF01349680]. 6.3, 12.2

[337] Veuillen, J., Hiebel, F., Magaud, L., Mallet, P., and Varchon, F. *Interface structure of graphene on SiC: an ab initio and STM approach*. *J. Phys. D: Appl. Phys.*, vol. 43 : 374008 (2010).
[doi:10.1088/0022-3727/43/37/374008]. (document), b, III

[338] Wallace, P. R. *The Band Theory of Graphite*. *Phys. Rev.*, vol. 71 : 622–634 (May 1947).
[doi:10.1103/PhysRev.71.622]. (document), 6

[339] Wang, J., Zhang, L., Zeng, Q., Vignoles, G., and Cheng, L. *Surface relaxation and oxygen adsorption behavior of different SiC polytypes: a first-principles study*. *J. Phys.: Condens. Matter*, vol. 22 (26) : 265003 (May 2010).
[doi:10.1088/0953-8984/22/26/265003]. 13.1

[340] Weinert, C. M. and Scheffler, M. *Chalcogen and vacancy pairs in silicon:*

Electronic structure and stabilities. *Defects in Semiconductors*, vol. 10-12 : 25–30 (1986). (document), 4

[341] Wenzien, B., Käckell, P., Bechstedt, F., and Cappellini, G. *Quasiparticle band structure of silicon carbide polytypes*. *Physical Review B*, vol. 52 : 10897–10905 (October 1995).
[doi:10.1103/PhysRevB.52.10897]. 7.2, 7.2

[342] Whitney, E. D. *Polymorphism in Silicon Carbide*. *NATURE*, vol. 199 (489) : 278-280 (1963).
[doi:10.1038/199278b0]. 7.1

[343] Wu, Q. and Yang, W. *Empirical correction to density functional theory for van der Waals interactions*. *The Journal of Chemical Physics*, vol. 116 (2) : 515-524 (2002).
[doi:10.1063/1.1424928]. 2.4, 6.2

[344] Wu, Y. Q., Ye, P. D., *et al. Top-gated graphene field-effect-transistors formed by decomposition of SiC*. *Applied Physics Letters*, vol. 92 (9) : 092102 (2008).
[doi:http://dx.doi.org/10.1063/1.2889959]. (document)

[345] Yang, Y. T., Ekinci, K. L., *et al. Monocrystalline silicon carbide nano-electromechanical systems*. *Applied Physics Letters*, vol. 78 (2) : 162-164 (2001).
[doi:10.1063/1.1338959]. 7

[346] Yazdi, G. R., Vasiliauskas, R., Iakimov, T., Zakharov, A., Syväjärvi, M., and Yakimova, R. *Growth of large area monolayer graphene on 3C-SiC and a comparison with other SiC polytypes*. *Carbon*, vol. 57 : 477–484 (2013). (document), 14.3

[347] Yin, M. T. and Cohen, M. L. *Phys. Rev. B*, vol. 29 : 6996 (1984). 4.2, 6.1, 14.1.2

[348] Yu, C.-J., Ri, G.-C., Jong, U.-G., Choe, Y.-G., and Cha, S.-J. *Refined phase coexistence line between graphite and diamond from density-functional theory and van der Waals correction*. *Physica B: Condensed Matter*, vol. 434 : 185 - 193 (2014).
[doi:10.1016/j.physb.2013.11.013]. 4.2, 14.1.2

[349] Yu, C.-J., Ri, G.-C., Jong, U.-G., Choe, Y.-G., and Cha, S.-J. *Refined phase coexistence line between graphite and diamond from density-functional*

theory and van der Waals correction. *Physica B: Condensed Matter*, vol. 434 : 185 - 193 (February 2014). ISSN 0921-4526.
[doi:10.1016/j.physb.2013.11.013]. 6.1, A, A, A.1, A, A.2, J

[350] Zacharia, R., Ulbricht, H., and Hertel, T. *Interlayer cohesive energy of graphite from thermal desorption of polyaromatic hydrocarbons*. *Phys. Rev. B*, vol. 69 : 155406 (April 2004).
[doi:10.1103/PhysRevB.69.155406]. 6.2, 6.4, 6.2, 6.5, 6.2, J.1, J

[351] Zhang, Y., Jiang, Z., *et al.* *Landau-Level Splitting in Graphene in High Magnetic Fields*. *Phys. Rev. Lett.*, vol. 96 (13) : 136806 (2006).
[doi:10.1103/PhysRevLett.96.136806]. (document)

[352] Zhechkov, L., Heine, T., Patchkovskii, S., Seifert, G., and Duarte, H. A. *An Efficient a Posteriori Treatment for Dispersion Interaction in Density-Functional-Based Tight Binding*. *J. Chem. Theory Comput.*, vol. 1 : 841 -847 (2005).
[doi:10.1021/ct050065y]. J.1

[353] Zheng, Q., Jiang, B., *et al.* *Self-Retracting Motion of Graphite Microflakes*. *Physical Review Letters*, vol. 100 : 067205 (February 2008).
[doi:10.1103/PhysRevLett.100.067205]. 6.2

[354] Ziambaras, E., Kleis, J., Schröder, E., and Hyldgaard, P. *Potassium intercalation in graphite: A van der Waals density-functional study*. *Physical Review B*, vol. 76 (15) : 155425 (October 2007).
[doi:10.1103/PhysRevB.76.155425].
[arxiv:0704.0055]. J.1

[355] Zywietz, A., Furthmüller, J., and Bechstedt, F. *Vacancies in SiC: Influence of Jahn-Teller distortions, spin effects, and crystal structure*. *Physical Review B*, vol. 59 (23) : 15166 (June 1999).
[doi:10.1103/PhysRevB.59.15166]. 7.1, 7.1, 7.2, J

Acknowledgements

The theory department of the Fritz Haber Institute (FHI) is a unique place with endless possibilities. I would like to thank Matthias Scheffler for giving me the opportunity to carry out the work leading to the PhD thesis presented here. I had the privilege to benefit from all what the FHI theory department has to offer. I had the opportunity to work on an exceptionally fascinating project in a very active and motivated group. I was given the chance to discuss my work with well-known experts at the department and on various conferences. Matthias, thank you for your continuous support, for sharing your experience and your expertise.

I further want to thank my two supervisors Volker Blum and Patrick Rinke. Volker, thank you for your never-ending enthusiasm for the project. All your late night work, even if it was not directly linked to my project, is highly appreciated. Patrick, thank you for being a wonderful group leader and a remarkably brilliant scientist, but most importantly for your friendship. I am very grateful that I could always rely on the two of you.

I am fortunate to be able to claim that I worked in one office with the best office mates imaginable: Carsten Baldauf, Franz Knuth and Florian Lazarevic. Carsten, our projects could not have been more different and yet there is so much I learned from you. I am picturing us being old and grey, sitting together with a hot beverage laughing about the old times and the vagaries of life, shall we set a date? Franz, you are most certainly an exceptionally gifted scientist and I had more than once the opportunity to benefit from your insights. However, I admire your baking skills - they are legendary. Florian Lazarevic, you are the first master student I accompanied, you made it a very rewarding experience.

I would also like to thank the HIOS team for adopting me into their group. Björn, Oliver and Patrick: your team spirit and our weekly meetings were a true enrichment. My dear lunch-time buddies, Carsten, Patrick, Oliver, Björn, Franz, Anthony, Markus and Arvid: your company while eating questionable mensa food made even the most ordinary day special – thanks for that. Wael, Honghui, Arvid, Julia and Patrick: I loved our lunch-time-runs. Hey, shall we have one next week or what about going for a run before breakfast at our next conference?

From the bottom of my heart, I like to thank all my proof readers: Viktor, Christian, Franz, Norina, Björn, Oliver, Luca, Patrick, Volker and my hus-

band Norbert.

I have not yet thanked all the Willstatians: your presence shaped the atmosphere in the Richard Willstätter Haus (RWH), turning it into a positive, supportive and most enjoyable workplace. It will be hard to find a workplace that is just remotely as fantastic as the RWH with you all in it. However, the FHI theory department is more than just the RWH. I would like to thank all my collegues and friends, who carried part of the work load at organising workshops, exercise groups, fare-wells, barbeques and the annual Christmas party. In particular, Christian Carbongo, I had the pleasure to be part of the preparation team of the Hands-On workshop 2014. If you ever end up organising a workshop again, do not forget to call me. I also would like to thank my collegues I shared a hotel room with during a conference: Franziska, Adriana, Tanja and Honghui you are genuinely wonderful room mates.

I also like to thank my collaborators. Timo Schumann, Myriano Oliveira and Marcelo Lopes from the Paul Drude Institut: our meetings and discussions have been truly inspiring. François Bocquet, Jessica Sforzini and Stefan Tautz from the Forschungszentrum Jülich: working with you on our joined publication showed me how much fun writing a paper can be. Randall Feenstra and Michael Widom from the Carnegie Mellon University, US: will we manage to unveil the secret of the SiC-graphene interface on the carbon side? Being part of such a challenging project and working with you is an honour! Silke Biermann and Philipp Hansmann from the École Polytechnique, Palaiseau: there is so much I learnt from you.

Alejandro, Samual and Yannick: meeting you on conferences, hanging out with you seriously discussing science or simply being silly is always fun. I would like to thank Heidi helping me with writing press releases and abstracts. A big thank you goes to everyone training side-by-side with me in the dance hall. Dancing with you guys takes my mind off work to give me a chance to re-energise and start working on my projects fresh and motivated.

Finally, I would like to say thank you to my close friends and my family. Dear Pasquale, we met at my very first week at the University of Regensburg. Before I had my first lecture, I already had a friend in you. I am proud to say I am a friend of the King of Phonons. I like to thank my family for their constant support and love. Jasmin, over the years I had in you one of my strongest supporters and a close friend – thank you. I like to thank my husband, Norbert, and my son, Paul for their love, support and understanding. Thanks for listening to to all my *today-in-the-office* stories.

- Nemec, L., Blum, V., Rinke, P., and Scheffler, M.
  Thermodynamic Equilibrium Conditions of Graphene Films on SiC.
  Phys. Rev. Lett., vol. 111 : 065502 (August 2013).
  [doi:10.1103/PhysRevLett.111.065502].

- Schumann, T., Dubslaff, M., Oliveira Jr, M. H., Hanke, M., Fromm, F., Seyller, T., Nemec, L., Blum, V., Scheffler, M., Lopes, J. M. J. and Riechert, H.
  Structural investigation of nanocrystalline graphene grown on $(6\sqrt{3} \times 6\sqrt{3})R30^{\circ}$*-reconstructed SiC surfaces by molecular beam epitaxy*.
  New Journal of Physics, vol. 15 (12) : 123034 (December 2013).
  [doi:10.1088/1367-2630/15/12/123034].

- Sforzini, J., Nemec, L., Denig, T., Stadtmüller, B., Lee, T.-L., Kumpf, C., Soubatch, S., Starke, U., Rinke, P., Blum, V., Bocquet, F. C. and Tautz, F. S.
  Approaching Truly Freestanding Graphene: The Structure of Hydrogen-Intercalated Graphene on 6H-SiC(0001).
  Phys. Rev. Lett., vol. 114 : 106804 (March 2015).
  [doi:10.1103/PhysRevLett.114.106804].

- Nemec, L., Lazarevic, F., Rinke, P., Scheffler, M., and Blum, V.
  Why graphene growth is very different on the C face than on the Si face of SiC: Insights from surface equilibria and the (3×3)*-3C-SiC*$(\bar{1}\bar{1}\bar{1})$ *reconstruction*.
  Phys. Rev. B: Rapid Comm., vol. 91: 161408 (April 2015).
  [doi:10.1103/PhysRevB.91.161408].

Selbständigkeitserklärung

Hiermit erkläre ich, die Dissertation selbstständig und nur unter Verwendung der angegebenen Hilfen und Hilfsmittel angefertigt zu haben. Ich habe mich anderwärts nicht um einen Doktorgrad beworben und besitze keinen entsprechenden Doktorgrad.

Ich erkläre die Kenntnisnahme der dem Verfahren zugrunde liegenden Promotionsordnung der Mathematisch-Naturwissenschaftlichen Fakultät der Humboldt Universität zu Berlin.

Berlin, den 26.05.2015

Lydia Nemec